2018

An Axion Search With The Majorana Demonstrator

Clinton Gray Wiseman
University of South Carolina

Recommended Citation

Wiseman, C.(2018). *An Axion Search With The Majorana Demonstrator.* (Doctoral dissertation). Retrieved from https://scholarcommons.sc.edu/etd/4970

An Axion Search With The Majorana Demonstrator

by

Clinton Gray Wiseman

Bachelor of Science
University of Kansas 2011

Submitted in Partial Fulfillment of the Requirements
for the Degree of Doctor of Philosophy in
Physics
College of Arts and Sciences
University of South Carolina
2018

Accepted by:

Vincente Guiseppe, Major Professor

Frank Avignone, Committee Member

David Tedeschi, Committee Member

Steven Elliott, Committee Member

Cheryl L. Addy, Vice Provost and Dean of the Graduate School

DEDICATION

To Shannon, for her unwavering support,
and for filling our house with boundless love,
whatever city we're in. You're my sunshine.
And to Money the rabbit, for being such a
wonderfully fuzzy writing buddy.

ACKNOWLEDGMENTS

I would like to thank Vincente Guiseppe for his mentorship and guidance. He is a consummate professional, and has given me more great advice than I know what to do with. To Vince, thanks for introducing me to the New Mexico Hatch chile and showing me how real experiments are built. To Frank Avignone, I'm glad that almost six years after you proposed this project to me I can finally deliver you some answers. Thanks to my fellow graduate students Ken Stephenson, Ricardo Hernandez, Nick Tyler, and Cory Dolbashian, who all gave me innumerable opportunities for stimulation and distraction. Finally, special thanks to Bill and Kathy Wiseman for the gift of education and doing their best to raise me right.

The best decision I made in graduate school was to get involved with MAJORANA. The collaboration is full of incredibly talented people who have helped me in so many ways. Brian Zhu has been the best analysis partner I could ask for, and the input of Ben Shanks, Graham Giovanetti, and Wenqin Xu has been invaluable in fleshing out the ideas in this thesis. I spent time at Los Alamos National Laboratory through a DOE SCGSR fellowship, where Steve Elliott, Brian Zhu, Brandon White, Ralph Massarczyk, and Pinghan Chu helped make the experience of living on the mesa unforgettable. I had a lot of fun with Robert Pattie and the gang at Bathtub Row Brewing, just across the street from Oppenheimer and Bethe's houses.

While I was on-site in South Dakota, Julieta Gruszko, Adam Bradley, Clara Cuesta, Micah Buuck, Ian Guinn, Tom Gilliss, Sam Meijer, Robyn Varland, and my bandmate Matthew Busch made some very long days in a laboratory a mile underground worth all the trouble.

ABSTRACT

The MAJORANA DEMONSTRATOR is an array of P-type point contact (PPC) germanium detectors enclosed in a multi-layered shield at the 4850' level of the Sanford Underground Research Facility. Its primary goal is to search for the neutrinoless double beta decay of ^{76}Ge. The initial 10 kg-y dataset, taken over a two year period, has energy thresholds as low as 1 keV. This allows concurrent rare event searches for the signatures of dark matter and solar axions in the low energy spectrum. Though the detectors are routinely operated with sub-keV energy thresholds, changing noise conditions in the array have made it challenging to reliably discriminate true physics signals from noise at the lowest energies. New pulse shape analysis (PSA) techniques have been developed to remove electronics noise, and reject energy-degraded "slow" events in the data. A novel training set of low energy small-angle Compton scatter events is used to determine the efficiency of the PSA cuts to 1 keV, the lowest energy threshold analyzed to date by MAJORANA. This dissertation gives an overview of the neutrino and axion physics relevant to the DEMONSTRATOR, presents the PSA techniques and their application to the low energy data set, and gives results from a search for solar axions.

TABLE OF CONTENTS

List of Tables

List of Figures

Chapter 1

Neutrino and Axion Physics

1.1 Symmetries in the Standard Model

Developed in the 1960s and 1970s, the Standard Model of particle physics represents a highly successful unification of three of the four known fundamental forces. Electromagnetism can be combined with the weak and strong nuclear forces in terms of an effective Lagrangian $\mathcal{L}$, describing the fundamental fields, particles, and allowed interaction terms. These interactions generally obey one or more discrete symmetries, where physical (or simply "allowed") behavior results under different transformations. For example, the C (charge) symmetry transformation replaces every particle in an interaction with its antiparticle (e.g. an electron is exchanged for a positron). The P (parity) transformation inverts the three spatial axes, replacing $\vec{x} \rightarrow -\vec{x}$, changing the helicity (projection of spin onto the direction of momentum) of a particle. Finally, under the T (time) transformation, the direction of time is reversible; the movie "looks physical" when played forward or backward.

The famous 1957 experiment by Wu, Ambler, and a team from the National Bureau of Standards [1] demonstrated that the weak interaction violates P-symmetry, by observing asymmetries due to neutrinos in the angular distribution of ^{60}Co decay products. Combined with the results of the later Goldhaber experiment [2], it was discovered that only certain types of neutrinos are observed in nature. As depicted in Figure 1.1, left-handed antineutrinos are not observed (violating C symmetry), nor are right-handed neutrinos (violating P symmetry). Despite failing to observe C

and P symmetry separately, the neutrino seems to obey the combination of the two symmetries, CP: applying C to a ν_L gives a $\bar{\nu_L}$ (not observed), then applying P in succession gives an allowed state, $\bar{\nu_R}$.

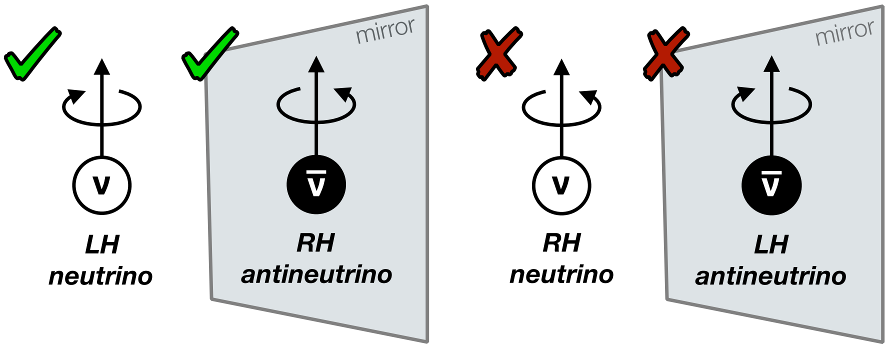

Figure 1.1: Right-handed neutrinos and left-handed antineutrinos are not observed in nature. (Illustration adapted from [3].)

Despite its numerous successes, the Standard Model is by no means a complete description of nature, even without considering gravity. Experimental tests of physics beyond the Standard Model (often abbreviated BSM) have shed light on a variety of important topics. Today, it is known that the massless neutrino described by the Standard Model does not exist. In addition to having a nonzero mass, the neutrinos we observe exist as a quantum superposition of three "flavors," electron (ν_e), muon (ν_μ) and tau (ν_τ). The probability to detect a neutrino as a particular flavor "oscillates," which we discuss in Section 1.2. Several unknowns remain; whether neutrinos violate CP, the exact mechanism allowing neutrino mass to be nonzero, and whether the neutrino is its own antiparticle – a Majorana fermion. Depending on the answers to these questions, neutrinos may play a pivotal role in explaining the observed matter-antimatter asymmetry in the Universe. Sections 1.2 and 1.3 discusses the current state of neutrino physics in more detail.

The abnormal behavior of the neutrino is by no means the only indication of a need to search for new physics; the neutron offers a clue as well. If the neutron violates CP symmetry, then the arrangement of its constituents (quarks and gluons) will not be perfectly spherical and it will possess a small electric dipole moment d_n, due to the asymmetry. The original choice for the QCD coupling constants for the neutron results in a prediction for the neutron electric dipole moment:

$$d_n \approx 10^{-16}\ e \cdot cm \tag{1.1}$$

Experimentally, it has been shown that d_n is at least *ten orders of magnitude* smaller than the above value. Direct (model-independent) measurements on free neutrons [4] give:

$$d_n < 3 \times 10^{-26}\ e \cdot cm \tag{1.2}$$

Measurements have also been carried out on trapped atoms such as ^{199}Hg [5], where a single valence neutron is the main contributor, resulting in an even more stringent but model-dependent limit, $d_n < 1.6 \times 10^{-26}\ e \cdot cm$.

The physics underlying d_n are flavor-conserving strong interactions from quantum chromodynamics (QCD), and result in CP-violation. Yet evidently, the strong force *rigorously* obeys conservation of CP, even despite the presence of CP-violating terms in the Standard Model. The CKM mixing matrix [6][7] describes the mixing of quark generations and contains a nonzero CP-violating term. Similarly, the mixing of the neutrino generations given by the PMNS matrix [8] contains a CP-violating phase δ_{CP}. While experiments have constrained its value, the current measurement error does not exclude $\delta_{CP} = 0$. Neither type of mixing plays a role in the flavor-conserving strong interactions, and the lack of a definitive explanation for the extraordinarily small value of d_n has become known as the *strong-CP problem*. We return to this problem in Section 1.5 to discuss an appealing solution; the *axion*.

1.2 NEUTRINOS

After the neutrino was proposed by Pauli in 1930, Fermi's 1934 paper on β-decay [9] established a theoretical framework for a single neutrino. The paper described a massless, spin-1/2, neutral particle, with an extremely small cross section for interaction with normal matter. In 1956, the reactor experiments by Reines and Cowan [10] were the first to directly detect neutrinos, and demonstrated the existence of *anti*neutrinos, which have opposite helicity and a "lepton number" $\ell = -1$. Certain reactions not observed in the reactor experiment are explained by their lack of lepton number conservation. For example, $\bar{\nu} + n \to p + e^-$ does not conserve lepton number; $\bar{\nu}$ has $\ell = -1$, the e^- has $\ell = 1$. [1] In 1964, the discovery of a second kind of neutrino associated with the muon ν_μ [11] led to a description of neutrino flavors, while the third generation ν_τ was not observed experimentally until 2000 [12]. Massless neutrinos of three flavors were incorporated into the Standard Model, but discrepancies with experiment would soon render them obsolete.

Originating in the 1960s, the "solar neutrino problem" resulted from the disagreement between the theoretical prediction of the neutrino flux from the Sun, and the measured value from early neutrino detectors. The first underground neutrino detector operated from 1968 to 1994 at the Homestake gold mine in Lead, South Dakota, and detected only about one-third [13][14] of the predicted number of neutrinos from the well-established model of the solar fusion process [15]. Compounding the issue, in the 1980s, the Kamiokande-II detector in Japan found one-half the predicted flux [16].

In 1969, Pontecorvo [17] proposed the idea that neutrinos originating from the Sun may be oscillating between flavor states in-flight, with the Homestake detector only sensitive to reactions involving the electron neutrino ν_e. The transformation

---

[1] Not being leptons, the n and p do not contribute.

between mass eigenstates i and flavor eigenstates f in its modern form is given by:

$$|\nu_f\rangle = \sum_{i=1}^{3} U_{fi}\,|\nu_i\rangle = U_{f1}\,|\nu_1\rangle + U_{f2}\,|\nu_2\rangle + U_{f3}\,|\nu_3\rangle \tag{1.3}$$

In this expression, the observed neutrino flavor eigenstate ν_f exists as a superposition of the three mass eigenstates ν_i, with the mixing determined by the components of the matrix U_{fi}. An important consequence of Pontecorvo's theory of neutrino oscillation is that the neutrino must not be massless; otherwise the flavor eigenstates are degenerate and there is no meaningful distinction between them. A standard expression of the PMNS mixing matrix [8] is given by Equation 1.4 for a neutrino obeying the Dirac equation. It is written in terms of the sines $s_{\alpha\beta}$ and cosines $c_{\alpha\beta}$ of the mixing angles $\theta_{\alpha\beta}$, and includes a CP-violating phase term δ_{CP}. [2]

$$U = \begin{pmatrix} 1 & 0 & 0 \\ 0 & c_{23} & s_{23} \\ 0 & -s_{23} & c_{23} \end{pmatrix} \begin{pmatrix} c_{13} & 0 & s_{13}e^{-i\delta_{CP}} \\ 0 & 1 & 0 \\ -s_{13}e^{i\delta_{CP}} & 0 & c_{13} \end{pmatrix} \begin{pmatrix} c_{12} & s_{12} & 0 \\ -s_{12} & c_{12} & 0 \\ 0 & 0 & 1 \end{pmatrix} \tag{1.4}$$

In 1998, oscillations of atmospheric neutrinos were discovered with the Super-Kamiokande detector [18], unambiguously establishing that neutrinos have a nonzero mass. The final resolution of the solar neutrino problem came in 2001 when the Sudbury Neutrino Observatory loaded its liquid volume with heavy water, enabling the simultaneous measurement of the ν_e and $\nu_\mu + \nu_\tau$ rates, bringing the observed flux of ^{8}B neutrinos into agreement with the original prediction of the standard solar model of Bahcall et al [15]. A large number of experiments have since been carried out to measure various neutrino properties, including the “mixing angles” $\theta_{\alpha\beta}$ and probe the differences between the neutrino mass eigenstates.

A simple illustration of neutrino oscillation is given by considering only two neutrino flavors α, β, and calculating the survival probavility for a given neutrino flavor

---

[2] The PMNS matrix describing Majorana neutrinos contains two additional phase terms.

not to oscillate into another flavor:

$$\begin{aligned} P_{\text{survival}} &= 1 - P(\alpha \to \beta) \\ &= 1 - \sin^2(2\theta_{\alpha\beta})\,\sin^2\left(\frac{\Delta m^2_{\alpha\beta} L}{4E}\right) \end{aligned} \tag{1.5}$$

Here the survival probability is a function of the neutrino's "flight distance" (baseline length) L, its kinetic energy E, the relevant mixing angle $\theta_{\alpha\beta}$, and the square of the differences between two of the mass eigenstates:

$$\Delta m^2_{ij} = m_i^2 - m_j^2 \tag{1.6}$$

By convention, the heavier eigenstate is labeled first, at index i. An illustration of the survival probability is given in Figure 1.2.

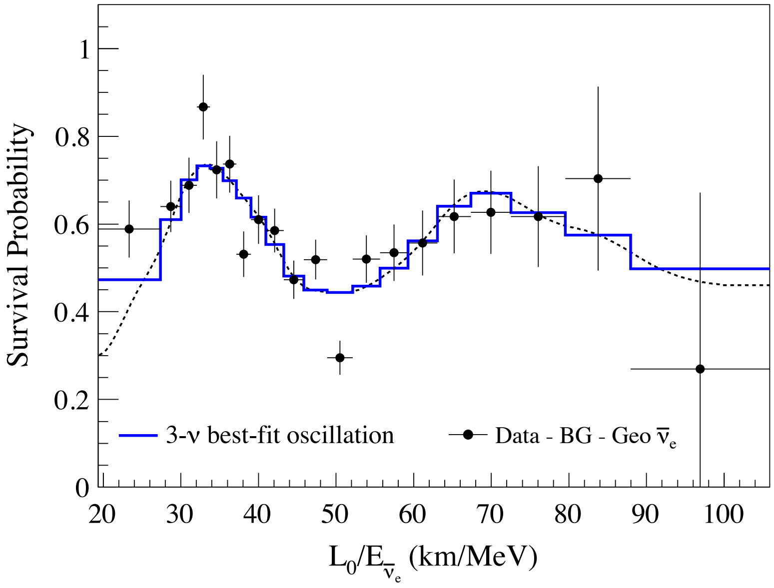

Figure 1.2: Neutrino oscillation results from KamLAND (Figure 5 of [19]), showing the L/E dependence characteristic of oscillation.

Neutrino oscillation experiments have provided values for the three mixing angles θ_{23}, θ_{13}, and θ_{12}. Crucially, these experiments cannot provide the values of the mass eigenstates m_i, only the squared differences Δm^2_{ij}. Solar neutrino experiments have measured [20]

$$\Delta m^2_{21} = \Delta m^2_{\text{sol}} = (7.53 \pm 0.18) \times 10^{-5}\ \text{eV}^2 \tag{1.7}$$

Atmospheric experiments, detecting cosmic neutrinos with very high kinetic energies, have determined the magnitude but not the sign of Δm^2_{23}:

$$|\Delta m^2_{23}| = \Delta m^2_{\text{atm}} = (2.44 \pm 0.06) \times 10^{-3}\ \text{eV}^2 \tag{1.8}$$

Currently, the best value for δ_{CP} comes from a combined global fit [20] showing a preference for 270°, and a very tentative preference for CP *conservation* at 1σ.

The results to date represent a great deal of progress in our understanding of the neutrino's properties beyond the Standard Model. However, they do not form a complete picture. In particular, the unknown sign in Δm^2_{23} has created the "neutrino hierarchy problem." The values of the mass eigenstates remain unknown, and while it is known that $m_2 > m_1$, it is not known if $m_3 > m_1$ as one might naively suspect. The choice $m_3 > m_1$ is known as the "normal hierarchy," while $m_1 > m_3$ is known as the inverted hierarchy, and both possibilities are depicted in Figure 1.3.

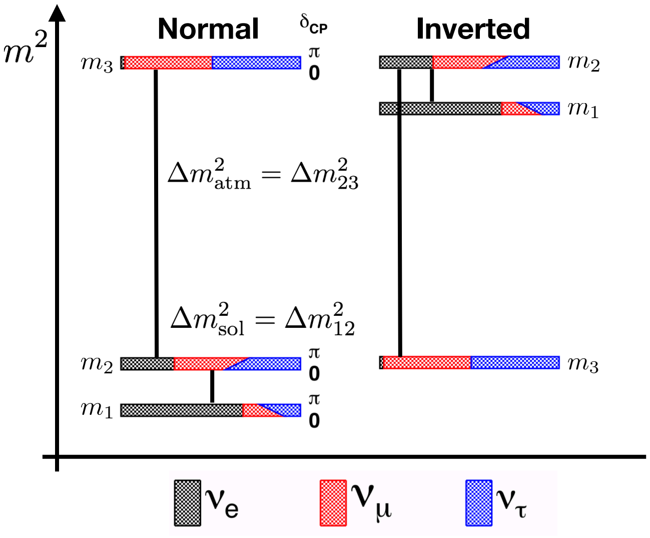

Figure 1.3: Depiction of the inverted and normal neutrino mass hierarchies. Adapted from material in Ref. [21].

In addition to the hierarchy problem, the best limit to date on the absolute value of any individual neutrino mass is < 2 eV, from the Troitsk [22] and Mainz [23] experiments. This poses a challenge for a model to explain in a natural way without fine-tuning of parameters. The mechanism by which neutrinos acquire mass is a subject of intense interest, as it may play an important role in understanding the prevalence of matter over antimatter in our Universe.

1.3 Neutrino Mass Mechanisms and Leptogenesis

Fermions are traditionally described by the Dirac equation acting on a two-component spinor state ψ. An alternative to the Dirac equation was proposed by Majorana in 1937 [24] which depends on both the state ψ and its charge conjugate $\psi^c = i\psi^*$. The standard Lagrangian description of each type of fermion is given by:

$$\mathcal{L}_D = \bar{\psi}(i\partial\!\!\!/ - m)\psi \tag{1.9}$$

$$\mathcal{L}_M = \bar{\psi}(-i\partial\!\!\!/\psi + m\psi^c) \tag{1.10}$$

Generally, neutrino mass terms are described by products of the multi-component spinors ψ: $\bar{\psi}m\psi$, $\bar{\psi}^c m\psi^c$, $\bar{\psi}m\psi^c$, $\bar{\psi}^c m\psi$. In order to be renormalizable, the mass terms must remain invariant under a global phase transformation $\psi \to e^{i\alpha}\psi$. An invariant mass term $\bar{\psi}m_D\psi$ appears in the Dirac equation, while the Majorana equation includes a term $\bar{\psi}m_M\psi^c$ which picks up a CP-violating phase α under the transformation, which appears in the PMNS mixing matrix for Majorana neutrinos.

The most general allowed Lagrangian description of the neutrino mass mechanism [21] is given in terms of two (possibly complex) mass terms m_D and m_M, and the neutrino fields ψ:

$$-2\mathcal{L} = \frac{1}{2}(\bar{\psi}\ \bar{\psi}^c)\begin{pmatrix} m_D & m_M \\ m_M^* & m_D \end{pmatrix}\begin{pmatrix} \psi \\ \psi^c \end{pmatrix} \tag{1.11}$$

Neutrinos are well-suited to description in the chiral representation, where the states ψ are decomposed into left- and right-handed components $\psi = \psi_L + \psi_R$, with two components each. The neutrino is then described by four independent fields $(\nu_L, \bar{\nu_L}, \nu_R, \bar{\nu_R})$. We have seen thus far that there is no compelling evidence for the existence of ν_R and $\bar{\nu_L}$ in nature. In the Dirac description of the neutrino, the two unobserved fields are declared “sterile” since W and Z bosons evidently do not couple to them, and the neutrino gains its mass via coupling to a Higgs field. The Higgs mass mechanism couples (ν_L, ν_R) and $(\bar{\nu_L}, \bar{\nu_R})$, changing the chirality but not the charge of a given state. A problem of fine-tuning remains, since the next-lightest lepton that gets its mass from the Higgs mechanism, the electron, is at least 10^6 times heavier than the neutrino.

The Majorana equation has the interesting feature that it only requires two independent fields (ν_L, ν_R). The associated mass terms couple $(\nu_L, \bar{\nu_R})$, and $(\nu_R, \bar{\nu_L})$ changing both the chirality and charge of a given state. Experimentally, we would observe ν_L as the neutrino and ν_R as the antineutrino, neatly avoiding the two “sterile” fields in the Dirac equation. If the neutrino obeys the Majorana equation (rather than Dirac’s), the neutrino is neutral; *it is its own antiparticle.*

We can write the mass Lagrangian in the chiral representation, leaving the Dirac mass term unchanged and breaking the Majorana mass terms into left- and right-handed components M_L and M_R:

$$\mathcal{L} = \frac{1}{2}(\bar{\nu}_L\ \bar{\nu}_R^c)\begin{pmatrix} M_L & m_D \\ m_D & M_R \end{pmatrix}\begin{pmatrix} \nu_L \\ \nu_R^c \end{pmatrix} \tag{1.12}$$

If the neutrino is a Majorana particle, one allowed mechanism explaining the observation of a very light neutrino is known as the Type 1 “see-saw.” In this model, we take the Dirac mass m_D to be very small, M_L to be zero, and $M_R >> m_D$. Diagonalizing the resulting mass matrix results in two eigenvalues:

$$m_1 = \frac{m_D^2}{M_R}, \quad m_2 = M_R \tag{1.13}$$

The Type 1 see-saw is then given by:

$$\mathcal{L} = \frac{1}{2}(\bar{\nu}\ \bar{N})\begin{pmatrix} m_D^2/M_R & 0 \\ 0 & M_R \end{pmatrix}\begin{pmatrix} \nu \\ N \end{pmatrix} \tag{1.14}$$

Here, we identify ν as the light neutrino we observe, and a new heavy neutrino N which only existed freely at very large energy scales in the very early Universe.

Just after the Big Bang, the Universe's superdense initial state could have no macroscopic separation of matter from antimatter. The fact that elements, stars, and galaxies we observe are all formed from regular matter – not antimatter – is evidence of *baryon asymmetry*. In 1966, Sakharov [25] proposed a set of conditions necessary for a baryon-generating interaction of elementary particles to produce matter and antimatter at different rates, in a process known as *baryogenesis*. In addition to the existence of a process which does not conserve baryon number B, it is necessary for this process to be CP-violating, as well as occuring outside of thermal equilibrium such that time reversal symmetry is also violated.

In 1979, Weinberg described a general method [26] to extend the Standard Model to incorporate baryon and lepton number-violating processes in terms of operators in the symmetry group $SU(3) \otimes SU(2) \otimes U(1)$. These operators $\mathcal{O}^d$ have dimension $d > 4$, are comprised of Standard Model fields, are non-renormalizable, and can be written as additions to the Standard Model Lagrangian $\mathcal{L}_{SM}$:

$$\mathcal{L} = \mathcal{L}_{SM} + \mathcal{L}_{\text{eff}}^{d=5} + \mathcal{L}_{\text{eff}}^{d=6} + ... \tag{1.15}$$

The new operators are weighted by $1/\Lambda$, where Λ is an energy scale:

$$\mathcal{L}_{\text{eff}}^{d} \propto \frac{1}{\Lambda_{NP}^{d-4}} \mathcal{O}^d \tag{1.16}$$

An important result is that if the energy scale of the new physics is sufficiently large ($\sim \mathcal{O}(10^{15})$, GUT-scale), then the operators with minimum dimension d will have the easiest observable consequences. The Type 1 see-saw neutrino mass mechanism, with its very heavy neutrino N, is of this type.

A simple modification of this type proposed in 1986 by Fukugita and Yanagida [27] allows the heavy Majorana neutrinos N to exist, and the see-saw mechanism to provide their mass. A mechanism that creates an excess of leptons over antileptons can in turn cause an excess of baryons, through an electroweak process known as a sphaleron transition [28]. This process is known as *leptogenesis*, and is an attractive solution to the baryogenesis problem.

A confirmation that the neutrino is its own antiparticle (a Majorana fermion) would provide a mechanism for leptogenesis and represent an important step forward in explaining the observed matter-antimatter asymmetry in the Universe. To date, the best current probe into the Majorana nature of the neutrino is through the process known as *neutrinoless double beta decay*.

1.4 NEUTRINOLESS DOUBLE BETA DECAY

Written in its modern form, the β-decay reaction converting a neutron into a proton reflects the discoveries of antineutrinos and neutrino flavor, and obeys lepton number conservation:

$$n \rightarrow p + e^- + \bar{\nu}_e \tag{1.17}$$

In 1935, Goeppert-Mayer calculated the probability of *double* β-decay, where two neutrons inside a nucleus spontaneously decay into protons, emitting two electrons and two electron antineutrinos [29]:

$$X(A, Z) \rightarrow X'(A, Z + 2) + 2\beta^- + 2\bar{\nu}_e \tag{1.18}$$

The $2\nu\beta\beta$ process can best be observed in nuclei with an even number of protons and neutrons, where single beta decay to a lower energy state is energetically or spin-inhibited, as depicted in Figure 1.4. It is an extraordinarily slow process, with typical half-lives $T_{1/2} \sim (10^{19} - 10^{21}$ years), and was not observed in the laboratory until 1987 in ^{82}Se [30]. The even-even mass-locked decays that forbid single beta decay are best for observing double beta decay. When single beta decay is allowed, it will overwhelm the double beta decay rate.

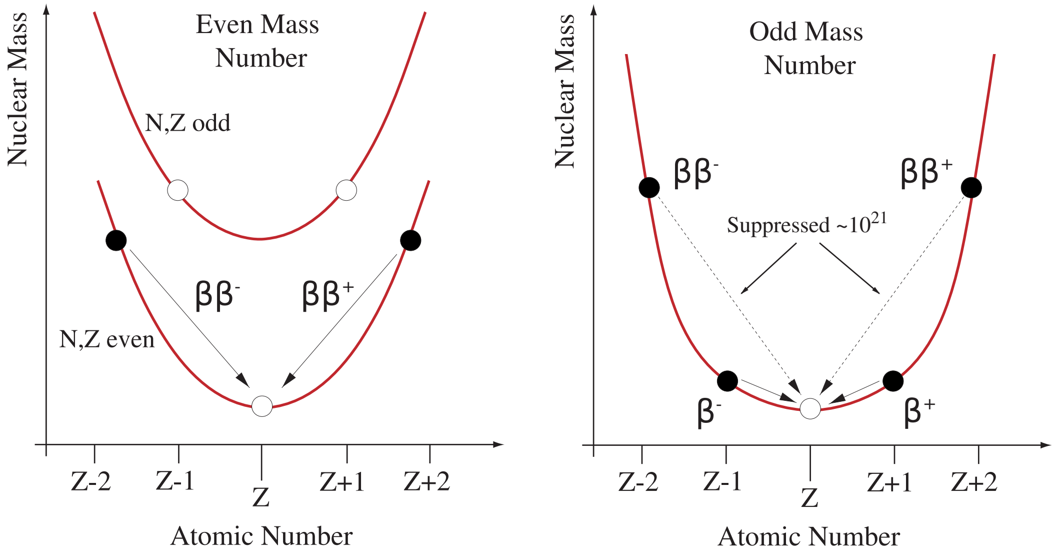

Figure 1.4: Generic level diagram for $\beta\beta$ decay to a lower energy state, showing the suppression in nuclei with odd mass number (Figure 9 of [31].)

In 1939, Furry [32] was the first to apply the Majorana equation to the neutrino, predicting the possibility of *neutrinoless* double beta decay:

$$X(A,Z) \rightarrow X'(A,Z+2) + 2\beta^- \tag{1.19}$$

This process clearly violates lepton number conservation ($\ell = 0$ before, $\ell = 2$ after). In modern terms, in $0\nu\beta\beta$ decay a virtual neutrino is exchanged between the two W bosons, as depicted in Figure 1.5.

Moreover, due to the "black box theorem" of Schechter and Valle [33], it is known that detection of $0\nu\beta\beta$ process is a model-independent probe of lepton number conservation; ℓ is violated whether the virtual neutrino exchanged is the light ν or heavy N of the Type 1 see-saw, or described by any other mechanism. If $0\nu\beta\beta$ is observed, then the neutrino must be a Majorana fermion, lepton number is not a universal symmetry, and the leptogenesis mechanism is a feasible solution to the baryogenesis problem.

The wide energy spectrum observed in $2\nu\beta\beta$ is similar to the spectrum as seen in β-decay which originally led Pauli to postulate a new particle; the kinetic energy in

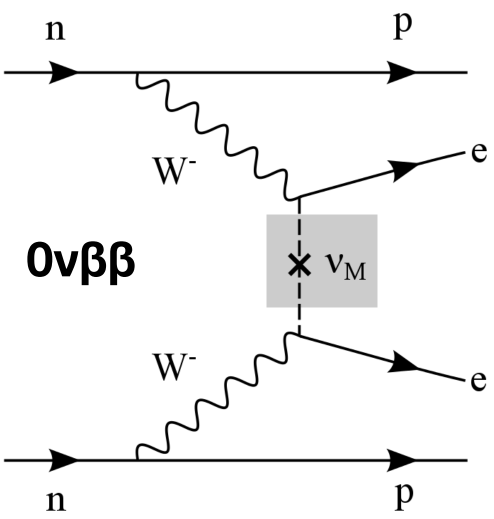

Figure 1.5: Feynman diagram of the $0\nu\beta\beta$ process.

the decay is divided between electrons (which are detectable) and neutrinos, which escape conventional detectors. Regardless of the underlying physics, $0\nu\beta\beta$ has a clear experimental signature; if no neutrinos are produced in the decay, then the available energy in the decay (known as its Q-value) is split between the two electrons. Since electrons do not generally escape a detector, a sharp peak at the exact energy Q would be observed, as shown in Figure 1.6. By searching for a peak at the Q of a given $2\nu\beta\beta$ candidate isotope, an experiment measures a half-life $T^{0\nu}_{1/2}$, or sets a lower limit on its value.

With the PMNS matrix for Majorana neutrinos (containing the additional CP-violating phases α), one can obtain an effective Majorana mass of the electron neutrino:

$$\langle m_{\beta\beta}\rangle \equiv \left|\sum_{i=1}^{3} U_{ei}^2\, m_i\right| \tag{1.20}$$

$$\langle m_{\beta\beta}\rangle = \left|m_1 c_{12}^2 c_{13}^2 + m_2 s_{12}^2 c_{13}^2 e^{i\alpha_{21}} + m_3 s_{13}^2 e^{i(\alpha_{31}-\delta_{CP})}\right| \tag{1.21}$$

The half-life $T^{0\nu}_{1/2}$ measured by an experiment can be related to this effective mass:

$$(T^{0\nu}_{1/2})^{-1} = G_{0\nu}(Q_{\beta\beta}, Z)\ |\mathcal{M}^{0\nu}|^2\ \langle m_{\beta\beta}\rangle^2 \tag{1.22}$$

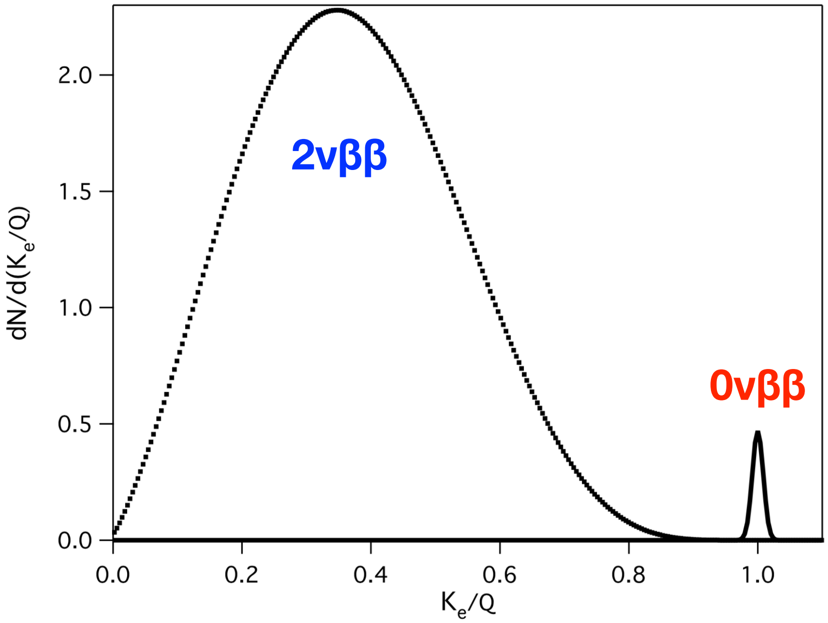

Figure 1.6: A simplified energy spectrum of the $2\nu\beta\beta$ and $0\nu\beta\beta$ processes with the $0\nu\beta\beta$ peak dramatically exaggerated, for arbitrary kinetic energies K_e up to Q.

$G_{0\nu}(Q_{\beta\beta}, Z)$ is a phase space factor for the decay which accounts for the kinematics of two-electron emission from a nucleus Z.

The nuclear matrix element $\mathcal{M}^{0\nu}$ depends on the nuclear physics of the transition between the parent and daughter nuclei, and is not exactly calculable. It has the approximate form [34]

$$\mathcal{M}_{0\nu} \approx \mathcal{M}_{0\nu}^{GT} + \frac{g_V^2}{g_A^2}\mathcal{M}_{0\nu}^{F} \tag{1.23}$$

Here, the total matrix element depends on the vector and axial coupling constants g_V and g_A, and the transition probabilities given by the Fermi and Gamow-Teller matrix elements. The Fermi transition describes a beta decay where the spins of the emitted particles are antiparallel, and the total angular momentum is conserved. In a Gamow-Teller transition, the spin if the parent nucleus can either remain unchanged or change by ± 1.

A similar expression to Equation 1.23 exists for $2\nu\beta\beta$ decays, and in order to match data an effective g_A must be used. This "g_A quenching" is a significant uncertainty in relating the half-life to the effective Majorana mass, going as the fourth power:

$$(T_{1/2})^{-1} \propto g_A^4 \tag{1.24}$$

Today, several models have been used to calculate the quenching factor directly (QRPA, IBM, *ab initio* shell model), and a major theory effort is underway to resolve the discrepancies from the competing models and reduce this uncertainty [35].

In addition to establishing the Majorana nature of the neutrino, $0\nu\beta\beta$ experiments can provide an important insight into the hierarchy problem depicted in Figure 1.3. In the context of the Type 1 see-saw mechanism described in Section 1.3, if the neutrino exchanged between the two W bosons is the light ν (not the heavy N), then the effective Majorana mass $\langle m_{\beta\beta} \rangle$ becomes a probe of the normal and inverted hierarchies. The normal and inverted hierarchies can overlap, making $0\nu\beta\beta$ an ineffective probe of the hierarchy, but this is not necessarily the case. Figure 1.7 illustrates that for low enough values of the lightest neutrino mass eigenstate, there is an observable difference between the normal and inverted hierarchy detectable by a $0\nu\beta\beta$ experiment.

If $0\nu\beta\beta$ is an allowed process, its half-life is extremely long ($> 10^{26}$y), and the height of the corresponding peak in the energy spectrum shown in Figure 1.6 will be exceedingly small. For most $0\nu\beta\beta$ candidate isotopes (^{136}Xe, ^{130}Te, ^{82}Se, ^{76}Ge), Q falls below the maximum of the standard gamma ray spectrum of the ^{238}U and ^{232}Th decay chains (∼2700 keV), which emit a host of γ-ray events which can potentially deposit energy in a detector in the Q region and obscure the $0\nu\beta\beta$ peak. An ideal experiment would contain no such backgrounds in the region of interest. Its sensitivity, S, to larger and larger values of $0\nu\beta\beta$ is proportional to the *exposure*. This quantity combines the amount of isotope being monitored M and the amount of time t the experiment is run:

$$S_{T^{0\nu}_{1/2}} \propto Mt \tag{1.25}$$

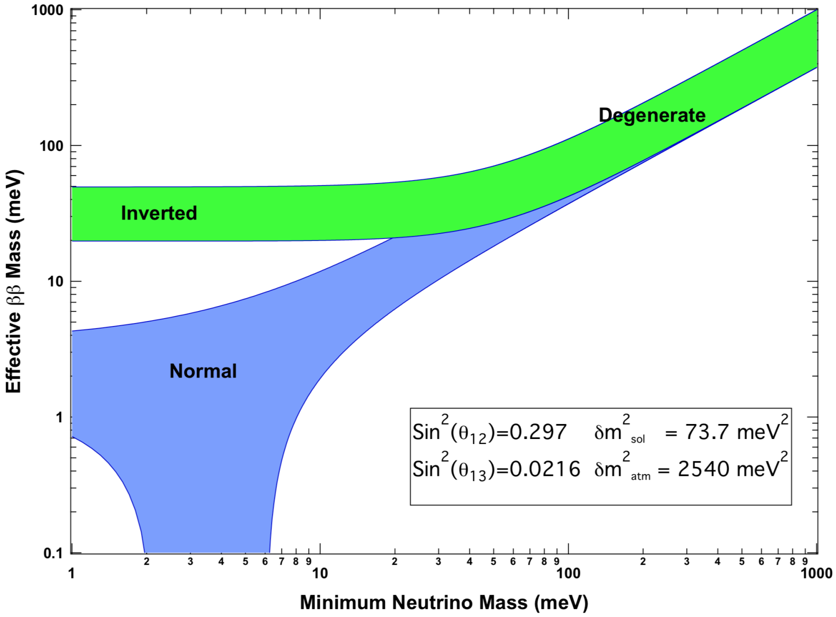

Figure 1.7: Illustration of $\langle m_{\beta\beta} \rangle$ as a probe of the normal and inverted neutrino hierarchies. (Figure 1 of [36].)

For all experiments to date, however, backgrounds at or near Q have been an unavoidable issue. For a realistic experiment with backgrounds, the sensitivity is driven by the *background rate* (B, in cts/(keV kg y)), and the *energy resolution* ΔE of the detector near Q:

$$S_{T^{0\nu}_{1/2}} \propto \sqrt{\frac{Mt}{B\Delta E}} \tag{1.26}$$

Larger background rates and energy resolutions limit the sensitivity to larger and larger values of the $0\nu\beta\beta$ half-life.

Many processes capable of depositing energy in a detector at the Q value have been identified, each making a contribution to the overall background rate in Equation 1.26. The production of radioactive isotopes by cosmic rays (“cosmogenic activation”) can be limited by keeping materials underground; however some isotopes with long half-lives, once produced in the detector material, may be irreducible over the lifetime of an experiment. In addition, most materials contain trace amounts of ^{238}U and ^{232}Th, each of which decay to a host of different isotopes (a “decay chain”) which

Table 1.1: Current $T_{1/2}^{0\nu}$ lower limits from the four leading $0\nu\beta\beta$ experiments.

Experiment	**$T_{1/2}^{0\nu}$ limit**	**Isotope**	**Exposure**	**Date**
KamLAND-Zen	$> 10.7 \times 10^{25}$y	^{136}Xe	504 kg-y	5/2016 [37]
GERDA	$> 9 \times 10^{25}$y	^{76}Ge	82.4 kg-y	3/2018 [38]
MAJORANA	$> 2.7 \times 10^{25}$y	^{76}Ge	26 kg-y	3/2018 [39]
CUORE	$> 1.3 \times 10^{25}$y	^{130}Te	86.3 kg-y	3/2018 [40]

can also emit radioactivity. This contribution from ^{238}U and ^{232}Th is known as *natural radioactivity,* since it is terrestrial in origin. Radioactivity from both natural and cosmogenic sources must be heavily suppressed in order to field a competitive experiment.

To illustrate the current state of the field, the best limits on the $0\nu\beta\beta$ $T_{1/2}^{0\nu}$ from the four leading experiments are given in Table 1.1. They are already larger than 10^{26}y, yet in order to probe the entire inverted hierarchy depicted in Figure 1.7, experiments must reach $\mathcal{O}(10^{28})$ or higher. This makes the reduction of backgrounds critical to a discovery.

Figure 1.8 demonstrates the importance of minimizing backgrounds in a practical experiment, showing the potential to discover $0\nu\beta\beta$ for varying background levels. Even for an ideal detector with no background, and a full metric ton of active material, an experiment would have to run for an entire year to make a discovery in the inverted hierarchy region. This is depicted by the blue band in Figure 1.8, which represents the lowest $T_{1/2}$ possible within the inverted hierarchy, accounting for the uncertainty due to the nuclear matrix elements. For a practical detector, even a background count rate of 1 count near Q *per ton, per year*, would obscure the $0\nu\beta\beta$ signal enough to require the experiment to run for 15-20 years to make the same discovery.

The reduction of radioactive backgrounds and minimization of energy resolution have been essential features of the current generation of $0\nu\beta\beta$ experiments. To take two examples, the GERDA experiment [41] submerges its $0\nu\beta\beta$ isotope ^{76}Ge in a

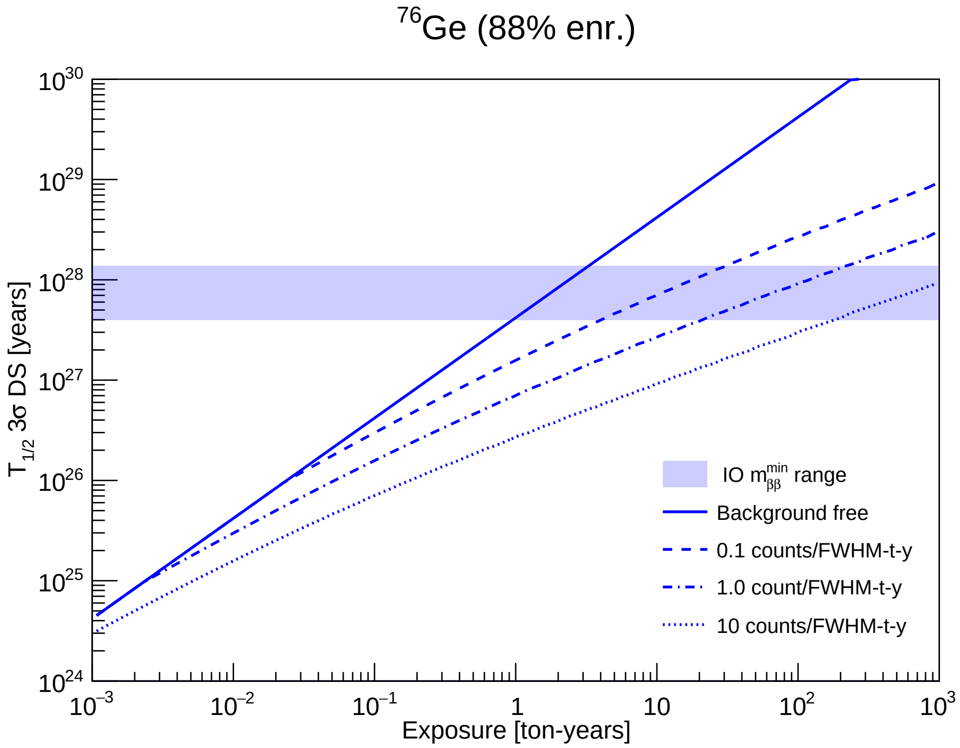

Figure 1.8: 90% discovery level for ^{76}Ge. (Courtesy J. Detwiler)

scintillating liquid argon (LAr) active shield, using light from the LAr to reject coincident events in the Ge originating from outside the detectors. The MAJORANA DEMONSTRATOR [42], which also uses ^{76}Ge, has focused on reducing the inherent radioactivity of its detector by minimizing their cosmogenic activation from exposure to cosmic rays on the surface. Both experiments minimize surface activation and use ultra-pure materials with little intrinsic radioactivity in the detector construction, however MAJORANA has taken the additional step of electroforming and machining its copper underground to further reduce its activation, which will be discussed in Chapter 2. Both experiments operate within multi-layered shields for additional protection.

Looking towards the next generation, the background goal of the proposed LEGEND-200 experiment [43][36] is $B < 2 \times 10^{-4}$ cts/(keV kg y). The most recent results from MAJORANA and GERDA at the time of this writing were given at the Neutrino 2018 conference [39][38]. Without the use of a LAr veto, MAJORANA has achieved a background of 11.9 ± 2 cts/FWHM/t/y, or 4.7×10^{-3} cts/(keV kg y). With the LAr veto, GERDA has reached a background of 6×10^{-4} cts/(keV kg y). The LEGEND-200 background goal is only a reduction by a factor 3 from this level. By combining the best features of both experiments, this goal is a feasible and well-motivated one on the path to a ton-scale $0\nu\beta\beta$ experiment.

Neutrinoless double beta decay experiments are powerful tools for probing the nature of the neutrino, despite never directly detecting one. They can potentially distinguish between the normal and inverted mass hierarchies (assuming the Type 1 see-saw mechanism and light Majorana neutrino exchange in the "black box"). Most importantly, they are also a *model-independent* way to establish that the neutrino is a Majorana fermion and that lepton number conservation is violated, supporting leptogenesis as an explanation of the current matter-antimatter asymmetry in our Universe.

1.5 AXIONS

The neutrino is by no means the only gateway to physics beyond the Standard Model. Another low-mass, low-cross section particle may provide an explanation for the *strong-CP problem* and even be the main component of the dark matter observed in our Universe. We begin by re-expressing the context for the proposal of the *axion*, and discuss a mechanism by which this ghostly particle may be produced.

As described in Section 1.1, the *strong-CP problem* requires an explanation of the apparent rigid adherence of the strong force to CP conservation, justifying the extraordinarily small upper limit on the electric dipole moment of the neutron. In the Standard Model Lagrangian, the CP violating term in the strong interaction (QCD) Lagrangian is represented in terms of the color field strength tensor $G^{a\mu\nu}$:

$$\mathcal{L} = -\bar{\Theta}\, \frac{\alpha_s}{8\pi} G^{\mu\nu a} \tilde{G}^{a}_{\mu\nu} \tag{1.27}$$

Here, α_s is the strong force coupling constant, and $\bar{\Theta}$ is known as the effective vacuum angle parameter, taking allowed values from $-\pi$ to π. A natural value for $\bar{\Theta}$ is a constant $\mathcal{O}(1)$; this does not violate any known physics and avoids the need to explain the "fine-tuning" of an excessively small value as a quirk of our Universe. With $\bar{\Theta}$ nonzero, a small amount of CP-violation is expected. Unfortunately, choosing $\bar{\Theta} \sim \mathcal{O}(1)$ leads to the erroneous prediction for the neutron electric dipole moment $d_n \sim 10^{-16}\ e \cdot cm$; the current limit is ten orders of magnitude smaller [44].

The problem of explaining why Nature seems to obey a certain symmetry (CP) so rigidly in one area but not another is a difficult one. To provide a more intuitive description of the issue, Sikivie gave an interesting analogy in a 1995 paper [45]. A group of people are playing snooker in a closed room, on a pooltable whose legs are covered by a curtain. The pooltable is a perfectly flat surface on which the balls roll normally, obeying a symmetry called S. If S were not a symmetry of the pooltable, it would be tilted and the balls would preferentially roll to one side, ruining the game. All of the players are content to simply play the game except one, who notices an alarming fact: the floor on which the pooltable sits is dramatically slanted to one side, breaking S symmetry. Not being able to see the point where the table legs touch the floor (they are covered by a curtain), the player then asks, *"if the whole floor is slanted, why is the pooltable flat?"*

The "thinking snooker player" (TSP) at first imagines that the maker of the pooltable may have simply adjusted the length of the table legs to restore S symmetry. TSP interrupts the game to make a careful measurement of the "flatness" of the pooltable and concludes that it is flat to a precision of 10^{-9}. [3] TSP reasons that it is not so easy to make a pooltable this flat on an *arbitrary* surface. Surely the maker of the pooltable has other clients in other playrooms with arbitrary S violation. Rather than spending a large amount of time adjusting four legs of every pooltable to 10^{-9}

---

[3] This choice in Sikivie's story is not accidental. 10^{-9} was the limit on $\bar{\Theta}$ in 1995.

precision, TSP imagines that the table maker must have had some way of making it flat for an arbitrary floor angle. TSP imagines a mechanism where the table is made flat by mounting the center of the table on an axle which is allowed to rotate, connected to a large weight below the floor. Gravity acts on the weight, pulling it down vertically, and the pooltable is automatically made horizontal, for any slanted floor. Even when the balls hit the wall and produce a vibration, or an earthquake causes the room to shake, the pooltable remains horizontal. The mechanism TSP has conceived is the analogy of Peccei and Quinn's solution to the strong-CP problem – an additional term to the Standard Model that *dynamically* balances out CP-violating behavior.

The Peccei-Quinn solution [46] to the strong-CP problem adds a new U(1) symmetry to the Lagrangian, which requires other terms to make $\mathcal{L}$ obey the symmetry. One such term has a factor ϕ_a/f_a:

$$\mathcal{L} = \left(\frac{\phi_a}{f_a} - \bar{\Theta}\right)\frac{\alpha_s}{8\pi}G^{\mu\nu a}\tilde{G}^a_{\mu\nu} \tag{1.28}$$

The fields $\bar{\Theta}$ and ϕ_a can be expressed as a single field, $a = \phi_a - \bar{\Theta}f_a$, which is minimized at zero expectation value, $\langle a \rangle = 0$. With an expectation value of 0, the $\bar{\Theta}$ dependence is cancelled by the total field, providing a natural explanation why the electric dipole moment of the neutron is so small. As the Universe cools after the Big Bang, at energies below the characteristic scale f_a the symmetry $U(1)_{PQ}$ is broken, and the a field becomes associated with a particle: a massless Nambu-Goldstone boson.

It was soon realized by Wilczek [47] and Weinberg [48] that the gluon fields G fluctuate dynamically (due to instanton effects in QCD), $\left\langle trG_{\mu\nu}\tilde{G}^{\mu\nu}\right\rangle \neq 0$. To preserve the cancellation and minimize energy, the a field must dynamically fluctuate, and its potential must be nontrivial with an expectation value $\langle a \rangle = 0$ [49]. Because of this nontrivial potential, the particle gains a mass and becomes a *pseudo*-Nambu-Goldstone boson, which Wilczek named the *axion*. The mass of the axion can be expressed in terms of the light quark masses m_u, m_d, the pion mass m_π, and the pion decay constant f_π:

$$m_a = \frac{z^{1/2}}{1+z}\frac{f_\pi m_\pi}{f_a} = \frac{0.60 \text{ meV}}{f_a/10^{10}\text{GeV}} \tag{1.29}$$

Here, the canonical value of $z = m_u/m_d$ is 0.56, though it can vary between 0.3–0.6 [50]. Originally it was assumed that the PQ scale f_a was related to the electroweak symmetry-breaking scale, $f_{\text{weak}} = (\sqrt{2}G_F)^{-1/2} = 247$ GeV. However, the associated "standard" and "variant" axions were quickly excluded by experiment [51].

A paper from Kim in 1979 [52] was the first to suggest a "very light axion" with $f_a \gg v_{\text{weak}}$. Shortly thereafter Dine, Fischler, and Srednicki [53], along with Zhitnitsky [54], proposed removing the constraint on f_a requiring it to be near the electroweak scale, allowing it to take on arbitrarily large values. [4] They called this model the "invisible axion," which remains appealing to this day on two main theoretical grounds. First, positive observation of axions would demonstrate that the Peccei-Quinn mechanism indeed solves the strong-CP problem. Second, their small but nonzero mass makes them a candidate to comprise all or part of the cold dark matter making up 25% of the observed energy density in the Universe [55].

Axions have calculable couplings to photons ($g_{a\gamma}$), electrons (g_{ae}), and nucleons (g_{an}), making them detectable via more than their gravitational effects. Generally the interaction Lagrangians for a wide class of axions and axion-like particles (ALPs) are given by

$$\mathcal{L} = f_a^{-1} J^\mu \partial_\mu \phi_a \tag{1.30}$$

Here, J^μ is the Noether current of the spontaneously broken symmetry at energy scale f_a, and ϕ_a is the pseudoscalar field associated with the axion. The couplings to normal matter are generally model-dependent. In the Kim-Shiftman-Vainshtein-Zakharov (KSVZ) or "hadronic axion" model, axions couple to electrons only at the higher-

---

[4] We note that this strongly resembles the behavior predicted by Weinberg in the context of SM extensions violating baryon and lepton number described in Section 1.3.

order loop level. This suppresses observable effects from axion-electron interactions. In the Dine-Fischler-Srednicki-Zhitnitsky (DFSZ) model, electrons couple to axions at the tree level.

Searches for axions have generally been divided between *cosmic axions*, which are distributed roughly uniformly at the galactic scale (similar to WIMPs) and *solar axions*, which are emitted directly from the Sun. One of the strongest hints for the existence of the axion is through considering stellar energy loss mechanisms [56]. It has been suggested that the cooling of white dwarf stars proceeds at a slightly higher rate than expected, admitting the possibility of an energy loss mechanism due to axions. The brightness of some white dwarf stars fluctuates with an extremely regular period, directly proportional to the cooling of the star. Isern [57] cites the period drift measurement of G117-B15A, a member of the ZZ Ceti family. Theoretical predictions indicate this drift should be no larger than 1.2×10^{-15} sec s^{-1}, but the measured value is $(4.89 \pm 0.53(\text{stat}) \pm 1.56(\text{sys})) \times 10^{-15}$ s s^{-1}, indicating the cooling is faster than expected. This could be attributable to observational error, since the data are only from one star, or modeling error, but the possibility of new physics should not be overlooked. One possibility is that axions are being emitted from the interior of the white dwarf via the process of electron axio-bremsstrahlung, in which the "braking radiation" from a decelerating electron comes in the form of an axion instead of a photon. If this method is invoked to explain the extra cooling, it allows one to estimate the axion-electron coupling constant $g_{ae} = (2 - 7) \times 10^{-13}$. This was presented by Corsico et al [58] for the star L19-2 where the period is once again faster than expected, placing a tighter bound on the coupling constant, $g_{ae} \leq 7 \times 10^{-13}$. We note also that the cooling mechanism could be explained by axion-like particles (ALPs), which are not standard Peccei-Quinn axions.

The axion's predicted couplings to normal matter must be small enough that they do not conflict with observed physics. Observations of stellar energy loss mechanisms and supernovae from astronomy have provided constraints on the allowed coupling of axions to matter. There are several areas in astronomy where the possible existence of axions or ALPs have been constrained by known processes:

- The neutrino burst from SN1987A matched very well with models which did not require the emission of axions as an energy loss mechanism. This constrains $f_a > 4 \times 10^8$ GeV and $m_a < 16$ meV [59].
- When axions encounter the Earth's magnetic field, they can convert to soft X-rays. The Newton-XMM satellite has set a limit for this process in terms of the product $g_{a\gamma} \cdot g_{ae} < 2.2 \times 10^{-22}$ GeV^{-1} [60].
- The measurement of the total solar neutrino flux by the SNO experiment was found to constrain nonstandard energy loss mechanisms to 10%, and requires $g_{a\gamma} < 7 \times 10^{-10}$ GeV^{-1} [61]. The limit from CAST is tighter, as shown in Figure 1.9.
- Studies of main sequence stars find that axion emission tends to increase the population of HB stars and decrease the RGB population, resulting in the constraints $g_{a\gamma} < 10^{-10}$ GeV^{-1} and $g_{ae} < 4.7 \times 10^{-13}$ [62].
- Studies of Cepheid variable stars find that too high a rate of axion emission would eliminate the observed "blue loop" phase of the evolution of the star. This constrains $g_{a\gamma} < 0.8 \times 10^{-10}$ GeV^{-1} [63].
- Neutron star cooling may also have an axion energy loss component, resulting from the axion-nucleon coupling g_{aN}. Keller and Sedrakian [64] give values for f_a and m_a that are dependent of a critical temperature T_c. For $T_c = 10^9$ K, an upper bound on the axion mass $m_a < 10^{-3}$ eV and a lower bound on the energy scale $f_a > 6 \times 10^9$ GeV is obtained.

In many cases, constraints from astrononomical observations on axion couplings to normal matter are more restrictive than current Earth-based experimental limits. New detector designs are continually pushing towards making a competitive measurement, providing an important cross-check on the astronomical observations. In Sections 1.6–1.8, we discuss the various couplings of axions to normal matter and describe the current state of experimental searches.

1.6 Axion-Photon Interactions

The interaction of an axion and a photon resembles a two-photon interaction, since the axion properties are closely related to another neutral particle, the pion. Their interaction can be written in terms of the electromagnetic field tensor $F_{\mu\nu}$, not coincidentally resembling the Maxwell equations for electromagnetism, and the coupling constant $g_{a\gamma}$ which determines the strength of the interaction:

$$\mathcal{L}_{a\gamma} = -\frac{g_{a\gamma}}{4}\ F_{\mu\nu}\tilde{F}^{\mu\nu}\phi_a \tag{1.31}$$

The coupling to photons can be written in terms of the axion mass:

$$g_{a\gamma} = \left(0.203(3)\frac{E}{N} - 0.39(1)\right)\frac{m_a}{\mathrm{GeV}^2} \tag{1.32}$$

Here, E and N are the electromagnetic and color anomalies of the axial current associated with the axion [44]. In the DFSZ model, $E/N = 8/3$, whereas for KSVZ $E/N = 0$.

After early experiments failed to find the electroweak axion [51] and the invisible axion was proposed [53], Sikivie was the first to provide a feasible mechanism for invisible axion searches [65][66], relying on the *inverse Primakoff effect.* In the presence of a large magnetic field, the axion can convert into a real photon with an energy equal to the axion mass m_a. This has found application in two main experiments: the axion *helio*scope CAST, and the axion *halo*scope ADMX, which have set the strongest current experimental limits on the $g_{a\gamma}$ coupling to cold axion dark matter.

The CERN Axion Solar Telescope (CAST) uses a large cylindrical superconducting test magnet from the Large Hadron Collider, aligning the cylinder with the Sun such than an axion traveling though the bore would be coverted into a detectable x-ray by the large **B** field. CAST was able to search for a wide range of axion masses, but was only sensitive to the $g_{a\gamma}$ predictions of the DFSZ and KSVZ models in a small region [67]. Recently a new helioscope design has been proposed, the International Axion Observatory (IAXO) [68], which would be several orders of magnitude more sensitive and able to more directly probe the axion model space.

Similar to the helioscope design, an axion haloscope such as ADMX employs a large magnetic field, but is designed to detect cold dark matter axions which would have extremely low kinetic energies. Using a tunable resonant cavity, with a large **B** field, at a resonant frequency equal to the axion mass, an axion is spontaneously converted into a detectable RF photon. The most recent result from ADMX is sensitive to axions with masses in the μeV-range, not finding evidence for a DFSZ axion signal with $g_{a\gamma} \approx 3.6 \times 10^{-16}$ [69].

It is also possible to observe solar axions coupling to photons in high-purity germanium (HPGe) detectors by looking for time-varying signals in different regions of the energy spectrum. If the axions incident on a detector line up with one of the crystal axes (Ge has a face-centered diamond cubic structure), then the axions will undergo coherent Bragg scattering, and have a higher probability of interacting within the detector. Since the detector is in the rotating Earth reference frame, the crystal axes move in time with respect to the sun, producing a daily modulating signal. This technique was first applied to Ge detectors in the 1990s [70] [71] and has recently been investigated in the context of the MAJORANA experiment where the crystal axes are unknown [72]. Theoretical predictions have also been made for the ^{130}Te CUORE experiment [73].

Figure 1.9 summarizes the current state of the search for axion-photon interactions, plotting $g_{a\gamma}$ versus the axion mass m_a and showing the exclusion regions from experiments to date. A broad choice of E/N values are possible, as shown by the yellow band.

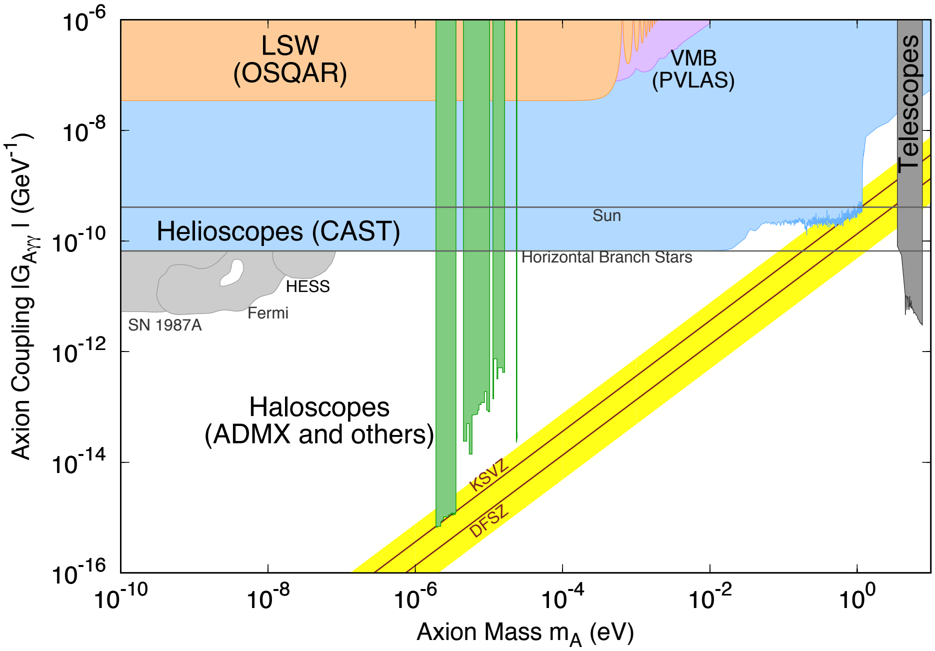

Figure 1.9: Current exclusion regions for $g_{a\gamma\gamma}$ as a function of axion mass. From "Axions and other similar particles", Figure 61.1 [44].

1.7 AXION-ELECTRON INTERACTIONS

Searches based on the axion-electron coupling can again be divided between solar axions and cosmic axions. We describe both approaches here, while Chapter 5 will focus on the search for solar axions. The interaction of axions with electrons may take the simplified pseudoscalar form [44]

$$\mathcal{L} = -i\frac{C_e m_e}{f_a}\ \bar{\psi}_e \gamma_5 \psi_e \phi_a \tag{1.33}$$

The factor C_e is model-dependent; in the DFSZ model

$$g_{ae} \equiv \frac{C_e m_e}{f_a} = \frac{\cos^2(\beta) m_e}{3 f_a} \tag{1.34}$$

For axions with keV-scale energies large compared to their mass, in the DFSZ model we can take $\cos^2 \beta \to 1$.

Setting limits on the axion-electron coupling g_{ae} requires a detector sensitive to the *axioelectric* effect [74]. The currently accepted form of the axion-electron cross section is given by

$$\sigma_{ae}(E) = \frac{g_{ae}^2}{\beta} \frac{3E^2}{16\pi\alpha m_e^2 c^4} \left(1 - \frac{\beta^{2/3}}{3}\right) \sigma_{pe}(E) \tag{1.35}$$

This process is analogous to the photoelectric effect, with an axion taking the place of the photon (see Figure 1.10). It depends on the photoelectric cross section as a function of energy $\sigma_{pe}(E)$ for the element in question, and a model parameter β. To date, high-purity germanium detectors [75] [42] and liquid Xe time projection chambers [76] [77] have utilized this method of detection.

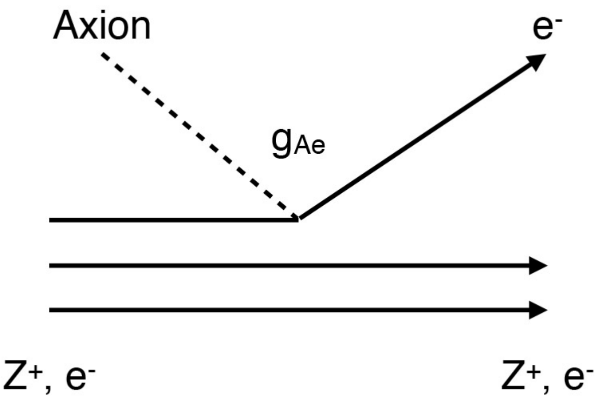

Figure 1.10: Generic depiction of the axioelectric effect; an axion takes the place of an incoming photon and causes ionization inside a material.

A large variety of physics processes take place in the Sun, allowing several possible axion production mechanisms. In hadronic models where axions do not couple to electrons at the tree level (KSVZ), the primary emission mechanism is the Primakoff effect, where the scattering of a photon with an electron produces an axion instead of a photon: $\gamma + Ze \rightarrow Ze + a$. In the case of axion-electron interactions in the DFSZ model, the flux of axions from the Sun is enhanced significantly [78] by considering the "ABC" axion-electron interactions: Atomic recombination and deexcitation, Bremmstrahlung, and Compton. Figure 1.11 depicts the allowed processes.

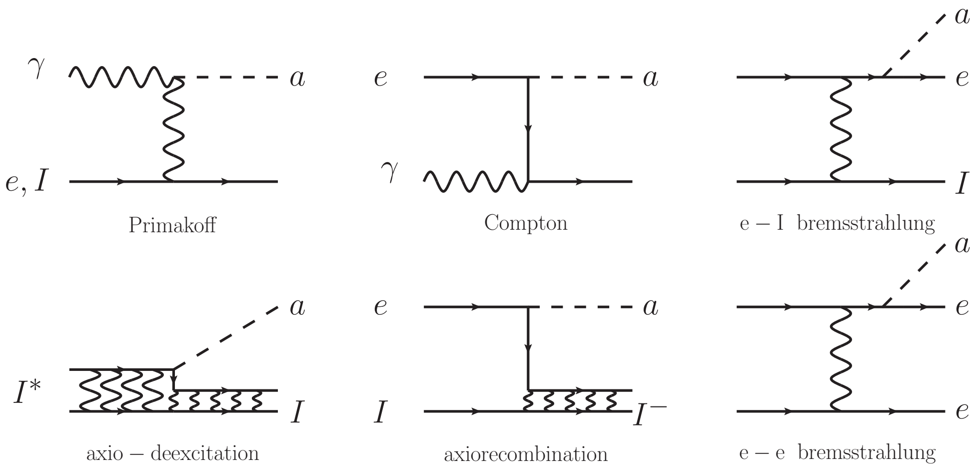

Figure 1.11: Solar axion production mechanisms (Figure 1 of [78]).

By taking into account libraries of monochromatic photon radiative opacities, and considering all the emission mechanisms in Figure 1.11, a total solar axion flux 30% higher than previous models was obtained by Redondo [78]. A notable feature of this flux is the presence of distinct peaks corresponding to atomic transitions in the keV-scale temperatures of the Sun's inner region. The search for solar axions from these processes presented in Chapter 5 will search for signatures of both the combined total flux spectrum and the individual peaks, whose fluxes are estimable from the total spectrum. The energy levels of the peaks deviate slightly from their laboratory values, due to the highly ionized plasma enviroment of the sun. Chapter 5 will discuss this energy shift in more detail, and provide estimates for the flux for several peaks. Figure 1.12 gives the total flux as calculated by Redondo.

Integrating the flux spectrum gives an expression for the expected number of axions passing through e.g. an Earth-bound detector. The number of axion interactions between energies E_1 and E_2 grows as a function of exposure:

$$N_{\text{exp}} = Mt \int_{E_1}^{E_2} \Phi_a \sigma_{ae} \, dE = M \; t \; C \tag{1.36}$$

In practice, an energy spectrum from a detector in the axion region of interest can be fit to a model comprising all known backgrounds. The axion flux can be converted

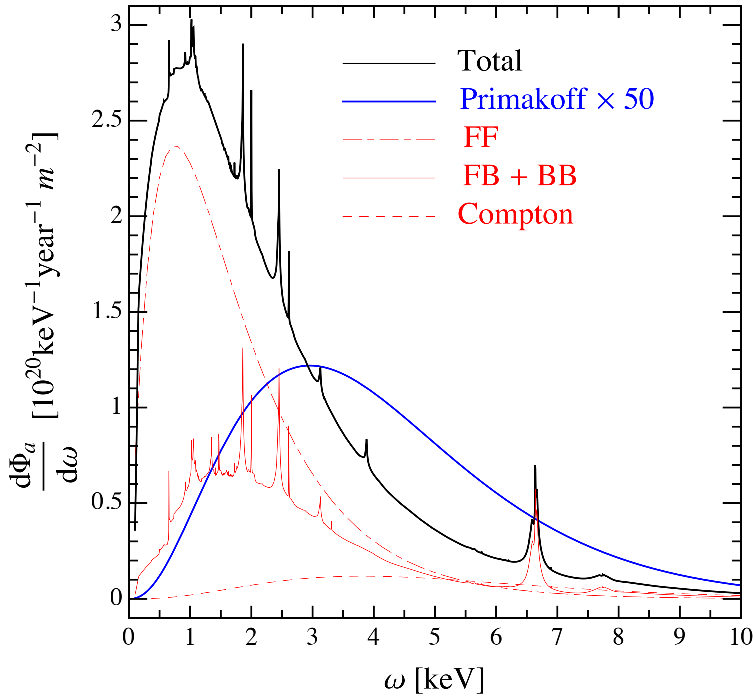

Figure 1.12: Total axion flux taking into account multiple production mechanisms. (Figure 2 of [78].)

to a probability density function and added as a fit component. If the spectrum is unknown, one can estimate the obtainable limit by assuming that the axion signal is no larger than the statistical $\sqrt{N}$ error:

$$N_{\mathrm{obs}} = \begin{cases} N_{\mathrm{fit}} & \text{if spectrum is known} \\ \sqrt{B \Delta E M t} & \text{if projection} \end{cases} \tag{1.37}$$

Both the flux Φ_a and the axioelectric cross section σ_{ae} are proportional to g_{ae}^2. In the case of no signal, an upper limit takes the form

$$g_{ae} \leq \left(\frac{N_{\mathrm{obs}}}{N_{\mathrm{exp}}}\right)^{1/4} \tag{1.38}$$

A projected limit for g_{ae} as a function of exposure is then given by

$$g_{ae}(Mt) = \left(\frac{\sqrt{B\ \Delta E\ Mt}}{Mt\ C}\right)^{1/4} = \left(\frac{B\ \Delta E}{Mt}\right)^{1/8} C^{-1/4} \tag{1.39}$$

The most stringent (Earth-based detector) limit to date on g_{ae} comes from a *cosmic* axion search by the LUX experiment [76]:

$$g_{ae} < 3.5 \times 10^{-12} (90\%\mathrm{CL}) \tag{1.40}$$

In this case, the expected flux of axions through the detector is dependent on assumptions on the local dark matter density ρ_{DM}. Here we outline the calculation used by the Majorana [79] and EDELWEISS [80] experiments, which used $\rho_{\mathrm{DM}} = 0.3$ GeV cm^{-3}. LUX and PandaX-II [77] have followed similar procedures.

The expected number of axion counts at an energy is determined by E, the dark matter flux Φ_{DM}, and the axioelectric cross section σ_{ae}:

$$\Phi_a(E, m_a)\frac{dN}{dE}(E, m_a) = \Phi_{\mathrm{DM}}(m_a)\,\sigma_{ae}(m_a)\,\eta(E)\frac{1}{\sqrt{2\pi}\sigma_E(m_a)}\exp\left(-\frac{(E-m_a)^2}{2\sigma_E^2(m_a)}\right)MT \tag{1.41}$$

$$\Phi_{\mathrm{DM}} = \rho_{\mathrm{DM}}\frac{v_a}{m_a} = 7.8 \times 10^{-4}\frac{\xi}{m_a}\ [\mathrm{barn}^{-1}\mathrm{day}^{-1}] \tag{1.42}$$

Here, σ_E is the energy resolution at $E = m_a$, MT is the detector exposure, and $\eta(E)$ is the cut efficiency. In the EDELWEISS and Majorana analyses $\xi = 0.001$ is taken to be the mean of the dark matter velocity distribution with respect to Earth. Current results from both solar and dark matter axion searches are given in Figure 1.13.

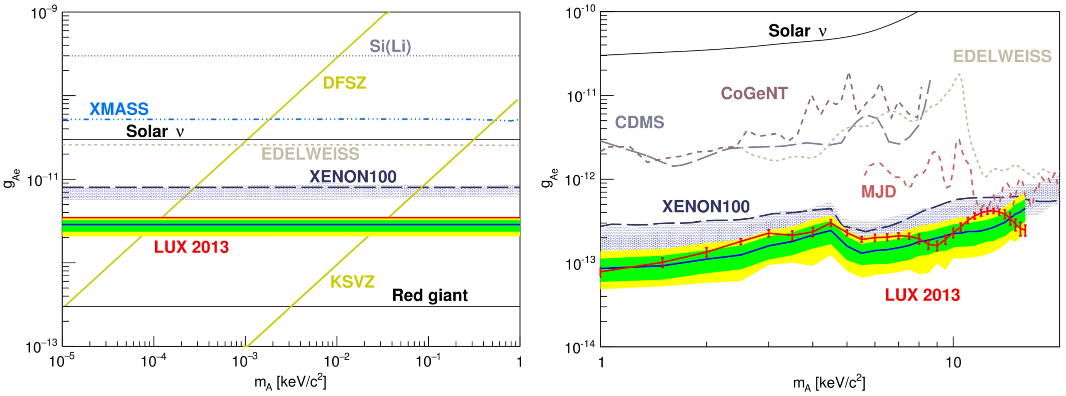

Figure 1.13: Limits on g_{ae} from current experiments from solar and dark matter axion searches. (Figures 6 and 7 from [76])

1.8 Axion-Nucleon Interactions

In addition to coupling to photons and electrons, the direct coupling of the axion field ϕ_a to the nucleon field $\psi_N = \binom{p}{n}$ was first evaluated by Haxton to analyze data from a laboratory search for MeV-energy axions emitted from a 1.115 MeV excited state transition of ^{65}Cu [81]. The Lagrangian is written in terms of the (model-dependent) g^0_{aN} isoscalar and g^3_{aN} isovector axion-nucleon coupling constants:

$$\mathcal{L} = i\bar{\psi}_N\gamma_5(g^0_{aN} + g^1_{aN}\tau_3)\ \psi_N\phi_a \tag{1.43}$$

The ^{57}Fe has a large solar abundance (its average density in the Sun's core is $9 \times 10^{-19}\text{cm}^{-3}$), and its first thermally excited state decays to the ground state, emitting a 14.4 keV monochromatic photon in the process. It is possible for this decay to instead emit a 14.4 keV monochromatic axion:

$$^{57}\text{Fe}^* \rightarrow {}^{57}\text{Fe} + a \tag{1.44}$$

The branching ratio for axion and photon emission is given in [81] as:

$$\frac{\Gamma_a}{\Gamma_\gamma} = \left(\frac{k_a}{k_\gamma}\right)^3 \frac{1}{2\pi\alpha}\frac{1}{1+\delta^2}\left[\frac{g^0_{aN}\beta + g^3_{aN}}{(\mu_0 - 1/2)\beta + \mu_1 - \eta}\right]^2 \tag{1.45}$$

Here the factors k_a, k_γ are the momenta of the outgoing axion and photon, respectively, and their ratio is often written simply as β. The expected axion flux Φ_a from this process is given in terms of an effective axio-nuclear coupling g^{eff}_{aN} [80]:

$$\Phi_{14.4} = \beta^3(4.56 \times 10^{23})(g^{\text{eff}}_{aN})^2/\text{cm}^2/\text{s} \tag{1.46}$$

The DFSZ and KSVZ models give different predictions for g^0_{aN} and g^3_{aN}, and differing predictions for the axion flux can be obtained by substituting them into the effective constant [82] [80]:

$$g^{\text{eff}}_{aN} = (-1.19g^0_{aN} + g^3_{aN}) \tag{1.47}$$

A search for 14.4 keV axions can be carried out by substituting Equations 1.46 and 1.47 into the expression for the expected number of axion counts (Equation 1.41) and substituting m_a with 14.4 keV. The reduced axion velocity β depends on the mass of the axion, which can range from 0 to 14.4 keV. We note that this type of search is independent of the predicted solar axion flux for the axion-electron coupling predicted by Redondo, since the source of axions is a nuclear (not an atomic) transition.

1.9 SUMMARY

In this chapter we have discussed the exciting probes of physics beyond the Standard Model which are possible with searches for neutrinoless double beta decay and solar/cosmic axions. Key challenges to be overcome by experiments in both cases are minimizing the contribution from unwanted radioactive backgrounds in the energy regions of interest, maximizing detector size and exposure, and minimizing detector energy resolution. The following chapters will discuss these searches in the context of the MAJORANA DEMONSTRATOR experiment.

CHAPTER 2

THE MAJORANA DEMONSTRATOR

2.1 OVERVIEW

The MAJORANA DEMONSTRATOR is a neutrinoless double beta decay ($0\nu\beta\beta$) experiment currently in operation at the Sanford Underground Research Facility [83] in Lead, South Dakota. It is located 4850' underground to provide shielding from cosmic rays, with a rock overburden equivalent to 4290 meters of water. Two vacuum cryostats house 44.1 kg of P-type point contact, high-purity germanium (PPC HPGe) detectors [84],[85], 29.7 kg of which have been enriched to a high concentration (88%) of the isotope ^{76}Ge to maximize the $0\nu\beta\beta$ discovery potential. The arrays are built with world-leading low-background materials, including underground-electroformed copper (UGEFCu) which was machined on-site at the 4850' level to nearly eliminate natural and cosmogenic radioactivity. The detector modules are operated within a multi-layered shield consisting of copper, lead, high-density polyethylene (plastic), a nitrogen gas purge, and an active muon veto system. Figure 2.1 gives a cross-sectional view of the DEMONSTRATOR.

In order for a $0\nu\beta\beta$ experiment to make a discovery at $T^{0\nu}_{1/2} \sim 10^{28}$y and beyond, it is essential to develop technologies which enable a large active mass, low backgrounds, and excellent energy resolution. The DEMONSTRATOR is so-named because it is intended to *demonstrate* feasible construction and operation techniques which can be scaled up to a future ton-scale experiment. The processing of the enriched Ge used by MAJORANA [87] can be scaled to create the necessary raw $^{\text{enr}}$Ge material,

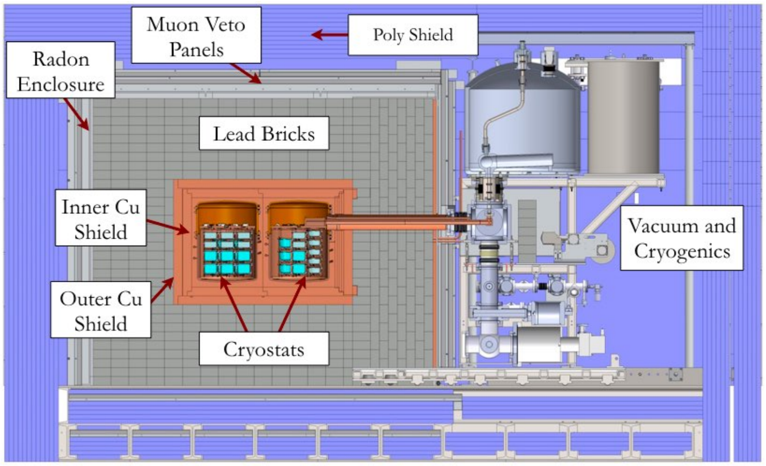

Figure 2.1: Cross section view of the MAJORANA DEMONSTRATOR [86].

and minimizes the rate of cosmic ray (cosmogenic) activation of radioactive isotopes by storing the material underground whenever possible. As evidence of its low backgrounds, the MAJORANA collaboration published competitive limits on $0\nu\beta\beta$ [42] in March 2018 with a (relatively modest) exposure of 9.95 kg-y. The cosmic ray flux at the 4850' level was measured using a >2 year dataset [88]. The calibration of the system using ^{228}Th line sources and a multi-peak energy calibration routine [89] employed across the entire energy spectrum gave the current world-leading energy resolution, 2.5 keV FWHM at the Q value of 2039 keV.

The DEMONSTRATOR is by no means limited to $0\nu\beta\beta$ physics. The excellent energy resolution and low thresholds of its PPC HPGe detectors make possible several competitive rare event searches, particularly in the low-energy (< 100 keV) regime. The initial commissioning dataset was used to set limits on bosonic dark matter, solar axions, Pauli exclusion principle violation, and electron decay [79]. Results from a longer dataset have yielded limits on the existence of “lightly ionizing particles” with fractional charges as low as $e/1000$ [90].

An essential feature of PPC HPGe detectors is their ability to distinguish between different types of physics events. The most significant pulse shape analysis (PSA) cuts developed for the $0\nu\beta\beta$ analysis focus on idenfitication and rejection of multi-site events in the crystal, and alpha events near its surface. At low energy, pulses originating from the *transition layer* are energy-degraded and present a significant background for rare event searches. We will defer a detailed discussion of the properties of the PPC HPGe detector signals to Chapter 3.

This Chapter will discuss the DEMONSTRATOR construction, data taking, and key analysis techniques leading to the 2018 $0\nu\beta\beta$ result, highlighting two main contributions by the author; the rejection of external events with the muon veto system, and the primary livetime and exposure calculation.

2.2 CONSTRUCTION AND OPERATION

Low levels of intrinsic radioactivity in the active detector volume are irrelevant if the hardware contains high-activity materials. To that end, radioactive backgrounds from hardware, cables, connectors, and electronics must all be minimized, with the highest priority on materials closest to the detectors. Different approaches to mitigate backgrounds are possible. The GERDA experiment utilizes a liquid argon (LAr) veto to identify scintillation light from these events in the argon and reject coincident events in the Ge, allowing them to use lower-purity commercial-grade materials at the expense of a low-energy program and backgrounds associated with the LAr itself. In contrast, MAJORANA has focused on developing custom ultra-low background materials, carefully limiting their natural and cosmogenic radioactivity by selecting parts based on radioassay measurements [91], an extensive parts tracking database [92], and development of detector hardware that minimizes the total mass required. To maintain material cleanliness, the DEMONSTRATOR was constructed in a class 1000 clean room.

Copper is an attractive choice for building custom components nearest the Ge detectors. It has no long-lived cosmogenic isotopes, and can be highly purified to limit ^{238}U and ^{232}Th contamination. It can also be machined into detector-grade support hardware, as shown in Figure 2.3, and is an excellent thermal and electrical conductor. With these considerations in mind, MAJORANA undertook a multi-year process of copper electroforming in the underground facility at the Sanford Lab[1], producing more then 2 tons of ultra high-purity, low-radioactivity material which has never been to the surface, with $\leq 0.1\ \mu$Bq/kg from the ^{238}U and ^{232}Th decay chains and minimal cosmogenic activation. The raw underground-electroformed copper (UGEFCu) was removed from its electroforming mandrels and machined into a wide variety of detector and shielding components by a dedicated machinist in an underground machine shop at the 4850' level. After machining, parts were chemically etched to remove surface contaminants and laser-engraved for tracking in the parts database.

Radon is a significant background concern, particularly for a mine environment such as Sanford Lab where levels are typically high. Its isotope ^{222}Rn is part of the ^{238}U decay chain, and its various decay "daughters" can deposit energy at the Q value of any $0\nu\beta\beta$ experiment. Furthermore, the daughters (or progeny) can "plate out" onto metals including copper, embedding directly on the surface of the material and emitting its radioactivity into the bulk of the material. An important example of this issue can be seen from the α-decay of ^{210}Po:

$$ {}^{210}_{84}\mathrm{Po} \rightarrow {}^{206}_{82}\mathrm{Pb} + \alpha \tag{2.1} $$

Here, the α particle is emitted with 5.2 MeV of energy, making it a potential source of background at the Q value. To mitigate the radon plate-out onto the UGEFCu components, parts were acid etched in an acidic hydrogen peroxide solution to remove micron-thick amounts from the surface, and passivated with citric acid before being stored in a nitrogen environment. Figure 2.2 depicts this process, and Figure 2.3 shows detector hardware for Module 2 in its N_2 storage "dry box." Gaseous radon is also removed from the inner shield volumes by an active nitrogen gas purge.

---

[1] additional electroforming also took place at a shallow underground lab at Pacific Northwest National Laboratory

Figure 2.2: UGEFCu fabrication, from electroforming (left), to machining (center), to acid etching (right).

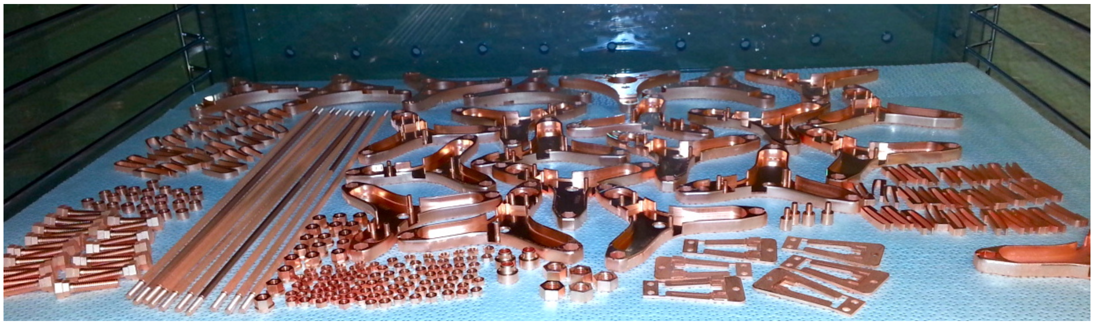

Figure 2.3: UGEFCu machined parts, ready for installation in Module 2.

The HPGe detector arrays were constructed in a dry nitrogen glove box. Detector units were assembled from bare $^{\mathrm{enr}}$Ge and $^{\mathrm{nat}}$Ge crystals, with UGEFCu hardware used to make an electrical contact wth the crystal bottom and provide support for the low-mass electronics front end boards (LMFE) [93]. Strings of detector units were then assembled and mounted inside each cryostat, using specially supplied Axon' low-mass cabling for high-voltage (HV) and signal readout, attached to the front end with custom UGEFCu and Vespel connectors. After string installation, the cryostat is closed and the module is stacked with Pb bricks before being transported into to the main shield. Figure 2.4 depicts this process.

Majorana published results in 2016 [91] from an assay of the radioactivity of the materials used in its construction, including cables, connectors, UGEFCu, lead shielding, and many other components. Taken together, they form a prediction for

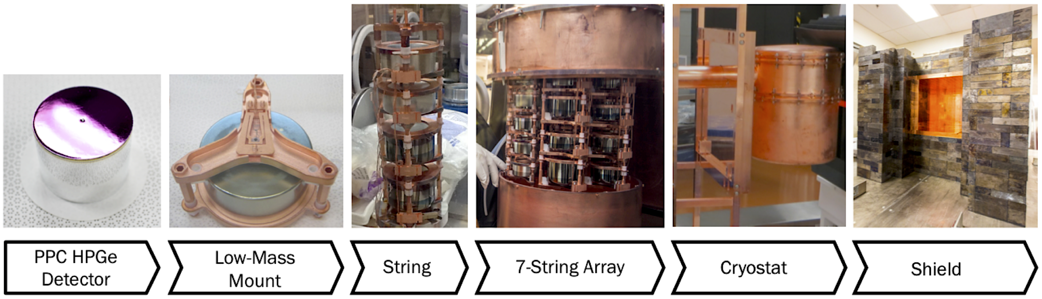

Figure 2.4: The modular design of the Demonstrator, illustrating the detector integration into the main shield. (Courtesy J. Gruszko [94].)

the expected background in the Demonstrator near the Q value of 2039 keV. Natural radioactivity is brought within acceptable tolerances by the use of UGEFCu and highly radiopure components. The contribution from Pb is minimized by a layer of UGEFCu shielding in the inner Cu volume, in addition to a layer of commercially sourced Cu. The various contributions to the background are given in Figure 2.5, in terms of counts in the 4 keV "region of interest" ROI around Q. Since that time, Majorana has changed its standard units to be in terms of the resolution (FWHM) of a peak at this energy. Projected backgrounds based on the assay are 3.5 counts/ROI/ton/y, or 2.2 counts/FWHM/ton/y (based on a 4 keV ROI and 2.5 keV FWHM).

To bring a detector module online, the cryostat is pumped to a 10^{-9} Torr vacuum and the components are cooled to liquid nitrogen temperature, 77 K. Bias voltages of 2–5 kV are applied to the detectors, and signals are read out by the data acquisition (DAQ) system. Both modules were first sealed, cooled down, and brought online while still positioned in the glove box. After initial testing was successful, they were moved into the main shield. Table 2.1 gives an installation timeline.

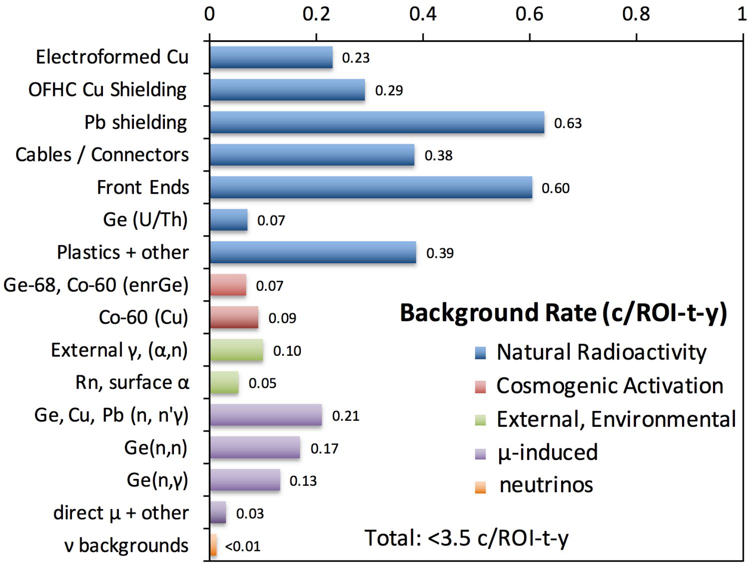

Figure 2.5: Background expectation based on results in Ref. [91], illustrating the expected contributions from various background sources. Since this publication, Majorana has changed its units from /ROI to /FWHM, with a projected background of 2.2 counts/FWHM/ton/y (using a 4 keV ROI and a 2.5 keV FWHM).

Table 2.1: Material content and installation timeline of Modules 1 and 2.

Module 1	**Timeline**
$^{\mathrm{enr}}$Ge 16.9 kg, 20 dets	9/2014 : Module commissioning
$^{\mathrm{nat}}$Ge 5.6 kg, 9 dets	5/2015–10/2015 : In-shield running
	10/2015–1/2016 : Offline (upgrades)
	1/2016–Present : In-shield running
Module 2	**Timeline**
$^{\mathrm{enr}}$Ge 12.9 kg, 15 dets	4/2016 : Module commissioning
$^{\mathrm{nat}}$Ge 8.8 kg, 14 dets	7/2016–Present : In-shield running

2.3 Software and Data Processing

The Majorana data acquisition system (DAQ) is primarily operated using the ORCA software suite [95], which is used as a common interface to control the cryogenic, vacuum, high voltage, and many other subsystems needed for consistent detector operation. Signals from the HPGe detectors are routed through a two-stage amplifier and digitized with 14 bit precision at 100 MHz using custom waveform digitizer boards originally developed for the GRETINA experiment [96]. The voltage and clock time value for each wavefrom recorded by the GRETINA cards is recorded by ORCA, along with details of the hardware configuration such as the HV setting and signal channel identifier for each detector. Physics data runs are generally divided into one-hour periods for normal data taking operations. Periods of physics operation are grouped into Data Sets, which are separated by significant hardware or software changes to the system. A "threshold finder" routine is also run periodically, individually adjusting the energy thresholds of each detector to be as low as possible while still maintaining a reasonable (∼1 Hz) trigger rate in each detector. Section 2.5 discusses the Data Sets in more detail and gives the livetime and exposure of each.

The MAJORANA and GERDA collaborations have developed a common suite of software analysis tools designed to process waveforms from HPGe detectors in an efficient and consistent fashion. The `OrcaROOT` software package processes raw data from ORCA into a format readable by the ROOT software package [97]. The MAJORANA-GERDA Data Objects library `MGDO` is a collection of C++ classes developed specifically to record waveforms and other relevant data from differing hardware into a consistent format for analysis. For example, an HPGe waveform consists of a voltage read out by an analog-to-digital (ADC) converter, paired with the timestamps of the digitizer clock. `MGDO` contains a class `MGWaveform` which provides a common interface and attributes for data taken with different systems [98].

The two electrons emitted in double beta decay have very short ranges, and will only deposit energy in a single detector. Thus, any event where multiple detectors are hit can be rejected from the analysis. Events in the output from ORCA are not initially grouped together according to their timestamps. The primary function of the `MJOR` "event builder" software is to group hits in individual detectors into *events* if they occur within a short time window ($< 10\ \mu$s) of each other. This granularity (multiplicity) cut enabled by the event builder provides a powerful means of background rejection and is a key advantage of a modular detector array.

Finally, the Germanium Analysis Toolkit `GAT` provides high-level analysis routines for event-built data. The "built" data output by `MJOR` contains the individual detector waveforms but performs only minimal secondary processing on the waveforms. `GAT` contains routines for measuring the energy and pulse shape characteristics of each waveform, pulser tagging and removal, as well as performing offline analysis corrections to waveforms due to nonlinearity effects. The GAT data removes raw waveforms to save disk space, and calculates energy and various pulse shape parameters. Finally, "skim" data are produced by the `GAT` app `skim_mjd_data`, which removes pulser events and calculates additional pulse shape analysis (PSA) parameters and cuts, producing spectra suitable for physics analysis. In addition to germanium data analysis, software has been developed to automatically analyze data from the Demonstrator muon veto system and reject any events in the HPGe detectors which are promptly coincident (< 1 sec) with muon candidates. The next section gives a brief background on underground cosmic rays and describes the muon veto analysis suite.

2.4 The Demonstrator Muon Veto Cut

Cosmic ray showers are produced in Earth's atmosphere by the interaction of a high-energy particle (usually a proton) with air molecules. The collision results in an "airshower" event, creating many different types of short-lived, high-energy particles. Due to their short lifetimes and interaction cross sections, most particles do not penetrate far into the Earth. This makes underground laboratories essential for experiments seeking to reduce the contribution of cosmic ray events. Unfortunately, muons created in airshowers are capable of traversing large distances in rock. Many are created with GeV-scale kinetic energy, and are minimally ionizing, undergoing fewer interactions with matter. The number of interactions with matter a given particle will encounter is proportional to the length traveled and the density of material. This is often called the "slant depth" and measured in meters-water-equivalent, where 1 mwe = 100 g/cm^2. The cosmic ray background is greatly suppressed at the 4850' level of SURF due to the 4260 mwe overburden.

The question of the necessary depth of a ton-scale $0\nu\beta\beta$ experiment is still an open one. Mei and Hime conducted a useful study in 2006 [99] comparing the relative depths of underground laboratories, correlating measurements of muon rates at different depths and offering predictions for the muon-induced flux of neutrons at each site. The results from the MAJORANA muon flux paper were in agreement with this study. The mountain overburden of the Gran Sasso laboratory in Italy offers reduced protection from side-going events, while the Sanford Lab has not yet been ruled out in favor of a deeper site such as Sudbury or Jinping, due in part to the effectiveness of a veto system at this depth.

The active muon veto system used by the DEMONSTRATOR is a segmented 32-panel array, consisting of 2.54-cm thick EJ-204B acrylic scintillator sheets, whose light output is collected by wavelength shifting fibers at a single photomultiplier tube just outside each panel [100]. The 32 panels completely surround the inner lead shield, taking up 37 m^2 and providing nearly 4π solid angle coverage. LEDs are embedded in each panel and flashed at regular intervals to monitor the gain stability of the system; typically an LED event occurs in all 32 panels simultaneously. The panels are arranged such that the top and sides consist of two layers of overlapping panels with four panels each. The bottom array consists of two orthogonal sets of six panels, placed inside the overfloor support structure under the lead shield. Data from the veto system taken during the construction of the DEMONSTRATOR was used to measure the muon rate at the 4850' level of Sanford Lab, finding that the muon rate is reduced from $\sim 1\ \mathrm{cm}^{-2}\ \mathrm{min}^{-1}$ at sea level to $(5.04 \pm 0.16) \times 10^{-9}\ \mathrm{cm}^{-2}\ \mathrm{s}^{-1}$ at the 4850' level [88]. The array is shown in Figure 2.6.

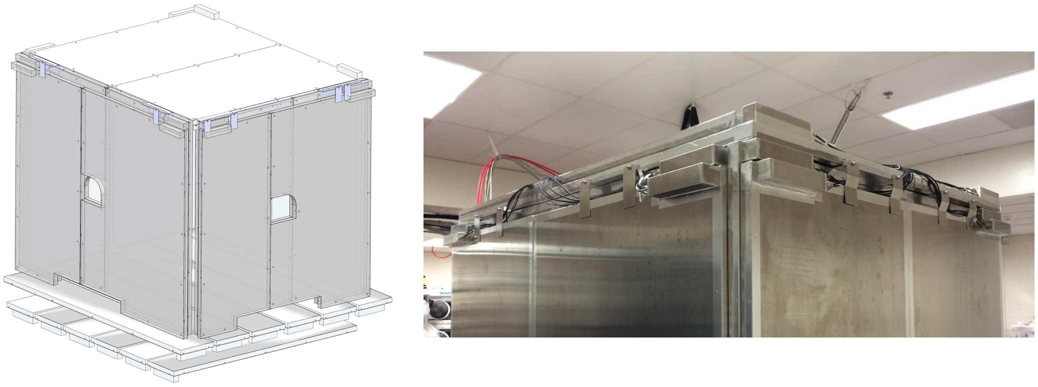

Figure 2.6: Left: depiction of the veto panel array, with visible cutouts for the HPGe cryostat crossarms. Right: Installed on-site at the 4850'.

Muons passing through the scintillator panels deposit energy proportional to the length they traverse. Environmental gammas tend to deposit less energy and have a much shorter mean free path. A major part of the veto panel design process ensured that the 2.5-cm thick panels have sufficient separation between gamma and muon events. Due to the modular design, different populations of events can be examined, including a population which has energy deposited in both top and bottom layers. This vertical pattern has a very high muon efficiency, since it is nearly impossible for gammas to traverse the entire inner lead volume of the DEMONSTRATOR. Figure 2.7 demonstrates the effectiveness of this vertical hit pattern cut in removing gamma events by comparing the surface calibration of a top panel to its underground spectrum with the vertical pattern cut applied, eliminating the gamma distribution entirely.

In order to trigger the array based on a geometric hit pattern, raw signals from the PMTs embedded in the scintillator panels are split into two paths. One path goes directly to two 16-channel CAEN792 QDC cards to measure the energy. The second path is through two 16-channel logical discriminators, which determine if a

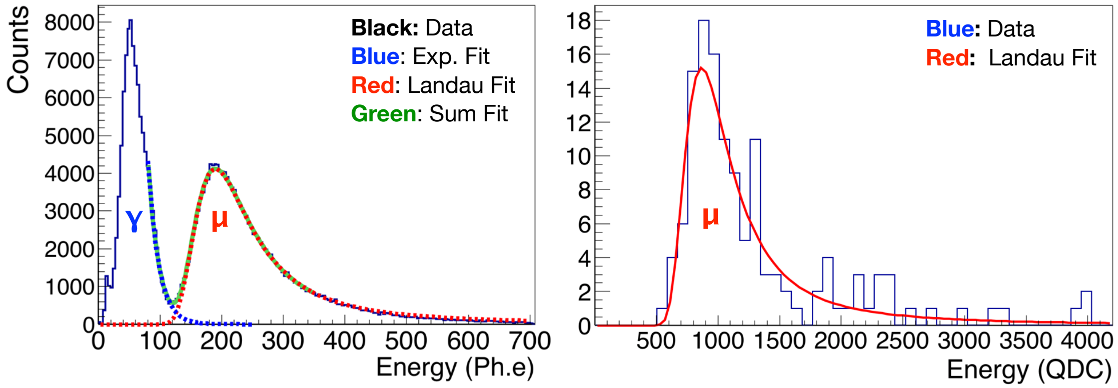

Figure 2.7: Left: Surface calibration of a top panel showing gamma and muon peak. Right: Underground data from the same panel, utilizing a vertical coincidence condition to remove the gamma peak.

given event has a hit pattern of interest and triggers the system. The muon flux measurement required at least one hit in each discriminator bank to be above the hardware threshold, and ensured the top-bottom coincidence by connecting the bottom and top veto panels to separate banks. Following the initial commissioning Data Set (see next section), the trigger logic was changed to allow any two panels with signals above threshold to trigger readout of the system. This was done with the intention of capturing a wider variety of potential muon-induced events, while not causing excessive dead time in the system due to single-panel triggers. Once triggered, all 32 QDC channels are read out simultaneously and assigned a timestamp from a 100 MHz clock card common to both HPGe and veto systems. Figure 2.8 illustrates both vertical and "2+" panel hit patterns.

The goal of the Majorana veto cut is to suppress all events in the HPGe detectors which are caused by direct muon or muon-induced events [101]. It is generally expected that the majority of muon-induced physics events are "prompt"; they will deposit energy in the Ge array nearly instantaneously after passing through the veto panels. A muon interacting in the lead, copper, or HPGe can produce a "shower" event, where the large variety of gammas can be expected to interact within this coincidence window. On a slightly longer timescale are the decays of excited isotopes

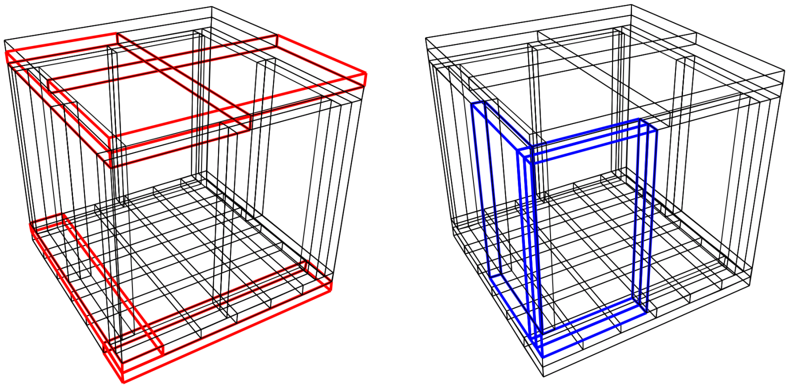

Figure 2.8: Two possible hit patterns in the veto array. Left: vertical 3-plane coincidence. Right: 2+ panel coincidence.

in Pb, Cu, and Ge, the majority of which decay in less than 1 second. “Delayed” coincidences are possible as well, with the half-lives of some isotopes produced being on the hour-scale or longer. These must be identified by other methods since the veto system cannot keep the Ge array “dark” for this long. In order to veto prompt coincidences, a time window of 0.2 ms before and 1 second after a muon candidate event was chosen. HPGe events which fall in this time window are removed from the final spectrum. Figure 2.9 shows simulation results for the time distribution of muon-induced events in the HPGe array, with the red line denoting the 1 second cutoff [102].

As described in the previous section, the MAJORANA event builder software transforms raw ORCA data into built data containing both germanium and veto data. Software routines have been developed with `MGDO` and `GAT` to process the output of the veto system. In particular, the `GAT` application `auto-veto` implements automatic error checking of the veto data, and performs QDC threshold identification, LED pulser rejection, and muon candidate identification, creating output for every run suitable for application of the veto cut to the HPGe data.

The standard analysis procedure for a veto data run is the following sequence:

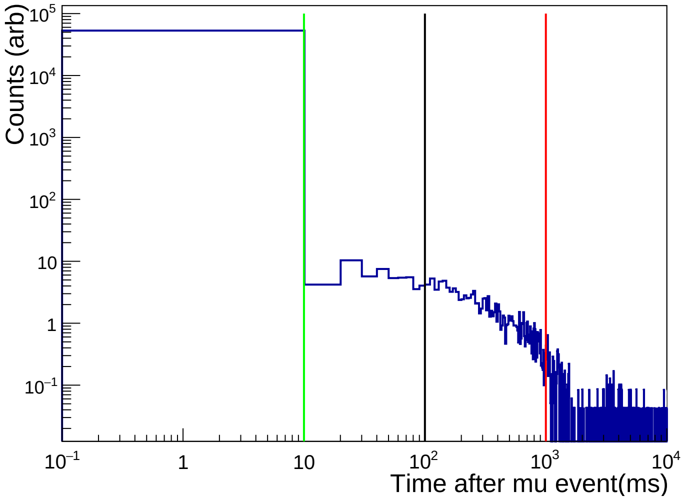

Figure 2.9: Results from simulation of the veto system [102] justifying the selection of a 1 second window for the removal of prompt coincidences.

- *QDC Threshold Identifcation*: When a panel does not record a meaningful energy deposition, a trigger of the array causes it to read its minimal value, producing a distinct peak in the lowest energy bin. This allows the software threshold of the panel to be measured.
- *Error Checks*: Veto data quality issues such as clock desynchronization and corrupted QDC information occur at a very low rate in the veto system. If these issues are detected by `auto-veto`, error messages in the standard data production allow monitoring and investigation of problematic runs.
- *Muon Identification*: Analysis of geometric hit pattern and energy deposited are used to identify muon candidates. These events are recorded in separate ROOT output files accessible by other `GAT` routines, containing timing and other information needed to apply the veto cut.

The trigger condition requiring energy depositions in two or more panels allows a wider variety of physics events to trigger the system, including muon shower events originating from nearby, where the muon itself does not cross the veto panels. `auto-veto` idenfities these additional hit patterns and flags these events as potential muon candidates, to be removed in the veto cut. If there is a gap between runs longer than 1 second, an additional veto period is imposed on the first second of a new run, in the event that a muon hit occurred immediately before the run started.

Muons directly impacting the HPGe detectors tend to leave large energy deposits >10 MeV in the detectors. Events possessing both a vertical hit pattern in the veto system and one or more overflow events in the HPGe array are nearly certain to be from muons. Figure 2.10 illustrates this by showing the time difference as recorded by the veto and Ge systems for these events. A clear peak stands out at $\Delta t \sim 0$ seconds, verify that the systems are indeed synchronized.

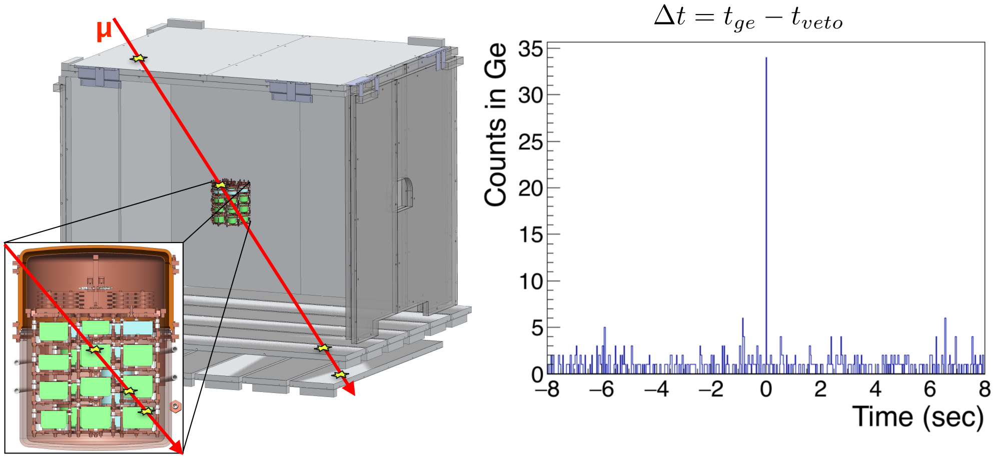

Figure 2.10: Left: Depiction of a muon passing through both the veto and HPGe systems. Right: Time difference between muon candidate events in both systems, showing clear evidence of synchronization.

The Demonstrator veto cut has been implemented with a maximally conservative strategy identifying any event with two or more panels hit as an event with the potential to deposit energy in the HPGe array. Due to the choice of coincidence window, the “deadtime” introduced by the veto system is small compared to the overall run time; roughly one vertical muon traverses the veto system every four hours. This deadtime is accounted for in the livetime calculations described in the next section.

2.5 Livetime and Exposure

Data taking for Demonstrator has been partitioned into Data Sets (DS) to reflect significant hardware or software changes to the system. The initial Module 1 commissioning data (DS0) was taken without the innermost UGEFCu shield layer, and after its installation in Fall 2015, the DS1 data set began. Module 2 took its first data with DS4 on a separate DAQ system, and the modules were first integrated in DS5. Grounding issues causing transient noise in the array were present with the two Modules running in tandem. These were largely eliminated by January 2017, and DS5 was partitioned into DS5A and DS5B to denote the high and low-noise period. It was during DS5B that the exposure reached 10 kg-y; the analysis was cut off at that point for the results in the 2018 $0\nu\beta\beta$ publication [42]. In order not to bias the development of pulse shape analysis and other algorithms to reject background events, the Majorana collaboration elected to employ a statistics-driven blindness scheme, in which runs alternate between open and blind in a 31/99 hour cycle. Blind data were taken during DS1 and DS2, paused for DS3 and DS4, and resumed in DS5C. The blind data will not be considered in this thesis. Table 2.2 sumamrizes the dates of operation for each Data Set, the active module, and a brief note on the significant change to the hardware configuration.

The Run Selection and Data Cleaning (RSDC) Working Group has provided a "good run list" for each data set [103]. The final run list for each data set is stored in the `GAT` database file `DataSetInfo`, along with the veto-only and bad detector lists and PSA parameters for each channel, to be accessed by multiple routines. When the skim file generator `skim_mjd_data` is run, it uses this file to skim data from good runs, calculate PSA parameters, and apply channel selection cuts.

It is essential that the skim data and the method used to calculate the corresponding exposure of a Data Set are completely consistent. The `GAT` application `ds_livetime` was developed to provide an accurate and robust means of performing

Table 2.2: Description of Data Sets to date by active module, calendar dates, and changes to the hardware configuration.

Data Set	**Duration**	**Hardware Status**
DS0 (M1)	26 June 2015 – 27 Oct 2015	Commissioning
DS1 (M1)	31 Dec. 2015 – 24 May 2016	Inner UGEFCu shield
DS2 (M1)	24 May 2016 – 14 July 2016	Waveform Multisampling
DS3 (M1)	25 Aug. 2016 – 27 Sept. 2016	Multisampling Deactivated
DS4 (M2)	25 Aug. 2016 – 27 Sept. 2016	First Module 2 data
DS5A (M1,2)	13 Oct. 2016 – 27 Jan. 2017	Integrated DAQ (noise issues)
DS5B (M1,2)	27 Jan. 2017 – 17 Mar. 2017	Optimized Grounding
DS5C (M1,2)	17 Mar. 2017 – 11 May 2017	Blind Cycle Resumed
DS6 (M1,2)	11 May 2017 – (ongoing)	Multisampling Resumed

this calculation for all Data Sets [104], by loading the run list in `DataSetInfo` and accessing each individual run, tracking all enabled detectors and taking into account all reductions from channel selection, muon veto, and other factors. The removal of individual detectors for certain periods corresponds to a decrease in *runtime* for the Data Set. Compounding this reduction in overall exposure is the *deadtime* from different sources. Generally, a channel is "dead" if it is not sensitive to an event at the $0\nu\beta\beta$ Q-value for any reason. We can define the *livetime* of an individual detector i to be the difference of its runtime (in days) with the various deadtime reductions k:

$$LT_i = RT_i - \sum_{k}^{type} DT_{ik} \tag{2.2}$$

If a detector is operated under its optimal bias voltage, or exhibits other anomalous behavior, it can exhibit degraded energy resolution and pulse shape discrimination. Its degraded signals are still usable in the multiplicity cut. These detectors are declared "veto-only" in the analysis and do not contribute to the total exposure. If data from a detector cannot be used at all, it is marked "bad" and removed completely, without contributing to exposure or multiplicity. Transient problems with gain drift, energy calibration, or pulse shape parameters can occur in a small sub-set of the Data

Set. To avoid removing misbehaving detectors entirely, the RSDC Group provides "channel selection" files to mark specific detector channels as bad or veto-only on a run-by-run, channel-by-channel basis [105].

Since midway through DS1, the DEMONSTRATOR has operated in a "continuous running" mode where there is no interruption in data taking when the DAQ system transitions between runs. By default in `ds_livetime`, the runtime is calculated by reading timestamps from the GRETINA trigger card (100 MHz clock) at the beginning and end of each run, producing a value accurate to 10 ns. In earlier Data Sets these clock packets are not available, and the UNIX start and stop timestamps (accurate to 1 second) are used to calcuate the runtime. Equation 2.2 implicitly assumes the different deadtime types k do not overlap and are not double-counted, which will be addressed below. The expression for the exposure E of a Data Set (in kg-y, kg-d, ton-y, etc.) is then broken down in a per-detector, per-run basis:

$$\begin{aligned} E &= \sum_{i,j}^{det,run} m_i \; LT_{ij} \\ &= \sum_{i,j} m_i \; (RT_{ij} - DT_{ij}) \end{aligned} \tag{2.3}$$

Here, the sum i is over all detectors, j over runs, using the active detector mass for each detector m_i [106]. The factors RT_{ij} and DT_{ij} are determined from the runtime of each run, the removal of channels for specific runs, and the individual deadtime contributions for each channel:

$$DT_{ij} = DT_{\text{hardware}} + DT_{\text{pulser}} + DT_{\text{LN fill}} + DT_{\mu \text{ veto}} \tag{2.4}$$

- *Hardware deadtime:* For very brief periods, the digitizer hardware is at times unable to trigger and record an event. Due to the low data rate, it is also possible that the DAQ could stop taking data for a period of time without an obvious effect. To calculate the extent of this deadtime, for run subsets defined between instances of running the threshold finder, the pulser period of each channel is measured. The expected number of pulser events is compared with the actual number found in each channel. Events are "lost" when they occur within a digitizer dead period, as when the GRETINA card has already triggered (typically on a noise event). The deadtime is then

$$DT_{ij,\text{hardware}} = RT_{ij}\ (1 - N_{\text{found}}/N_{\text{expected}}) \tag{2.5}$$

- *Pulser deadtime:* The pulser input signal is a square wave, producing an equal number of positive and negative triggers. Every signal that is tagged as a pulser event comes from the positive-going part of the waveform, and there is a corresponding deadtime $DT_{\text{retrigger}}$ of 62μs or 100μs (depending on multisampling being active) from the negative-going component. Typically the pulser period is 8.388608 seconds. This deadtime is calculated in each run, for each channel, multiplying by the number of found pulser events:

$$DT_{ij,\text{pulser}} = N_{\text{found}}\ DT_{\text{retrigger}} \tag{2.6}$$

- *LN fill deadtime:* The automatic LN fill system is known to produce large amounts of microphonic noise while a fill is taking place, potentially affecting the energy estimation of events in the $0\nu\beta\beta$ region of interest, or increasing the hardware deadtime. When a module fills, a veto period of ~20 minutes is applied to its detectors. The UNIX times of these LN fills are tagged by the `GAT` app `ln_fill_tag` based on the derivative of the LN fill level recorded to a database, and stored in `DataSetInfo` [107]. To ensure the full fill window is vetoed, the app sometimes reports multiple "tags" for a single fill, and `ds_livetime` calculates a non-overlapping dead time for each run of approximately "15 minutes before, 5 minutes after," applying it to all channels in the appropriate module.
- *Muon veto deadtime:* As described in Section 2.4, simulations have shown that the energy spectrum from muon shower events passing through (or near) the

modules is mostly prompt, occuring 1 second or less after the initial event. When the data from the muon veto analysis identifies a muon candidate event, a veto period of approximately 1 second is applied globally to both modules, using exactly the same algorithm in `skim_mjd_data` and `ds_livetime` to generate the candidate list.

It is also important to mention that `skim_mjd_data` uses a "hit skipping" algorithm to merge events in the high-gain (HG) and low-gain (LG) channels into a single energy spectrum, since this has an effect on the livetime. During the skimming process, for each event the code preferentially keeps the HG hit and discards the LG hit unless one of the following conditions are met and the LG hit is kept instead:

- A HG hit does not exist for this event
- The HG channel has been marked "bad" or "veto-only" by the RSDC group (and the LG is unmarked)
- The HG hit is saturated (usually above 3 MeV)
- The HG hit is marked as "late trigger" by the `GAT` data cleaning processor.

With this scheme in mind, the number of pulsers in each channel was calculated, dividing each Data Set into subsets delineated by threshold finder runs. The corresponding hardware and pulser deadtimes were then calculated in three modes – HG hits only, LG hits only, and an "OR" mode which finds the deadtime of the final merged spectrum. The results of this calculation were then directly applied in `ds_livetime` to find the hardware and pulser deadtimes for each mode, channel, and run in every subset.

The impact of each deadtime can be quantified either in terms of its effect on exposure, or its effect on livetime. The accounting by exposure requires that each deadtime type is independently tracked for each detector, and while this is in principle not difficult, a simpler method is to look at the "deadtime fraction" for each type k:

$$F_k = \frac{\sum_{ij}^{run,chan} DT_{kij}}{\sum_{ij} RT_{kij}} \tag{2.7}$$

Here the fraction F_k is calculated by summing the deadtime for each channel j in every run i, and dividing by the sum of each channel's runtime for every run. Although the sum of runtimes for each channel is significantly larger than the true runtime, it is easy to see that if a channel is 100% dead, its fraction F_k will equal 1, as expected. Deadtimes from each contribution are on the order of 1% or much less, and any double-counting arising from overlapping periods (e.g. a pulser event during a muon veto dead period) in the current calculation is negligible.

The uncertainty of the exposure has several important contributions, which we include. Since the exposure calculation for an individual channel (as in Equation 2.3) is the product of the active mass and the livetime, we expect the uncertainty for a single channel to be expressible as:

$$\sigma_{exp}^{i} = (m_i LT_i)\sqrt{\left(\frac{\sigma_{m_i}}{m_i}\right)^2 + \left(\frac{\sigma_{LT_i}}{LT_i}\right)^2} \tag{2.8}$$

The total exposure uncertainty for the full Data Set can then be expressed as:

$$\sigma_{exp}^{tot} = \sum_{i}^{dets} \sigma_{exp}^{i} \tag{2.9}$$

The linear sum of the uncertainties is required here because the uncertainties of the active masses are highly correlated; the uncertainty is statistical and not random. The uncertainty on the livetime depends on contributions from the runtime uncertainty and the hardware deadtime uncertainty, but it is at least 3 orders of magnitude smaller than the active mass uncertainty, and is subdominant regardless of whether it is added linearly or in quadrature. Table 2.3 reports the final runtime, average livetime, and exposures for the 2017 analysis, taking all channel selection, uncertainty, and deadtime contributions into account. Further information, including the complete output of `ds_livetime` for each Data Set, can be found in the internal document [104].

Table 2.3: Runtime and final exposure summary for all Data Sets.

DS	Runtime (d)	Avg. Livetime (d)	$^{\mathrm{enr}}$Ge Mass (kg)
DS0	45.919	43.217 ± 0.661	10.695
DS1	58.768	52.488 ± 2.902	11.901
DS2	9.576	9.399 ± 0.081	11.310
DS3	29.879	29.248 ± 0.107	12.631
DS4	19.146	18.751 ± 0.030	5.471
DS5-M1	121.082	106.712 ± 3.145	12.631
DS5-M2	121.082	106.712 ± 3.145	5.811
DS5A-M1	81.589	71.374 ± 2.289	11.667
DS5A-M2	81.589	71.510 ± 2.289	5.811
DS5B-M1	39.493	37.169 ± 1.143	12.631
DS5B-M2	39.493	37.169 ± 1.143	5.811

DS	$^{\mathrm{enr}}$Ge Exp. (kg-d)	$^{\mathrm{nat}}$Ge Exp. (kg-d)	Deadtime(%)
DS0	460.052 ± 6.959	171.021 ± 3.941	6.323
DS1	661.811 ± 9.693	63.294 ± 1.468	5.374
DS2	106.286 ± 1.554	10.679 ± 0.248	1.864
DS3	368.523 ± 5.410	81.741 ± 1.881	2.353
DS4	102.858 ± 1.473	73.845 ± 1.701	1.804
DS5-M1	1396.710 ± 20.587	423.878 ± 9.751	8.675
DS5-M2	538.224 ± 7.594	539.938 ± 12.423	23.505
DS5A-M1	904.553 ± 13.363	285.417 ± 6.568	4.974
DS5A-M2	356.031 ± 5.009	342.168 ± 7.873	24.906
DS5B-M1	492.158 ± 7.224	138.461 ± 3.183	1.339
DS5B-M2	182.193 ± 2.585	197.769 ± 4.550	20.611
Totals	9.95 (kg-y)	3.74 (kg-y)	

2.6 Recent Majorana Results and Conclusion

The Majorana Collaboration published its first $0\nu\beta\beta$ result in Physical Review Letters in March 2018 [42], alongside the GERDA and CUORE experiments. To conclude our overview of the Demonstrator and its $0\nu\beta\beta$ physics program, here we briefly summarize the results.

With the inner UGEFCu shield installed and noise conditions optimal, Data Sets 1–4 and 5B represent the lowest-background configuration. DS0 had higher background without the inner shield, and the electronics noise conditions in DS5A resulted in degraded pulse shape discrimination performance [108] [109]. The low-background configuration has 5.24 kg-y of enriched exposure. Figure 2.11 shows the comparison of the high- and low-background configurations with all PSD, data cleaning, and veto cuts applied.

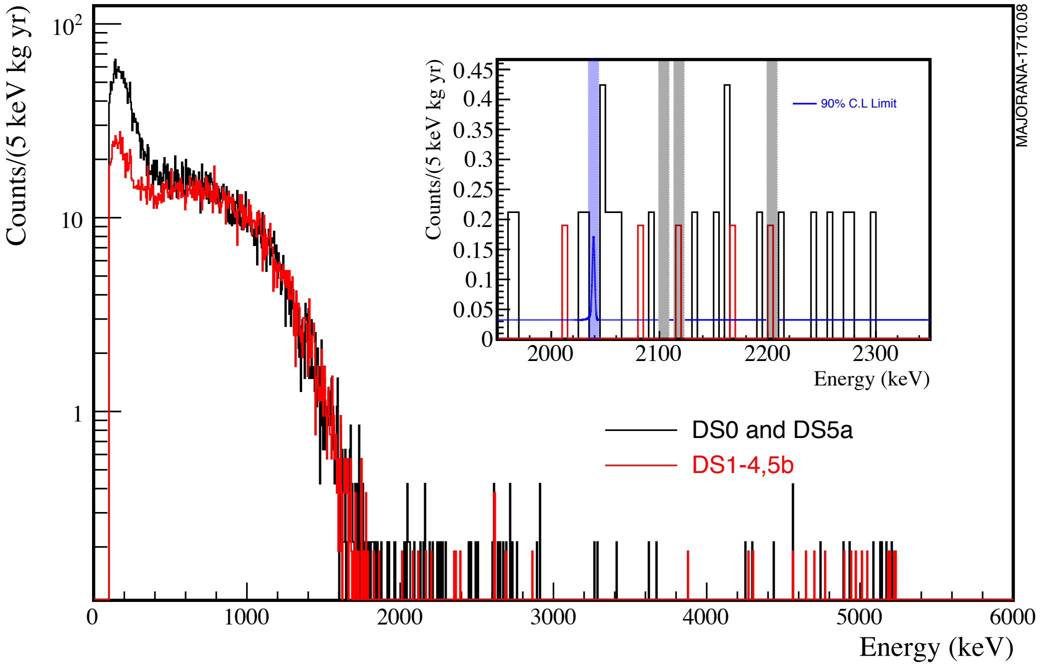

Figure 2.11: Energy spectrum comparing the difference in high (DS0–5B) and low-background (DS1–4,5B) configurations.

Since there are no events at the Q value passing cuts in any Data Set, the true background at the Q value is estimated from the counts in the surrounding spectrum 1950–2350 keV. Three ±5 keV regions in this window containing known gamma lines are also excluded; ^{208}Tl at 2103 keV, and two ^{214}Bi lines at 2118 and 2204 keV. In addition, a 10 keV window centered at the Q value was excluded. In the low-background configuration, only three counts pass cuts and contribute to the background rate B, showing excellent agreement with the predictions from the radioassay program [91].

$$B = 4.0^{+3.1}_{-2.5} \text{ counts/(FWHM t yr)} \tag{2.10}$$

The combined energy spectrum from all datasets is shown in Figure 2.12, highlighting the effectiveness of the data cleaning and muon veto cuts.

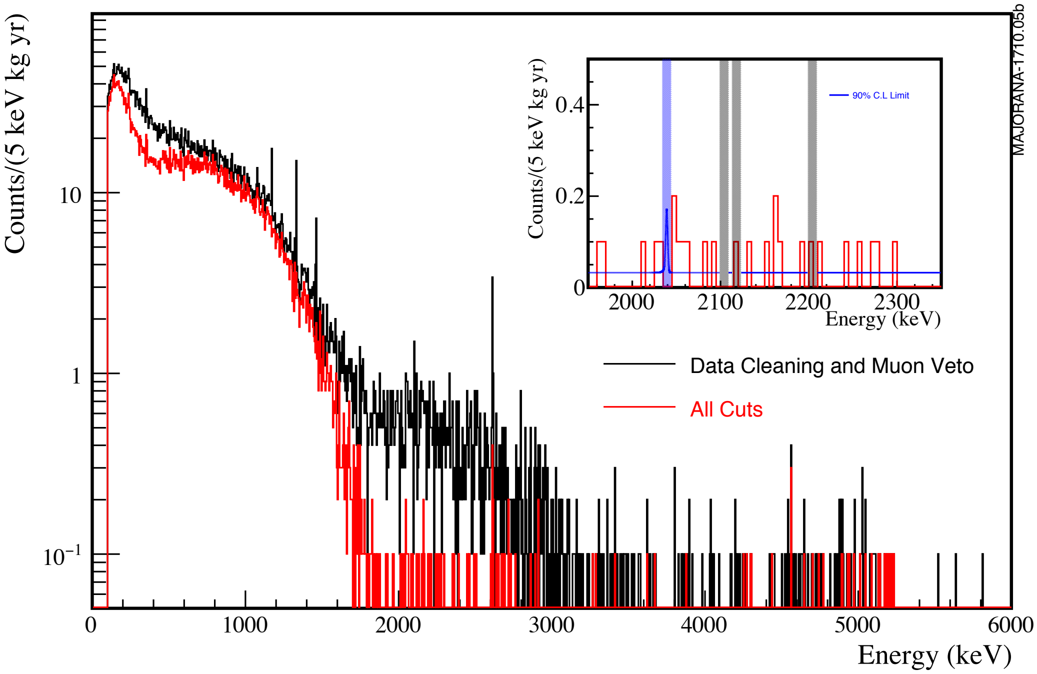

Figure 2.12: Combined energy spectrum from DS0-5, showing the effect of data cleaning and muon veto cuts.

With the full 9.95 kg-y of data, the DEMONSTRATOR observes no counts in the 4.32 keV window around 2039 keV, and uses the entire dataset to calculate its limit on the $T^{0\nu}_{1/2}$. This puts the DEMONSTRATOR in a "background-free" regime. The resulting limit on the half-life is computed via a likelihood analysis [110]: and the resulting limit on the half-life is [110]

$$T^{0\nu}_{1/2} \geq= 1.9 \times 10^{25}\text{yr (90\%CL)} \tag{2.11}$$

Using the following values for the nuclear matrix element and the quenching factor $g_A = 1.27$:

$$|\mathcal{M}_{0\nu}|^2 = (2.81 \text{ to } 6.13) \tag{2.12}$$

The Demonstrator sets an effective Majorana mass limit on the neutrino:

$$\langle m_{\beta\beta} \rangle < (240 \text{ to } 520) \text{ meV} \tag{2.13}$$

Comparison to the current best limits was given in Chapter 1. The Demonstrator has set competitive limits on $0\nu\beta\beta$ with a relatively small exposure compared to other experiments; this illustrates the extreme importance of backgrounds and energy resolution. Most recently, results were presented at the Neutrino2018 conference [39] which utilize Data Set 6 through 15 April 2018, including blind data, for a combined $^{\text{enr}}$Ge exposure total of 26 kg-y. The improved result on the $0\nu\beta\beta$ half-life is

$$T^{0\nu}_{1/2} \geq= 2.7 \times 10^{25} \text{yr (90\%CL)} \tag{2.14}$$

Using the same values for the nuclear matrix element and the quenching factor, we find

$$\langle m_{\beta\beta} \rangle < (200 \text{ to } 433) \text{ meV} \tag{2.15}$$

The background rate is also updated:

$$B = 11.9 \pm 2.0 \text{ counts/(FWHM t yr)} \tag{2.16}$$

The background rate B is taken from the “low-background” configuration which omits Data Sets 0 and 5A. This is higher than the rate given in the 2018 PRL. A partial improvement may be obtained by further optimization of the pulse shape discrimination parameters for Data Set 6, which uses waveform multisampling. However, it is likely that the true background is higher than the initial 2018 result, since the additional exposure from the unblinded data has reduced the uncertainty on B. Majorana is continuing to work to improve its background model and improve analysis routines, which will both be the focus of a future publication.

The following chapters will move to the low-energy rare event searches possible with the Demonstrator, beginning with a description of signal formation in HPGe detectors.

CHAPTER 3

LOW-ENERGY SIGNALS IN HPGE DETECTORS

3.1 OVERVIEW

In both $0\nu\beta\beta$ and low energy searches, the process of interest can produce ionization from interactions with the electrons and nuclei of a detector material. Semiconductor-based radiation detectors are well-suited to detect these ionization signals. They have orders of magnitude more charge carriers than gas-based detectors, excellent energy resolution, and can be made sensitive to very small energy depositions. In Section 3.2, we first give an overview of radiation detection in semiconductors, before specializing to a discussion of the P-type Point Contact High-Purity Germanium (PPC HPGe) detectors used in the MAJORANA DEMONSTRATOR. Section 3.3 discusses the characteristics of the ionization signal that make it possible to both determine the energy deposited and to identify and reject unwanted events based on differencences in the pulse shape. Section 3.4 discusses low energy ionization events in particular, with special focus on the difficult problem of degraded-energy signals originating from the outer regions of the detector. Finally, we present new pulse shape analysis (PSA) techniques developed for the MAJORANA low energy program in Sections 3.5 and 3.6.

3.2 RADIATION DETECTION IN SEMICONDUCTORS

The electrical properties of a material are determined in part by the amount of energy it takes to move a given electron from a bound state in the *valence band* to a freely moving state in the *conduction band*. The difference in energy between the valence and conduction bands is known as the *band gap*. Metals have no band gap; their valence and conduction bands partially overlap, allowing free electrons to easily move through the material. Insulators have a large band gap ($\sim$ 10 eV) which generally prohibits conduction and keeps electrons confined to their atomic orbitals. In semiconductors, the energy required to move a valence electron into the conduction band is both nonzero and relatively small, and the conductivity depends significantly on the temperature, band gap, impurity concentration, and the presence of an electric field.

When a valence electron is energetically excited into the conduction band, either from thermal fluctuations, an applied electric field, or interaction with ionizing radiation, it leaves behind a temporarily vacant atomic orbital. This vacancy is quickly filled by another electron from deeper within the valence band, leaving another vacancy in a different orbital and position. Rather than describing the behavior of the vacancies in terms of the large number of deeply bound electrons, in semiconductors the vacancies are treated as a small number of *net positive* charges moving through the valence band, analogous to the motion of electrons through the conduction band. These pseudo-charges are called "holes." When an electric field is applied to the semiconductor, the holes tend to move across the material in the opposite direction as the free electrons, though not necessarily at the same speed. Unlike metals, where only the electron motion is considered, in a semiconductor the electrons and holes represent two distinct populations of charge carriers, and the motion of both determines the conductivity.

The Fermi-Dirac distribution gives the probabilitiy that a given energy state is occupied by an electron. From this distribution, the *Fermi level* is defined as the energy level with a 50% chance of being occupied. In a completely pure (*intrinsic*) semiconductor, at a given temprature the number of electrons in the conduction band would exacly equal the number of holes in the valence band, and the Fermi level will be in the middle of the band gap. In practice, it is difficult to make perfectly intrinsic semiconductors. Residual impurities in the atomic lattice strongly influence the conductivity and create a slight excess of electrons or holes. It is also common to deliberately introduce impurities into the crystal lattice of the semiconductor, a process known as *doping*.

In an *n-type* semiconductor, a *donor impurity* is introduced by doping a pure material with pentavalent atoms, whose outer shell contains a single electron. This extra electron is very loosely bound and is much more easily excited into the conduction band, becoming the majority charge carrier of the material. In a *p-type* semiconductor, an *acceptor impurity* is introduced by doping with a trivalent atom containing an unfilled atomic orbital. Valence electrons are more easily excited into these extra orbitals than into the conduction band, and the holes become the majority charge carrier. Figure 3.1 illustrates the difference between n- and p-type semiconductors, showing the effect each type of impurity can have on the Fermi level.

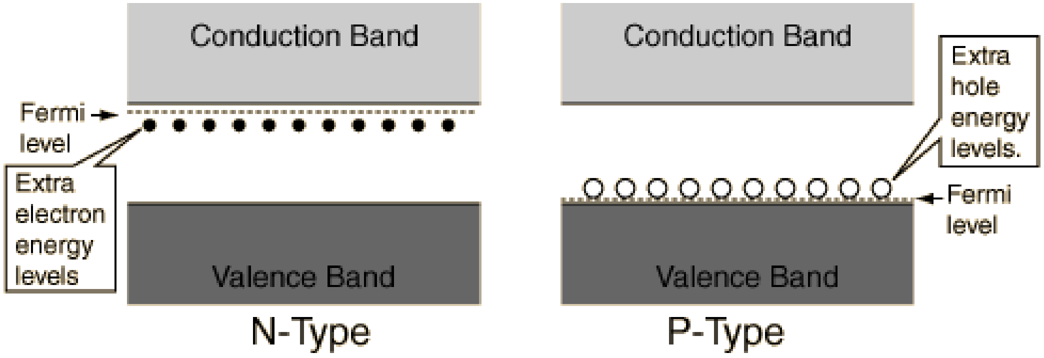

Figure 3.1: Two types of semiconductors: *n*-type (with donor impurities) and *p*-type (with acceptor impurities). An intrinsic semiconductor has no impurities and valence electrons must cross the full band gap to become conducting. Illustration from [111].

In the ideal case, when a p-type material is placed in direct contact with an n-type material, a *p-n junction* is created. The boundary between the two materials is known as the *depletion region* and is depicted in Figure 3.2. Here, electrons from the n-side diffuse across to the p-side and combine with a hole, creating a negative ion on the p-side and a positive ion on the n-side. Without any impurities there are no excess free charge carriers, and a static charge is built up which impedes further motion. The region is naturally very thin, but can either be eliminated or made larger by applying an electric field.

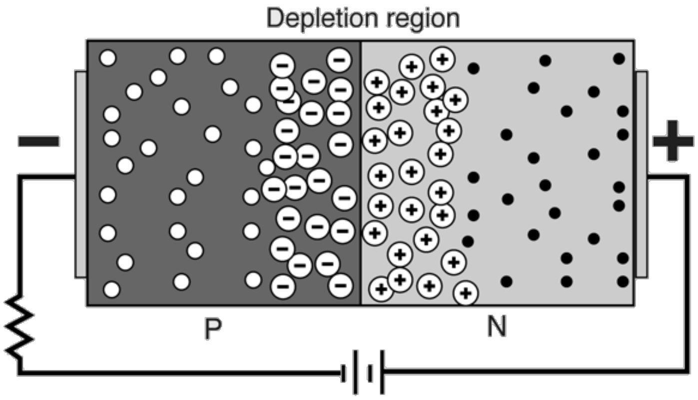

Figure 3.2: A reverse-biased p-n junction, illustrating the static charge built up in the depletion region. As the bias voltage is increased, the resulting electric field forces the static charges farther and farther apart, leaving a region in the middle with no charge carriers. Illustration from [111].

If a positive voltage is applied to the p-side of the junction, the resulting electric field in the material provides an extra force helping donor electrons to overcome the charge barrier, allowing current to flow. This is known as *forward-biasing* a p-n junction. Conversely, applying the positive bias to the n-side of the junction increases the energy necessary for an electron to move across the gap. This *reverse-biasing* further impedes the flow of current through the junction, separating the static charges built up at equilibrium and removing any remaining free charge if there are impurities present. The effect of the bias voltage V_b on the width d of the depletion region can be illustrated with a one-dimensional model [112], where is proportional to the square root of V_b:

$$d \simeq (2\epsilon\mu\rho V_b)^{1/2} \tag{3.1}$$

Here, ϵ_d is the dielectric constant ($\epsilon_d = 16\epsilon_0$ in Ge), ρ is the resistivity of the material, and μ is the mobility, a parameter describing how easily the majority charge carriers are able to move through the crystal lattice.

In practice, semiconductor junctions are not created by simply placing p- and n-type materials in mechanical contact with each other. The macroscopic gaps between the two materials would be too large for meaningful conduction to occur. Typically, material of one kind is chemically or mechanically deposited into the surface of another to form a strong connection. It is also common to make materials which are heavily doped, whose increased concentration is denoted by a plus sign, n^+ and p^+. These materials are sometimes known as “blocking contacts” and are often used to make a connection to a metal conductor.

In a real reverse-bias junction, the flow of current is not completely suppressed. Even at large biases, a leakage current tends to flow through the junction. Since germanium has a relatively small band gap (~ 0.7 eV at 77 K), it is typically cooled with liquid nitrogen in order to reduce thermal generation of charge carriers, which contribute to the leakage current and degrade the energy resolution. Modern manufacturing techniques allow for a large intrinsic volume with electrical impurity concentrations of less than 10^{10} atoms/cm^3.

The first germanium detector used for radiation detection was constructed by Tavendale in 1963 [113], which used Ge doped with Li throughout the crystal, creating a p-type material. The Ge(Li) detector design was the standard for many years until advances in the Ge purification process eliminated the need to dope the crystal. A high-purity germanium (HPGe) detector has a p-i-n structure, where a large “blank” of intrinsic (or nearly intrinsic p- or n-type) material is implanted with n^+ and p^+ contacts on its surface. The n^+ contact is created by lithium diffusion onto one surface, and the p^+ contact is made by implanting boron onto the other. At these contacts a bias voltage on the order of $1 - 5$ kV is applied to deplete the intrinsic region of any remaining free charge carriers. In order to withstand this relatively large voltage difference, HPGe detectors use a thin *passivated surface* made from amorphous germanium to separate the two contacts, which has a very high resistivity even at the low temperatures at which the detector is operated. Figure 3.3 shows a cross-section of the Majorana $^{\text{enr}}$Ge detector design, depicting the blocking contacts and passivated surface, as well as the UGEFCu "HV ring" which supplies the bias voltage to the n$^+$ contact. Other features illustrated in the figure including the contact geometry, weighting potential, and transition region, will be discussed shortly.

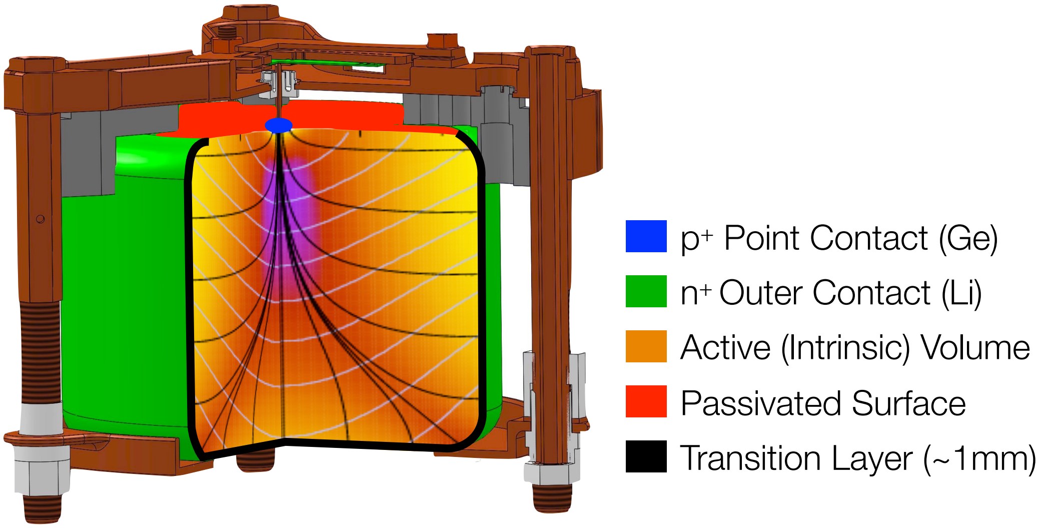

Figure 3.3: Cross section of a Majorana PPC detector unit, showing its UGEFCu and plastic mounting hardware, and the internal weighting potential.

A reverse-biased p-i-n junction is a highly efficient radiation detector. Any particle or process capable of producing ionization within the depletion region will produce electron-hole pairs which are then swept by the internal electric field to the n- and p-sides of the junction. These detectors are most commonly used for gamma ray spectroscopy, but many other particles can produce detectable signals, some from within the detector itself. As described in Chapter 1, the two β particles emitted in $0\nu\beta\beta$ and $2\nu\beta\beta$ are easily detectable. The ^{238}U and ^{232}Th decay chains produce a wide variety of decay products which can originate outside the detector or from within as part of the impurities in the crystal lattice. Isotopes which are cosmogenically activated (such as ^{3}H) within the detector produce detectable decay products. Appreciable ionization signals can also come from the interaction of neutral particles. For example, the elastic scattering of a neutron with a detector nucleus can produce ionization as the impact dislocates it from the lattice and the "recoil" ionizes the material. Both WIMPs (weakly interacting massive particles) and neutrinos are theoretically detectable via the nuclear recoil signal. These signals have a *quenched* (degraded) energy that is most commonly described in terms of Lindhard's 1963 model [114], though there is significant experimental interest in verifying its predictions with dedicated measurements [115] [116]. Since solar or dark matter axions mainly interact with the valence electrons (via the axioelectric effect) and not the nucleus, our main focus will be on signals from electron ionization rather than nuclear recoils.

The electrical signal produced by the ionizing radiation at the n$^+$ and p$^+$ contacts can be understood (and modeled) in terms of the Shockley-Ramo theorem [117]. One notable feature of these signals is that some amount of charge is induced on the electrode *before* the charge carriers have arrived. The instantaneous current induced by the motion of a charge is

$$i = q\boldsymbol{v} \cdot \boldsymbol{E}_0 = -q\boldsymbol{v} \cdot \nabla\phi_0 \tag{3.2}$$

Here, $\boldsymbol{E}_0$ and ϕ_0 are known as the *weighting field* and *weighting potential.* They are not equivalent to the actual electric field and potential within the semiconductor, but are useful proxies to determine the total induced charge Q on the electrode, which depends only on the end points of the moving charge q's path:

$$Q = q\ \Delta\phi_0\Big|_{\text{endpoints}} \tag{3.3}$$

The weighting potential in the detector volume $\phi_0(\boldsymbol{x})$ can be solved either analytically or numerically. It uses two main simplifications. First, the voltage on the electrode of interest is set to unity, while the other electrode(s) are set to zero. Second, the potential is given by the solution of the Laplace equation, $\nabla^2\phi = 0$, which does not consider the effect of free charge in the volume (ignoring trapped charges or impurities). This reduces the problem to one of electrostatics. In addition to considering only the end points and total charge Q, the time-dependent output signal $Q(t)$ can be determined by recalculating the weighting potential at every step along the moving charge's path. The Shockley-Ramo theorem can be applied to multiple charge carrier populations to produce an overall signal.

The geometry of an HPGe detector has a significant effect on its charge collection properties. In the standard planar configuration, a cylinder of intrinsic material is given an n^+ contact on one end and the p^+ on the other. A coaxial configuration places the contacts in the inner and outer radius. The central bore can go all the way through the detector in a fully coaxial configuration, or can terminate in the middle for a semi-coaxial. In any configuration, the HPGe diode is still fundamentally a p-n junction, and the spatial charge built up when no bias voltage is applied does not dissipate. As the reverse bias voltage is increased, it is driven closer to the contacts and begins to resemble a charged capacitor. The value of the capacitance per unit area is given in terms of the number of static charges N, the volume V, and the dielectric constant ϵ:

$$C = \frac{\epsilon}{d} \simeq \left(\frac{e\epsilon N}{2V}\right)^{1/2} \tag{3.4}$$

If the detector capacitance is large, static charge builds up at the contact and can create significant electronics noise in the charge-sensitive preamplifier readout. A major innovation from Luke et al [84] in 1988 was to reduce the capacitance of the detector by making the n^+ contact of an n-type HPGe detector very small. The potential of this design was not realized until work by Barbeau, Collar, and Tench in 2007 [118] were able to use low-noise FET amplifiers to exploit the low capacitance. The PPC detectors in the MAJORANA DEMONSTRATOR were fabricated with Ge which underwent process of enrichment and zone refining described in Chapter 2 and Ref. [87]. As shown in the Majorana configuration in Figure 3.3, in the PPC geometry the p^+ contact is made only in a very small region on one surface of the detector. The resulting weighting potential inside the intrinsic (or *bulk*) volume is then highly localized around the point contact. A completed $^{\mathrm{enr}}$Ge detector unit for Majorana is shown in Figure 3.4.

The advantage of the localized weighting potential of the PPC design can be seen by considering the motion of the charge carriers after an ionization event. The production of electron-hole pairs by an ionizing particle is not limited to the initial interaction. Secondary high-energy ionized electrons can generate more electron-hole pairs nearby, and some particles with a large mean free path in the material (gamma rays in particular) are capable of interacting multiple times within the depletion region. In the presence of a large bias voltage, the resulting "charge clouds" from each interaction will be driven by the electric field to the contacts in a relatively short time. In the PPC geometry, the holes are drawn to the point contact, traversing a region where $\Delta\phi_0 \sim 1$, while the electrons stay in a region of low weighting potential over their full path, $\Delta\phi_0 \sim 0$. Because of this asymmetry, signals in PPC detectors tend to be "hole-dominated," with the hole motion primarily responsible for the amplitude of a given signal. The holes must traverse a relatively large distance in the crystal before reaching areas of large weighting potential, and the charge cloud is stretched out in the process, arriving at slightly different times. It is because the signal does not occur "all at once" that useful information can be extracted from the pulse shape.

Semiconductor radiation detectors such as germanium and silicon have good energy resolution because they are able to collect all the charge deposited before it diffuses or recombines inside the crystal lattice. The average number of electron-hole pairs produced is known as the *ionization energy* of the material. For germanium cooled to liquid nitrogen (LN) temperatures of 77 K, the ionization energy is 2.96 eV [112]. Germanium and silicon both have very low ionization energies, allowing

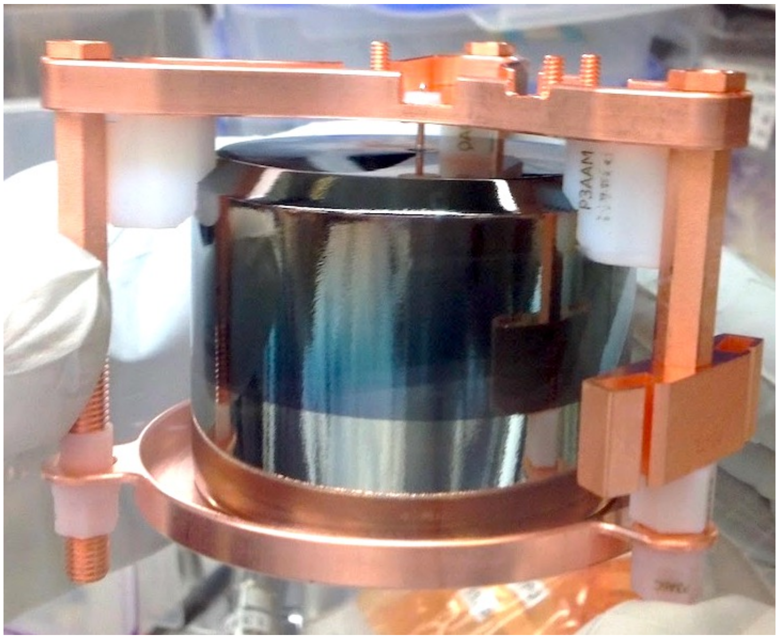

Figure 3.4: A completed MAJORANA $^{\mathrm{enr}}$Ge PPC detector unit, with point contact and passivated surface visible.

large numbers of electron-hole pairs to be produced even for a relatively low-energy (keV-scale) interaction, making it easier to detect and amplify the signal. This charge from a given interaction is generally proportional to the energy deposited in the detector, though the number of charge carriers produced is not strictly a Poisson process. Generally, fewer charge carriers are produced than expected, and a *Fano factor* is usually introduced to quantify the reduction for a given material. Once the charge Q has been induced on the p$^+$ contact, it is read out by a charge-sensitive preamplifier circuit.

An innovation of the original PPC HPGe design from Barbeau, Collar, and Tench was the implementation of low-noise readout electronics to amplify the detector signal. Their detector used a "pulse reset" preamplifier, positioning a JFET transistor and feedback resistor very close to the p$^+$ contact to reduce stray capacitance and series noise. Any charge from ionization is drained away at a set interval on the μs-scale. This limits the detector's ability to observe large-amplitude pulses. A variation on the pulse reset preamplifier was designed for MAJORANA, using a resistive feedback amplifier. When a charge builds up on the p^+ contact, it is actively bled away by the JFET through the feedback resistor, with a characteristic decay constant of $\tau = 72\ \mu$s. This enables higher-energy pulses to be read out at arbitrary times. The low-mass front end (LMFE) boards contain the circuit components on a fused silica substrate, mounted directly below the point contact pin and held in mechanical contact by a copper spring. Each LMFE contains a single low-noise JFET transistor and a feedback resistor made from amorphous Ge, both attached to the substrate with silver epoxy. The output signal is then sent through ∼2 meters of 0.4 mm diameter low-mass, ultra-pure Cu coaxial cables outside the cryostat for subsequent amplification [119].

Signals from the Majorana PPC detectors are passed through two stages of amplification in dedicated electronics boxes [93]. The first stage amplification consists of a tunable preamplifier sensitive to rise times on the order of 10 ns. The second stage amplifies the signal further before being sent to the GRETINA digitizer boards. Controller cards inside the electronics boxes are connected to each detector, and send an electronic pulser signal directly into the LMFE circuit, allowing gain shifts and detector live time to be monitored. The electronics boxes are also connected to high voltage (HV) power supplies that supply the detector bias voltage, and low voltage (LV) supplies which provide power for the JFET resistive feedback circuit. Finally, the output from the second stage is passed to the 100 MHz GRETINA waveform digitizers and recorded by the ORCA data acquisition system. The next section will discuss the analysis of the resulting pulse shapes (waveforms) generated in the Majorana PPC detectors.

3.3 Signals in Majorana PPC Detectors

Demonstrator waveforms undergo several steps of offline processing in order to determine their energy (in keV) and pulse shape characteristics. In the $0\nu\beta\beta$ analysis this is done with the GAT toolkit. The Low-Energy Analysis Toolkit (LAT) has been developed as a specialized extension for low energy signals.

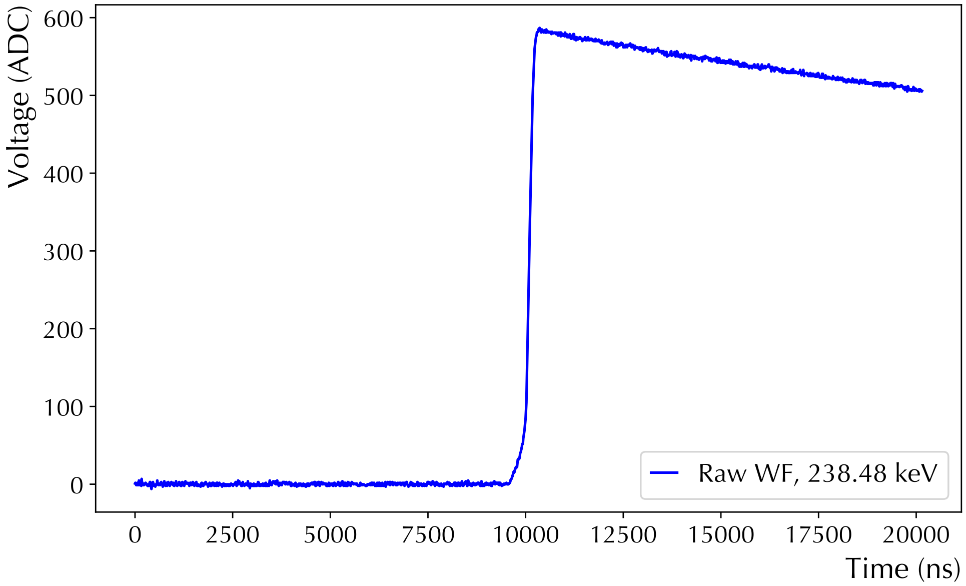

Figure 3.5: An example baseline-subtracted waveform.

A typical waveform is shown in Figure 3.5, with a constant DC offset (the *baseline*) removed. Noise fluctuations are visible, though for high-energy events the signal clearly dominates. The sharpest rise in the signal occurs when the holes cross the large weighting potential near the point contact. If the ionization is within the main bulk of the detector, the electron cloud does not move across a large $\Delta\phi_0$ and only minimally contributes to the waveform shape. However, depending on the interaction location within the detector, the signal can exhibit asymmetries in the rising edge. If the event is multi-site, the rising edge will be distorted as charge clouds from individual interactions arrive at the p^+ contact.[1] Finally, the charge collected from the event is drained away exponentially by the resistive feedback circuit (RC time constant $\tau = 72\ \mu s$).

---

[1] To a *much* lesser extent, the arrival of the electron component of each charge cloud at the n^+ contact will also affect the rising edge.

The energy of a given signal is determined in several steps, and relies on a *trapezoidal filter* algorithm [120], with several added corrections to improve the energy resolution. Figure 3.6 illustrates the process used by MAJORANA to determine the uncalibrated energy.

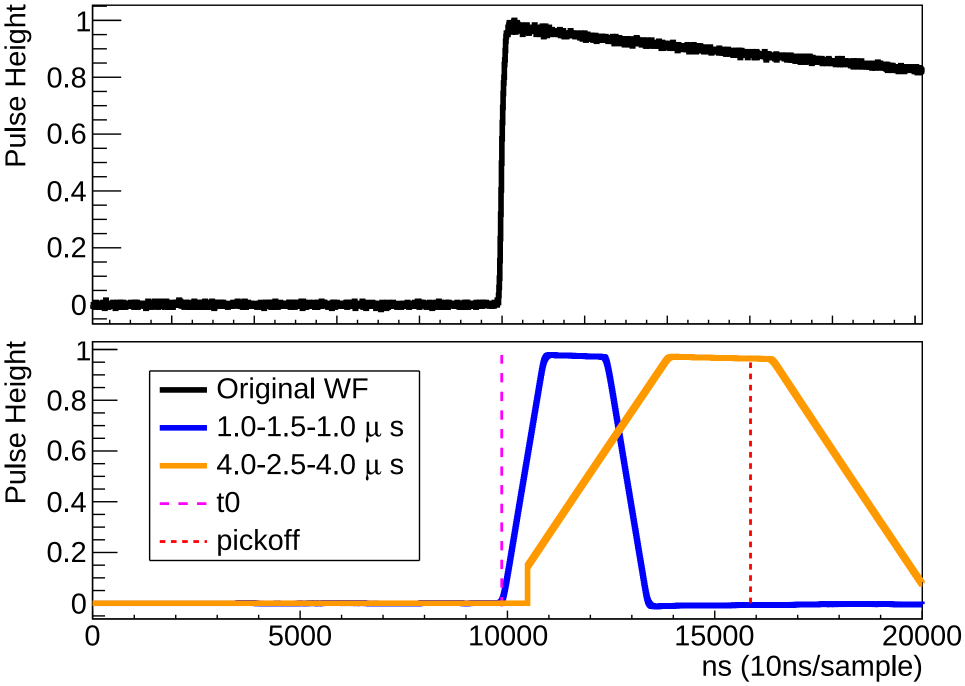

Figure 3.6: Illustration of the fixed-time pick-off technique used to evaluate waveform energies. Amplitudes have been normalized to better illustrate the algorithm. (Courtesy B. Zhu)

The trapezoidal filter keeps a running sum of the ADC values in two time windows separated by a fixed gap, swept across the waveform. The summation windows are the "rise" and "fall", and the time between them is the "flat top." A given trapezoidal filter is typically referred to by listing the three times, in the form (*rise, flat, fall*). As the filter is moved across the waveform, the difference of the two sums is taken. When the first window crosses the rising edge, the difference is positive and the trapezoid output slopes upward, and then becomes negative as the second window crosses the rising edge[2]. Longer trapezoids (4–2.5–4 μs) are less sensitive to small noise fluctuations in the signal and are generally used to determine the energy deposited in the detector. Shorter values (1–1.5–1 μs) are more sensitive to sudden changes and are used to determine the starting point t_0 of the rising edge when the difference between the windows crosses a set threshold. The rising edge typically occurs near 10 μs, though lower-energy signals may appear to occur earlier.

The simplest way to determine the energy from the trapezoidal filter is to record the maximum value of the long trapezoid. However, several factors will then degrade the resulting energy resolution:

- *Baseline noise.* Noise on the waveform will consistently bias the maximum value of the filter *higher* than if no noise were present, producing a small positive shift in the resulting energy.
- *ADC nonlinearity.* The true voltage produced by the physics event does not have a perfectly linear relationship with the digitized (ADC) values in the waveform, resulting in a measurable offset at every ADC value. This nonlinearity is corrected for with dedicated measurements of each GRETINA digitizer channel applied to each ADC value of every waveform recorded.
- *Pole-zero correction.* The resistive feedback circuit always bleeds away charge with its time constant τ, even during the rising edge. A software decay constant equal and opposite to the physical τ can be added to the filter to compensate, known as a *pole-zero* correction.
- *Charge trapping.* The pulse shape can also be stretched out when residual charged impurities in the bulk region effectively scatter the charge cloud as it traverses the detector, affecting the collection time and shape of the rising

---

[2] The implementation of the trapezoidal filter in GAT is calculated *recursively* as in [120], but the principle is the same.

edge. This is partially addressed by the pole-zero correction, and partially by changing the point on the long trapezoid taken to be the energy.

The algorithm used by MAJORANA to determine the energy takes each of these factors into account. Raw waveforms are corrected for their ADC nonlinearity, and the energy is determined by a *fixed-time pickoff* algorithm. A short trapezoid (blue curve in Figure 3.6) is used to find the start time t_0 of the rising edge, and the value of a long trapezoid (orange curve) is recorded at a fixed time after t_0, 0.5 μs. Taking the value at a fixed time eliminates the upward bias from Gaussian noise, and choosing a time significantly later than the maximum value accounts for the longer collection time if charge trapping is present. This uncalibrated energy is recorded in GAT as `trapENF`.

To convert `trapENF` to the real energy of the ionizing event, an energy calibration is done using a ^{228}Th line source, which is periodically inserted around the cryostat in a helical track. The energy spectrum from the calibration source provides a large number of well-defined peaks. A multi-peak fitting algorithm is applied to the spectrum, tracking the peak location and energy resolution as a function of energy. The energy corrections discussed above result in a world-leading energy resolution for the DEMONSTRATOR of 2.5 keV at 2039 keV, the $0\nu\beta\beta Q$ value. The energy resolution σ as a function of energy is then parameterized and fit to the spectral peak data:

$$\sigma = \sqrt{p_0^2 + p_1^2 E + p_2^2 E^2} \tag{3.5}$$

Here, p_0 accounts for electronics noise, p_1 is due to the Fano factor discussed above, and p_2 accounts for charge trapping. A complete overview of the calibration system and analysis procedure is given in Ref. [89]. Taken all together, the GAT variable `trapENFCal` takes all corrections and energy calibration into account, and is the main energy estimator used in the low energy (LAT) analysis.

There are three main sources of ionization from gamma radiation: photoelectric absorption, pair production, and Compton scattering. The mean free path of a typical gamma-ray is comparable to the size of the PPC detector, and it will frequently deposit energy at multiple sites in the detector via Compton scattering. This is unlike the $2\nu\beta\beta$ and $0\nu\beta\beta$ processes, where the betas emitted only travel a very short distance. In PPC detectors, there is a distinct difference between waveforms of single and multi-site events. The current pulse (derivative) from a waveform will be sharply peaked in a single-site event, and spread out in a multi-site event. This is illustrated in Figure 3.7. By comparing the maximum value of the current to the estimated energy of the pulse, a separation between single- and multi-site events can be achieved. This technique is known as A/E when the ratio of the current maximum A to the energy E is taken, and "A versus E" (or `avse` in GAT) when the cut value for the current maximum depends on the energy. The A/E method was first used in HPGe by the GERDA experiment [121], and the `avse` method is used by MAJORANA [108].

The second major source of background for the $0\nu\beta\beta$ analysis is due to alpha radiation. As discussed in Chapter 1, the progeny of ^{222}Rn can plate out on surface near the HPGe and emit alpha particles. The mean free path of an alpha is typically not large enough to penetrate the n$^+$ contact, but if it strikes the detector at the thinner passivated surface or at the p$^+$ contact itself, it can deposit up to ~ 5 MeV. These events can be highly energy degraded, and create a significant background at the Q value. This alpha particle background was observed during the commissioning dataset (DS0), and a characteristic pulse shape was identified. Evidently, the alpha signal creates *delayed charge recovery* (DCR) long after its initial rising edge is seen. The leading hypothesis for this slow charge collection is that ionization created by an alpha particle at the passivated surface experiences a significant amount of charge trapping, with some charge carriers trapped on the surface itself. They very slowly move to the n$^+$ contact along the passivated surface, resulting in a much longer

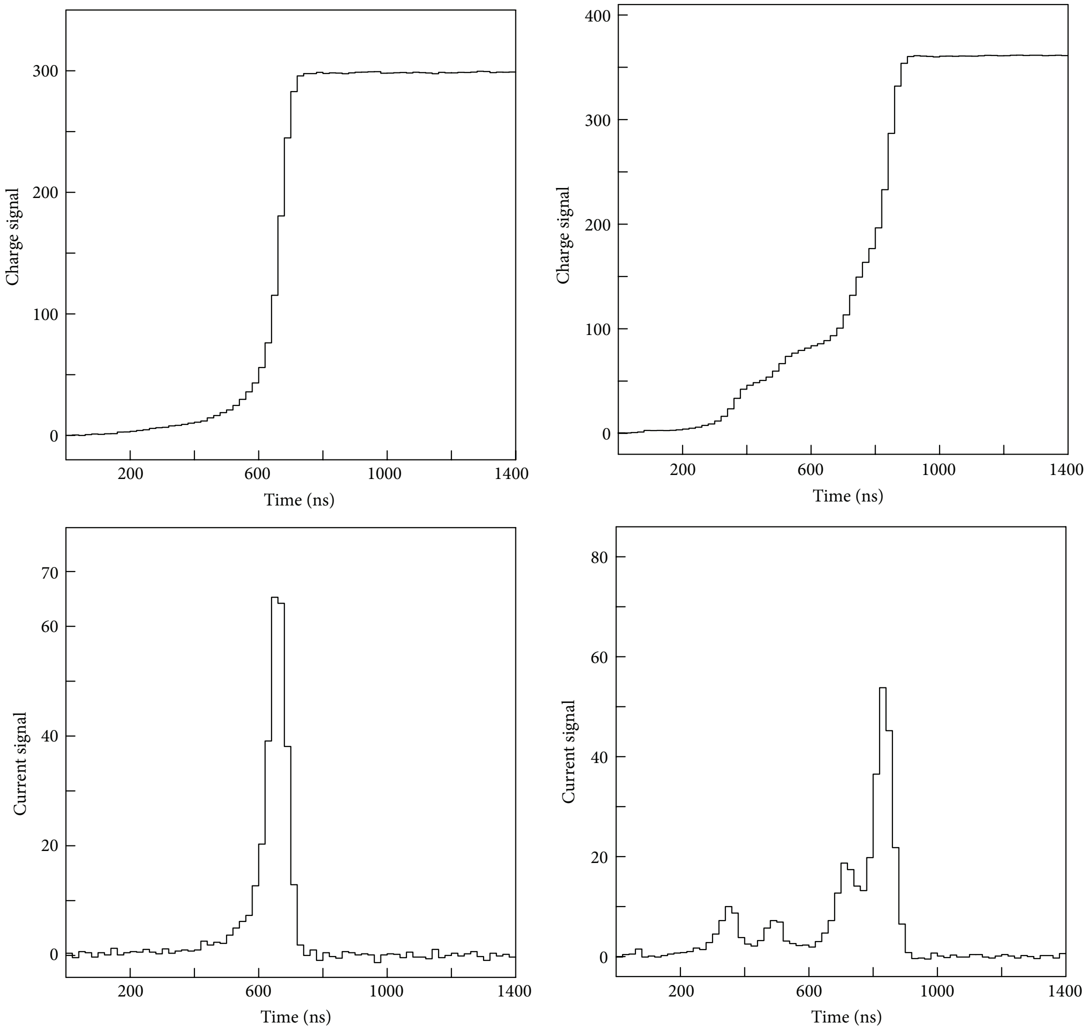

Figure 3.7: Top: waveforms of single (left) and multi-site (right) events. Bottom: Current from each signal. The single-site is sharply peaked, while the multi-site is significantly broadened. Figure from [86].

collection time [122]. The characteristic pulse shape of the alpha events is shown in Figure 3.8.

The `dcr99` parameter in GAT is a measure of the waveform slope in two regions; one measuring the slope of the last 1 μs, and one measuring the slope from 2–3 μs after the 97% maximum of the rising edge is reached. By comparing the two slopes, alpha events are rejected in the $0\nu\beta\beta$ analysis [123]. The DCR signal has also been simulated with the `siggen` software package developed by the MAJORANA collabora-

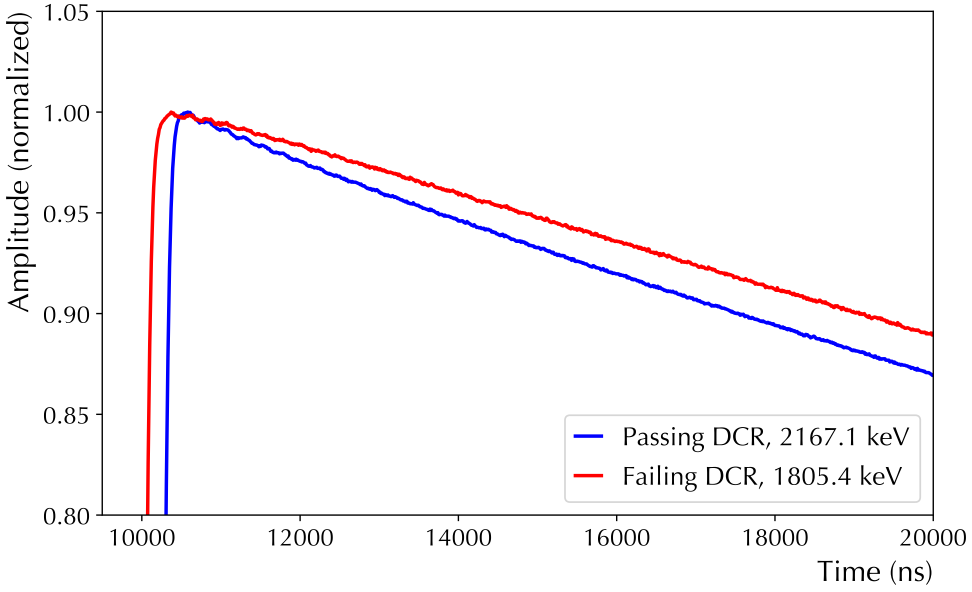

Figure 3.8: A "fast" gamma waveform (blue) and a "slow" alpha waveform (red) cut by DCR, whose slow surface collection appears to change the slope of the tail.

tion [124], and initial results are consistent with the data. Dedicated measurements are underway to more fully understand this effect [94][123].

The `avse` and `dcr99` cut parameters are excellent examples of the pulse shape discrimination capability of a PPC detector, but they do not play a significant role in the low energy analysis. In the next section we specialize to low-energy waveforms and discuss three main experimental challenges: *changing detector thresholds*, *slow pulses*, and *high-frequency noise.*

3.4 Low Energy Signals

For the lowest-energy ionization events, distinguishing signals from noise poses a significant challenge. In the ideal case, the noise on the detector baseline will be Gaussian-distributed and small enough that sub-keV energy depositions are distinguishable. This Gaussian baseline noise is the absolute limiting factor. If a signal does not rise above this noise by a detectable amount, it is not distinguishable from the baseline fluctuation. In practice, the Demonstrator noise is *not* simply Gaussian, and includes many spurious noise populations, including (but not limited to) periods of high-frequency (HF) and low-frequency (LF) noise, untagged pulsers, pulser retrigger events, and unstable detector baselines. Fortunately, these transient electronics noise populations typically have distinguishing features in their waveforms that allow them to be removed. To first illustrate the feasibility of a 1 keV analysis with the Demonstrator Data Sets, Figure 3.9 shows a 1 keV waveform from calibration data with a visible rising edge above the Gaussian noise.

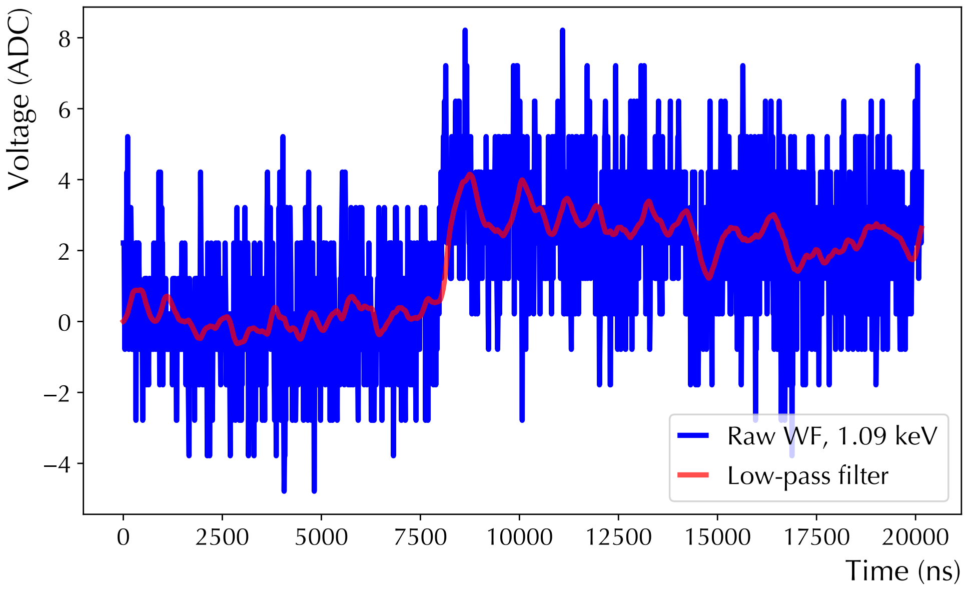

Figure 3.9: A 1 keV wavefrom from calibration data (blue), and a Butterworth low-pass filter (red). A clear rising edge is still visible above the baseline noise.

We note that LAT applies the ADC nonlinearity correction to all waveforms before analysis, using the same algorithm and input data as in GAT. The application of the cuts to the full Majorana Data Sets 0–5 and the determination of the detector thresholds on a run-to-run basis will be discussed in Chapter 4. The next two sections (3.5 and 3.6) will discuss the digital signal processing methods used by the LAT toolkit.

3.5 Slow Pulse Identification

The most troublesome background for many HPGe low energy rare event searches has been the identification of degraded-energy events originating from near the surface of the detector. In a PPC, the lithium diffusion process to form the n^+ contact (shown in Figure 3.3) creates a *dead layer* where the large number of Li atoms effectively cancel out the electric field present in the bulk. There is no well-defined separation between the dead layer and the bulk material, since the concentration of Li atoms decreases as a function of distance into the crystal. This transition is illustrated in Figure 3.10.

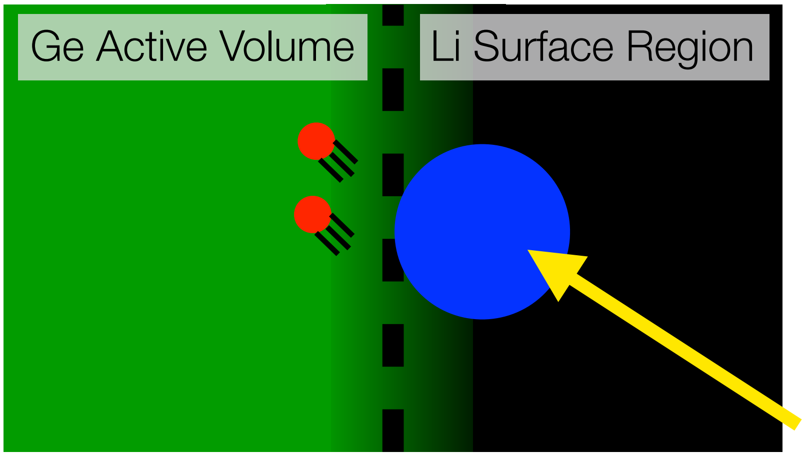

Figure 3.10: Illustration of the transition region near the n^+ contact. Charge deposited diffuses outward (blue circle), and only a fraction moves into the active region (red circles).

The charges created by an ionizing event in the dead layer feel no force from the electric field, and move by diffusion through the region until recombination, producing no signal. The dead layer is typically ∼1 mm thick, and has the advantage of blocking alpha particles from entering the bulk. When an ionizing event occurs in the transition layer, some (but not all) of the charges created will diffuse into the active region; the holes are then swept by the electric field to the point contact. The result is an energy-degraded *surface event*, also known as a *slow pulse*, where the amplitude of the pulse is no longer proportional to the energy deposited, by an unknown amount.

The shape of the slow pulse distribution is difficult to predict for a given experiment. Though it tends to rise exponentially at low energies, its exact shape is dependent on both the transition layer properties (which are different for every detector), and the external and internal backgrounds in the detector environment. The depth of the transition layer will vary for every detector, and the depth of the Li diffusion can increase over time if the detector is not maintained at cryogenic temperatures [113]. Without a detailed background model from simulations incorporating dedicated measurements of the transition layer, the slow pulse distribution is often treated as an irreducible contamination. If the analysis focuses on setting an upper bound (not reporting discovery), as will be the case in Chapter 5, slow pulse contamination of the spectrum can significantly affect the limits an experiment can set.

Experiments such as EDELWEISS [80] and CDMS [125] identify surface events by adding additional contacts at the surfaces of the detector, while PPC-based experiments do not have this capability. In a PPC detector at energies well above the baseline noise, most slow pulses are visibly different from fast events from the bulk, and can be identified by pulse shape analysis. Figure 3.11 illustrates this difference.

The distiction between fast and slow is especially problematic at the lowest energies, where baseline noise obscures the features of the rising edge. This difficulty has led to a variety of techniques by different experiments to measure the "slowness" of a pulse. The CoGeNT analysis employs a rise time cut [85], by calculating the times at which the waveform rises to 10% and 90% of its maximum value, and taking their difference, t_{10-90}. Slower waveforms will tend to have longer rise-times, and this approach is very well motivated, providing the signal remains sufficiently above the baseline noise. The MALBEK analysis [126] applied the t_{10-90} technique to a PPC

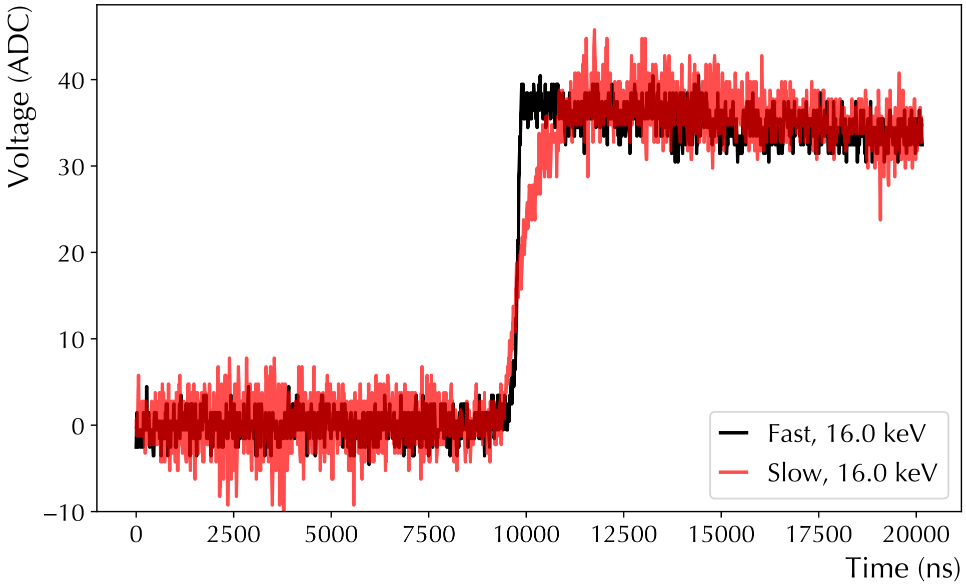

Figure 3.11: Two pulses with the same measured energy. The fast pulse (black) is from the bulk, while the slow pulse (red) is from the edge and has a degraded energy, not equal to the energy deposited by the incident particle.

detector very similar to CoGeNT. A second approach was also investigated using wavelet denoising techniques, smoothing the pulse before calculating the rise time, known as the w_{par} method. The MAJORANA commissioning data analysis [79] used an energy cutoff of 5 keV, retaining relatively high signal-to-noise. This enabled a somewhat simpler filter to be used, similar to the A/E parameter discussed in Section 3.3. The ratio of the maximum value of a “triangle” filter (a very short trapezoidal filter with no flat top, 100–10–100 ns) to the pulse energy was taken, known as the T/E method.

Both the TEXONO [127] and CDEX [128] experiments have taken the approach of fitting each waveform to an analytic function. Since there is no analytic form for a PPC signal, the choice of function is somewhat arbitrary, and heuristic functions need only be chosen by how well they match the data and how many free parameters they contain. Both TEXONO and CDEX use pulse-reset preamplifiers [129] to amplify their signals before being digitized, as opposed to the resistive feedback circuit used by MAJORANA. The waveforms from both experiments (Figure 4 in [127] and Figure 2 in [128]) appear to have no decaying tail [3]. They therefore choose a hyperbolic tangent function (which has no decay), with a τ parameter representing the slowness of the waveform.

In the analysis of Data Sets 0–5 described in Chapters 4 and 5, an approach based on waveform fitting has been implemented in the LAT toolkit. Fitting each waveform has the advantage of using every sample to optimize the fit, rather than losing information by applying a filter. It requires more computational power to fit every waveform, and care must be taken to optimize the speed of the fitting algorithm, and to avoid convergence to local minima. If an analytic function can be used, it can greatly increase the speed of the fit, rather than (say) regenerating a simulated waveform at every fit step. The heuristic function chosen to match DEMONSTRATOR waveforms is an exponentially-modified Gaussian (xGauss) [130]:

$$\mathrm{xG}(t) = \frac{A}{2\tau}\,\exp\!\left(\frac{t-\mu}{\tau} + \frac{\sigma^2}{2\tau^2}\right)\,\mathrm{erfc}\!\left(\frac{1}{\sqrt{2}}\left(\frac{\sigma}{\tau} - \frac{t-\mu}{\sigma}\right)\right) + B \tag{3.6}$$

The parameters of the xGauss function correspond well to the characteristics of a DEMONSTRATOR waveform. Setting τ to –72 μs gives the xGauss an exponentially decaying tail. The mean μ roughly corresponds to the 50% rise time. The amplitude A is proportional to the energy, and is the height of the maximum value of the function. The constant offset B accounts for the detector baseline. Most importantly, varying the parameter σ changes the slope of the rising edge, giving a heuristic xGauss waveform a *slowness* parameter. In the LAT analysis, σ is called `fitSlo`.

The set of fit parameters for each waveform are determined by minimizing a log-likelihood function. To illustrate the procedure, we begin by defining the likelihood $L(X;\theta)$ as the probability of a data set X being observed, given the choices of pa-

---

[3] It is unclear from the text if this is from an offline pole-zero correction, digitizing the pulse reset output directly, truncating the waveform, or an unreported hardware optimization; Figure 3 of Ref. [129] shows a decaying waveform, with a much longer timescale.

rameters θ. The likelihood is written in terms of a joint density function f, which is a generalization of a probabilility density function for a particular x_i, associated to the set X as a whole:

$$L(\theta) = f(X;\theta) \tag{3.7}$$

For the waveform fit, we define $\theta = \{A, B, \mu, \sigma\}$ (the decay τ is held constant), and the set of fixed waveform ADC values $X = \{x_1 \ldots x_n\}$. When the data are independent and identically distributed, f can be written

$$f(X;\theta) = \prod_{i=1}^{n} f(x_i;\theta) \tag{3.8}$$

If the expected value is different for each x_i (as in the case of the waveform model), f can still be formed:

$$f(X;\theta) = \prod_{i=1}^{n} f_i(x_i;\theta) \tag{3.9}$$

To compare the data X to the xGauss model G with the joint density function, we can assume that the data x_i deviates from the prediction of the model $\mu_{G,i}$ at each point by a Gaussian with deviation σ_G:

$$f_i(x_i;\mu_{G,i},\sigma_G) = \frac{1}{\sigma_G\sqrt{2\pi}} \exp\left(\frac{-(x_i - \mu_{G,i}(\theta))^2}{2\sigma_G^2}\right) \tag{3.10}$$

The deviation σ_G is taken to be the Gaussian noise of the waveform. If non-Gaussian noise is present, it will drive σ_G to larger values. The noise is measured for each waveform from the first 500 samples (5 μs), before the rising edge begins. The likelihood for the waveform fit can be written as

$$L(\theta) = \prod_{i=1}^{n} \frac{1}{\sigma_G\sqrt{2\pi}} \exp\left(\frac{-(x_i - \mu_{G,i}(\theta))^2}{2\sigma_G^2}\right) \tag{3.11}$$

Many standard optimization routines are written to *minimize* an arbitrary function rather than maximize it. The likelihood function can be easily converted to this form by taking the *negative log-likelihood* (NLL):

$$-\ln L(\theta) = \frac{1}{2}\sum_{i}\left(\frac{x_i - \mu_{G,i}(\theta)}{\sigma_G}\right)^2 - \ln\left(\frac{1}{\sigma_G\sqrt{2\pi}}\right) \tag{3.12}$$

The likelihood function L in our case is given by a product of exponential functions with a negative argument ($\sim e^{-x}$), up to a scaling term. It will be maximized when the absolute value of the argument is minimized. Taking the logarithm of L converts the product of exponentials into a sum of their arguments, and multiplying by -1 cancels an overall negative sign. A minimum-finding optimization routine can then be used to find the minimum value of $-\ln L(\theta)$ for a set of parameters θ. Since the expression is positive, the function will be minimized when the parameters θ are minimized. Therefore, the same set of parameters which make $-\ln L(\theta)$ a minimum will naturally maximize L. In addition, the logarithm is simpler computationally (multiplication becomes sums), and is numerically more stable, since very small values of the likelihood close to zero are converted to larger negative values, easier for a finite-precision machine to handle.

Initial values for each parameters are determined as follows. The amplitude A is given by `trapENFCal` and B is the baseline calculated from the first 500 samples of the waveform. The rising edge parameter μ is the maximum value of the energy trapezoid minus 4 μs; it can be seen from Figure 3.6 that this corresponds to the rising edge of the waveform. The initial value for σ is set to a constant value of 600, rather than tying the initial guess to another slowness parameter such as t_{10-90}, which tends to diverge at energies under 5 keV. In practice, if the minimization algorithm is able to quickly explore the parameter space for σ, the initial setting as a constant does not have a large effect on the outcome.

Minimization of the parameters is done in LAT with the L-BFGS-B algorithm from `scipy.optimize.minimize` [131]. It permits bounds on the parameters, which constrain τ at -72 μs, and the slowness σ (`fitSlo`) to be larger than 2 (avoiding convergence to a local minima at $\sigma = 0$). It also allows either an analytical or numerical gradient to be used in determining how much to vary the parameters at each step. The xGauss has an analytical gradient that can be used directly, but the numerical gradient was found to have better convergence, both in terms of speed and avoiding local minima. An example result of the waveform fit is shown in Figure 3.12, showing the initial guess, best fit function, along with the "traces" for this fit, showing the values chosen at each fit step and the convergence of the L-BFGS-B minimizer.

It is important to note a few of the advantages and drawbacks of using the xGauss function for waveform fitting. Although it is only a heuristic description, the xGauss has few parameters, all roughly corresponding to characteristics of PPC waveforms. It has proven extremely useful for rejection of non-Gaussian noise, where the `fitSlo` parameter converges to very large values. To illlustrate the effectiveness of the fit, Figure 3.13 shows three waveforms at 1 keV. One is "fast" with a relatively small `fitSlo` value, one "slow" with a larger value, and one from an electronics noise signal with an unphysically large value.

Speed is an essential feature of the waveform fitting algorithm, as the DEMONSTRATOR dataset contains data from many detectors in period spanning more than two years. The current version of the fitting algorithm runs in ~0.1 seconds per waveform, and the entire dataset can be processed in roughly a day on the NERSC Cori supercomputer. Chapter 4 will discuss the parallel processing of MAJORANA data in the LAT analysis in more detail.

Most DEMONSTRATOR waveforms have some degree of asymmetry about the upper and lower rising edges. In the current implementation, the xGauss model does not have an asymmetry parameter. This would not be acceptable in the high-energy $0\nu\beta\beta$ analysis, where the signal dominates over the noise. At low energy, the noise on the waveforms tends to obscure the asymmetric features of fast pulses. While slow pulses can be more asymmetric (usually with a more rounded upper edge), the `fitSlo` parameter is still correlated with the slowness of the waveform.

Multi-site events are not a significant background for the low energy analysis, espcially under 50 keV. Absorption of the gamma in a single photoelectric interaction

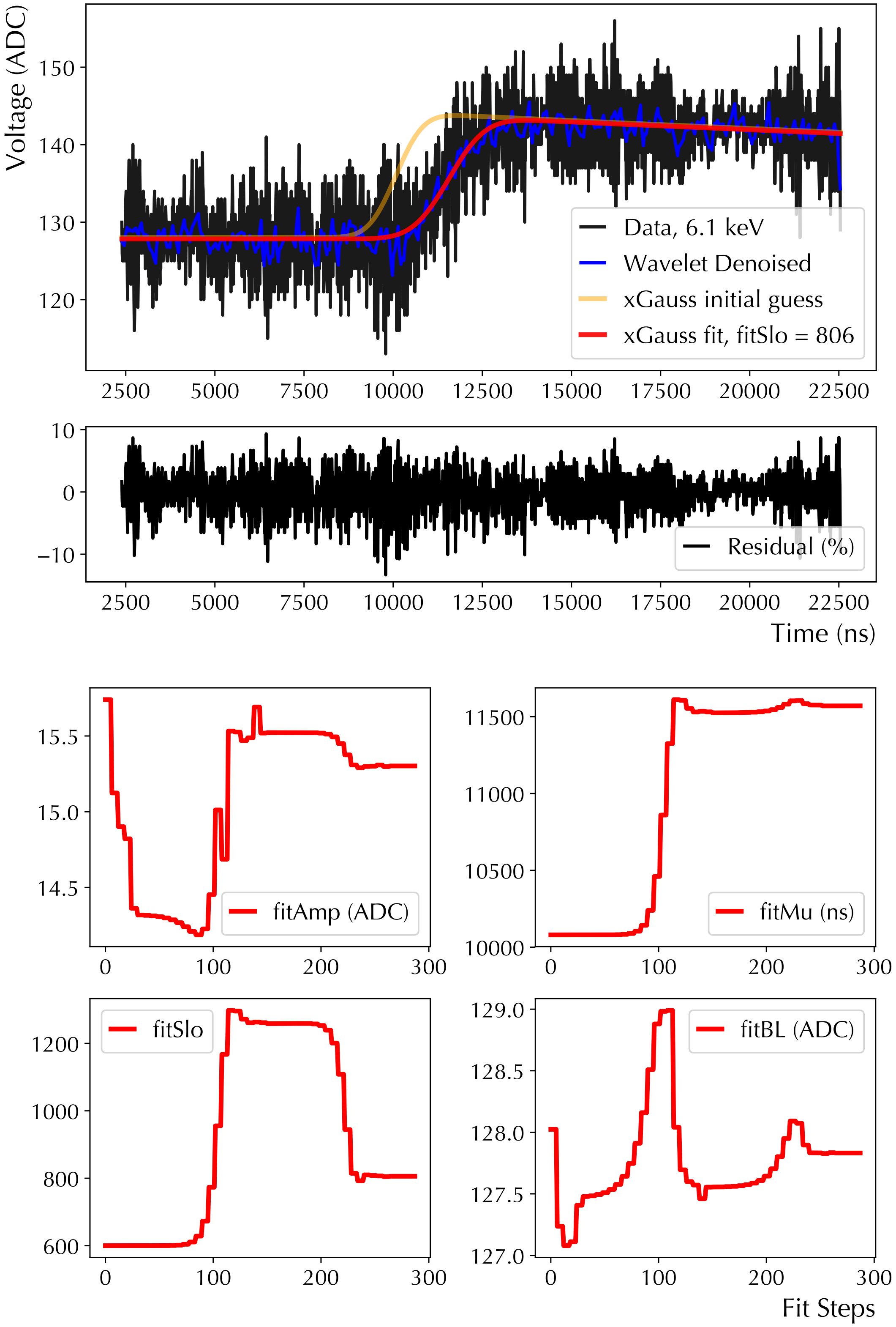

Figure 3.12: Illustration of an xGauss fit in LAT (0.071 sec), showing residuals and fit trace (parameter values used by the minimization algorithm). Fit is done to the denoised waveform (see Section 3.6).

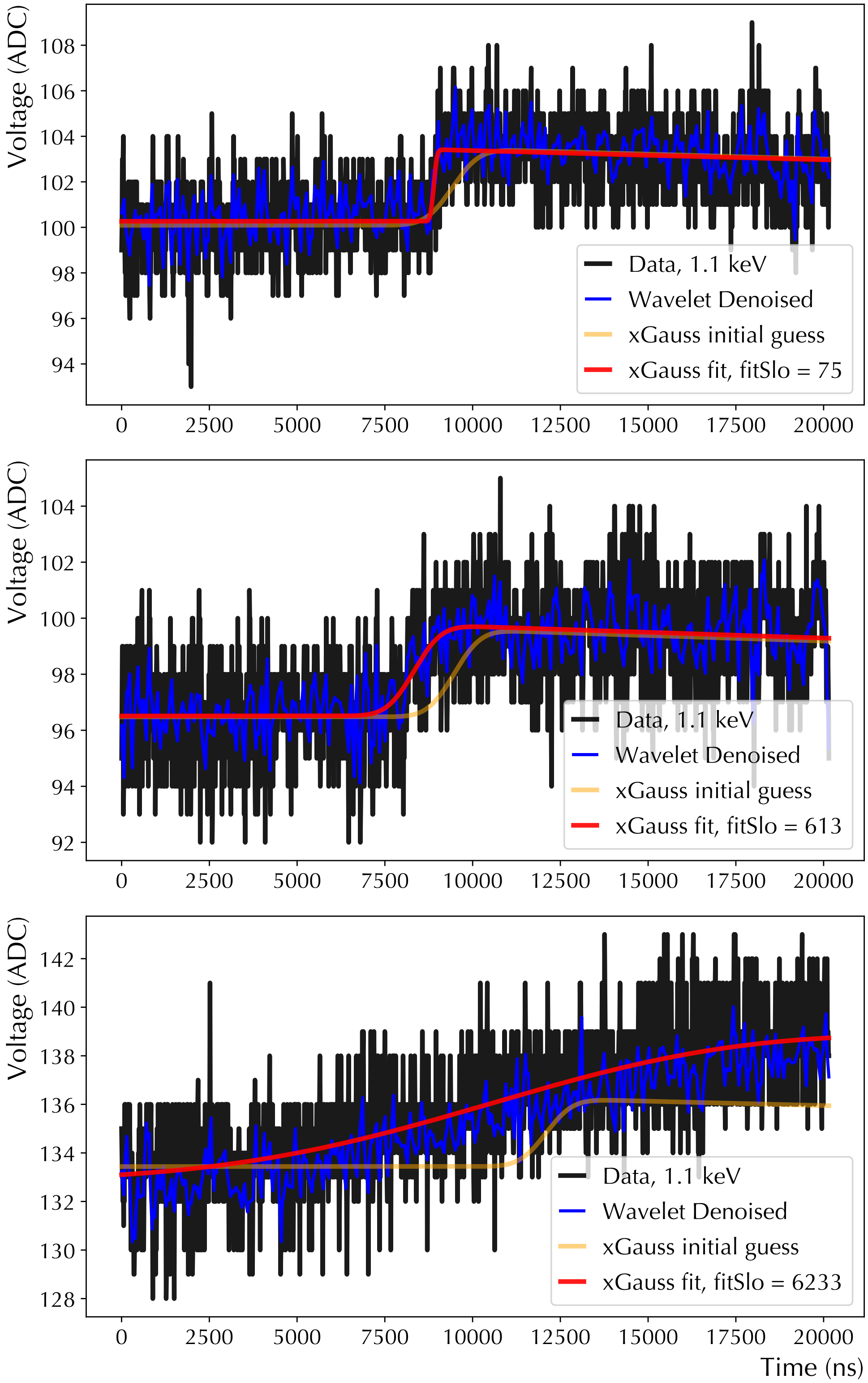

Figure 3.13: Three waveforms with the same evaluated energy, with distinct values of the `fitSlo` parameter. Even at 1.1 keV, there is a visible difference between a “fast” (bulk) signal (top) and a slow signal (middle).

predominates for energies below ∼140 keV (Figure 12.17 of Ref. [112]). While multi-site events do not contribute in the low-energy region (especially under 50 keV), they can affect the tuning of pulse shape cuts based on calibration data at higher energies. The second most likely interaction is a single-site Compton scatter, which is used to determine the efficiency of the `fitSlo` cut. The method is based on small-angle Compton scatters in calibration data and will be discussed in Chapter 4.

3.6 High-Frequency Noise Identification

The Demonstrator detectors periodically experience bursts of high-frequency (HF) noise. They can trigger the readout on an otherwise quiet detector, or superimpose themselves on an otherwise good physics waveform. The main cause of this noise has been theorized to come from ground loops in the system, though its detailed origin remains unknown at present. It was most prevalent in DS5A, when Module 1 and 2 were first operated in tandem with the same DAQ system. Efforts to clear these ground loops in early 2017 were largely successful, and DS5B is indeed significantly quieter than 5A. Spurious HF bursts still occur in the system to the present day, though at a much reduced rate. HF bursts are seen in the earlier Data Sets as well. This motivates a dedicated high-frequency cut.

The HF bursts typically occur in the 10–50 MHz frequency range. The rise time of a typical physics event is on the order of 200–500 ns, corresponding to a frequency of 2–5 MHz if it were oscillatory. Because the physics events are not oscillatory, they are not well-localized in the Fourier power spectrum. Integrating over the high-frequency regions of the power spectrum can be effective in rejecting waveforms with large HF bursts, but at low energy the effectiveness is reduced as the Gaussian noise becomes more prominent. An HF electronics burst on a waveform does not necessarily mark an event as “bad,” unless it interferes with the energy estimation or the calculation of other pulse shape parameters. For example, a burst well after the rising edge does not affect the energy determination, `fitSlo`, or the estimation of the baseline noise. On the other hand, if the burst occurs on or near the rising edge of the waveform, it obscures the shape of the rising edge and can significantly affect the energy and slowness. To localize these HF features in our waveforms, the LAT analysis implements a Wavelet Packet Decomposition (WPD) technique to analyze each waveform in both the time and frequency domains. The Discrete Wavelet Transform (DWT) was used in the MALBEK analysis to calculate the w_{par} parameter [132]. The methods are very similar and rely on a similar transformation procedure. Both the MALBEK and LAT analysis employ the `PyWavelets` package to perform the decomposition [133]. An example of the output is shown in Figure 3.14.

A wavelet transformation can be applied to a set of time series data, such as a set of waveform ADC values $X = \{x_1 \ldots x_n\}$, in a set of three steps. In the *split step*, the input data is divided into odd and even indexes, X_{odd} and X_{even}. In a finite data set, the odd elements are moved to the second half of the array, leaving the even elements in the first. In the *predict step*, the odd elements are replaced with the difference between the odd elements and a prediction function, known as the *wavelet function*. The differences that replace the odd elements will reflect high frequency components of the signal, and can be viewed as a high-pass filter for the odd half of the dataset, X_{odd}. They are often known as the *detail* coefficients. The *update step* replaces the even elements with a local average, using the *scaling function*. This results in a smoother representation for the even half of the input data set, and acts as a low pass filter for the even half of the data, X_{even}. These values are often known as the *approximation* coefficients of the transform. The choice of wavelet and scaling functions is generally made based on the expected signal shape. If we expect the waveform to look like a step function, the Haar wavelet is a good choice, since it is also a step function. If we expect a slower rise, the Daubechies-2 wavelet can

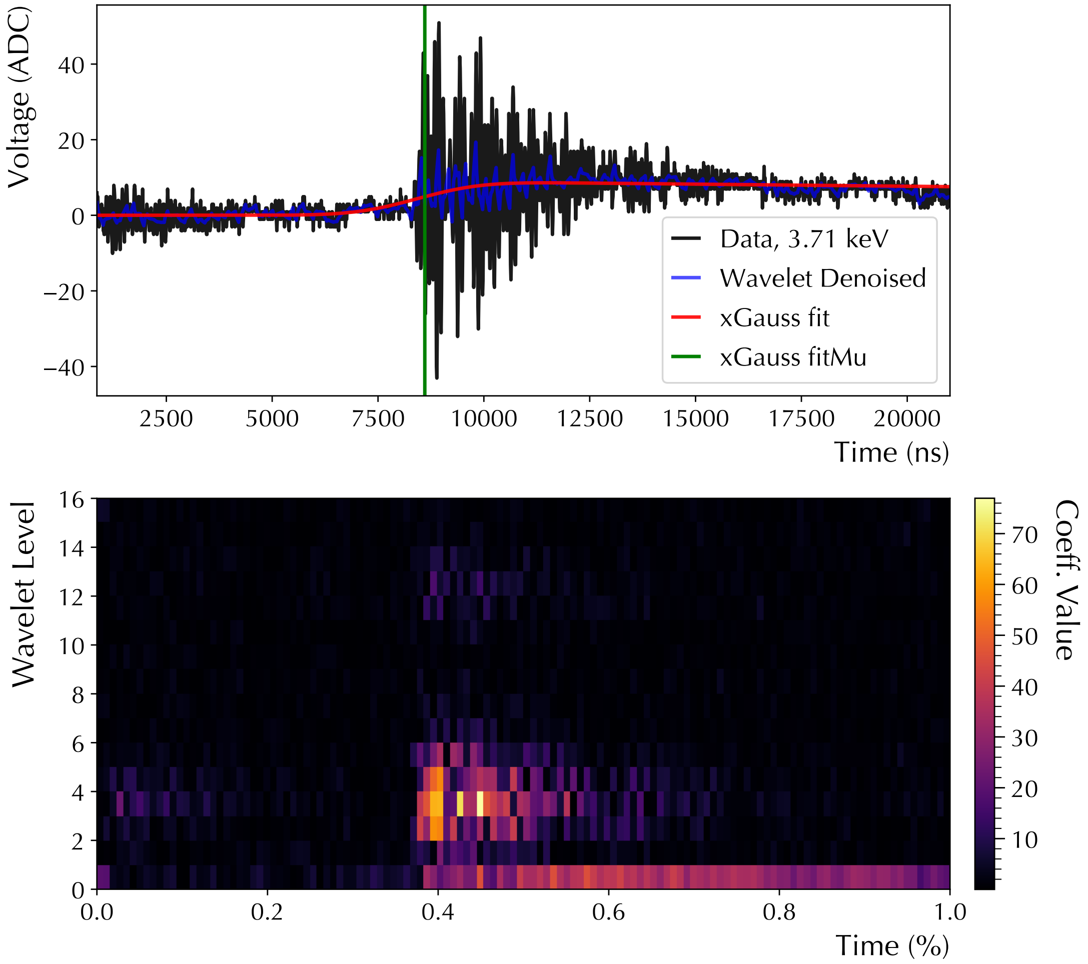

Figure 3.14: Wavelet packet coefficients for a waveform with significant HF noise. True physics signals are nearly always localized in the bottom frequency band.

be used. The LAT analysis uses Daubechies-2 by default; early tests showed the difference between the two was minimal for DEMONSTRATOR waveforms.

Both the Discrete Wavelet Transform and the Wavelet Packet Transform are recursive – the wavelet transformation is performed mutliple times on the output of the previous transform. Each “level” of the transformation splits the data in half, reducing timing resolution by a factor of 2 and gaining high-frequency information. In the DPT, each level of the transformation is applied only to the low-pass output, while the WPT applies the transformation to both the low- and high-pass output of each step, retaining more high frequency information.

The wavelet coefficients (from either the discrete or wavelet packet methods) can be used to *denoise* a waveform. The DWT removes high-frequency noise from a signal, while the wavelet packet method can be made to retain some combination of low and high-frequency behavior if desired. In the current LAT analysis, the use of the wavelet packet transform and the xGauss waveform fit are intertwined. For each waveform, the wavelet packet coefficients are evaluated, and the denoised waveform is used as an *input* to the waveform fit, using only the low-frequency coefficients of the wavelet packet decomposition (making it identical to a DWT). This is done to ensure that HF bursts do not bias the essentially low-frequency, non-oscillating waveform model.

To identify events with HF noise on the rising edge, the wavelet packet coefficients are summed in a region surrounding the edge found by the waveform fit. DEMONSTRATOR waveforms without multisampling have 2016 samples spaced at 10ns intervals. A level 4 decomposition splits the time axis into 128 bins of 160 ns, leaving some time resolution intact. With a level 4 decomposition, frequencies are split into 16 sub-bands, each roughly 3.125 MHz wide. The frequency behavior of the rising edge can effectively be singled out with the lowest two sub-bands ranging from approximately 0–6.25 MHz with most of the power contained within the lowest frequency sub-band. The low-frequency behavior of the waveform mainly appears in the bottom two levels of the wavelet packet coefficients; these are ignored in the sum. HF noise can be isolated by taking the sum of the wavelet coefficients in the higher frequency bands a region ± 1.28 μs on either side of the rising edge, or 8 bins of the level 4 decomposition. The sum of the coefficients is called `riseNoise` in the LAT analysis and is proportional to the amount of high frequency noise on the rising edge of the waveform. This technique is illustrated in Figure 3.15, and the determination of the cut efficiency is done from calibration data and discussed in Chapter 4.

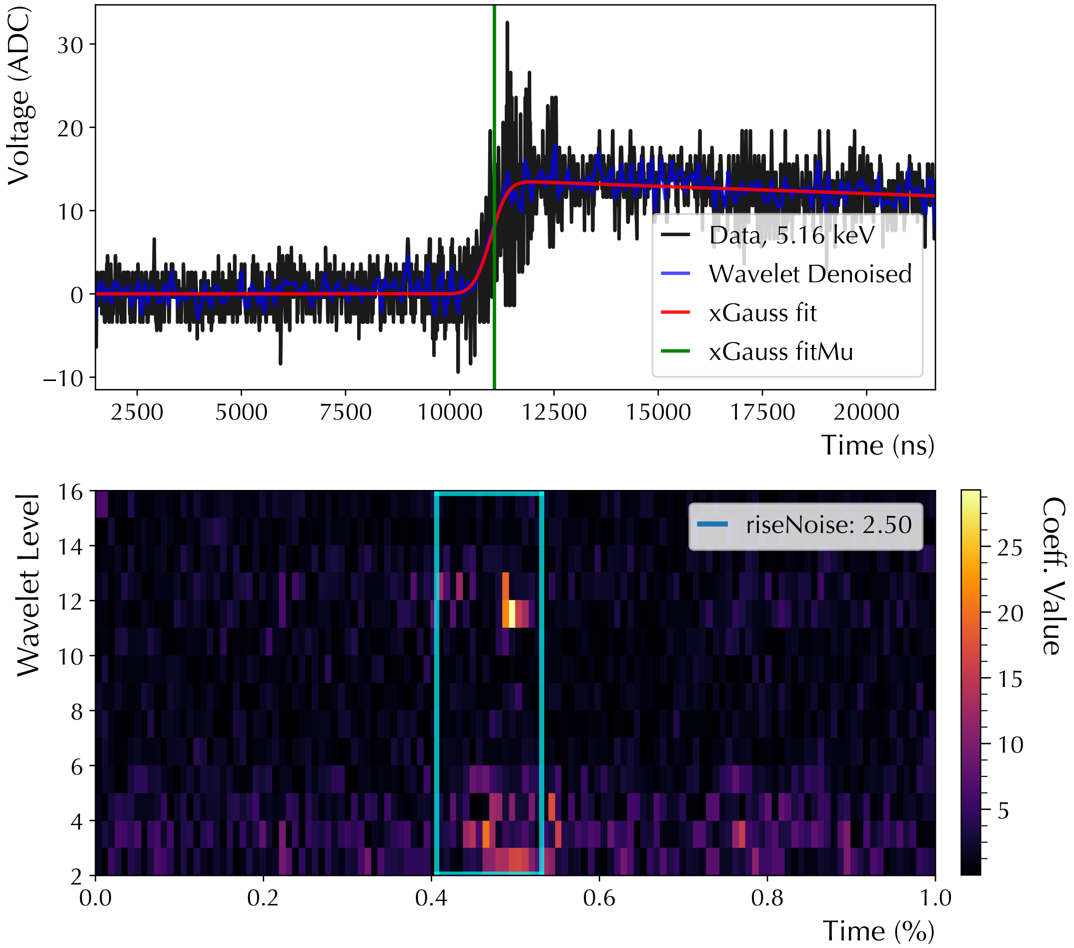

Figure 3.15: A waveform with HF noise on its rising edge (top), and the corresponding wavelet packet coefficients (omitting the two lowest-frequency levels). The `riseNoise` summation window is shown in blue.

3.7 SUMMARY

In this chapter we have discussed the characteristics of high and low-energy ionization events in PPC HPGe detectors, and the characteristics of the resulting waveforms in the DEMONSTRATOR. Two pulse shape analysis techniques for the low energy analysis were outlined. Every waveform passing basic data cleaning cuts is denoised by a wavelet packet transform and fit to an xGauss model to measure its characteristics. The *slowness cut* will use the variable `fitSlo` from the waveform fit to measure the relative slowness of a pulse, and rejects other populations of low-frequency electronics noise. The *high frequency cut* will use the variable `riseNoise` to identify and remove waveforms with burst noise on the rising edge. The application of these techniques to Data Sets 0–5 and evaluation of the cut efficiency will be discussed in the next Chapter.

CHAPTER 4

LOW ENERGY TOOLKIT (LAT) ANALYSIS

4.1 OVERVIEW

A consistent analysis of the combined Data Sets in the low energy region is a challenging task. Data were taken through several significant hardware and software upgrades, including the addition of the inner UGEFCu shield and the installation of Module 2. Detectors have been brought online and offline, have had their HV bias voltages and signal readout channels changed, and ^{228}Th calibrations routinely provide new information on gain changes and pulse shape performance. The detector energy thresholds also fluctuate, most significantly due to changing electronics noise conditions in the array over time. This is most notable before and after Data Set 5A, when Module 1 and 2 were first run in tandem, and significant HF noise believed to originate from electrical ground loops was observed on the waveforms. The ground loops were largely eliminated between DS5A and DS5B. A consistent analysis must track each detector through these varying operational states. In addition, the new pulse shape analysis (PSA) techniques discussed in Chapter 3 require the processing of a large number of waveforms, which is a computationally intensive task. The Low-Energy Analysis Toolkit, LAT, has been developed with these challenges in mind. This Chapter will describe its application to Data Sets 0–5C, concluding with spectra ready for physics analysis, with known exposure and signal detection efficiency.

Between the beginning of Data Set 0 in June 2015 and the conclusion of Data Set 5 in May 2017, 10.35 kg-y of $^{\mathrm{enr}}$Ge and 3.92 kg-y of $^{\mathrm{nat}}$Ge data were collected by the Demonstrator. Data Set 5C was not included in the $0\nu\beta\beta$ analysis discussed in Chapter 2, but has since been analyzed and made available by the Majorana Working Groups. This Data Set also marked the resumption of blinded data taking, in which 75% of the background data are made inaccessible to avoid biasing the development of analysis cuts. Data Set 6 is ongoing at this time and will also be omitted here. The exposure totals for the open Data Sets are given in Table 4.1.

Table 4.1: Exposure summary for all open data in Data Sets 0–5C, using high-gain deadtime. The exposure reduction for the low energy analysis is *not* shown, and uncertainties will be given in Section 4.9.

DS	Avg. Livetime (d)	$^{\mathrm{enr}}$Ge Exp (kg-d)	$^{\mathrm{nat}}$Ge Exp (kg-d)
DS0	43.217 ± 0.661	454.6044	164.5279
DS1	52.488 ± 2.902	656.1512	62.8630
DS2	9.399 ± 0.081	105.8213	10.5222
DS3	29.248 ± 0.107	368.5627	81.7384
DS4	18.751 ± 0.030	102.8491	73.8435
DS5A	71.374 ± 2.289	1244.7021	616.6332
DS5B	37.169 ± 1.143	672.7652	335.9027
DS5C	10.652 ± 0.284	174.4739	86.0294
Totals		10.3489 (kg-y)	3.9208 (kg-y)

Not all of the low energy Demonstrator data are suitable for analysis. Detector data from a particular time period can be declared unfit if the calculation of its PSA parameters fails, or if the rate remains anomalously high (a "burst") following the application of PSA cuts. This process of run and detector selection is accounted for in the LAT analysis, removing bad data from the final spectrum, efficiency calculation, and exposure. As the following sections will show, PSA and burst cuts dramatically reduce the noise in the data while retaining a majority of the exposure.

The LAT analysis can be divided into four main tasks. Section 4.2 will describe the data processing procedures necessary to produce LAT data with new pulse shape parameters at event energies as low as 0.7 keV. Sections 4.3–4.8 describe the PSA cuts and the evaluation of their efficiencies (retention of good physics events). Section 4.7 describes the "burst cut" that performs the final run and channel selection. Finally, Section 4.9 describes the evaluation of the final low-energy exposure for each Data Set, and gives the final spectra and efficiency corrections.

4.2 Data Processing

LAT is an extension of the GAT software discussed in Section 2.3, utilizing the combined results of several MAJORANA Working Groups. The Energy Estimation group provides the main energy parameter `trapENFCal`, and the Data Quality group provides an official list of runs to be included in each Data Set, as well as lists of detectors declared "good," "bad," or "veto-only." Detectors can be labeled in this manner for the span of the entire Data Set, or a short period of runs. This information is summarized in the GAT library file `DataSetInfo`.

Background data from each Data Set are grouped into subsets, each containing roughly 30–50 one-hour runs. Periodic ^{228}Th calibrations are used to update energy and PSA parameters. Each calibration has a corresponding *run coverage* where its results are applied. The correspondence of background to calibration ranges is not necessarily one-to-one and can be different for each Module, as illustrated for the case of DS5A in Figure 4.1. The production of LAT data from skim files does not depend on matching background ranges to calibration ranges; each is treated separately. Later stages of the processing, beginning with the PSA cut tunings, must account for the run coverages of each calibration in each module in each background subset.

The LAT analysis was primarily done using the computational facilities of the National Energy Research Scientific Computing Center (NERSC). Its PDSF cluster

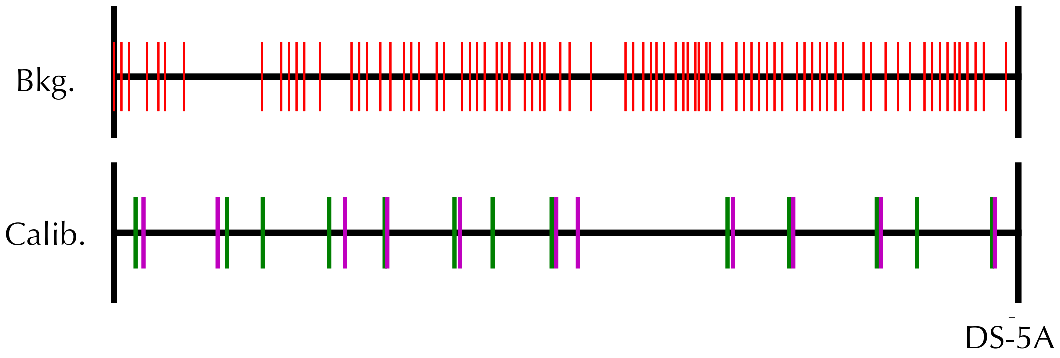

Figure 4.1: Illustration of the splitting of a Data Set into subsets. The first run in each of the 80 background subsets is marked in red, the 13 Module 1 calibrations in green, and 11 Module 2 calibrations in magenta.

was the main workhorse, while the larger Edison and Cori systems were used in the waveform fitting step for their increased throughput. Each stage of LAT data processing is controlled by a manager program, `lat-jobs`. `lat-jobs` calls other LAT programs to run on a multi-core batch system, and is capable of submitting many jobs in parallel to dramatically decrease processing time. Commands to execute individual jobs and their output are saved for repeatability and error checking.

The starting point for LAT is the production of *skim files*, which contain energy and pulse shape parameters for all hits passing basic data cleaning cuts, including removal of pulser events (See Section 2.3). The files are produced with a lower energy threshold (0.7 keV) than used for $0\nu\beta\beta$, which can significantly increase their size if low energy noise is present. Except for the lower energy threshold, these files are completely consistent with the $0\nu\beta\beta$ analysis. They use the same run lists, muon and LN fill vetos, pulser tag removal, bad and veto-only detector lists, energy calibration, and channel selection. By starting at the "skim level", the LAT analysis benefits from the entire GAT analysis chain, with all its consistency checks.

After the initial set of background and calibration skim files are produced, the waveforms of all events passing basic data cleaning cuts are retrieved from the built data and saved for additional processing. This is done by the LAT program `wave-skim`. The saved waveforms are also corrected for ADC nonlinearities at this stage, using the same algorithm and input data as in GAT. A basic data cleaning cut is applied to the skim data at this step. It removes LN fill and muon veto periods, and events from bad/veto-only detectors. For both background and calibration data, only high-gain channels are selected. Additionally, a multiplicity cut `mH==1` is imposed on the background data, while the calibration data processed with LAT allows higher multiplicities but removes events with energy over 250 keV to reduce file size. Figure 4.2 gives the data cleaning cuts used by `wave-skim`.

```
All: !(C==1 && isLNFill1) && !(C==2 && isLNFill2)
     && C!=0 && P!=0 && D!=0
     && isGood && !muVeto && gain==0
     && trapENFCal > 0.7
Bkg: && mH==1
Cal: && trapENFCal < 250
```

Figure 4.2: The data cleaning cut used by `wave-skim`, for both background and calibration files.

The main LAT program, `lat`, applies the PSA techniques discussed in Chapter 3, including the waveform fitting and calculation of wavelet parameters. The waveform fit requires a significant amount of computational power. Even a relatively fast (0.1 sec) fit becomes a bottleneck when the data set is large. The low energy skim files contain ∼2 million events per gigabyte. The combined DS0–5C background set is 120 GB, and the calibration files are 164 GB. Running a 0.1 second waveform fit on every entry in this data set would take more than two years if run on a single CPU. Fortunately, this waveform analysis is an "embarassingly parallel" problem. Each waveform can be fit separately without any dependency on other fits. Before the main LAT program is run, a "split step" is performed by `lat-jobs`, which subdivides each `wave-skim` output file into ∼50 MB chunks, each of which takes three to four hours to process.

In addition to the waveform fit and wavelet packet decompositions, the main LAT program uses the saved waveforms to calculate a number of new pulse shape parameters, not all of which have been used in the final analysis. Unused parameters include an asymmetric trapezoid, an optimal matched filter energy estimator, a polynomial fit to the waveform tail, a time-domain matched filter with a template pulse from `siggen`, time points (10%, 90%, etc. rise times) for both raw and denoised waveforms, high- and low-pass filters, and a new multi-site event tag. Despite the presence of these extra parameters, a speed profile of the LAT program showed that their CPU usage is not significant compared to the processing time needed for the waveform fit. Since they do not excessively slow down the processing, they have been kept in the output in the hopes of being useful to future analyses.

The main LAT program is run on the Cori or Edison supercomputers at NERSC, which consist of thousands of individual compute nodes, each containing 48 to 272 CPU threads, depending on the system. The splitting of the `wave-skim` input to the main program enables a much higher throughput on these systems. The total production time for both background and calibration LAT data (containing the waveform fit results), is reduced from >2 years on a single CPU to roughly two days.

After the LAT data is produced, they must be checked to ensure there are no corrupted files or missing events. The skim file generator selectively accepts events from the GAT files provided certain cuts are passed. For each event, the run number and entry in the `TTree` is saved. The GAT program `validate-skim` checks that each entry in the skim files matches correctly with the GAT file, and that the channel number for the detector and the event timestamps match. As a first consistency check, this is run on every low energy skim file generated by `lat-jobs`.

The program `lat-check` was developed to ensure the integrity of the LAT data. Skim and `wave-skim` files are checked that the trees are readable and contain no corrupt entries. The “split skim” and LAT files are checked to make sure they contain the same number of entries as their parent `wave-skim` files. Additionally, the LAT files are checked for the existence of the new PSA parameters, and checked again that the metadata saved in the `MGTWaveform` objects matches the data in the rest of the tree.

The `DataSetInfo` library file provides a starting point for the GAT analysis of each Data Set. A complementary module has been developed for LAT, `dsi`. It provides lookup functions for background and calibration data, as well as “special” runs, simulation data, and read/write access to the LAT database `calDB`. `calDB` stores threshold, PSA, and other detector-specific parameters for each background and calibration subset, and its use will be described further in Section 4.3.

Recognizing the impact that changing detector thresholds and HV bias changes can have on the analysis, the program `lat-settings` was developed to access the raw ORCA settings for all runs in each Data Set, and identify any background subsets where the threshold or HV settings were changed during the subset. The background subset is then divided accordingly into periods before and after each change. These changes, along with detector channel maps for each Data Set, are saved into dictionaries usable by the entire LAT analysis through lookup functions in `dsi`.

The application of PSA cuts, run and channel selection, and the final exposure calculation depend heavily on a consistent framework for analysis, which is provided by the `dsi` module. `dsi` provides a “good channel list” for each Data Set, and multiple maps relating the analysis channel numbers to the detector position and its serial numbers. The “good channels” for the low energy analysis are taken to be any detector that is not on the *global* bad or veto-only lists marked in `DataSetInfo`. If a detector is temporarily made veto-only within the Data Set, its events are removed by the skim file generator. Most studies done in the following sections rely on the breakdown of Data Sets into subsets, and by channel number. Consistent use of the good channel list provided by `dsi` ensures that no detectors are missed in each step of the analysis.

4.3 Pulse Shape Analysis Overview

After the initial LAT data have been produced and checked, we begin the calculation and tuning of pulse shape analysis cuts. The development of robust cuts at low energies in the Demonstrator data is complicated by two main factors. First, the extremely low backgrounds in the enriched detectors make it difficult to unambiguously identify spectral features in the background data that could be used for calibration and cut tuning. Second, over the two year operational period of Data Sets 0–5, the electronics noise conditions in the array and the detector energy thresholds have changed over time. To begin, we note that the waveforms in the Demonstrator can be roughly classified into four main categories:

1. Fast single-site events from the detector bulk
2. Slow surface events (energy degraded)
3. Electronics noise signals (most below ~2 keV)
4. Multi-site events (negligible below 50 keV)

Typical examples of 1–3 were shown in Figure 3.13.

Three main pulse shape analyses are performed by LAT: detector thresholds, waveform fitting, and wavelet packet decomposition. Respectively, these give the energy threshold, slowness (`fitSlo`), and high-frequency (`riseNoise`) parameters. The cut values are generally chosen to maximize acceptance for the desired signal (fast events), with low sacrifice (accidental rejection) and high rejection of unwanted events. The resulting *efficiency* of a particular cut value at different energies must then be evaluated.

The detector thresholds are evaluated for both background and calibration data, since both contain enough noise and high-energy triggers to evaluate the trigger efficiency. The `fitSlo` and `riseNoise` cuts are set using data from each calibration, and the results are applied to the background data. The efficiency of the `riseNoise` cut is relatively simple to determine. Since its goal is to reject electronics noise, and is not intended to distinguish between fast and slow physics events, no additional cuts beyond basic data cleaning are needed for the calibration waveforms. Every detector in each calibration run has a large data set of low energy physics pulses which can be used to find the efficiency. The determination of the `fitSlo` efficiency is more challenging. A method based on high-multiplicity calibration data has been implemented which relies on small-angle Compton scattering. This is a relatively rare process in the calibration data, and data from all calibrations must be combined to build up suitable statistics in each detector. The individual detector efficiencies, usually given as a function of energy, can then be combined into a total efficiency for the entire Data Set. The following sections describe the implementation of the low-energy PSA cuts and the determination of the efficiency of each.

4.4 DETECTOR THRESHOLD EVALUATION

During physics data taking, the GRETINA digitizer cards continuously record ADC values from each detector into a circular buffer. The data are passed through an on-board (4–1.8–4 μs) trapezoidal filter with no pole-zero correction. To trigger the DAQ system's readout of the buffer, the output of the filter must exceed a user-specified value which is set in ORCA [1]. If the threshold is set too low, the system will

---

[1] The energy is also estimated using the maximum of the on-board trapezoid, but the raw waveform is not pole-zero or nonlinearity corrected and the on-board output is not used in the final analysis.

excessively trigger on Gaussian noise fluctuations. If set too high, low energy physics events may be missed. The trapezoid threshold is related to the energy threshold of the detector, but the energy calibration from ADC (which is proportional to voltage) to keV must be taken into account.

The energy threshold of a detector can be calculated by mimicking the onboard trapezoid of the GRETINA card and finding the ADC value at which a signal must rise above to cause the system to read out. The conversion to keV can then be done using the calibration constants provided by the Energy Estimation Working Group. By overlaying the trapezoid output for both high and low energy waveforms, the Gaussian component of the baseline noise can be evaluated, along with the threshold for physics events. When a detector has a working pulser, a large population of both high and low-amplitude events is available run to run. The pulser signal is a square wave with a period $T \sim 8$ seconds. It is not perfectly square, and there is an "overshoot" at its rising and falling edges as the voltage briefly exceeds the target. If a channel is set to trigger on positive pulses only, it will see a large pulser amplitude event as expected, followed by a very small upward-going event at $T/2$ from the overshoot of the negative-going part of the square, with a constant positive slope. This retrigger event typically has a reconstructed energy of < 1 keV. To illustrate the algorithm, Figure 4.3 shows the trapezoid filter output for all waveforms in a channel in a single run, from a detector with a working pulser.

The lower plot in Figure 4.3 shows that physics events (in red) have a characteristic spread around ADC$= 0$, in the first nonzero sample of the trapezoid. The fluctuations are dependent on the Gaussian fluctuations in the baseline, and by histogramming the first sample of many waveforms and fitting it to a Gaussian, the width σ is a measure of the baseline noise. Also apparent in Figure 4.3 is a "crossing point" where the physics signals rise above the retrigger events. This provides a convenient way to measure the height of a trapezoid necessary to trigger the system by examining the

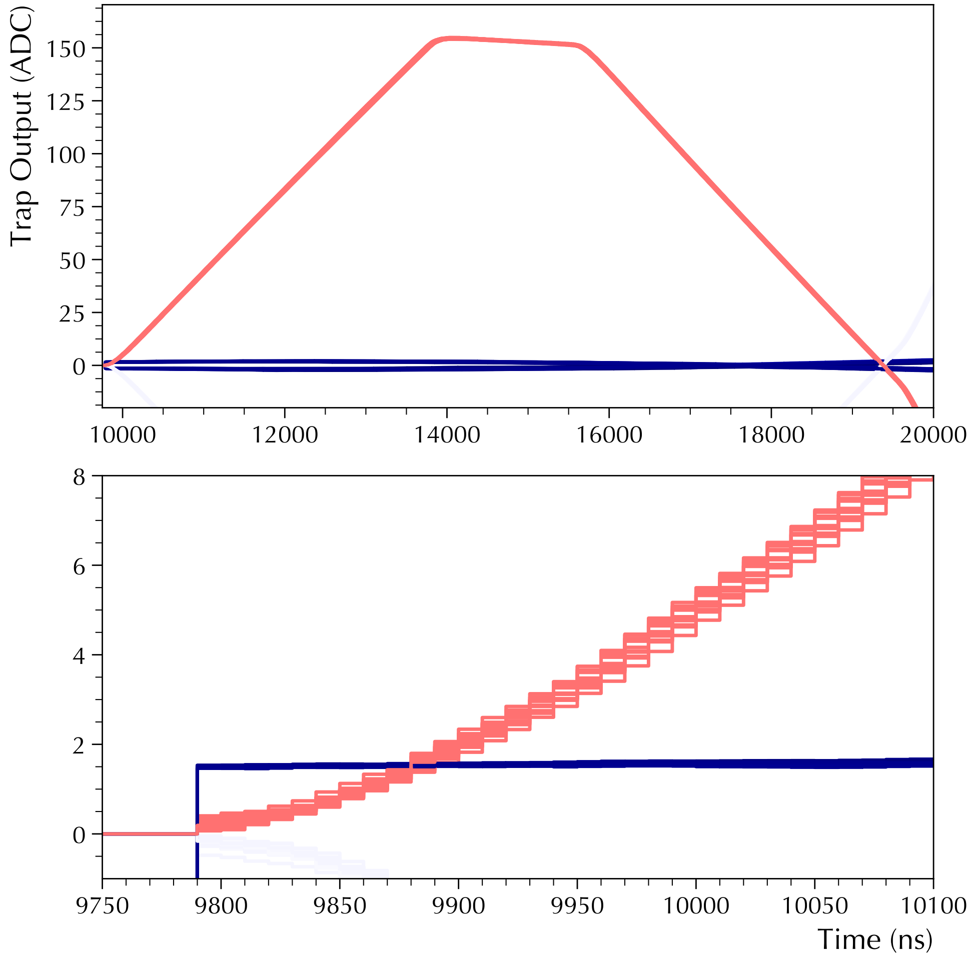

Figure 4.3: Top: Output of the (4–1.8–4 μs) trapezoid with no decay constant used by `auto-thresh`, colored according to energy. Red are pulser events, blue are pulser retriggers (white are negative-trigger pulser events, not relevant here). Bottom: Zoomed-in output, showing the spread in baseline noise at the first sample (9800 ns), and the crossing point (∼9880 ns).

typical ADC value of the crossing point for every detector. The energy of the crossing point can change depending on the detector gain and trigger settings, but the sample at which it occurs is found to be relatively constant, occuring at the 8–9th sample of the trapezoid output. If a detector does not have a working pulser and lacks a large enough number of high energy events in a single run, a threshold can still be found by combining multiple runs together, and finding the typical ADC value at the 9th sample. The ADC values at the crossing point are histogrammed and fit to a

Gaussian as well; the mean value μ is taken to be the energy at which a given signal has a 50% chance of triggering the system.

Finding the spread in the noise samples σ measures the baseline noise on a detector, and finding the mean μ of the crossing point determines the 50% trigger threshold. From these two parameters, the trigger efficiency curve as a function of energy is determined by forming an error function:

$$\mathrm{Eff}(E) = \frac{1}{2}\left(1 + \mathrm{erf}\left(\frac{E-\mu}{\sqrt{2}\sigma}\right)\right) \tag{4.1}$$

Figure 4.4 shows the trigger efficiency as a function of energy.

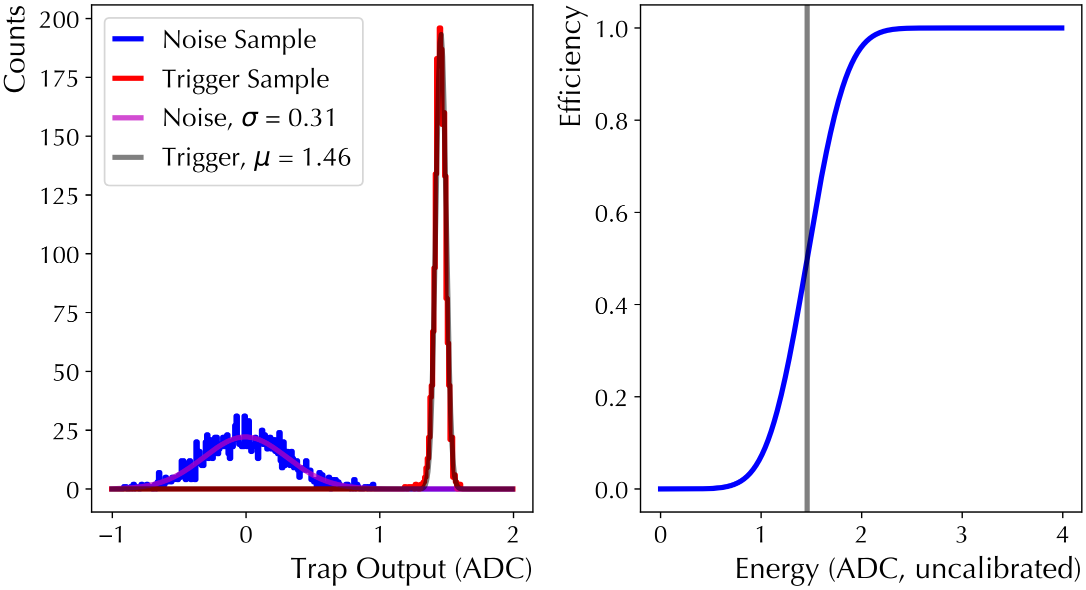

Figure 4.4: Example threshold calculation for C2P1D3, run 60001538. Left: Histograms of noise and trigger samples with Gaussian fits. Right: The (uncalibrated) trigger efficiency as a function of energy based on the fit parameters.

One potential source of systematic error in this method is the use of the maximum value of the trapezoid output rather than a fixed-time pickoff. This can in principle change the location of the crossing point μ, and alter the shape of the trigger efficiency function. In the current DS0–5 LAT analysis, the *energy threshold* of a detector is defined as $\mu + 3\sigma$, or 99% above the mean value of the error function. Using the 99% value makes the current analysis insensitive to deviations in the efficiency from the

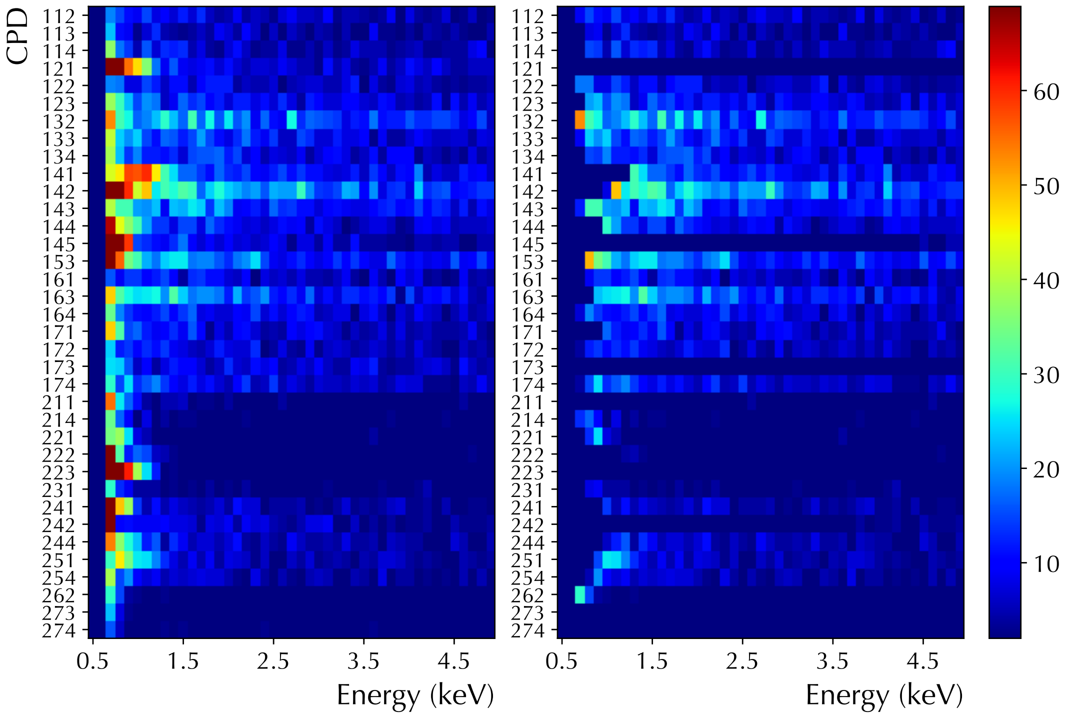

Figure 4.5: Hits below 5 keV in a DS5 M1 calibration run, before (left) and after (right) application of the threshold cut. "CPD" refers to the Cryostat, Position, and Detector number of each detector. The excess of hits in the lowest bins of several detectors are visibly excluded after the cut is applied. (Some detectors in this run fail the calculation due to non-Gaussian noise features and are cut completely.)

shape of the error function, and helps ensure that signals caused by Gaussian noise are eliminated. As a final step, the GAT energy calibration database is accessed to convert the threshold to keV. Figure 4.5 shows the threshold cut applied to a calibration run, removing Gaussian noise.

The GRETINA digitizer card has an unfortunate behavior which complicates the triggering issue further. Each time it is reinitialized, the effective energy threshold of the card can change. The onboard energy trapezoid $S(n)$ is calculated from the raw signal $v(n)$ according to the recursive algorithm in [120]. It is dependent on the first value $S(0)$. Gaussian noise on the baseline causes a corresponding spread in $S(0)$ around the true value μ. The current version of GRETINA firmware assumes the value of $S(0)$ is the true value μ, without accounting for its deviation $\Delta S(0)$ from the true value. This is called the *baseline offset*, and it can raise or lower the effective threshold of the digitizer. Postitive $\Delta S(0)$ raises the effective threshold of the card, while negative values lower the threshold and potentially increase the number of noise triggers.

In Data Set 0, the cards were reinitialized at each 1-hour run boundary, and it was not until midway through Data Set 1 that a "continuous running" mode was implemented that avoids the reset in typical data taking. However, DAQ errors, changes in noise, and high voltage breakdown events can all necessitate the system be stopped, the cards reinitialized, and the thresholds reset. A "threshold finder" program was written in ORCA to optimize the threshold settings for each detector, and was semi-frequently run by DAQ operators throughout Data Sets 1–5 to maintain a stable data rate. Over the operational period, the threshold finder has been improved to account for the baseline offset problem, reinitializing a given card many times based on a measurement of the true baseline noise. This capability was added during Data Set 5.

The `auto-thresh` program from LAT has been implemented into GAT as part of the standard processing of each run. The variables `threshKeV` (μ) and `threshSigma` (σ) are saved into the standard output. For calibration runs, each detector has a large enough number of hits that the threshold variables can be applied directly. For background runs, detectors without pulsers will often fail to fit correctly in single runs.[2] To address this issue, detector thresholds are recalculated for the combined set of runs in a background subset.

LAT also accounts for instances of the threshold finder being run *within* a subset. `lat-settings` was used to perform a scan over all data runs, identifying the run boundaries between which the threshold finder was run. If a background subset contains a change in thresholds, the runs in the subset are split, and `auto-thresh`

---

[2] C1P4D5 and C2P4D2 in Data Set 5.

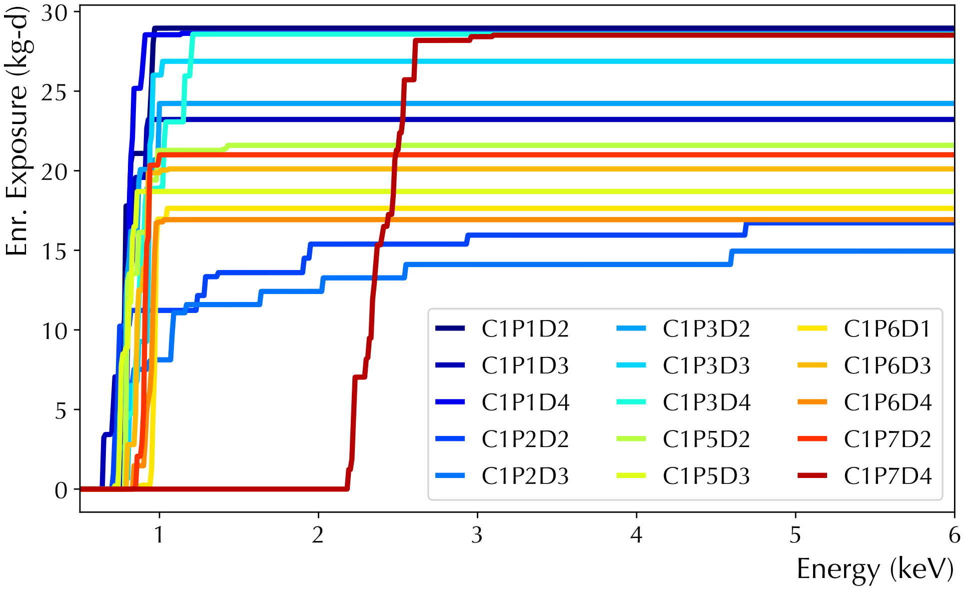

Figure 4.6: The combined trigger efficiencies for each enriched detector in Data Set 3, multiplied by exposure. C1P7D4 has a consistently higher threshold due to noise in DS3.

is run on each sub-subset. This ensures that an incorrect (mismatched) threshold value is never applied to a detector in any given background run. The Gaussian fits performed by `auto-thresh` are quite robust, but can fail in the case of low statistics, or when a detector has anomalous noise. In the cases where the fit fails in a background subset (or sub-subset), the detector is marked "bad" and rejected for the corresponding background runs.

Finally, the `threshKeV` and `threshSigma` parameters for each detector in every background subset are saved into the `calDB` to determine the total efficiency for each Data Set. Each curve has a maximum at 1, and if the curves from every detector in every subset are scaled by the corresponding exposures, we obtain a measure of how much exposure effectively exists in a given Data Set for a certain energy threshold. As an example, the combined trigger efficiencies for each detector in Data Set 3 are shown in Figure 4.6.

4.5 SLOW EVENT REJECTION

In HPGe detectors, the transition between the dead and active parts of the crystal is not a sharp boundary. If an ionization event occurs very close to the bulk side, at the edge of the transition region, it will be only very slightly energy degraded. As a result, there is not always a clear distinction between fast (bulk) and slow (transition) pulses. This is especially important at very low energies, where the reduced signal to noise ratio can obscure fine features of a waveform. Given a particular slowness parameter (t_{10-90}, T/E, `fitSlo`), the distributions of fast and slow events in normal background and calibration data will have some overlap region where it is difficult to unambiguously classify a signal. The expected shape of the slow pulse distribution in background data is generally unknown and difficult to model. For a particular choice of cut parameter, some "bleed over" of slow pulses into the final spectrum is likely to occur, and is known as the *slow pulse contamination.*

To evaluate the performance of a slowness parameter, a suitable training set of events must be found where the fast and slow distributions are known *a priori*. It can be a comparison against cosmogenic peaks (very difficult in the $^{\mathrm{enr}}$Ge) or from specialized calibrations. The *signal acceptance efficiency* of a particular slow pulse cut is defined by the ratio of fast events in the training set that pass the cut, to the known total. If the cut is overly aggressive, it will begin to excessively remove fast events. This is the *signal rejection efficiency*. Since the slow pulse distribution is not known in background data, the rejection efficiency is difficult to quantify, and the preferred method of previous low energy HPGe experiments (including CoGeNT [85], MALBEK [126] and MAJORANA [79]) is to use the *fast signal acceptance* as the efficiency correction to the final energy spectrum. Any remaining slow pulse contamination after cuts is treated as an irreducible background. A similar method will be applied here which makes use of a new training set unique to the DEMONSTRATOR.

In the Data Set 0 analysis [79], which set an energy floor of 5 keV, the efficiency of the T/E slow pulse cut was determined from a set of external pulser measurements from three detectors taken after the conclusion of the Data Set. In this type of measurement, signals from a precision waveform generator with varying rise times are attenuated and capacitively injected at the HV ring (n^+ contact) of a detector. Although no charge is made to actually drift through the detector, a change in voltage at the n^+ contact induces a change at the p^+ side which depends directly on the capacitance of the detector. This induces a signal that more realistically reproduces the detector response to a physics event than the LMFE-side pulser.

The rise times of the external pulses were chosen to match typical fast events for each detector.[3] This produced a fast event training set which was used to find the fast signal acceptance, by finding the energy-dependent fraction of events passing a given cut value to the total. The acceptance was parameterized by an error function (much like the trigger efficiency function in Figure 4.4). Since only three detectors were instrumented, the most conservative acceptance was chosen to apply to all detectors, which ranged from 96% at 5 keV to 100% at 20 keV. The number of slow pulses is known to be zero in the external pulser training set, and the signal rejection efficiency is not measured but is qualitatively expected to be high (low-sacrifice), since the cut is set at the upper fast pulse limit. The lowest-energy data taken is shown in Figure 4.7.

Unfortunately, the external pulser measurements on which the DS0 efficiency was determined cannot form the basis for the DS0–5 efficiency at this time. At the time of the DS0 measurement, Module 2 was still under construction; to date, none of its detectors have had external pulser data taken. The characteristic rise time of pulses from a given detector can be affected by changes to its HV bias or the pulse shape electronics in the preamp, and many detectors in the array have undergone such

---

[3] However, they do not *exactly* match the spread in rise times seen in physics data; they are somewhat narrower.

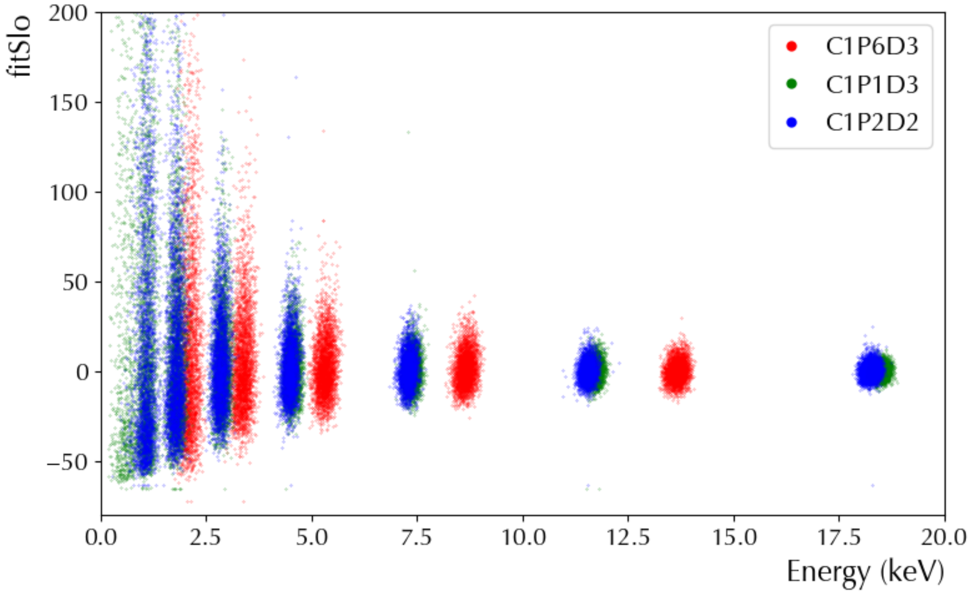

Figure 4.7: External pulser data for the three detectors in Data Set 0. The modes of each detector's `fitSlo` distribution have been aligned at zero

adjustments. For this reason, even a set of dedicated external pulser measurements taken for all detectors today would not necessarily be applicable to the array in past configurations without a detailed study. To consistently analyze DS0–5, a new set of fast events to train the slowness cut is needed.

The modular design of the detectors in the Demonstrator allow many possible hit patterns for gamma ray scattering events, while the world-leading energy resolution allows populations of events with carefully controlled energies to be studied. When the ^{228}Th calibration source is deployed, it emits a well-known gamma spectrum with a variety of well-defined peaks. The resulting spectrum is a mix of fast and slow pulses as gammas from the ^{228}Th calibration source either Compton scatter [134] in one or more detectors or are stopped, depositing the remainder of their total energy via the photoelectric effect or pair production. By applying the detector threshold cut to remove Gaussian noise triggers, the sum energy of the event `sumET` and an updated multiplicity `mHT` can be updated from their original skim file values (`sumE` and `mH`). Figure 4.8 shows the resulting sum energy spectrum for a 5-hour Module

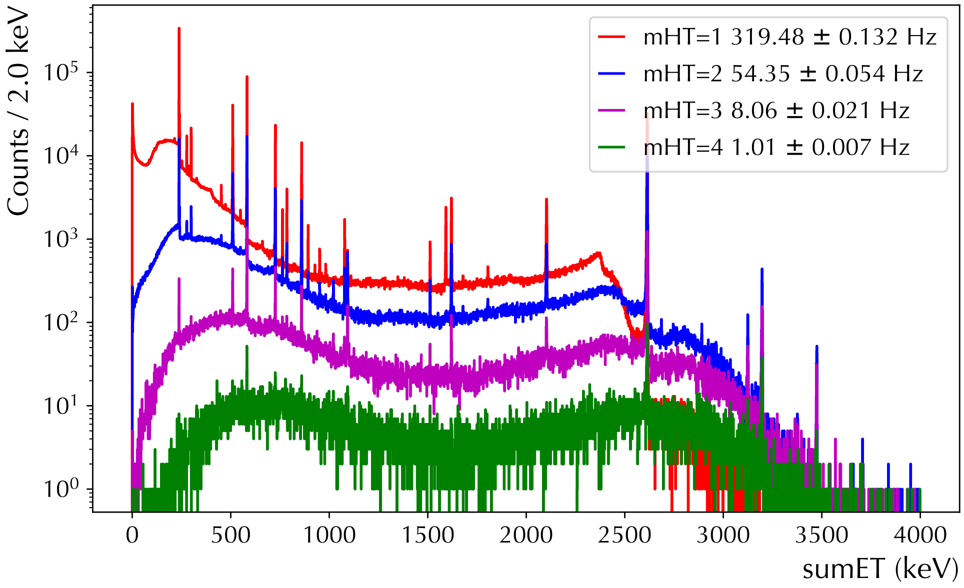

Figure 4.8: Calibration sum energy spectrum. The sum energy `sumET` and multiplicity `mHT` are recalculated after the threshold cut is applied.

1 calibration run. From this, the event rate for each `mHT` can be measured. Since the error is statistical, the accuracy of the measured rate goes as $1/\sqrt{N}$, and 10,000 counts are needed for a 1% error. We find that ~5100 seconds of data are necessary to measure the `mHT==4` rate to 1%.

If a population of events is Poisson-distributed with a known rate λ, then the probability of observing n hits in a time window t is

$$P(n) = \frac{(\lambda t)^n}{n!} e^{-\lambda t} \tag{4.2}$$

For an event to have `mH > 1`, coincident detector hits must fall within a time window dictated by the MAJORANA event builder software. It uses a moving window with a width of 4 μs. For any given hit, if another hit occurs within ± 4 μs, they will be grouped together into a single event. For an `mH==2` event, we can take $t = 8$ μs as the time window. `mH==3` will be 12 μs, and so on. We can denote the probability of getting n multiplicity m events as $P_m(n)$. Assuming Poisson statistics for each multiplicity m and using the measured rates from Figure 4.8, we can find the probability that an accidental coincidence of two $m = 1$ events falls within the $m = 2$ time window and is declared `mHT==2`:

$$P_1(1) = \lambda_1 t e^{-\lambda_1 t} = 3.819 \times 10^{-3} \tag{4.3}$$

$$P_1(2) = ((\lambda_1 t)^2/2!)\ e^{-\lambda_1 t} = 1.459 \times 10^{-5} \tag{4.4}$$

$$P_2(1) = \lambda_2 t e^{-\lambda_2 t} = 6.518 \times 10^{-4} \tag{4.5}$$

$$P_1(2)/P_2(1) = 0.0112 \tag{4.6}$$

From this we see that accidentally coincident `mHT==1` events make up only 1.12% of the `mHT==2` population.

Several of the prominent gammas forming the spectral lines in Figure 4.8 are typically emitted in coincidence with other gammas [135]. For example, the 2614.5 keV gamma from ^{208}Tl is frequently accompanied by gammas at 510, 583, or 860 keV, and may naturally be expected to create a high-multiplicity event. The most prominent line under 500 keV in the ^{228}Th spectrum is at 238.632 keV and is from ^{212}Pb. It has the interesting property that it is not strongly coincident with other gammas. This implies that an `mHT==2` event with a sum energy of 238 keV is likely to be comprised of a single Compton scatter in the first detector, and photoelectric absorption of the remainder of the event energy. Figure 4.9 shows the sum energy peak at 238 keV, selecting only `mHT==2` events in calibration data from an arbitrary calibration run.

The energy lost by an incident photon as it scatters off an atom can be derived from the Compton formula. It is proportional to the scattering angle θ, and predicts that small-angle scatters deposit correspondingly small amounts of energy.

$$E' = \frac{E}{1 + \frac{E}{m_e c^2}(1 - cos\theta)} \tag{4.7}$$

Here the recoil of the atom (nucleus) is assumed to be negligible and m_e is the mass of the electron in the atom the gamma interacts with. Figure 4.10 depicts the small-angle Compton scatter in two HPGe detectors.

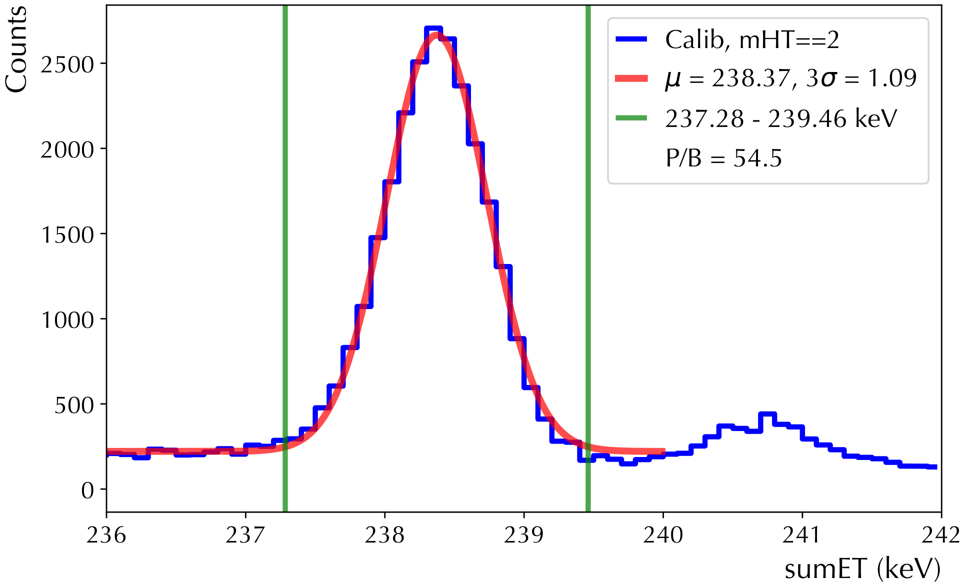

Figure 4.9: Calibration events with `sumET`=238 keV. There are 54 times as many events in the peak as in the flat background under it.

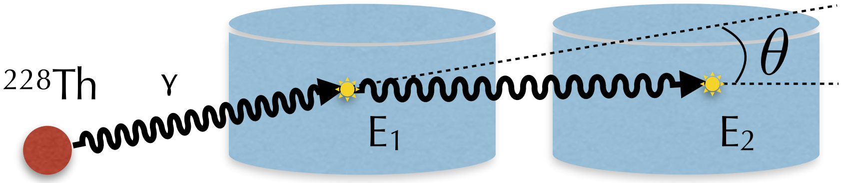

Figure 4.10: Illustration of a small-angle Compton scatter. A gamma is emitted from the ^{228}Th calibration source, scatters in one detector, and deposits the remainder of its energy in the second detector.

The mean free path of a 238 keV gamma in Ge can be found from the attenuation coefficients in the XCOM [136] database:

$$l = ((\mu/\rho)\rho)^{-1} = (0.1278\ \mathrm{cm}^2/\mathrm{g} \cdot 5.323\ \mathrm{g/cm}^3)^{-1} = 14.69\ \mathrm{mm} \tag{4.8}$$

Since a typical detector radius is 30 mm, the 238 keV gamma is easily able to penetrate through the dead layer and into the bulk when it Compton scatters. Given the low signal-to-noise ratio of low energy events, there is no significant difference between events depositing energy 14 mm into the crystal or at the center. Both are comfortably within the bulk and produce a fast rising edge signal.

By selecting `mHT==2` events in calibration data whose sum energy is within 3σ of the 238 peak, we isolate a population of hit pairs. For convenience we denote these events `m2s238`. The low-energy hit is a small-angle Compton scatter, and the high-energy hit is the photoelectric absorption of the remainder of the energy. The case $\theta = \pi$ gives the maximum energy deposit E_C allowed for a single Compton scatter:

$$E_C = E\left(1 + \frac{2E}{m_e c^2}\right)^{-1} \tag{4.9}$$

For the case of the 238.6 keV gamma, $E_C = 123.3$ keV is the maximum energy allowed for a single scatter. Figure 4.11 shows the hit energies of the `m2s238` events from a 5-hour Module 1 calibration run. The Compton edge is clearly visible, and hit energies down to 1 keV are present. This is evidence that a population of Compton scatters has been isolated. Simulations have been developed by the MAJORANA collaboration which support this conclusion, and also provide an estimate of the number of events in the transition layer, shown in Figure 4.11. Results from the simulations are not included in the current analysis for more than qualitative comparison. However, the `m2s238` population is a strong candidate for a realistic simulation, since it involves well-understood physics processes, unlike the full low energy background model.

The slow pulse contamination in the `m2s238` events will be proportional to the background under the sum energy peak. Significantly energy-degraded hits would not have a combined total of 238 keV and cannot contribute to the peak center. By selecting events within 3σ of the peak, we obtain a population where there are (on average) 54 times as many events in the peak as in the flat background underneath, shown in Figure 4.9. If *all* of the background events were energy-degraded, it would constitute 1.85% of the total events (and 3.7% of the hits); the true slow pulse contribution is likely much lower. It is also a possibility that one or both of the hits is only slightly energy degraded and still falls in the 3σ peak region. The width of this region is 2.18 keV, which is the maximum allowed energy degradation possible between the two hits. This would also introduce an asymmetry in the sum peak, with

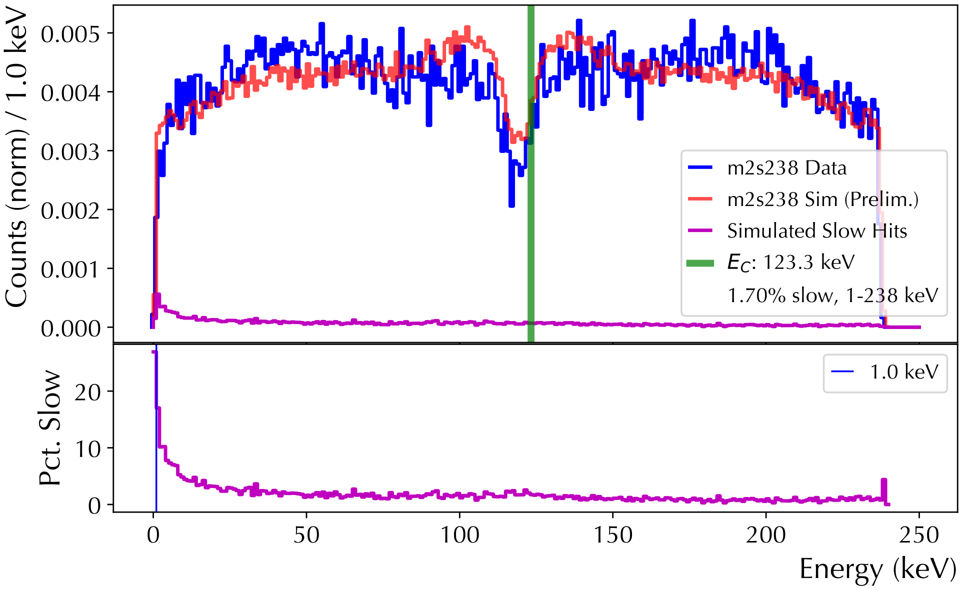

Figure 4.11: Hit energies of the `m2s238` population, from data and a preliminary simulation. The green line is at the Compton edge E_C. The bottom plot gives the fraction of slow events in the simulated `m2s238` data.

more events on the low side than the high. Since the peak is well-described by a symmetric Gaussian, we treat this contribution as negligible. In what follows, we assume the `m2s238` population has an upper limit of 3.7% slow pulse contamination from the background under the sum peak. The exact energy dependence is unknown, but it is consistent with past experiments to expect more slow pulses at lower energies. We also note this prediction is (at least qualitatively) consistent with the preiliminary simulation in Figure 4.11, which predicts 1.7%, with an unknown uncertainty.

The rate of `m2s238` events is relatively small. For example, in an arbitrary one hour DS1 calibration run, only 3953 `m2s238` events were observed, a rate roughly 1.1 Hz between all operating detectors. The individual detector rates are much lower, and due to the position of the detectors relative to the calibration track, Compton scatters in some detectors are much more likely than others. Figure 4.12 shows the relative position of the Module 1 detectors to the calibration track.

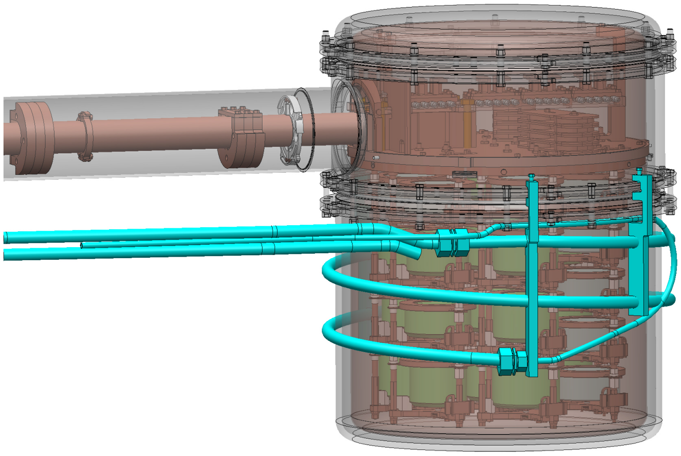

Figure 4.12: Calibration track of the ^{228}Th line source [89].

In order to build up sufficient statistics for `m2s238` hits in each detector, it is necessary to combine data from every calibration run in every Data Set together. As an estimate of the data needed, we can assume the low energy hits under 50 keV are evenly split between the 17 operating detectors in Data Set 1, resulting in a rate of 0.0002 cts/bin/sec/detector. To get 100 cts/bin/detector, roughly 200 hours of calibration data are needed. Table 4.2 gives the total run time of calibration data used by the LAT analysis in each Data Set.[4] Figure 4.13 shows the combined total of `m2s238` events for all standard calibration data. A clear deficiency is seen in Module 2 detectors, which have not had enough time to build statistics.

The distribution of `fitSlo` for each detector is sharply peaked around the detector's typical rise time. There is evidently a "fast band" as a function of energy, with each detector having a typical maximum. In order to effectively combine `m2s238` events across all Data Sets, it is necessary to align each distribution. This is done by finding the maximum of the distribution for hits between 10–200 keV, where the maximum of the distribution has no significant shift. Both the unshifted and shifted distributions versus energy for a typical calibration run are shown in Figure 4.14. A

---

[4] Several "long calibration" runs were taken which were not part of the processing. In a future analysis, they would add 58 hours of data, increasing the total by a factor 1.2.

Table 4.2: Total runtime of all calibration data in each Data Set, and an estimated number of `m2s238` counts per bin, per detector.

Data Set	Num. Runs	Run Time (hrs)	Expected Cts. (/bin/det)
DS0	717	49.22	35.4
DS1	691	60.41	43.5
DS2	94	13.23	9.5
DS3	137	10.22	7.4
DS4	169	13.43	10.0
DS5	731	89.92	64.7
Totals	2539	236.43	170.5

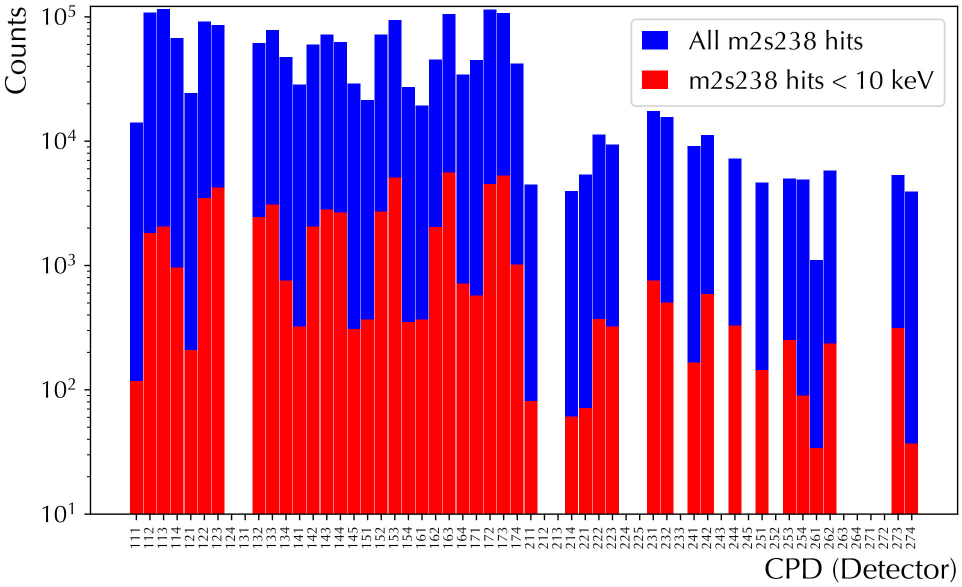

Figure 4.13: Total `m2s238` counts, for each detector in all Data Sets.

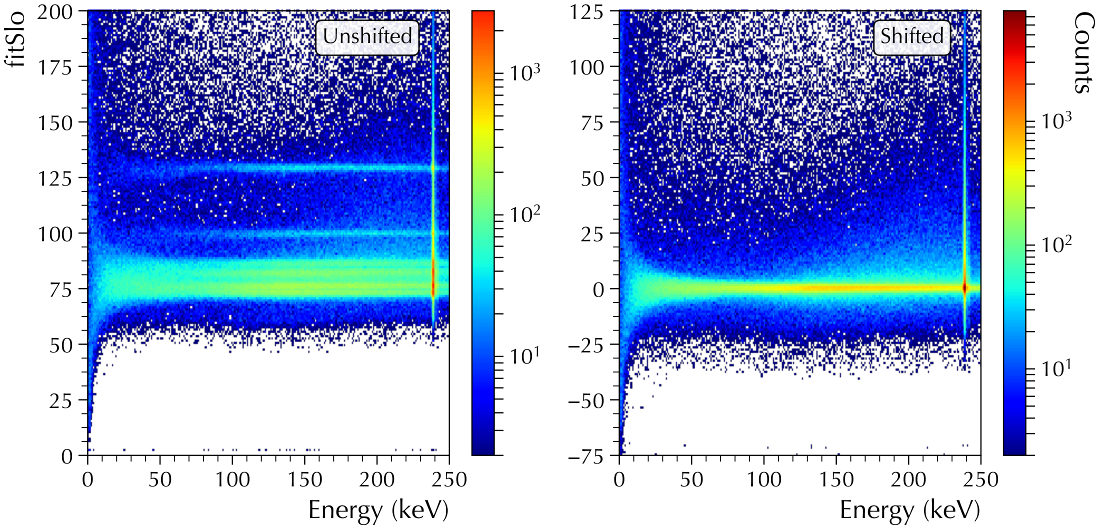

Figure 4.14: Unshifted and shifted `fitSlo` values for all events in DS1 calibration set 1. After shifting, a much more visible "fast band" is apparent.

contribution from multi-site events can be seen above 100 keV, appearing slower than typical events due to the longer rise time. The multi-site events also broaden the 238 keV sum energy peak, but no cut is applied, since the behavior of `avse` at lower energies has not been well-tested at this time, and the effect on the peak-to-background ratio of the 238 keV sum peak will be negligible. Figure 4.15 shows the distributions from a 5-hour Module 1 calibration, illustrating the slow pulse contribution in the tail in typical calibration events and its significant reduction by the `m2s238` cut.

In LAT, the maximum value of the `fitSlo` distribution from 10–200 keV is measured at every new calibration subset and stored in the `calDB` database. This enables tracking of the stability of the maximum of each detector, as well as allowing aligned distributions to be created from multiple Data Sets. If detector properties such as HV bias, depletion, or preamp tuning change the typical rise time of a detector, the maximum of the `fitSlo` distribution may change. To illustrate this, Figure 4.16 shows the maximum `fitSlo` value for each calibration in Data Set 4. There is a noticeable downward shift at the last calibration. This was due to electronics preamp tuning in Module 2, which lowered the typical rise times in each detector.

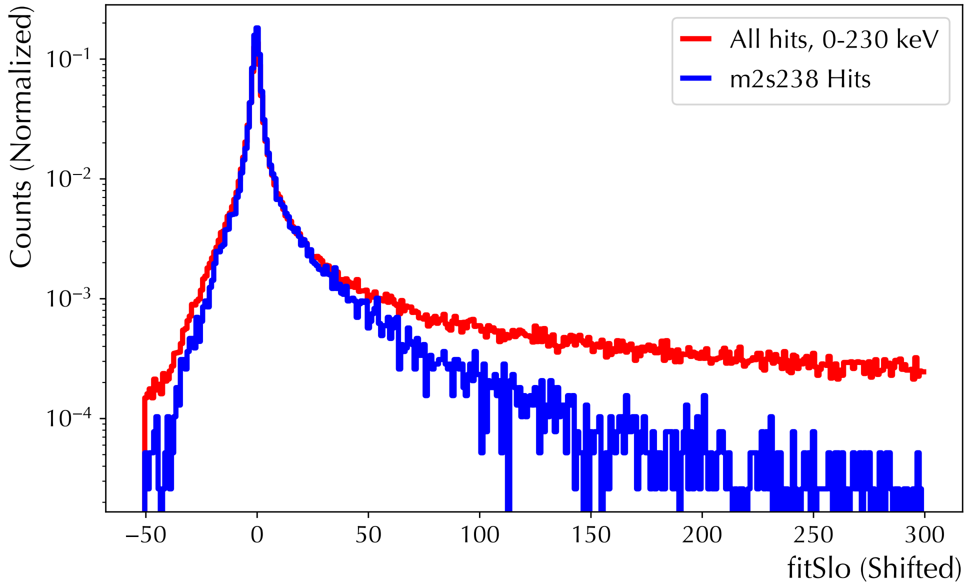

Figure 4.15: The shifted `fitSlo` distribution. Note the extended tail at high `fitSlo` values is significantly reduced by the `m2s238` restriction.

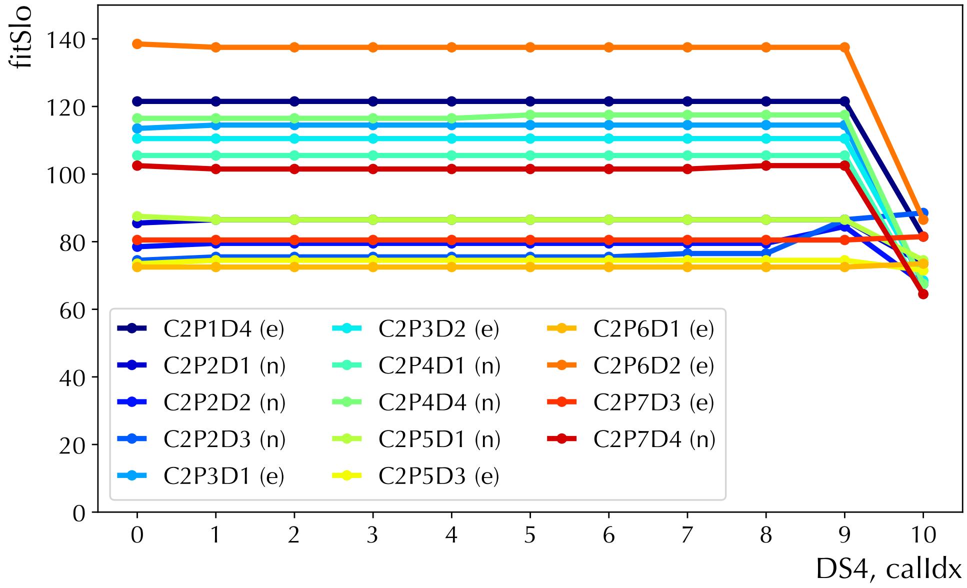

Figure 4.16: Maximum values of the `fitSlo` distribution for each detector in each DS4 calibration set. The shift of all detectors at the end is due to preamp tuning.

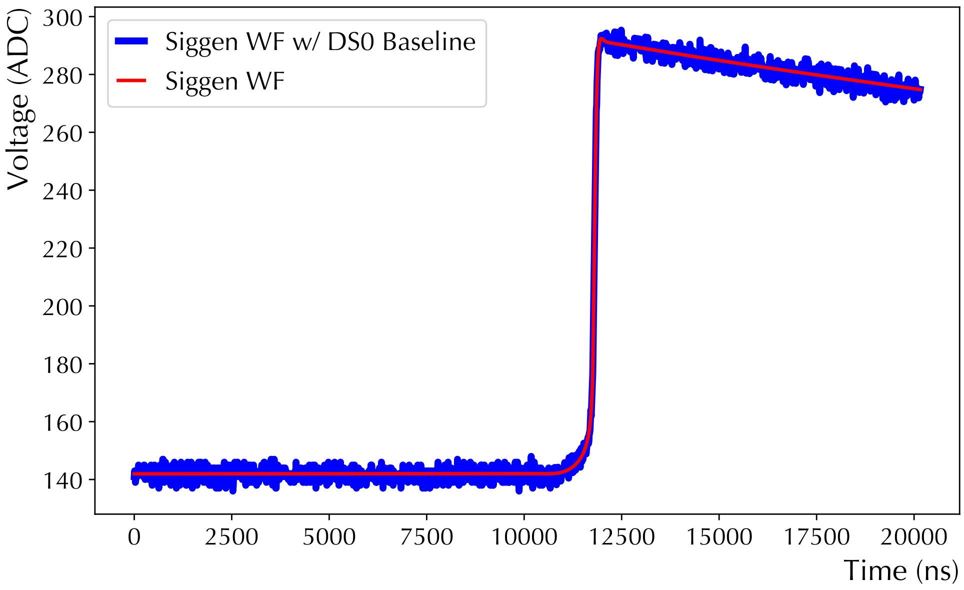

Figure 4.17: A waveform simulated by the `siggen` software, and convolved with DS0 baseline noise.

From the external pulser data in Figure 4.7, it is apparent that even under ideal conditions, there is a broadening of the fast event distribution at low energies. This is due to the worsening S/N ratio, and poses a problem for all proposed slowness parameters. As the fast event distribution spreads out, it is more likely that a slow event will pass a cut and contaminate the final spectrum. To examine the fast event acceptance more closely, a study was performed which compared external pulser data from C1P6D3 with events from its `m2s238` population, and simulated waveforms. The simulated waveforms were generated by the `siggen` software package with a (preliminary) realistic electronics model for C1P6D3. Waveforms from three positions in the detector were generated, convolved with typical Data Set 0 baseline noise, and fit with an xGauss function with the same algorithm used by LAT. The conversion from ADC to keV was done with the calibration constant for this detector in the closest Data Set 0 run range to the external pulser runs. An example simulated waveform is shown in Figure 4.17.

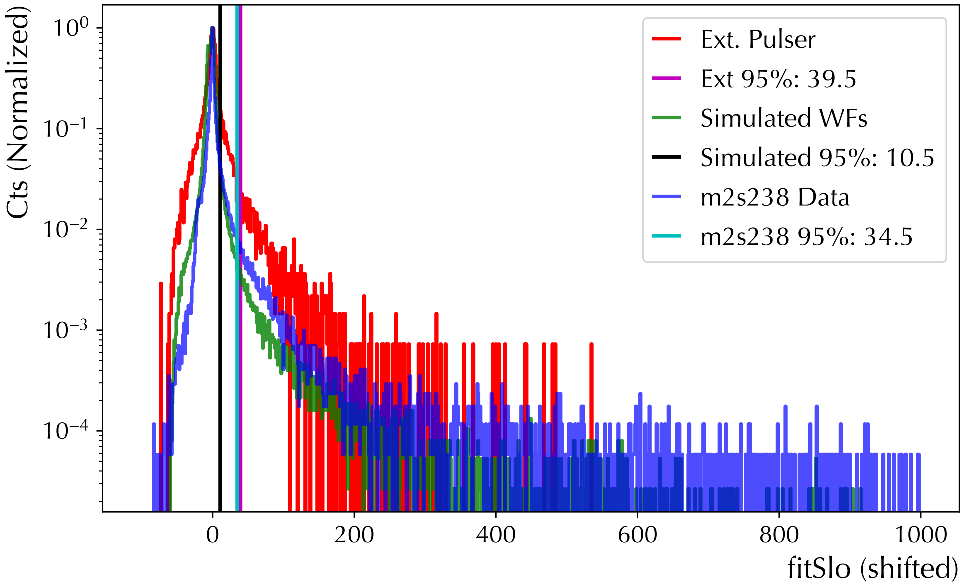

Figure 4.18: `fitSlo` distributions for external pulser, simulated waveforms, and m2s238 data, showing 95% cut values.

The fast acceptance study illustrates the broadening of the fast event distribution in each population. This motivates the choice of slowness cut used by LAT and gives a first example of determining the fast signal acceptance efficiency. The `fitSlo` distributions are shown for each population in Figure 4.18. They are shifted to zero using the same method described above, though the external pulser and simulated data only reach 50 keV. From each distribution, the 95th percentile value of `fitSlo` is found; only 5% of the events have larger values. The choice of 95% is not entirely arbitrary. In the earlier discussion of the `m2s238` sum energy peak, an upper bound on the number of slow events was estimated at 3.7%. The exact shape of the slow event distribution is difficult to predict without accurate simulation, and is expected to broaden and increase at low energy. By removing events with slowness larger than 95%, we stay with a conservative cut value until a sufficiently detailed simulation (or additional study) motivates a change.

Figure 4.19 highlights two important features of the fast event distribution as it spreads out at lower energies. For each slice (plotted in blue) the 95% value is marked

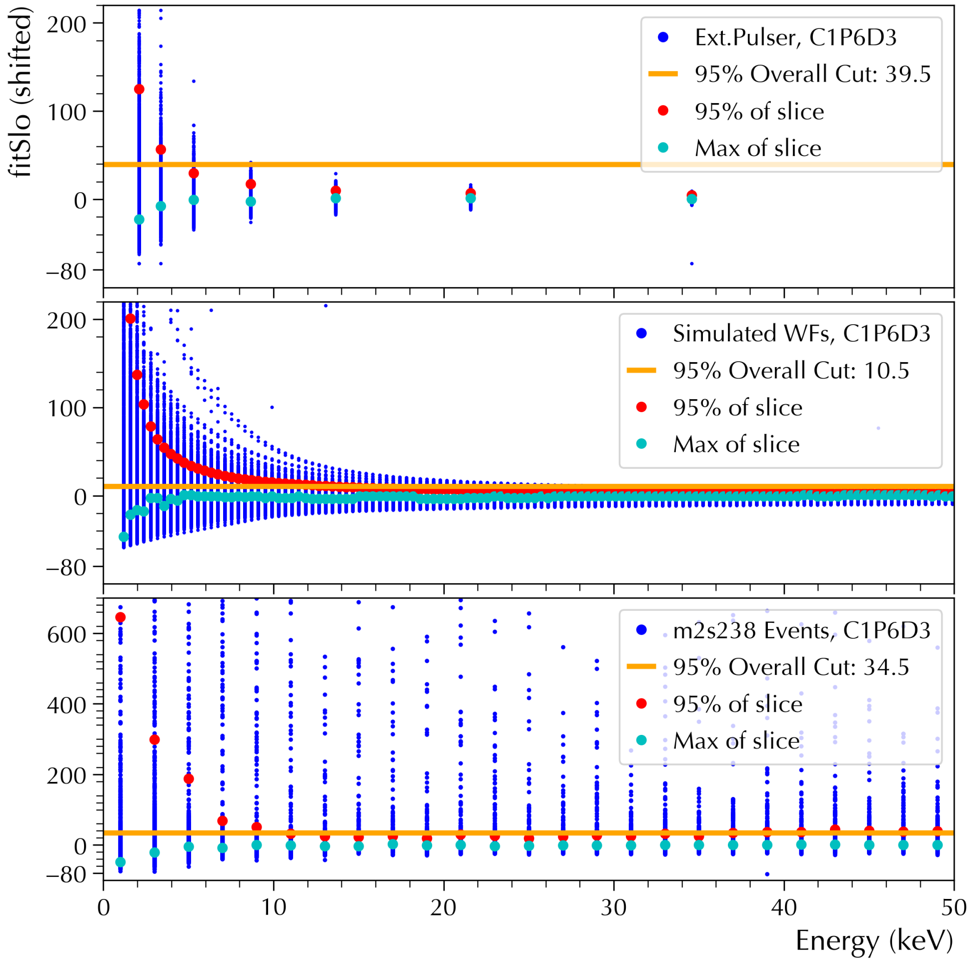

Figure 4.19: `fitSlo` vs. energy for external pulser (top), simulated waveforms (middle), and `m2s238` data (bottom), illustrating the upward drift in the 95% value as a function of energy.

in red. These values tend to the 95% line at higher energy, and grow to larger values at lower energies. The upward drift in the simulated waveforms matches the external pulser data reasonably well. The lowest-energy external pulser (∼1.1 keV) has a shifted `fitSlo` 95% value of 50, as do the simulated waveforms. This correspondence may be affected by the way the noise is added to the simulated waveforms. The `m2s238` data, which contains both real noise and rise time distributions, and a slow pulse contamination, drifts the most.

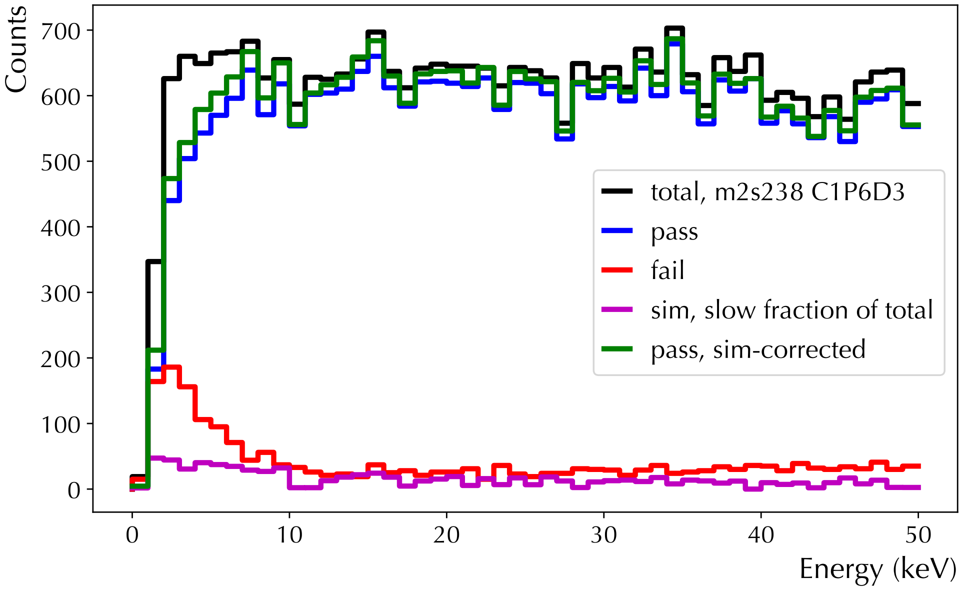

Figure 4.20: `m2s238` hits from C1P6D3 passing/failing the 95% cut, plotted along with the simulated slow pulse contribution.

The modes (or maximum values) of the slices are also shown in Figure 4.19. They illustrate that the most probable value tends to lower `fitSlo` values at lower energies. By rejecting events with energies above the 95% line, more events will be rejected at lower energies (since the distribution widens), but the maximum of the distribution will not be cut. The fast signal acceptance can therefore be determined by finding the number of events passing and failing a flat 95% cut at each bin energy. Figure 4.20 shows the `m2s238` hits passing and failing a 95% cut, as well as a comparison to the preliminary simulation.

Since there is no analytic expectation for the shape of the slow pulse distribution or the widening of the fast pulse distribution, the efficiency curve is fit to a heuristic function, the CDF of a Weibull distribution [137]:

$$W_{\mathrm{CDF}}(E, c, \mu, \tau, A) = A\ (1 - \exp(-((E - \mu)/\tau)^c)) \tag{4.10}$$

Here, c is an asymmetry parameter, μ and τ scale and shift the distribution. To fit all detectors in Module 1 and Module 2, a set of constraints were used. The maximum

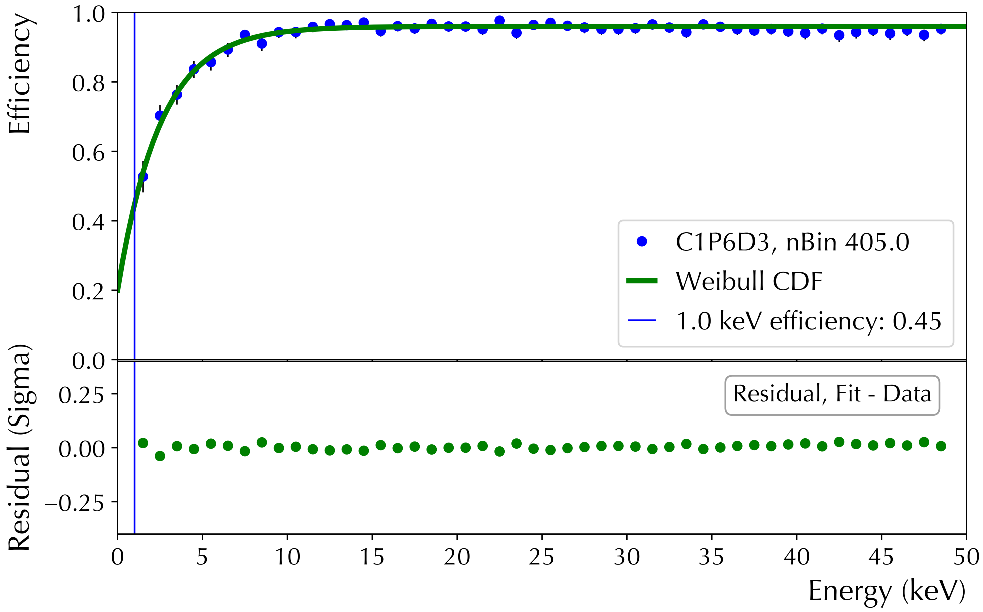

Figure 4.21: The 95% fast signal acceptance efficiency for C1P6D3, determined by the `m2s238` data. `nBin` is the average number of counts passing the cut in each bin under 10 keV.

energy of the fit was 30 keV. Lower limits were specified for c (1), μ (-20), τ (0), and A (0). An upper limit on A was set at 0.99. For detectors with sufficient statistics, the fit converges to 95% at energies above 20 keV, matching the expectation of the 95% `fitSlo` cut. The Weibull fit leaves smaller residuals than an error function or xGauss distribution, and generally describes the asymmetric acceptance curve to within 1% when the detector has good statistics. Error bounds are computed using confidence intervals for a binomial population [138]. The Clopper-Pearson method is used, which allows asymmetric upper and lower error bars, and does not allow them to exceed 0 or 1. Figure 4.21 shows the fast acceptance efficiency of C1P6D3 using this method. The residual between the fit and the data points is given in terms of the deviation σ (using each upper or lower error bar). It can be seen that the heuristic Weibull function is in agreement over the entire energy range to much less than 1 σ for a high-statistics detector.

The uncertainty in the efficiency as a function of energy becomes more significant when fewer events are available, and results in larger error bars. Effectively, the Weibull fit is attempting to match the top half of a CDF function without information on the bottom half. As a result, the uncertainties in the fit parameters can be very large, despite the apparent closeness of the fit. In addition, the error in each bin is not constant, since fewer events are found in lower-energy bins. To quantify the uncertainty in the fit, it was decided for this analysis to fit two additional Weibull functions to the points at the upper and lower error bar for each detector. These "upper" and "lower" efficiency curves form an envelope for each detector, with an example given by Figure 4.22. They can be combined with the exposures of each Data Set to form an upper and lower limit on the overall efficiency correction to the spectrum. This is discussed in Section 4.9.

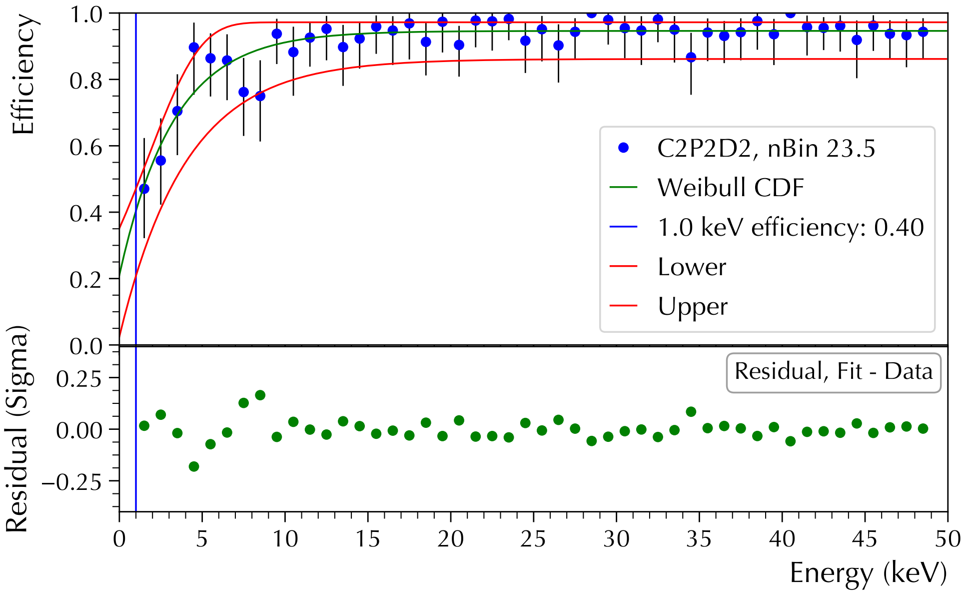

Figure 4.22: Uncertainty in `fitSlo` efficiency for C2P2D2, showing the upper and lower envelope in red.

In the current analysis, several detectors do not have enough statistics under 10 keV for their acceptance to be reliably determined. This is partly due to their location relative to the calibration track; detectors in position 1 (top) and position

4 (bottom) are disfavored to get a low energy Compton scatter. To determine if a detector has enough hits, the average number of counts in 1 keV bins between 0 and 10 keV was computed. As an absolute minimum, we require that the average number of counts in each bin be larger than 4; statistical error must not exceed 50% of the actual value. This results in the exclusion of only five detectors, all in Module 2, driven by insufficient statistics. This could be remedied in a future analysis by including all calibration runs from Data Set 6. Table 4.3 summarizes the fit results for every detector Modules 1 and 2, giving the uncertainties in the fit parameters, the average counts in 1 keV bins under 10 keV, and their inclusion or exclusion in the DS0–5 LAT analysis. Figure 4.23 compares the difference between a high-statistics and low-statistics detector.

To apply the `fitSlo` cut to every detector in each background subset, cut values from each combined `m2s238` distribution are saved into the LAT `calDB`, along with the value of the 10–200 mode in that subset. The cut then rejects all events with values larger than the 95% cut value plus the 10–200 mode of each detector in each background subset. The final 95% `fitSlo` efficiencies can be weighted by each detector's exposure in the same manner as the trigger efficiency in Section 4.4. An example is shown for Data Set 3 in Figure 4.24.

One final correction to the efficiency has been investigated but not implemented in the current analysis. If an `m2s238` simulation including transition layers for each detector is trustworthy, the fast acceptance could in principle be corrected for the slow pulse contamination. The slow pulse distribution rises at low energy, as shown in Figure 4.20. Since the contamination exists, the 95% cut value used is *higher* than it would be if there were no slow pulses. This implies that the fast event acceptance is slightly higher than 95%, by a fraction proportional to the slow pulse contamination. In the current analysis, we treat this as a systematic error on the fast signal acceptance. We take the error to be 3.7% based on the background under

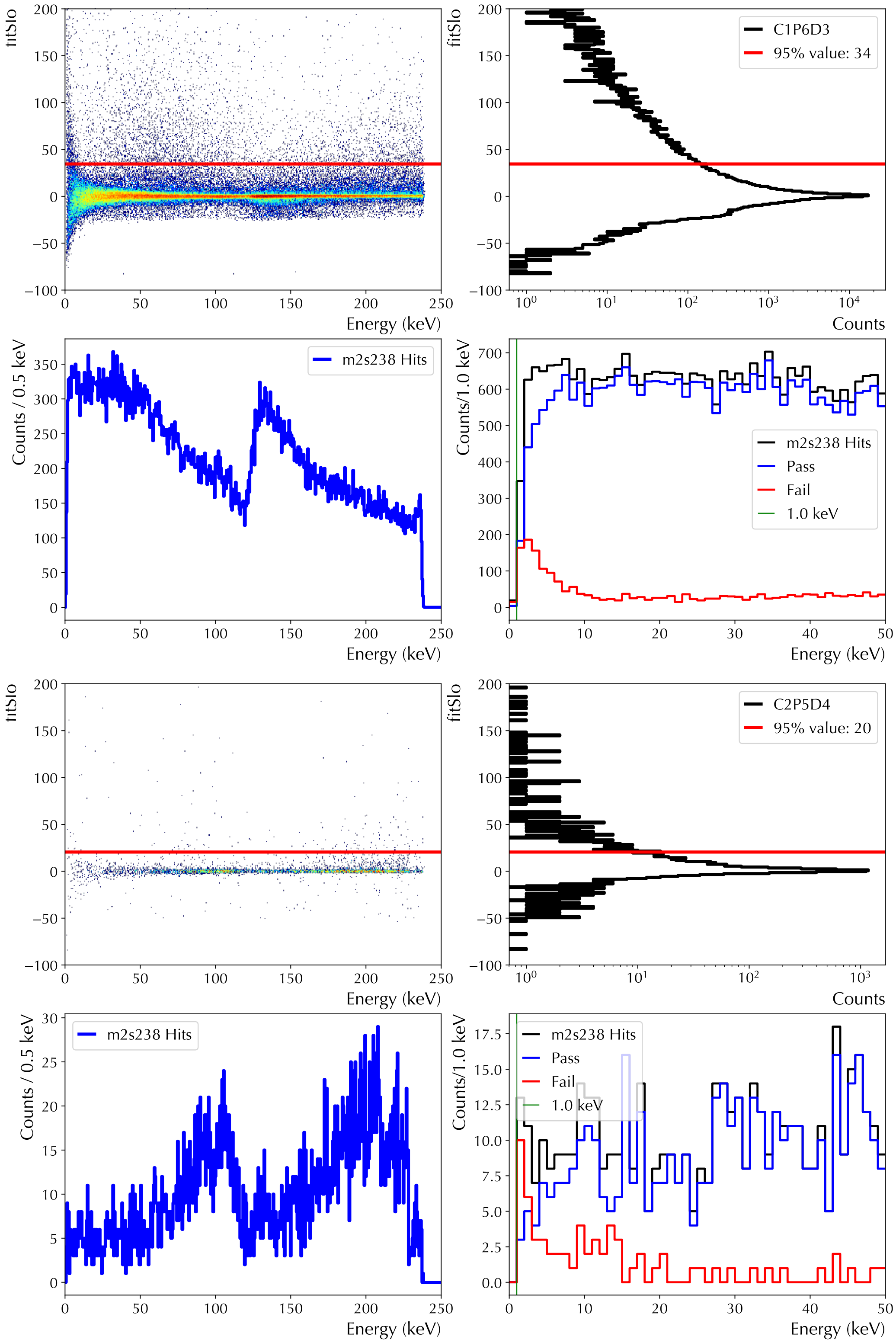

Figure 4.23: Top 4: C1P6D3, with a large population of `m2s238` events. Bottom 4: C2P5D4, with the least number of hits under 10 keV allowed in the current analysis.

Table 4.3: 95% acceptance efficiency results for each detector. (Detectors with no data in any Data Set are omitted). Detectors excluded from the analysis due to their `fitSlo` statistics are marked in Column 2.

CPD	Exc?	A	c	μ (keV)	τ (keV)	Acc.@ 1 keV	cts/bin, 0–10 keV	Max. Fit Residual(σ)
111		0.953	1.0	-5.61	8.11	0.53	7	0.299
112		0.946	1.6	-3.89	5.91	0.50	122	0.043
113		0.956	1.2	-2.91	5.16	0.49	136	0.030
114		0.894	1.0	-1.06	4.27	0.34	56	0.202
121		0.906	1.0	-3.97	9.47	0.37	10	0.446
122		0.969	7.3	-20.00	20.82	0.64	279	0.040
123		0.951	1.1	-1.13	2.60	0.53	309	0.027
132		0.959	1.0	-0.15	2.06	0.41	179	0.032
133		0.963	2.5	-6.50	8.02	0.55	229	0.040
134		0.932	1.0	-1.05	4.75	0.33	43	0.116
141		0.990	1.0	-6.70	14.04	0.41	16	0.314
142		0.952	1.5	-3.01	5.62	0.43	136	0.041
143		0.962	3.7	-20.00	21.37	0.59	197	0.046
144		0.964	4.2	-19.40	21.56	0.53	181	0.040
145		0.904	1.4	-0.07	5.37	0.09	15	0.164
151		0.923	1.0	-0.29	3.76	0.27	21	0.187
152		0.969	1.3	-0.55	2.53	0.40	204	0.041
153		0.957	1.0	-1.19	2.58	0.55	375	0.032
154		0.932	1.0	-0.38	2.42	0.40	23	0.122
161		0.951	1.2	-3.74	5.86	0.52	24	0.196
162		0.962	1.7	-3.71	5.48	0.52	146	0.054
163		0.960	1.0	-0.59	2.53	0.45	405	0.039
164		0.912	1.0	0.40	2.59	0.19	43	0.087
171		0.913	1.0	0.27	4.67	0.13	26	0.611
172		0.965	1.5	-3.20	4.82	0.53	327	0.049
173		0.963	1.1	-1.95	3.79	0.51	372	0.033
174		0.936	3.3	-20.00	20.33	0.63	72	0.071
211	**X**	0.908	1.1	-0.03	5.64	0.12	**3**	**0.503**
214	**X**	0.920	4.5	-20.00	27.73	0.23	**2**	**1.646**
221	**X**	0.990	1.2	-0.90	10.66	0.11	**2**	**0.761**
222		0.946	1.0	-0.82	3.27	0.40	23	0.181
223		0.959	1.0	-0.78	3.66	0.37	21	0.126
231		0.951	5.6	-20.00	21.12	0.59	57	0.053
232		0.956	1.0	-0.84	2.29	0.53	37	0.063
241		0.885	1.2	-3.32	6.43	0.41	9	0.233
242		0.962	5.1	-20.00	22.70	0.47	39	0.227
244		0.941	1.0	-0.49	3.16	0.35	21	0.195
251		0.922	1.0	0.78	3.29	0.06	7	0.275
253		0.952	1.0	0.58	0.87	0.36	19	0.106
254		0.895	1.0	-0.11	3.86	0.22	4	0.376
261	**X**	0.903	2.4	1.30	0.28	0.00	**2**	**1.949**
262		0.968	1.1	-0.95	4.10	0.34	15	0.148
273		0.952	1.0	-3.03	3.28	0.67	23	0.094
274	**X**	0.883	1.0	0.11	3.72	0.19	**1**	**7.772**

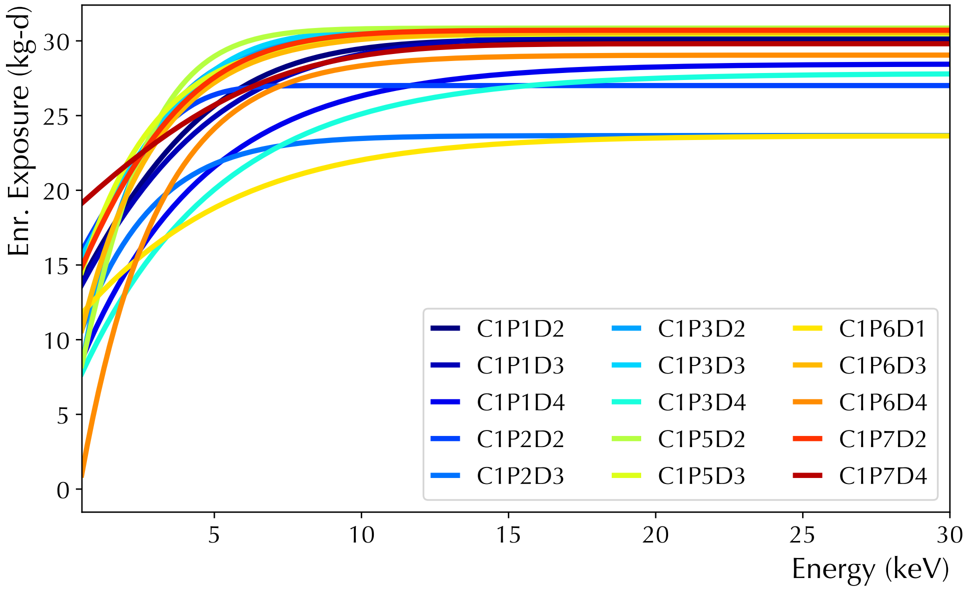

Figure 4.24: 95% fast acceptance efficiency for each detector in Data Set 3, scaled by exposure, without including trigger efficiency corrections.

the 238 keV sum energy peak, which could be reduced with a detailed simulation. However, if the correction from simulation were known as a function of energy for every detector, a correction like the one in Figure 4.25 could be applied.

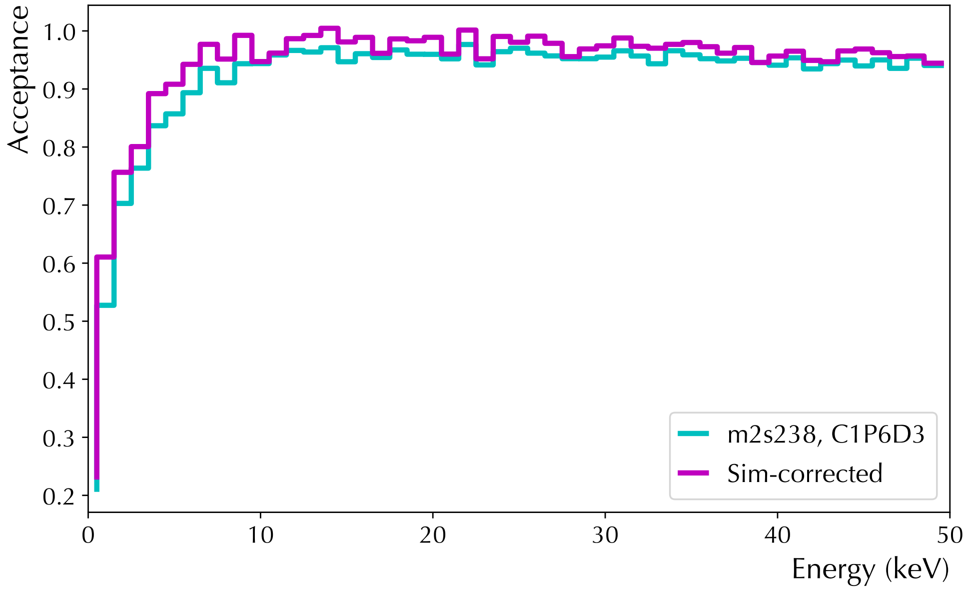

Figure 4.25: Fast event acceptance for C1P6D3 with a simulated slow pulse correction. The resulting efficiency is slightly increased overall.

4.6 HF Noise Removal

The high-frequency parameter `riseNoise` described in Chapter 3 is sensitive to noise in a time window around the rising edge of a waveform. Its purpose is to distinguish between electronics noise and physics, without making a distinction between slow, fast, or multi-site physics events. To illustrate its effect on background data, Figure 4.26 shows a flat `riseNoise` cut applied to Data Set 1, after thresholds have been applied (but before a `fitSlo` cut). A clear HF population is removed.

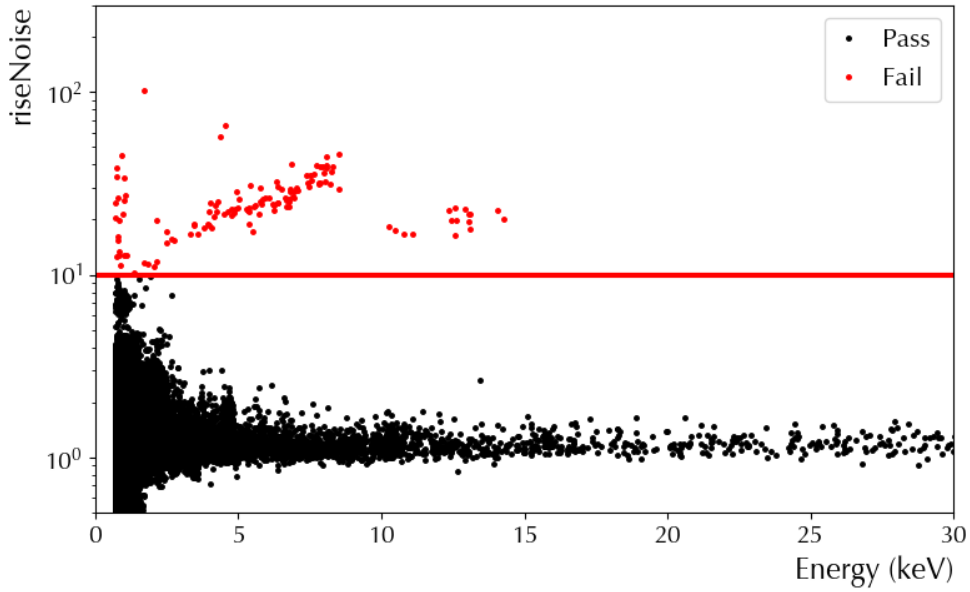

Figure 4.26: A simple flat `riseNoise` cut applied to Data Set 1 after threshold cuts are applied. There is a clear HF population that is removed above 2 keV.

The noise conditions in the Demonstrator change frequently. To set a robust high-frequency noise removal cut, we require a population of physics events relatively uncontaminated by HF noise, which we find in the calibration data. The ^{228}Th data at every new calibration is used to calculate typical physics values of the `riseNoise` parameter for every detector. Since only a threshold cut is needed to remove Gaussian noise, there is a very large available population of events for every detector in each calibration set.

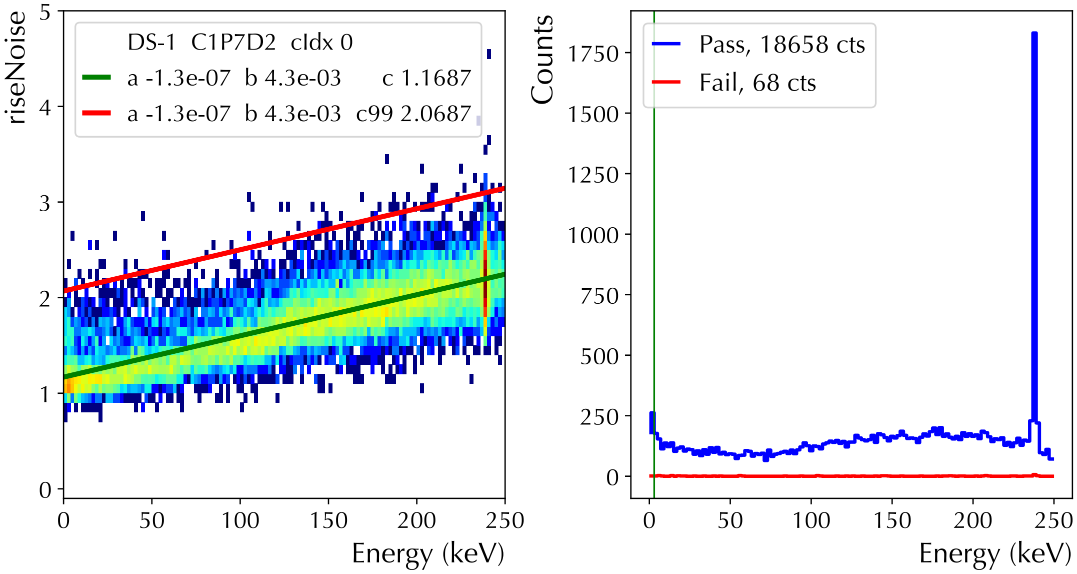

Figure 4.27: Typical 99.5% `riseNoise` cut (in red). From 0–250 keV, the typical value increases linearly with energy.

The values of the wavelet packet coefficients tend to rise linearly with energy. This causes the typical value of `riseNoise` to increase linearly as well, as shown in Figure 4.27. Each detector's distribution is then fit to a second-order polynomial, $aE^2 + bE + c$, and the linear offset term c is shifted upward to larger values until 99.5% of the events are retained. The `riseNoise` cut is therefore tuned to retain 99.5% of all events above the detector threshold, at energies 0–250 keV. The results are stored in the LAT `calDB` and applied to the corresponding background data.

The large number of hits in the 238 keV peak tends to pin a linear fit at high energy, while any excess of low energy events not removed by the threshold cut can affect the low end. The curvature term a is typically very small, unless an unwanted noise population exists in the data for a certain detector. From the saved fit coefficients in the `calDB`, outliers in calibration data can be detected.

The outlier constraints are given in terms of percent deviation from the mean value of each parameter in all Data Sets, $a = [-500, 2000], b = [0, 200], c = [50, 200]$. Figure 4.28 shows the deviation (in percentage) for the fit coefficients of each detector, over the calibration subsets in Data Set 0 (Module 1) and Data Set 5 (A+B, Module 2). Any detector with any of its three coefficients outside the outlier range is flagged as a potentially noisy run and its `riseNoise` distribution is saved for manual inspection. For example, in Data Sets 1 and 3, an intermittent population of HF noise was found in detector C1P7D3, which causes excessive curvature in the fit. The detector is then rejected for all background subsets where this population is present in the calibration. Figure 4.29 shows this anomalous `riseNoise` distribution and the incorrect fit. Another cause for rejection is an excess of low-energy triggers caused by HF noise. They can cause excess curvature in the fit and is shown in Figure 4.30. This is observed most prominently in Data Set 5A, which is known to have HF noise originating from electronics ground loops. A summary of detectors with noise issues in calibration runs causing the `riseNoise` fit to fail is given in Table 4.4. The corresponding background data are removed for these detectors. The reduction in exposure is given in Section 4.9.

4.7 BURST CUT

Following the application of the LAT PSA cuts, some noise populations persist for certain detectors in specific periods. To quantify these bursts, the low energy count rate of each detector in every background subset is measured by LAT. The resulting rates for each `CPD/bkgIdx` pair are the number of counts between 0–5 keV, scaled by the detector exposure calculated by `ds_livetime`, in units of cts/keV-kg-d. Rather than removing noisy detector `CPD/bkgIdx` pairs by hand, a more robust method to detect anomalous rates was implemented. It employs the “Tukey fence,” a common method to detect outliers in a data set which contains extreme values [139]. If we take a list of N measurements (detector rates):

$$\lambda = \{r_1, r_2, \ldots, r_N\} \tag{4.11}$$

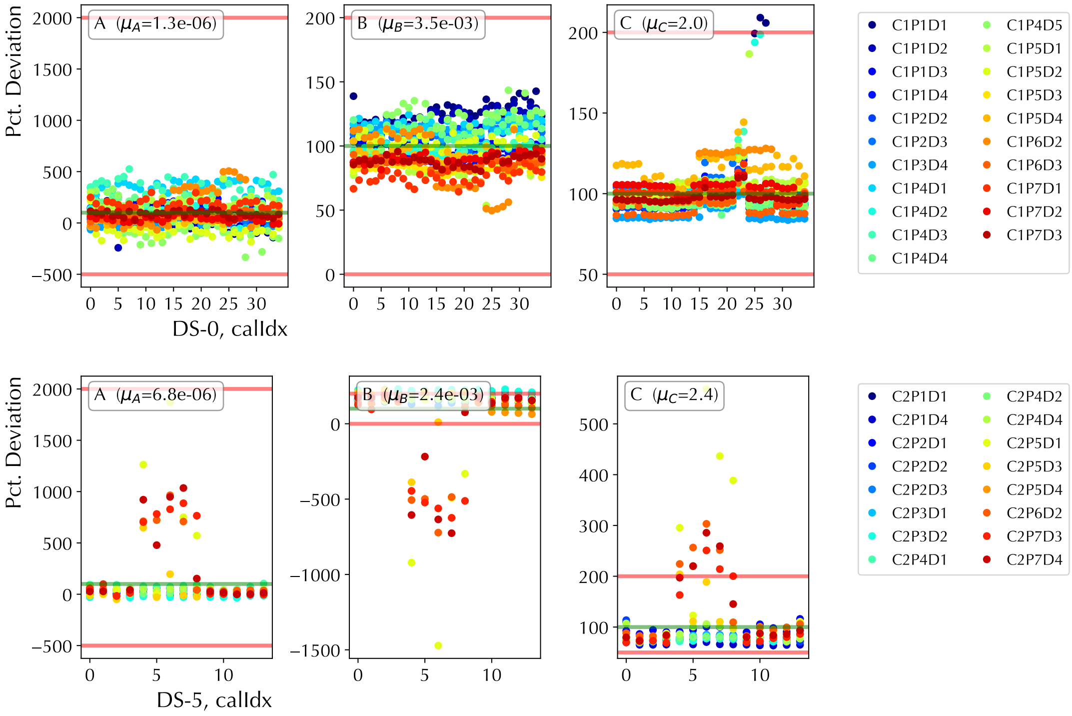

Figure 4.28: Stability of the `riseNoise` fit coefficients. Upper: Data Set 0 (35 sets), Lower: Data Sets 5A and 5B, Module 2 (14 sets).

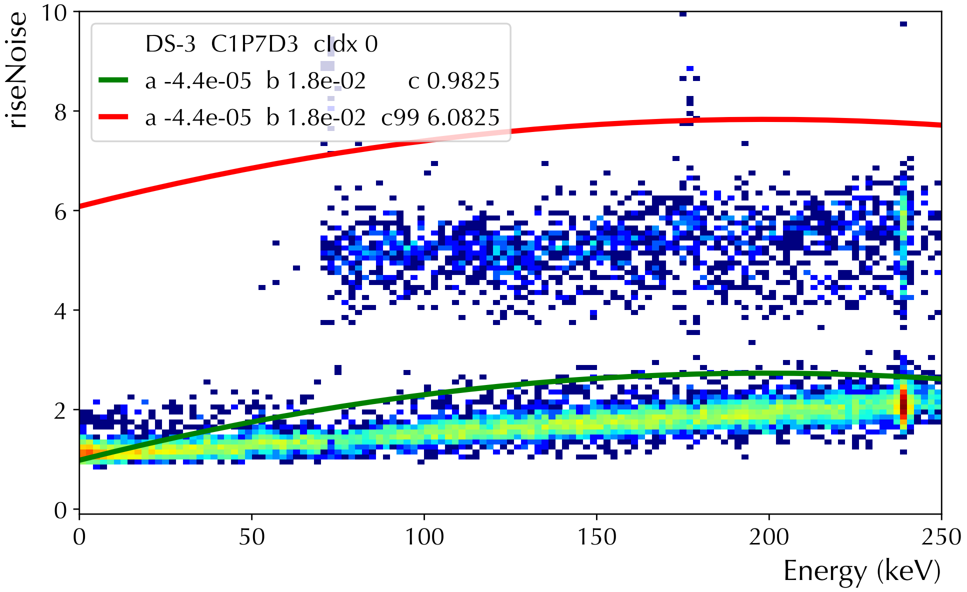

Figure 4.29: An anomalous HF noise population is observed in a C1P7D3 calibration, causing the detector's corresponding background data to be rejected.

Table 4.4: Calibration subsets observed to have anomalous noise in certain detectors, causing their corresponding background data to be rejected.

DS	n_{cal}	CPD	`calIdx`	Notes
DS0, M1	35			
DS1, M1	57	173	29–56	Anomalous HF (Fig. 4.29)
		121	56	Threshold noise (Fig. 4.30)
DS2, M1	11			
DS3, M1	9	173	0–9	Anomalous HF
DS4, M2	11	222	7	High energy threshold
		223	1,4,7,8	HF burst
		244	4,7,8	”
		261	4,7,8	”
		262	4	”
DS5, M1	24	112	8	Threshold noise
		121	7,8	”
		133	7,8	”
		134	7	”
		161	7	”
DS5, M2	21	251	4,6,7,8	”
		253	4	”
		262	4,5,6,7	”
		273	4,5,6,7,8	”
		274	4,5,6,7	”

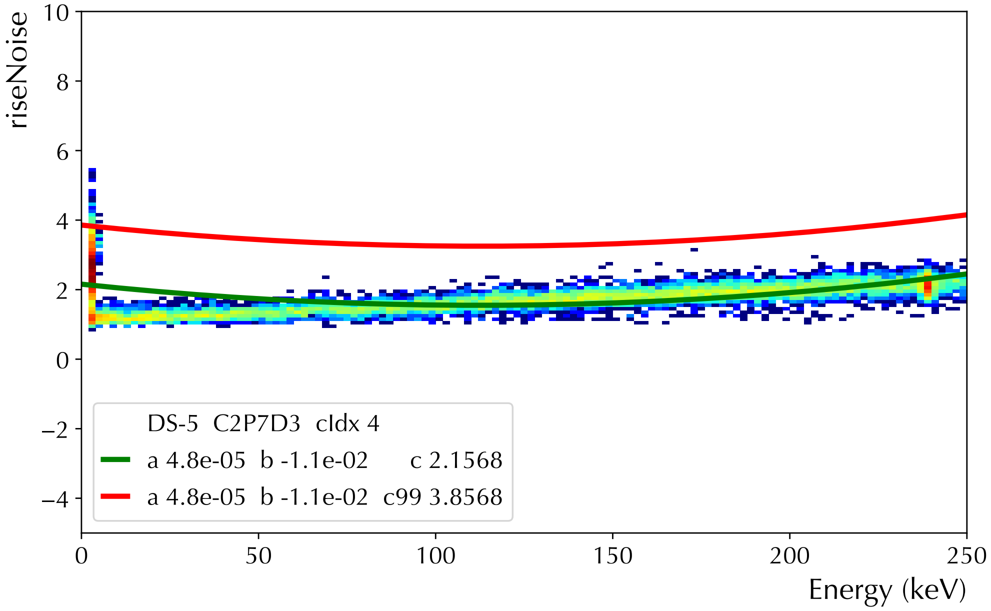

Figure 4.30: Low-energy noise with a strong HF component. This is symptomatic of the ground loop problems in Data Set 5A.

The lower (25%) and upper (75%) quartiles Q_1 and Q_3 can be used to define the *interquartile range*:

$$IQR \equiv Q_3 - Q_1 \tag{4.12}$$

If a given data point lies outside the range defined by the "fence" k,

$$[Q_1 - k(Q_3 - Q_1), Q_3 + k(Q_3 - Q_1)] \tag{4.13}$$

it is declared an outlier. The traditional choice of "Tukey fence" is $k = 1.5$. If the rates are Gaussian-distributed, this choice can be interpreted by noting that Q_3 is positioned at 0.675σ, the width of the IQR is 1.35σ, and the upper value of the fence is then 2.7σ. This choice of fence would declare 0.7% of the measurements to be outliers.

Since the enriched and natural detectors are expected to have different rates at low energies due to their differing cosmogenic activation, for each Data Set, two separate sets of 0–5 keV rates λ_{enr} and λ_{nat} are created. By combining all enriched detectors together (and separately, all natural detectors), the majority of `CPD/bkgIdx` rates r_i will be "average" to begin with, since bursts tend to be isolated to a small subset of detectors. Since extreme outliers can affect the IQR width, a two-step process of "closing the fence" is employed. The enriched and natural rates are first scanned for extreme outliers with $k = 5$. These outliers are logged for removal, and the scan is repeated a second time with $k = 2$. The fence $k = 2$ is somewhat arbitrary, but for Gaussian-distributed rates it would allow rates to fluctuate by more than 3σ.

Due to the low overall background rates in the Demonstrator, a detector seeing no physics counts in a given background index is quite likely. This makes the application of the *lower bound* of the Tukey fence unnecessary. In addition, if too large a number of the rates r_i are zero, it can make the median zero, and reduce the width of the IQR. To avoid this problem, the outlier detection algorithm considers only nonzero rates r_i. The reduction in the spectrum after the application of PSA cuts is dramatic. The largest reduction comes from a single detector in Data Set 0, C1P5D3. The set of background ranges $[21-25, 29-36, 39-43, 45, 52-54, 56, 68, 69, 71]]$ constitute the majority of the noise events and are removed. Figure 4.31 shows the rates for all Data Sets before and after the application of the burst cut, and Table 4.5 gives the corresponding exposure-weighted 0–5 keV rates. Figure 4.32 gives the combined enriched and natural spectra for DS0–5C after PSA cuts, before and after the burst cut.

Table 4.5: Average rates (cts/keV/kg/d) for enriched and natural detectors after the application of the burst cut. Errors are given in terms of the standard deviation.

DS	n_{enr}/n_{tot}	$r_{enr,0-5}$	$r_{enr,5-20}$	n_{nat}/n_{tot}	$r_{nat,0-5}$	$r_{nat,5-20}$
DS0	878/933	0.38 ± 0.56	0.07 ± 0.12	499/506	1.35 ± 1.04	1.06 ± 0.57
DS1	721/731	0.13 ± 0.18	0.04 ± 0.06	50/50	1.32 ± 0.71	0.96 ± 0.39
DS2	110/111	0.11 ± 0.15	0.05 ± 0.06	8/8	2.17 ± 0.52	0.94 ± 0.15
DS3	354/362	0.08 ± 0.13	0.03 ± 0.05	74/77	1.21 ± 0.63	0.74 ± 0.28
DS4	89/89	0.14 ± 0.22	0.06 ± 0.09	46/46	0.91 ± 0.81	0.77 ± 0.51
DS5A	1083/1099	0.08 ± 0.15	0.04 ± 0.13	631/639	0.82 ± 0.72	0.59 ± 0.38
DS5B	679/687	0.10 ± 0.15	0.03 ± 0.05	337/342	0.97 ± 0.71	0.57 ± 0.33
DS5C	179/180	0.14 ± 0.21	0.03 ± 0.05	91/95	0.79 ± 0.52	0.56 ± 0.30

4.8 TIME OFFSET CUT

Following the application of the PSA and burst cuts to the DS0–5 data, an additional noise population remained, contributing to the spectrum below 2 keV. A scan of the waveforms revealed the population to be composed entirely of pulser retrigger events. As described in Section 4.4, pulser retrigger events occur when the DAQ triggers on the overshoot of the negative-going component of the pulser square wave signal. The resulting waveform has a constant upward slope and a very small calculated energy, typically below 2 keV. An example is shown in Figure 4.33.

A large majority of the retrigger events were observed to have distinctively large `tOffset` values that allow them to be removed with negligible sacrifice of physics events. They are observed to occur in all Data Sets, as shown in Figure 4.34.

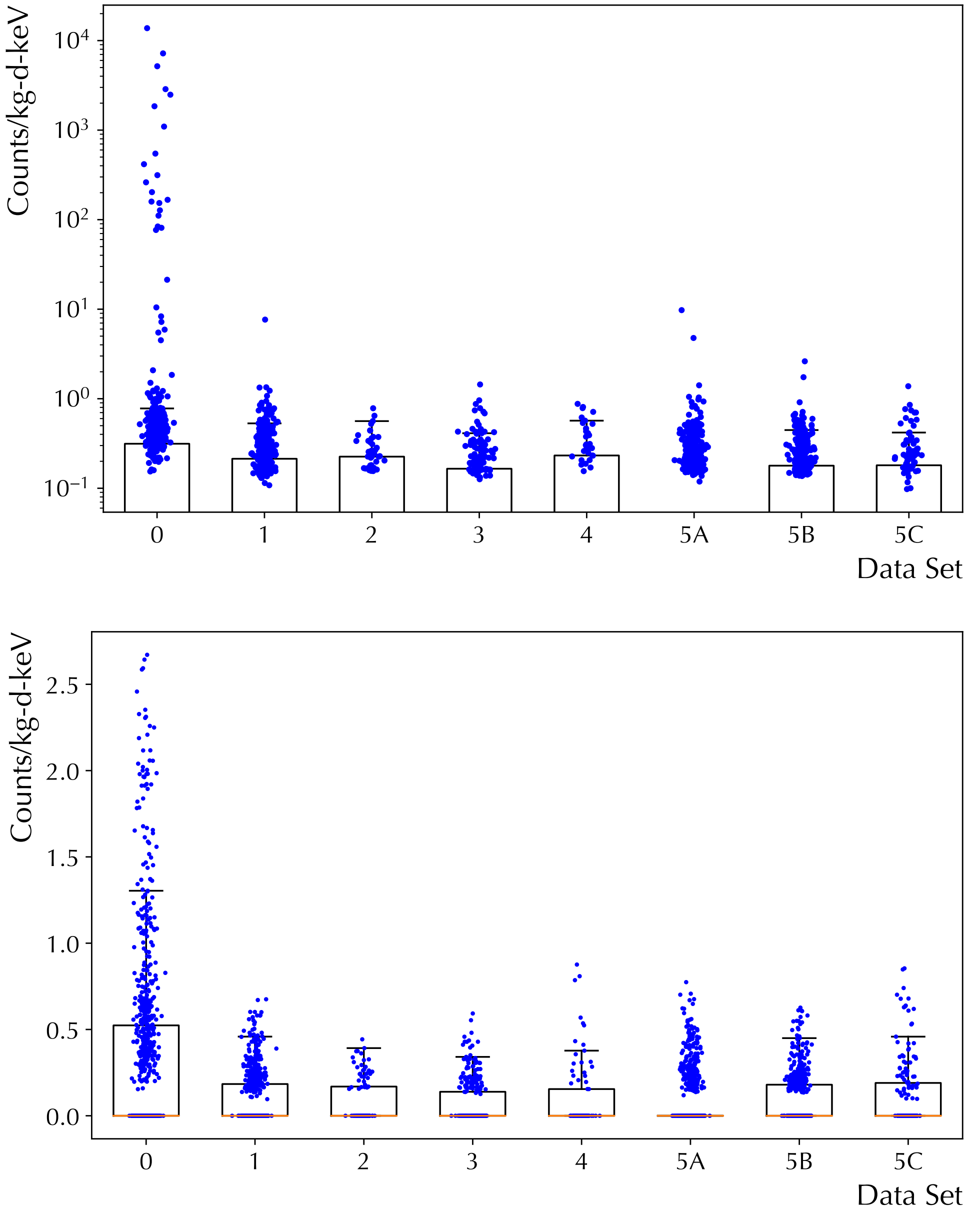

Figure 4.31: Top: DS0–5C rates before the burst cut. Bottom: after the burst cut. After the cut, the drop after DS0 is consistent with the installation of the inner UGEFCu shield.

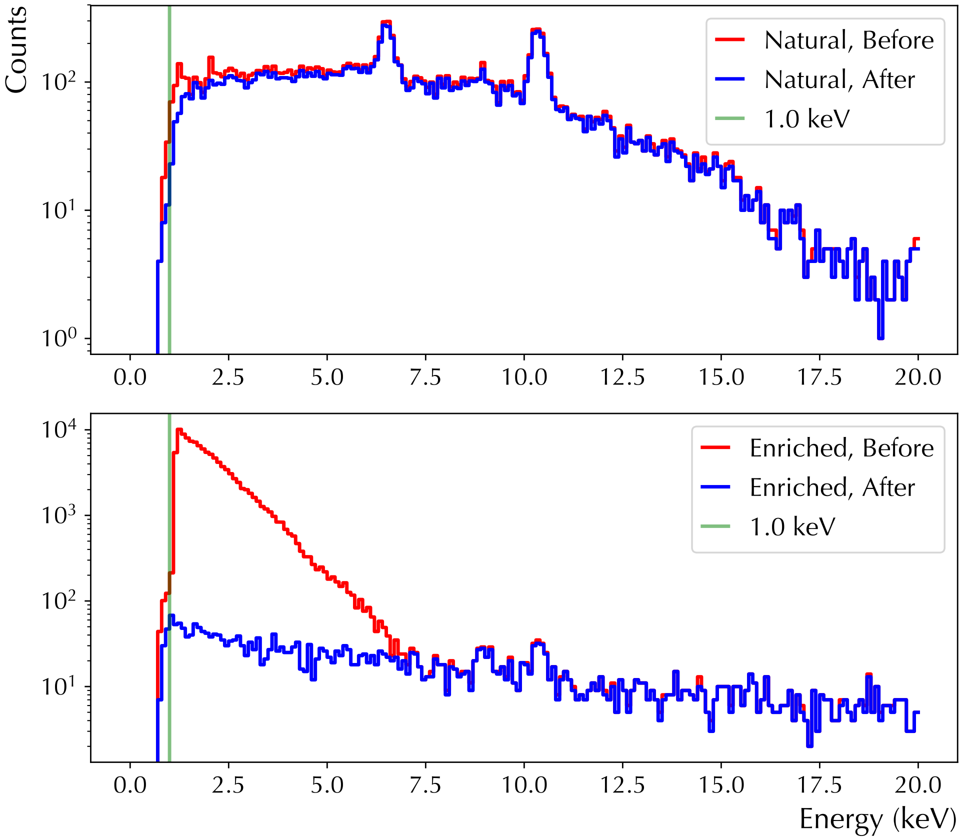

Figure 4.32: Spectra for enriched and natural detectors, DS0–5C, after PSA cuts, before and after application of the burst cut.

The parameter `tOffset` is determined by the MAJORANA event builder software, which groups individual detector hits into events, using a moving time window of 4 μs, as described in Section 4.5. Typically there is a time lag between high-gain and low-gain channels, and between different detectors. Most often, the LG event is given a larger `tOffset` value than its corresponding high-gain event. Figure 4.35 shows this for a Data Set 1 calibration run by plotting the difference between the high gain and low gain offsets, `tOffset_HG - tOffset_LG`. Even during calibration when the physics rate is high, the difference between `tOffset` values of a high gain and low gain trigger is never larger than 4 μs. This means than an event in background data with a `tOffset` larger than $\sim 4\mu$s is not explained by a delay between the high and low gain channels.

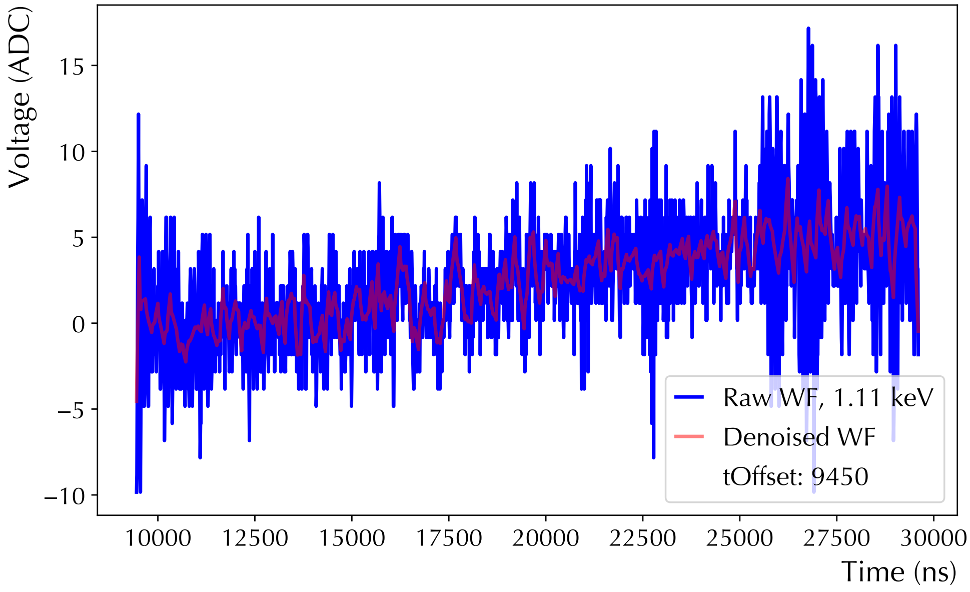

Figure 4.33: A retrigger waveform passing `riseNoise`, `fitSlo`, and burst cuts. There is a large offset (9.45 μs) between this waveform and the one causing the initial trigger of the array.

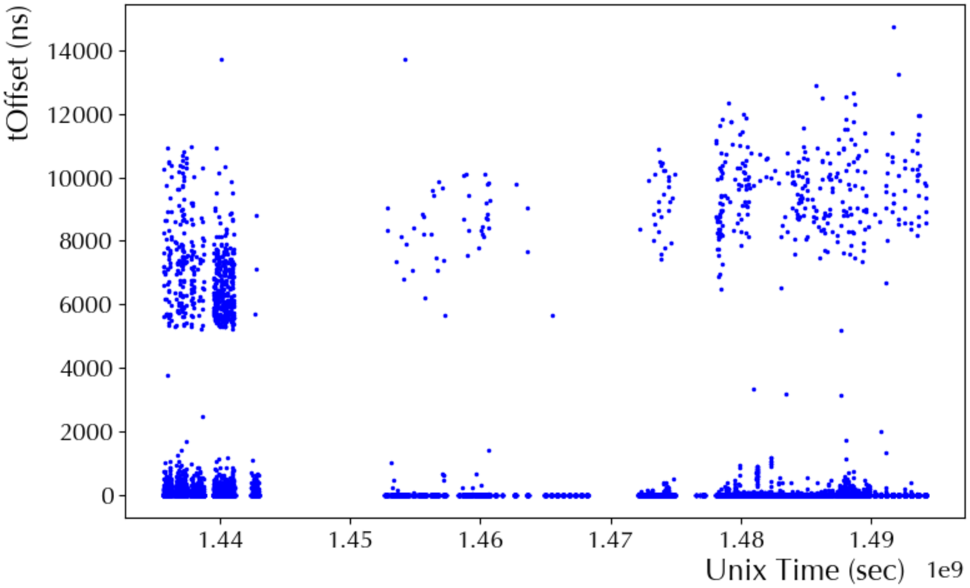

Figure 4.34: `tOffset` for all hits passing threshold, PSA, and burst cuts. A clear population of outliers is observed above `tOffset` > 4000.

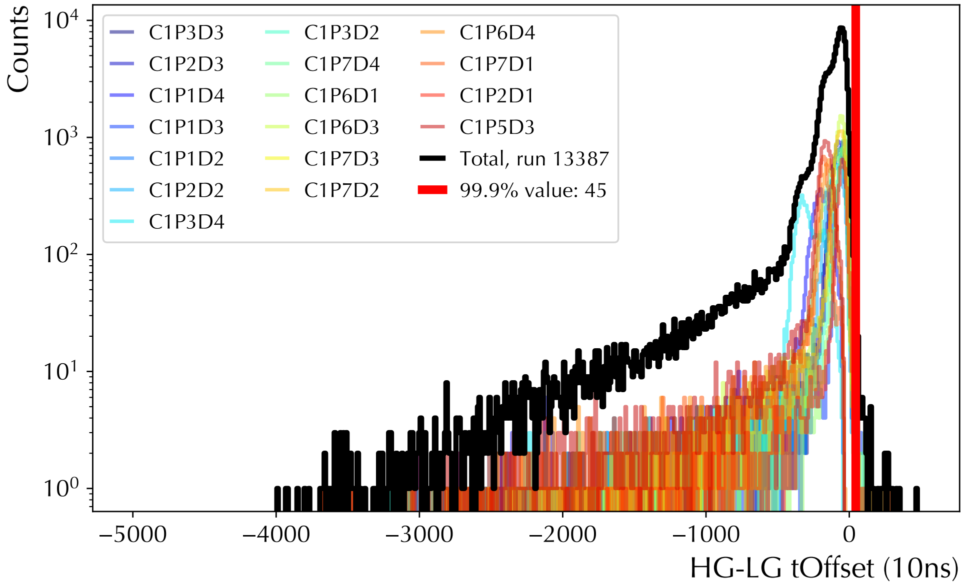

Figure 4.35: The difference `tOffset_HG - tOffset_LG` for events in a calibration run. The wide spread in negative values shows that high-gain channels nearly always trigger before low-gain channels (when both exist), and the difference is limited to less than 4 μs.

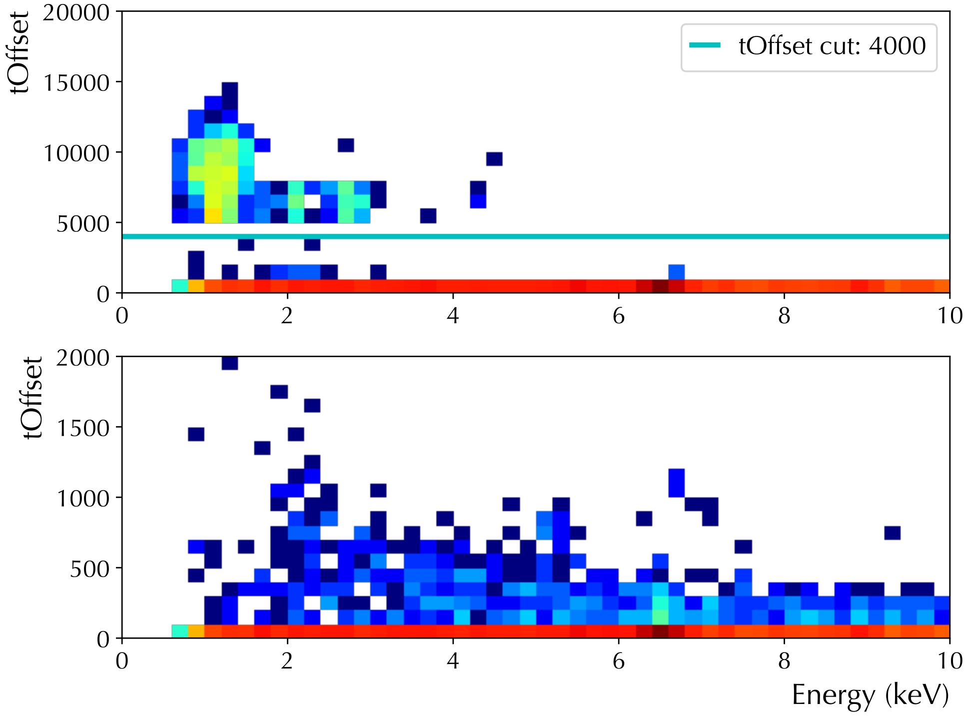

Figure 4.36: `tOffset` as a function of energy. The retrigger population is well separated from the physics distribution.

At low energies, it is more likely that either the high-gain or low-gain channel will not trigger the system readout, and only one channel will be observed. The basic data cleaning cut applied to the LAT data by `wave-skim` (Section 4.2) enforces a high-gain multiplicity cut `mH==1`, where the multiplicity `mH` is calculated by the skim file generator[5]. Hence, at low energies we may expect to see good high-gain physics events with nonzero `tOffset` values, without an accompanying low-gain hit.

If a hit triggers the system, the event builder will group any second hit into the event if it falls within 4 μs. The event time window is then extended 4 μs from the second hit. Hence, in order to observe a `tOffset` of 9.45 μs as in Figure 4.33, we would require at least two additional events in other detectors. This violates the implied single-detector requirement of the multiplicity cut. Since wave-skim applies the `mH==1` cut, these additional events must also occur without their accompanying high-gain events. Figure 4.34 shows the events with large `tOffset` as a function of time through DS0–5, and Figure 4.36 shows their distribution with energy.

By requiring `tOffset < 4000` in the final LAT spectrum, we impose a cut requiring that each event has a plausible chance of being the first one to trigger the system, in the initial event builder window. Figure 4.36 illustrates the final cut used.

4.9 Final Exposure and Efficiency

To conclude this Chapter, we summarize the results of the LAT analysis with final exposures, efficiencies, detector rates, and spectra. The effect of the data cleaning cuts on the intial spectrum, in the order they were applied, is illustrated in Figure 4.37. It is notable that the LAT analysis has reduced the counts in bins under 5 keV by as much as five orders of magnitude.

---

[5] The low-gain hits are discarded by `wave-skim` since their calibration at low energy is untrustworthy and would unnecessarily slow down the waveform fitting step.

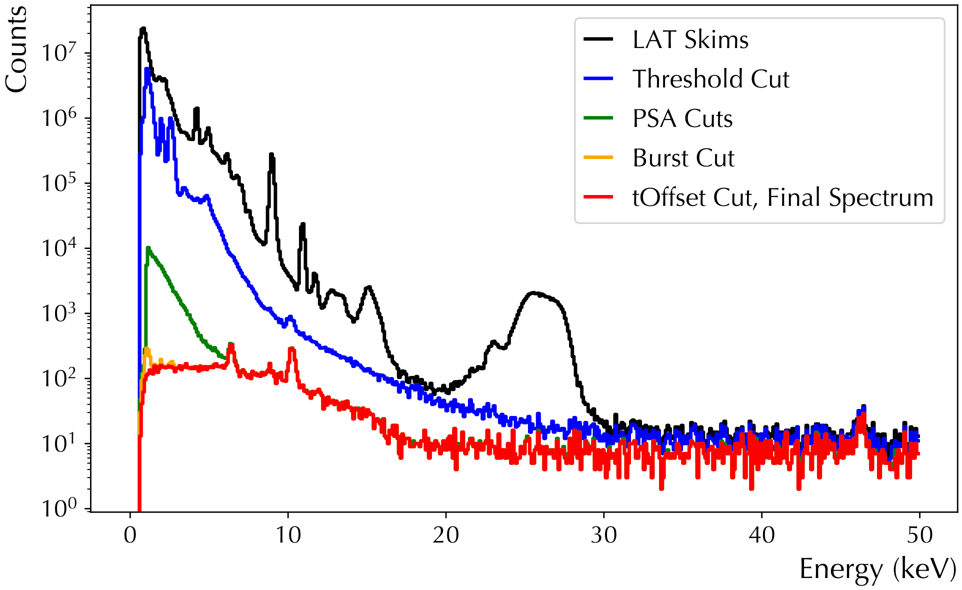

Figure 4.37: Hit spectrum for all enriched and natural detectors in DS0–5C, showing the reduction in spectrum after each cut is applied.

The enriched and natural livetime and exposures are calculated on a run-by-run basis using output from the GAT app `ds_livetime`, described in Chapter 2. Since the LAT analysis does not use low-gain channels, the deadtime is calculated from high-gain channels only. This results in very slightly lower ($< 1\%$) exposures than the $0\nu\beta\beta$ analysis. The uncertainties in the exposure of each Data Set depend on the separate uncertainties in livetime and the active detector mass. The total livetime uncertainty, which depends on uncertainties in the run start and stop times, hardware and pulser deadtime, and the muon and LN veto cuts, was found to be negligible compared to the active mass uncertainty [140]. The active mass uncertainties are on the order of 1% of the total mass of each detector.

To obtain the final exposure for the DS0–5C analysis, we take the livetime uncertainty to be negligible, and include only the active mass uncertainties in the exposure calculation. The LAT exposure calculator `lat-expo` takes into account all runs and channels removed by the PSA and burst cuts. The exposure of every channel in every background subset is calculated, and uncertainties are added *linearly*, as described in

Table 4.6: Final exposures (in kg-d unless marked otherwise) and uncertainties for each Data Set, showing the removal due to PSA and burst cuts. Top: Enriched, Bottom: Natural.

DS	No Cuts (kg-d)	PSA Cut	Burst Cut	**Final Enriched Exposure**
DS0	454.60 ± 6.87	28.24 ± 0.51	25.45 ± 0.39	400.91 ± 5.97
DS1	656.15 ± 9.61	18.18 ± 0.28	6.43 ± 0.09	631.54 ± 9.24
DS2	105.82 ± 1.55	0.22 ± 0.00	1.28 ± 0.02	104.32 ± 1.53
DS3	368.56 ± 5.41	29.16 ± 0.45	4.45 ± 0.07	334.95 ± 4.90
DS4	102.85 ± 1.47	33.53 ± 0.50	0.00 ± 0.00	69.32 ± 0.98
DS5A	1244.70 ± 18.15	407.56 ± 5.80	11.56 ± 0.17	825.58 ± 12.17
DS5B	672.77 ± 9.78	44.38 ± 0.59	4.24 ± 0.07	624.15 ± 9.12
DS5C	174.47 ± 2.53	0.01 ± 0.00	0.44 ± 0.01	174.03 ± 2.53
Total				**8.665 ± 0.054 (kg-y)**

DS	No Cuts (kg-d)	PSA Cut	Burst Cut	**Final Natural Exposure**
DS0	164.53 ± 3.79	5.57 ± 0.13	1.03 ± 0.02	157.93 ± 3.64
DS1	62.86 ± 1.46	33.34 ± 0.77	0.00 ± 0.00	29.52 ± 0.68
DS2	10.52 ± 0.24	5.34 ± 0.12	0.00 ± 0.00	5.18 ± 0.12
DS3	81.74 ± 1.88	31.25 ± 0.73	1.84 ± 0.04	48.65 ± 1.11
DS4	73.84 ± 1.70	50.69 ± 1.16	0.00 ± 0.00	23.15 ± 0.54
DS5A	616.63 ± 14.19	276.97 ± 6.37	2.20 ± 0.05	337.46 ± 7.77
DS5B	335.90 ± 7.73	108.98 ± 2.50	0.55 ± 0.01	226.37 ± 5.22
DS5C	86.03 ± 1.98	20.34 ± 0.47	2.34 ± 0.05	63.35 ± 1.46
Total				**2.441 ± 0.028 (kg-y)**

Chapter 2. This is done because the active mass uncertainties are correlated [104]. The final uncertainty in the exposure of each Data Set is on the order of 1%, very similar to the $0\nu\beta\beta$ exposures. Table 4.6 gives the final exposures and uncertainties for each Data Set, before and after cuts.

The two most significant uncertainties in the overall detector efficiency as a function of energy are from the exposure, and the uncertainty in the `fitSlo` best fit. The exposure uncertainty contributes as the individual trigger and PSA efficiencies are weighted by exposure and added together. With the scaling to exposure, the plot can be interpreted as the "effective" exposure for each detector type as a function of energy. We note the enriched detectors have ∼ 2.5 kg-y of exposure at 1 keV.

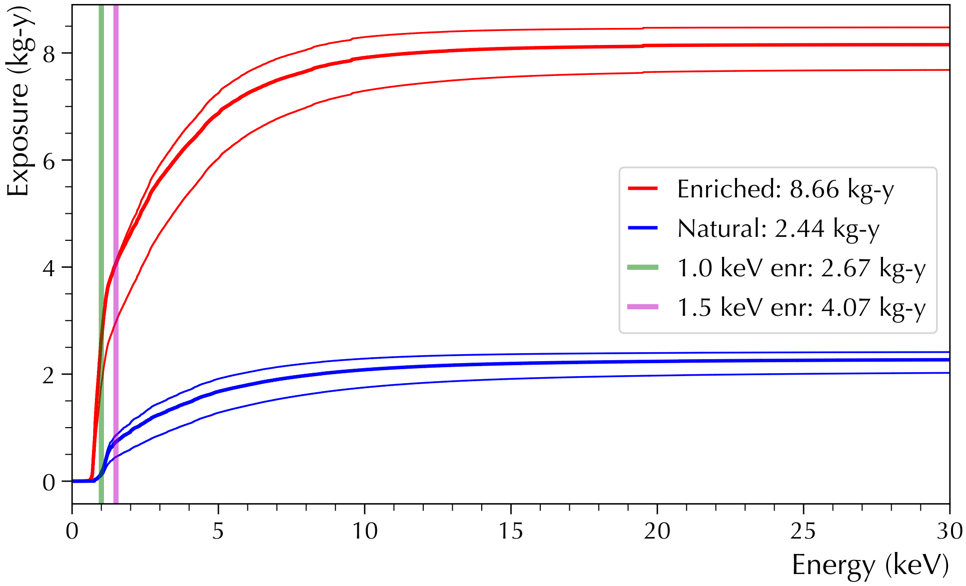

Figure 4.38: Total efficiency for enriched and natural detectors from DS0–5C. The thin lines denote the combined uncertainty due to `fitSlo` and the exposure.

Figure 4.38 shows the total combined efficiencies for enriched and natural detectors over the full DS0–5C. The uncertainty in the efficiency curve is depicted as well (thin lines), where the upper and lower envelope curves are determined by combining the uncertainty in the exposure for each detector with the energy-dependent uncertainty from each `fitSlo` fit, discussed at the end of Section 4.5. The difference between the lower and best-fit efficiency at high energy is ~ 0.5 kg-y in the $^{\mathrm{enr}}$Ge. The uncertainties are mainly driven by Module 2 detectors with reduced `m2s238` statistics, and can be improved in future analyses by including more calibration data in the acceptance measurement. The efficiencies for each detector in each Data Set are stored separately by LAT, so that different combinations of detectors and Data Sets can be more easily accessed by the axion analysis in the next Chapter.

The rate between 20–40 keV is used to quantify the flat background above the ^{3}H endpoint at 18 keV. It is notable that after the inner UGEFCu shield was installed between Data Set 0 and Data Set 1, we observe a factor of four reduction in the background rate. When the Data Sets are combined together, the larger back-

Table 4.7: Efficiency-corrected rates from 20-40 keV, a “background index” measuring the flat background above the tritium endpoint.

DS	r_{nat} (/keV/kg/d)	r_{enr} (/keV/kg/d)
DS0	0.08299 ± 0.00557	0.05150 ± 0.00275
DS1	0.03226 ± 0.00805	0.01438 ± 0.00116
DS2	0.03066 ± 0.01874	0.01367 ± 0.00278
DS3	0.02933 ± 0.00597	0.01419 ± 0.00158
DS4	0.01600 ± 0.00640	0.01447 ± 0.00350
DS5A	0.02129 ± 0.00193	0.01356 ± 0.00098
DS5B	0.02054 ± 0.00231	0.01311 ± 0.00111
DS5C	0.02085 ± 0.00441	0.01214 ± 0.00203
DS0–5C	0.03272 ± 0.00147	0.01845 ± 0.00059
DS1–5C	0.02190 ± 0.00133	0.01366 ± 0.00054

ground contribution from Data Set 0 is less obvious in the spectrum, but the results in Table 4.7 show a 25% reduction in the total rate. This makes Data Set 0 an obvious candidate for removal in the axion analysis if background (not exposure) is the limiting factor.

Finally, Figures 4.39–4.42 give the spectra and the fast pulse acceptance efficiency for the enriched and natural detectors, with and without Data Set 0. In the next Chapter, we will apply the results of the LAT analysis to a search for solar axions.

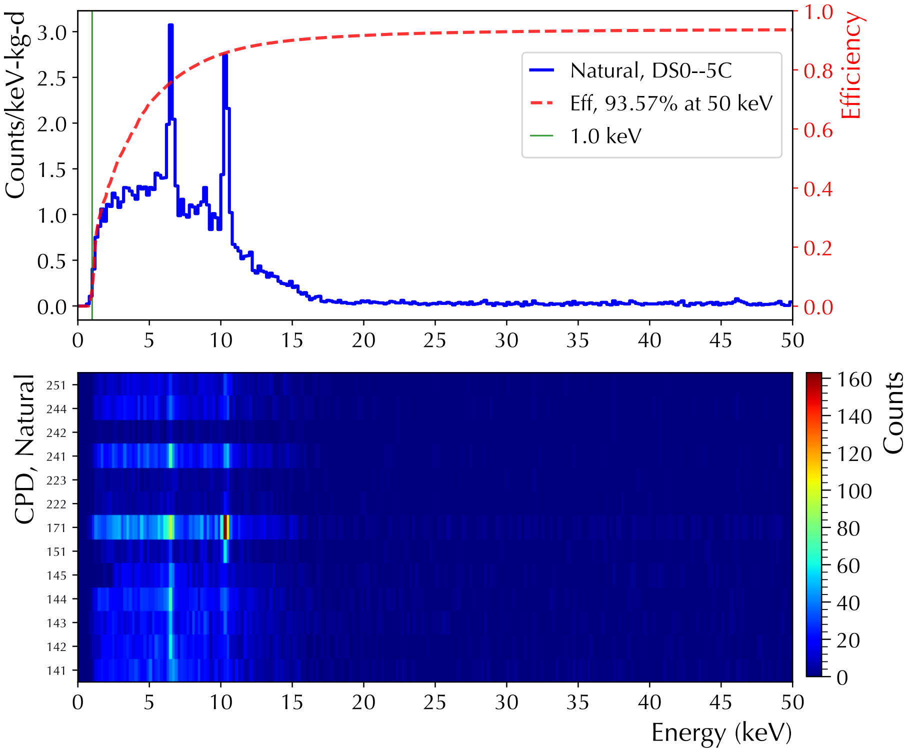

Figure 4.39: DS0–5C, Final Natural Spectrum

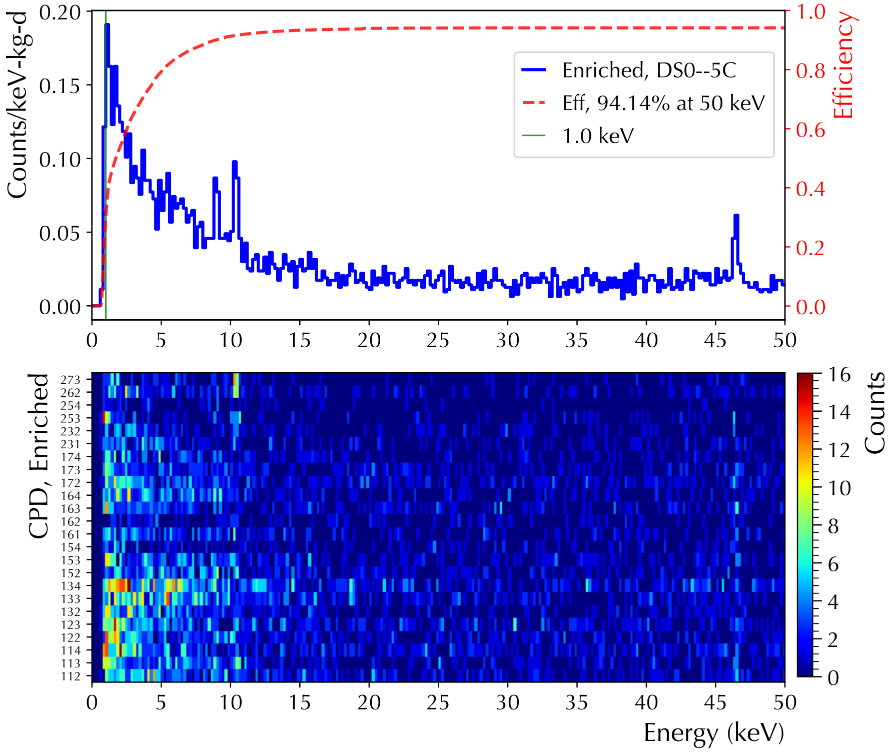

Figure 4.40: DS0–5C, Final Enriched Spectrum

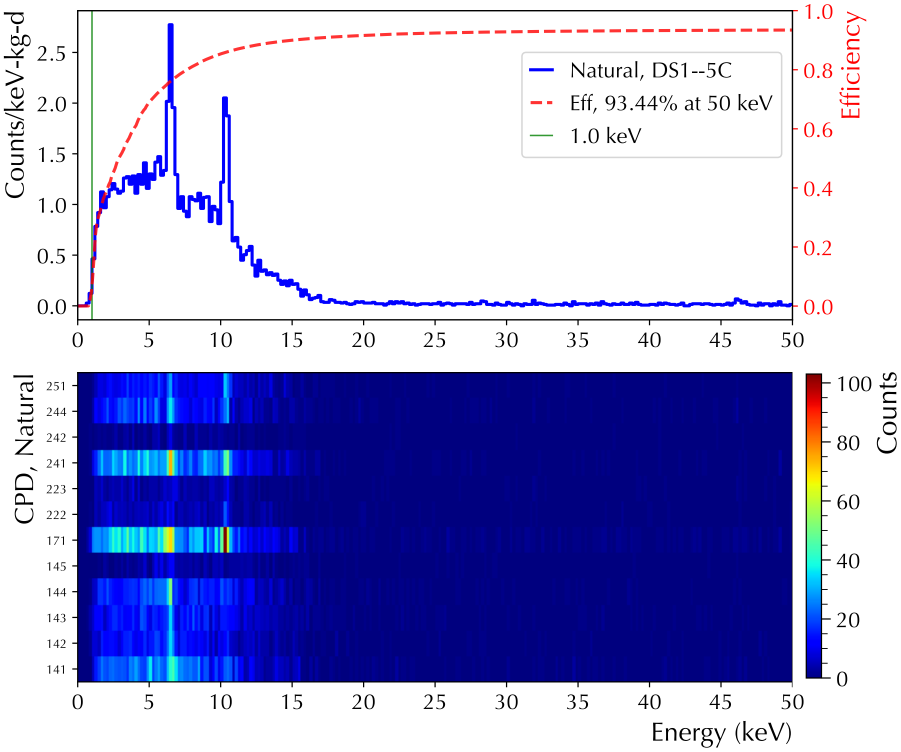

Figure 4.41: DS1–5C, Final Natural Spectrum

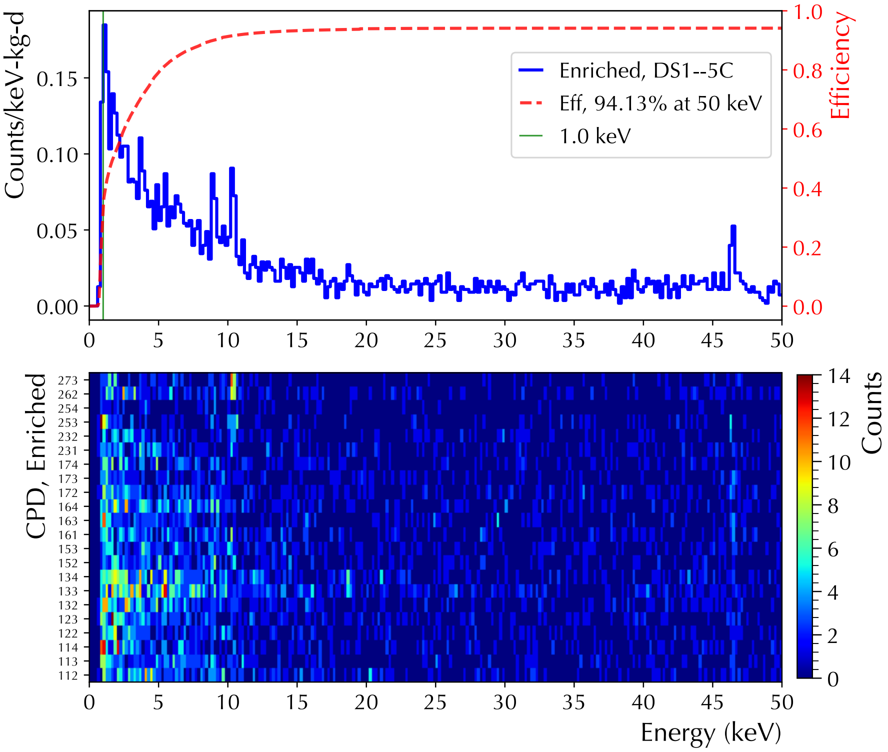

Figure 4.42: DS1–5C, Final Enriched Spectrum

CHAPTER 5

SOLAR AXION SEARCH

5.1 OVERVIEW

The energy spectra resulting from the LAT analysis may form the basis of several rare event searches. This Chapter will focus on a search for solar axions, probing the axion-electron coupling g_{ae} and the effective axio-nuclear coupling $g_{ae}\ g_{aN}^{\mathrm{eff}}$. Results from the axion search depend heavily on the expected *background model* of the spectrum at low energies, and proper accounting for systematic effects such as energy estimation, resolution, and cut efficiency. The presence of spectral lines in both the $^{\mathrm{nat}}$Ge and $^{\mathrm{enr}}$Ge spectrum allows a check on the resolution and energy estimation in the low energy region. To search for a physics signal, the expected background and signal models are fit to the spectrum using an unbinned extended maximum likelihood method from the `RooFit` toolkit [141], described in Section 5.2. Upper limits on the signal are then calculated by a profile likelihood method, accounting for systematic uncertainties when they are known.

Upper limits on the g_{ae} coupling are set based on the expected solar axion flux calculated by Redondo [78] and shown in Figure 1.12. It consists of a large continuum component with several distinct peaks. Two strategies for setting a limit will be investigated here. The first is to search for the contribution of the entire spectrum to the data, along with a background model consisting only of known (physically motivated) backgrounds such as tritium and cosmogenic lines. This *continuum fit* approach has the advantage that the dominant component of the axion flux is in its continuum, and a potential disadvantage if backgrounds not accounted for by the model are encountered. It has been used by other experiments including MALBEK [132], LUX [76], and PandaX [77]. The second strategy is to isolate the expected flux due only to the peaks in the axion spectrum, and search for "bumps" in the data in a small energy region centered around the peaks. The large xenon TPCs used by LUX and PandaX do not have sufficient resolution to separate the peaks from the continuum. The energy resolution of the DEMONSTRATOR is narrow enough ($\sim$ 0.1 keV) under 5 keV that a direct search for the peaks is feasible. This *peak fit* method searches for a Gaussian peak on top of a continuum background, modeled with a heuristic function. This can be advantageous if the continuum background has a simple, smooth shape, and even if its underlying source is not completely understood. The effectiveness of this method can also be increased by simultaneously searching for multiple peaks. Results from the two methods, including discussions of systematic uncertainties, will be presented in Sections 5.4 and 5.5.

Upper limits on the axio-nuclear coupling $g_{ae}\, g_{aN}^{\text{eff}}$ can be set by searching for peaks with energies matching nuclear transitions in the Sun. The strongest limits can be set when the energy region of interest is free from other spectral features. In the DEMONSTRATOR data, this is true for the 14.4 keV axion from the ^{57}Fe transition discussed in Chapter 1. MAJORANA first searched for this peak using Data Set 0 [79], and in Section 5.6 we present results from an updated search using the DS1–5C spectrum.

Finally, Section 5.7 summarizes the results of the current analysis, and discusses prospects for improvements to the background model and future low energy searches with the DEMONSTRATOR.

5.2 STATISTICAL METHOD

Fitting an observed energy spectrum to a combination of known spectral shapes is a problem well suited to the method of *extended maximum likelihood* (EML). In the standard maximum likelihood (ML) approach, the probability density function (PDF) $\mathcal{P}(x_i;\theta)$ modeling the set of data $\{x_i\}$ with the set of parameters $\{\theta\}$ is normalized to one, as are the data. In this method, the shape of the distribution is of primary interest, not necessarily its amplitude. In the extended approach, the normalization is allowed to vary as a free parameter, which is very useful in problems where the number of events contained in a particular distribution is of interest [142]. Adopting notation from Section 5.4 of Barlow [143], the standard and extended normalizations are given by

$$\int \mathcal{P}(x;\theta)\ dx = 1 \text{ (standard)}, \quad \int \mathcal{Q}(x;\theta)\ dx = v \text{ (extended)} \tag{5.1}$$

A particular choice of $\mathcal{Q}$ will predict v events in the observed range. This value, which incorporates information from the shape, can be a better estimate of the "true" total number than the actual number of observed events N. When N events are observed, the standard likelihood term must then be multiplied by the Poisson probability of observing N events when v events are expected:

$$L(\theta) = \prod_i^N \mathcal{P}(x_i;\theta) \text{ (standard)} \tag{5.2}$$

$$L(\theta) = \frac{v^N e^{-v}}{N!} \prod_i^N \mathcal{P}(x_i;\theta) \text{ (extended)} \tag{5.3}$$

The goal of the minimization procedure is to find the set of *estimators* $\{\hat{\theta}\}$ that maximize the likelihood function, representing the most probable value of the parameters given the data. Computer optimization routines generally opt to minimize the negative log likelihood ($-\ln L$, or NLL), which is equivalent and requires less large number manipulation, decreasing the necessary computation time. Using the

EML expression and dropping constant terms, we obtain the negative log likelihood in terms of Q and v, which is minimized by the `RooFit` toolkit:

$$\ln L(\theta) = N \ln v - v + \sum_i^N \ln \mathcal{P}(x_i;\theta) \tag{5.4}$$

$$= \sum_i^N \ln(v\mathcal{P}(x_i;\theta)) - v \tag{5.5}$$

$$= \sum_i^N \ln \mathcal{Q}(x_i;\theta) - v \tag{5.6}$$

$$-\ln L(\theta) = v - \sum_i^N \ln \mathcal{Q}(x_i;\theta) \tag{5.7}$$

For our purposes, the data $\{x_i\}$ is the set of hit energies $\{E_i\}$, and the PDF function $\mathcal{Q}$ is a combination of multiple background, signal, and efficiency shapes. The set of parameters $\{\theta\}$ to describe the background model include the number of counts from each background, and any shape parameters (μ and σ of a Gaussian peak, for example) that are allowed to float. Assuming the model and initial parameter values are reasonable, the `RooFit` minimization algorithm will converge, producing the set of estimators $\{\hat{\theta}\}$.

When an expected signal PDF (from axions) is added to the total model, its parameters are minimized along with the background model. Often it is desirable to know more than the most likely value for the signal of interest, but also the upper bound on its allowed value given the data. This can be accomplished through the method of *profile likelihood*. The parameter of interest μ is varied from its minimum value $\hat{\mu}$, while the others (often called *nuisance parameters*) are held constant at their most likely values $\hat{\theta}$. The relative change in the likelihood is computed:

$$\lambda(\mu) = \frac{L(\mu,\hat{\theta})}{L(\hat{\mu},\hat{\theta})} \tag{5.8}$$

According to Wilks' theorem [144], the profile likelihood ratio is related to the chi-squared distribution:

$$-2\ln \lambda(\mu) = \chi^2(\mu) \tag{5.9}$$

This provides a natural connection between the best fit value in the model, and the degree of confidence in the fit. By scanning upwards from the minimum value $\hat{\mu}$ until $-2\ln\lambda(\mu)$ reaches the desired χ^2 confidence level (here we use 90% or 2.71), an upper limit on the allowed signal can be calculated. In the event that the best fit $\hat{\mu}$ is less than zero, a new profile likelihood curve must be created before scanning upwards,

$$-2\ln\lambda'(\mu) = -2\ln\lambda(\mu) + 2\ln\lambda(0) \tag{5.10}$$

such that $-2\ln\lambda'(\mu = 0) = 0$. This adjustment will not be needed in the current analysis, as sections 5.4 and 5.5 will show.

5.3 BACKGROUND MODEL

The background model for the DEMONSTRATOR used in this work consists of the tritium beta decay spectrum, several spectral lines, and a flat continuum background accounting for stray Compton scatters and other events. The `RooFit` framework allows both analytic functions (`RooGaussian`, `RooExponential`, etc.) and histograms (`RooDataHist`) to be used as PDF objects in the fit. The shape parameters to analytic function PDFs can easily be allowed to float in `RooFit`. The cosmogenic peak study presented in this Section will use these floating parameters and the most prominent cosmogenic peaks to evaluate the effectiveness of the energy estimation and resolution function at low energies.

The fast pulse acceptance efficiency of the data must also be accounted for. Since it is never 100% in the energy region under study, we expect that the actual number of events that have occured from a given background will always be higher than what is observed in the data. Since the efficiency is known from the LAT analysis, it can either be used to modify the expected shape of each PDF, or be applied as a set of weights $\{w_i\}$ correcting each individual hit in the set $\{E_i\}$. In principle these methods are equivalent; one can either modify the expected background shape to account for the

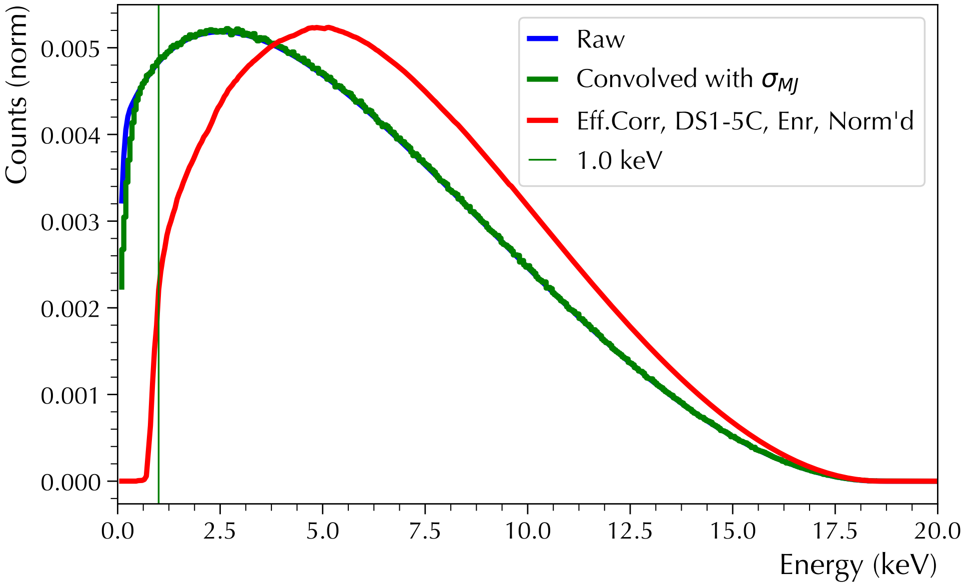

Figure 5.1: Tritium PDF, showing the (unnecessary) correction for energy resolution, and the effect of the efficiency correction.

efficiency, or weight the data according to it. The choice to weight the data was made for the axion peak fit analysis, and will be discussed further in Section 5.5. Modifying the expected background PDF has the advantage of not altering the observed data according to a particular efficiency, and may reduce bias in making observations from a spectrum. After the fit has been done to the modified PDF, to obtain the "true" number of counts, the efficiency correction is reversed, resulting in the original shape with a higher number of counts. This is the approach taken for the continuum fit in Section 5.4. As an example of modifying a PDF to account for the cut efficiency, Figure 5.1 shows the expected shape of the tritium distribution before and after applying the DS1–5C enriched efficiency correction given in Chapter 4. Chapter 4 also provided upper and lower bounds on the efficiency, which will be utilized in the following sections.

The tritium background is due to β-decay of ^{3}H (sometimes written as T_2), which has an 18.6 keV endpoint and a relatively long 12.32 year half-life. The isotope is cosmogenically produced within HPGe crystals, and can become the dominant background at low energy if the detector is kept at ground level for a long period of time. Even brief exposures to the cosmic ray flux at high altitudes by transport via airplane can create excessively high tritium levels. The manufacture, processing, and storage of the $^{\mathrm{enr}}$Ge detectors used in the DEMONSTRATOR was done to minimize surface exposure time at all points during the manufacturing process [87]. This resulted in significantly lower levels of tritium than in the $^{\mathrm{nat}}$Ge detectors, many of which were stored for an extended period in Los Alamos at an elevation of ∼2200 meters. The shape of the decay rate as a function of measured energy E represents the PDF $\mathcal{P}_T$. It is given by [145]:

$$\mathcal{P}_T(E; m_e, E_0) = C \cdot F(E, Z = 2) \cdot p \cdot (E + m_e) \cdot (E_0 - E)\sqrt{(E_0 - E)^2 - m_\nu^2} \quad (5.11)$$

Here, C is a normalization factor, F is the Fermi function accounting for the Coulomb force between the emitted β and the final state nucleus, p is the momentum of the outgoing β particle, m_e and m_ν are the electron and electron neutrino masses, and E_0 is the endpoint energy for zero neutrino mass, 18.6 keV. The expression for F contains a complex-valued gamma function. Rather than include this complicated functional form as an analytic expression in `RooFit`, the shape of the beta decay spectrum for $m_\nu = 0$ was sampled by MAJORANA [146] at closely spaced intervals. The features of the curve are much wider than the energy resolution σ_{MJ} (given in the next section), making a correction for resolution of this PDF unnecessary. The final tritium PDF used in the fit (with its efficiency corrected shape) is given in Figure 5.1.

Several spectral lines are observed in both the $^{\mathrm{nat}}$Ge and $^{\mathrm{enr}}$Ge data. The lines below ∼15 keV are due to cosmogenic activation within the detectors. The $^{\mathrm{nat}}$Ge shows a much higher rate, as expected. In the final LAT spectra presented in Chapter 4, there is also a spectral line at 46 keV from ^{210}Pb distributed roughly uniformly across all detectors. There is a possibility that the rising spectrum below 10 keV in the $^{\mathrm{enr}}$Ge may be due in part to a low energy continuum from ^{210}Pb decays. Simulation studies of this background are highly geometry-dependent and remain preliminary (see Section 5.7); it is not included in the current model. We also note that the included spectral lines are consistent with the recent cosmogenic study from CDMSlite [147] and the MALBEK background model [132]. Table 5.1 gives a list of isotopes included in the fit below 15 keV, along with their energies and half-lives. These spectral lines are modeled in the background with a Gaussian peak shape, and efficiency corrected by the same method described above for the tritium PDF.

Table 5.1: Cosmogenic peaks included in the background model. Data from [135]. The ^{68}Ga is included because it is produced by the decay of ^{68}Ge. [147]

Isotope	E (keV)	$T_{1/2}$
^{49}V	4.97	330 d
^{54}Mn	5.99	312 d
^{55}Fe	6.54	2.7 y
^{57}Co	7.12	78 d
^{65}Zn	8.98	244 d
^{68}Ga	9.66	1 h
^{68}Ge	10.37	287 d

Combining the tritium, spectral lines, and adding the flat background, the final model used in the likelihood fit contains 9 parameters representing the number of counts in each background, and additional parameters for μ, σ if Gaussian peaks are allowed to float. It can be expressed as:

$$\mathcal{P}(x;p) = p_0 + p_1 \mathcal{P}_T + \sum_{i=2}^{7} p_i \, \mathcal{P}_{G,i} \tag{5.12}$$

A representation of the full background model with arbitrary amplitudes is given in Figure 5.2.

The expected energy resolution for both sets of detectors has been calculated for each Data Set by the MAJORANA Energy Estimation Group [148], and follows a second-order polynomial form. When the spectra from different Data Sets are combined, the resulting peak width is a combination of the resolution in different Data Sets, weighted by the exposure of each. To account for this, an exposure-weighted resolution function was employed to calculate the Gaussian width σ_{MJ} of

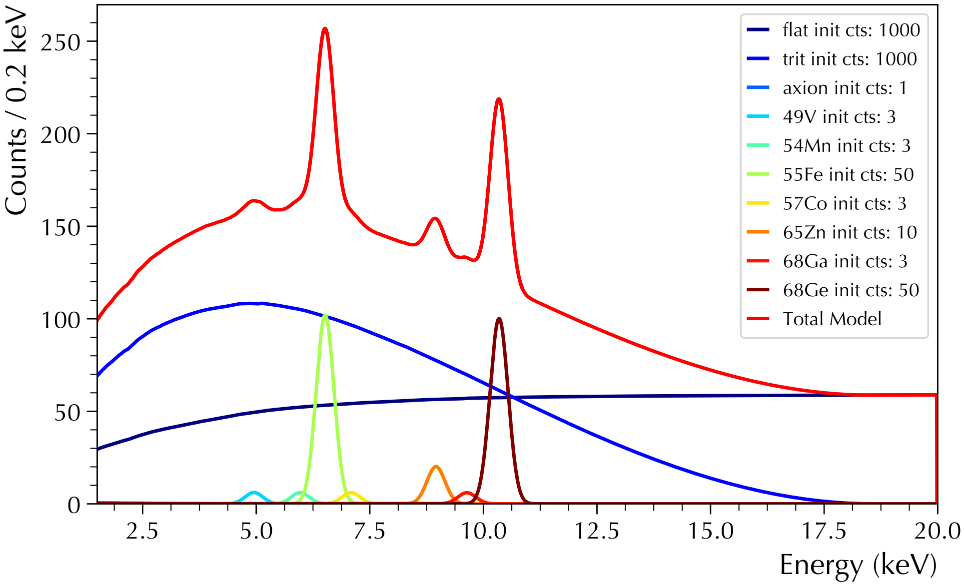

Figure 5.2: The background model under 20 keV, using the enriched efficiency correction from DS1–5C, showing the initial parameter values. An additional Gaussian component from ^{210}Pb at 46.5 keV is not shown.

the peaks, using the official resolution parameters and the final exposures η_i after low-energy run and channel selection for N Data Sets.

$$\sigma_{MJ}(E) = \frac{\sum_i^N \sqrt{p_{0,i}^2 + p_{1,i}^2 E + p_{2,i}^2 E^2} \cdot \eta_i}{\sum_i^N \eta_i} \tag{5.13}$$

The energy resolution for the enriched and natural detectors in each Data Set, and the exposure-weighted resolution, is shown in Figure 5.3.

To examine the energy estimation and peak resolution, a peak shape study was performed on both the natural and enriched detectors above 5 keV. Their corresponding DS1–5C spectra were fit with the tritium spectrum, a flat background, and analytic Gaussian peaks from Table 5.1 whose mean and width were allowed to float, in addition to their amplitudes. The ^{54}Mn and ^{57}Co peaks had negligible amplitude and were omitted from this study, but will be included in the next section. The parameter constraints for each peak are given in Table 5.2, and the resulting fits are shown in Figure 5.4.

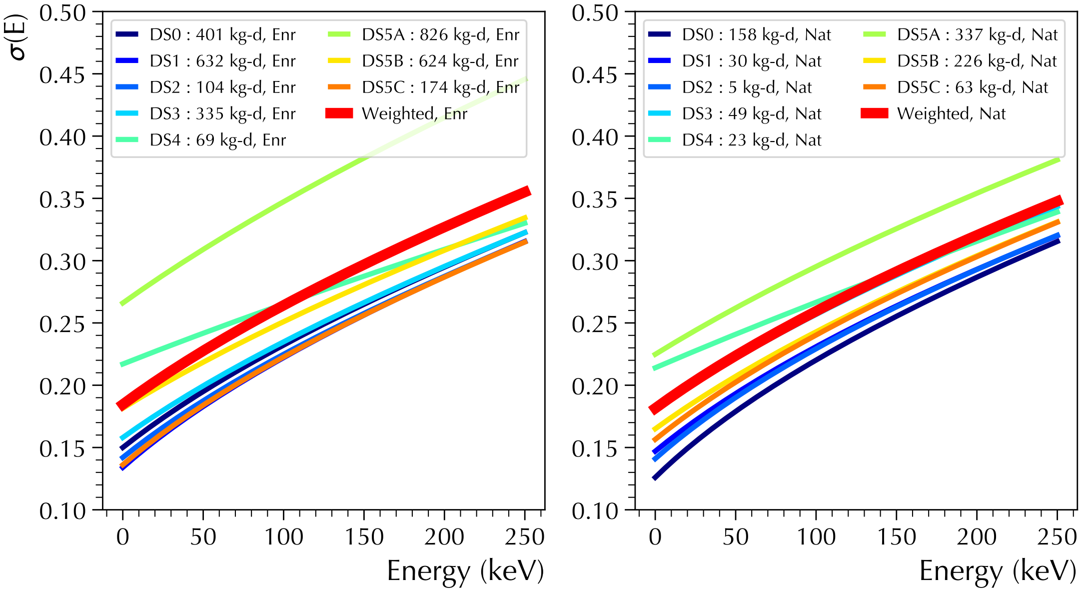

Figure 5.3: The enriched and natural energy resolution of each Data Set, with the exposure-weighed resolution for DS1–5C marked in red.

Table 5.2: Float parameter ranges for the mean μ, width σ, and number of counts A in each Gaussian peak.

Param.	Bound
μ	$E_{\text{lit}} \pm$ 0.3 keV
σ	$\sigma_{MJ} \pm$ 0.1
A	0 – 1000 cts

The strongest cosmogenic peaks in both the $^{\text{nat}}$Ge and $^{\text{enr}}$Ge spectrum provide an important check on the energy estimation and actual resolution of the detectors. As with the tritium background, the relative height of the cosmogenic peaks depends on their surface activation time. With only 478 kg-d of exposure in Data Set 0, clear peaks in the $^{\text{nat}}$Ge detectors from ^{55}Fe and ^{68}Ge were observed [79], but only weak peaks in the $^{\text{enr}}$Ge were seen. By combining Data Sets 0–5C, two clear cosmogenic peaks can be seen under 15 keV from ^{68}Ge and ^{65}Zn, along with several smaller contributions. A ^{65}Zn peak is observed in the $^{\text{nat}}$Ge as well, though its height relative to the ^{68}Ge peak is different. This is most likely due to differences in the manufacturing process (before and after zone refinement) between the two detector

Table 5.3: Results from the largest-amplitude cosmogenic peaks, comparing their fit energies with literature values (in keV) and their widths with the expected value σ_{MJ} (in keV). Counts are given with the efficiency correction applied.

Isotope	Cts (corr.)	μ_{lit}	μ_{fit}	Diff. (%)	σ_{MJ}	σ_{fit}	Diff. (%)
Natural Detectors, DS1–5C, 2.01 kg-y							
^{55}Fe	532.26	6.54	6.50	0.04 (0.6)	0.1991	0.1629	0.0362 (22.24)
^{68}Ge	487.31	10.37	10.38	-0.01 (-0.1)	0.2023	0.1760	0.0263 (14.93)
^{68}Ga	38.0	9.66	9.62	0.04 (0.5)	0.2017	0.1376	0.0641 (46.61)
Enriched Detectors, DS1–5C, 7.57 kg-y							
^{68}Ge	38.89	10.37	10.35	0.02 (0.2)	0.1992	0.1121	0.0871 (77.64)
^{65}Zn	49.91	8.98	9.00	-0.02 (-0.2)	0.1979	0.1339	0.0640 (47.83)

types, and varying isotope production rates. We note that the ^{55}Fe and ^{68}Ga peaks appear distorted, especially in the enriched spectrum. It is likely that the number of counts in the tritium spectrum and these peaks (along with their widths) are being overestimated due to this excess of events at low energies. Because this tends to artificially lower the observed excess, the mean values and widths of the peaks are fixed to their expected values for the continuum fit axion search discussed in the next section. Before fixing the peak parameters, the mean values and widths were measured for the most prominent peaks, and compared with their literature energy value E and the expected resolution $\sigma_{MJ}(E)$. The spectra from the floating peak fit to 5 keV are shown in Figure 5.4.

The results in Table 5.3 show that in both the $^{\text{enr}}$Ge and $^{\text{nat}}$Ge detectors, the energy estimator `trapENFCal` used by the LAT analysis is generally accurate to less than half a typical histogram bin width. Moreover, the most prominent peaks do not appear shifted by any constant value above or below their literature values. In the $^{\text{enr}}$Ge DS1–5C data, the difference is (coincidentally) nearly symmetric. This helps to justify the choice to fix the mean energies of the Gaussian peaks to their literature values in the following sections. Table 5.4 gives the efficiency correction applied to the data and the resulting rates in the peak fit region from 5–20 keV, and in the low-energy region 1.5–8 keV. (Table 4.7 gave the rates in the 20–40 keV "background

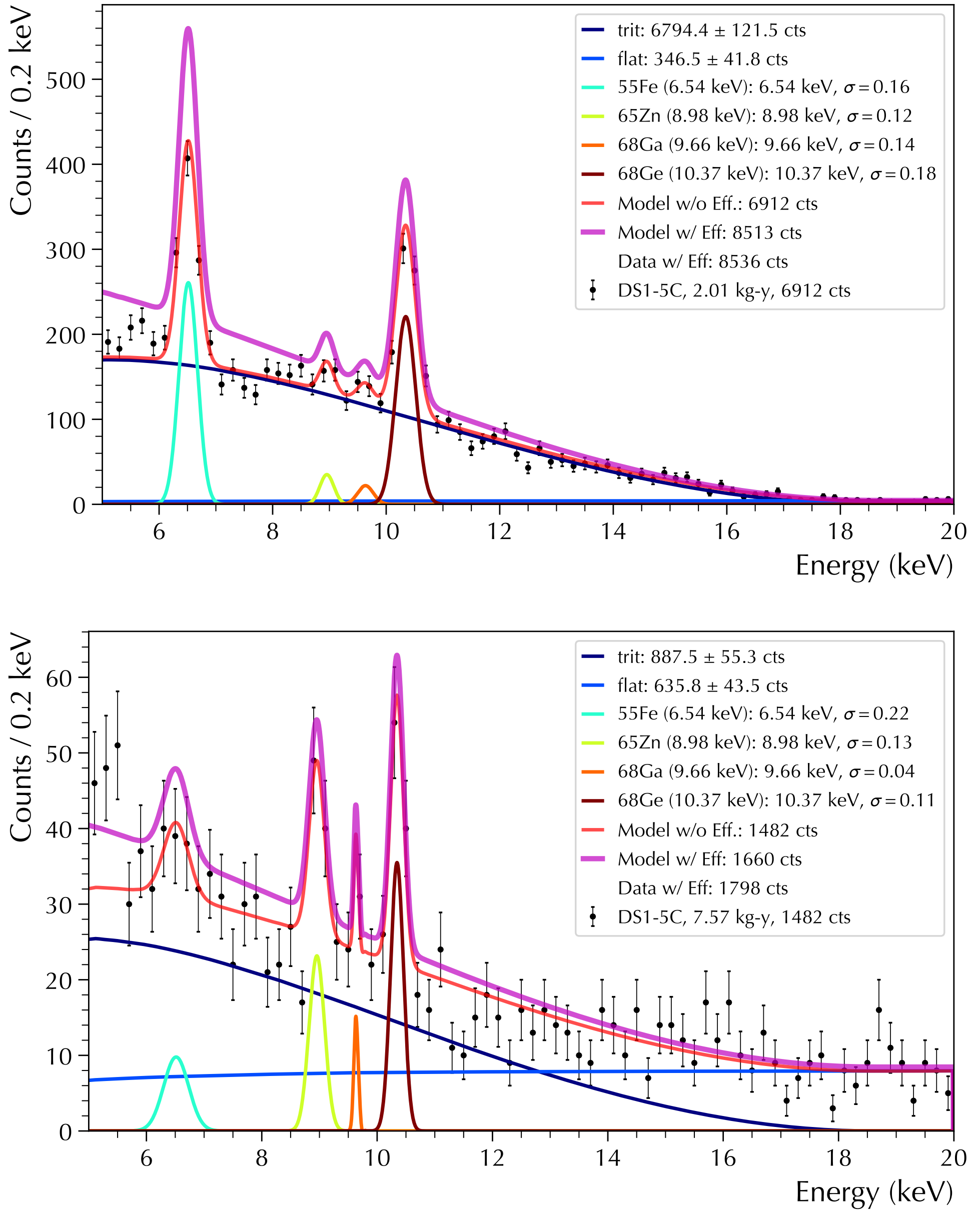

Figure 5.4: DS1–5C ^{nat}Ge (top) and ^{enr}Ge (bottom) spectra, fit to the background model above 5 keV, with floating Gaussian peaks. Only peaks with relatively large amplitudes are included in this study.

Table 5.4: Counts in the final spectra (DS1–5C) before and after the efficiency correction. Efficiency-corrected rates (in cts/kev/kg-d) are given for the 5–20 and 1.5–8 keV regions.

	Exposure (kg-y)	Raw Cts 5–20 keV	Corr. Cts 5–20	Corr. Rate 5–20	Corr. Rate 1.5–8
^{nat}Ge	2.009	6912	8536.53	0.776	0.857
^{enr}Ge	7.567	1482	1798.40	0.043	0.040

Table 5.5: Results from the background peak study above 5 keV, where the mean and width of each Gaussian peak is allowed to float. The efficiency-corrected counts are given, along with the correction factor f_ϵ from the raw values.

Bkg.	Num.Cts (corr)	f_ϵ	μ (keV)	σ (keV)
Natural Detectors, DS1–5C, 2.01 kg-y				
^{55}Fe	696.74 ± 47.08	1.31	6.5 ± 0.01	0.16 ± 0.01
^{65}Zn	64.53 ± 43.03	1.20	9.0 ± 0.05	0.12 ± 0.06
^{68}Ga	44.75 ± 42.37	1.18	9.62 ± 0.08	0.14 ± 0.06
^{68}Ge	566.35 ± 41.80	1.16	10.38 ± 0.01	0.18 ± 0.01
Tritium	6794.45 ± 121.55	1.23	–	–
Flat Bkg	346.50 ± 41.79	1.16	–	–
Enriched Detectors, DS1–5C, 7.57 kg-y				
^{55}Fe	31.21 ± 46.52	1.17	6.48 ± 0.14	0.22 ± 0.08
^{65}Zn	43.17 ± 43.96	1.11	9.0 ± 0.04	0.13 ± 0.03
^{68}Ga	7.99 ± 43.49	1.10	9.65 ± 0.03	0.04 ± 0.02
^{68}Ge	54.48 ± 43.22	1.09	10.35 ± 0.03	0.11 ± 0.03
Tritium	887.48 ± 55.26	1.14	–	–
Flat Bkg	635.77 ± 43.53	1.10	–	–

index" region.) Finally, the fit values and associated errors for all components of the background model are given in Table 5.5, for both enriched and natural detectors.

5.4 CONTINUUM SPECTRAL FIT

Setting a limit on the axion-electron coupling via the profile likelihood method requires construction of the appropriate axion PDF, $\mathcal{P}_a$. It is obtained by convolving the expected solar axion flux Φ_a with the axioelectric cross section σ_{ae} given in Chapter 1 (Equation 1.35). The σ_{ae} term is dependent on the photoelectric cross section for germanium, σ_{pe}, which is shown in Figure 5.5. It contains two significant discontinuities in the axion energy region of interest, which are related to the binding

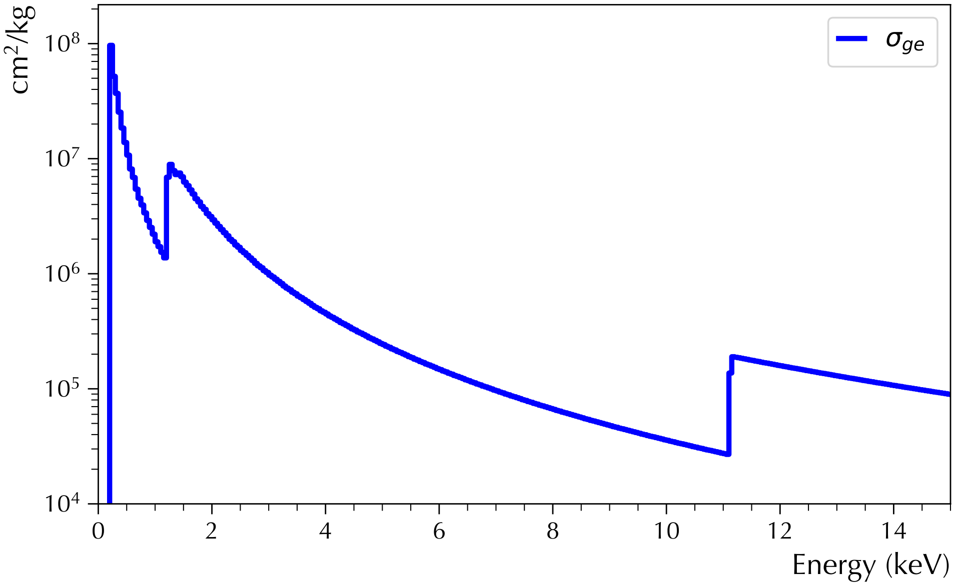

Figure 5.5: Germanium photoelectric cross section σ_{ge} as a function of incident photon energy, obtained from MUCAL [149].

energies of electrons in the K (innermost), L, and M shells. The binding energy of the K-shell is 11.104 keV, and an incident photon needs at least this much energy to eject an electron from this shell. It requires less energy to eject an outer-shell electron. There are multiple edges corresponding to the L-shell at 1.41, 1.25, and 1.22 keV [149]. Between the discontinuities, the attenuation of photons in Ge decreases smoothly. The data for the cross section σ_{pe} used in this work was created using a tool from Ref. [149].

The axioelectric cross section σ_{ae} is then calculated according to Equation 1.35. It contains a variable term for the axion mass m_a, which is often taken to be very small or zero. This is the case for the continuum fit discussed in this section. In Section 5.6, the mass term will be varied for the search for axions from nuclear transitions. Figure 5.6 gives the axioelectric cross section for two values of m_a.

The final axion PDF $\mathcal{P}_a$ is constructed by convolving the axioelectric cross section with the axion flux from Redondo, shown in Figure 1.12. It is calculated assuming $g_{ae} = 1$, for the purpose of setting a new limit on the value. We then convolve

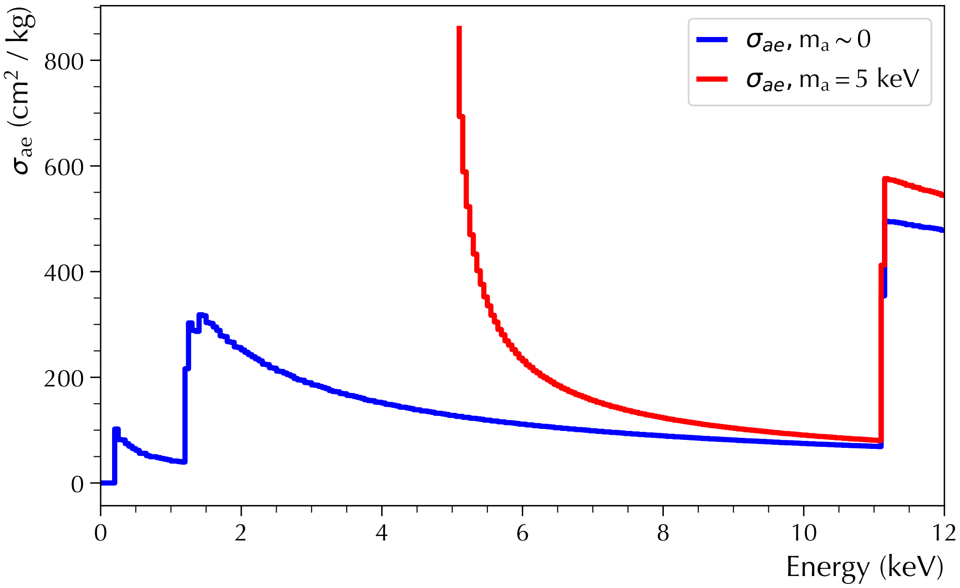

Figure 5.6: Axioelectric cross section σ_{ae}, for two values of the axion mass m_a.

the function with the expected energy resolution, σ_{MJ}, which is typically ~ 0.15 keV under 5 keV. Figure 5.7 gives the resulting PDF, which is normalized to one by `RooFit` and included as a component in the spectrum fit described in the previous section.

The continuum fit was performed for both the $^{\mathrm{enr}}$Ge and $^{\mathrm{nat}}$Ge detectors, with and without the axion signal, in the region 1.5–20 keV, for various Data Set combinations. In all cases, the best limit was obtained using the DS1–5C data, excluding Data Set 0 due to its lack of inner copper shield and resulting higher backgrounds. In all Data Set combinations, the upward-going excess of events most visible in the $^{\mathrm{enr}}$Ge spectrum causes a significant number of counts to be attributed to axions. This is apparent in both spectra (though much more pronounced in the $^{\mathrm{enr}}$Ge), and the fit results are shown in Figure 5.8.

Despite the large "observed" axion-like signal, no attempt to claim discovery is being made here. The obtained values for g_{ae} (whose calculation will be outlined below) have been excluded by other experiments by over a factor of four [77]. Instead,

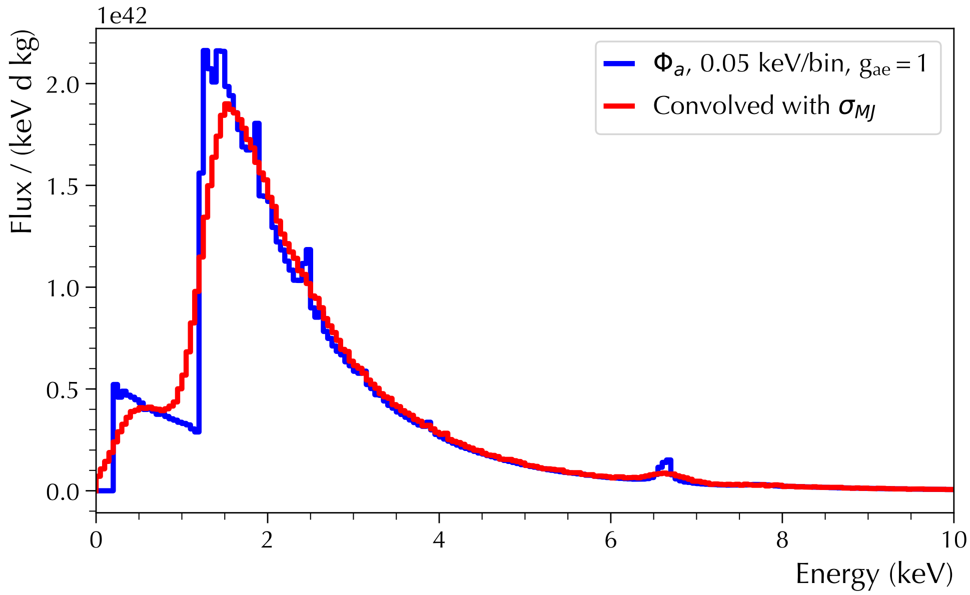

Figure 5.7: Axion PDF $\mathcal{P}_a$ used in the continuum fit, with $g_{ae} = 1$, and convolved with the expected energy resolution σ_{MJ}.

we take the upper limit of the profile likelihood interval to be an upper bound on the number of axion signals, just as would be done if the interval was consistent with zero counts. Clearly, a background signal not accounted for in the model is contaminating the spectrum, resulting in a slowly rising continuum at low energy. The axion PDF is the only signal in the model with this approximate shape, and the fit routine gives it a correspondingly high value. It also likely affects the number of events attributed to the spectral lines under ∼7 keV, especially in the ^{55}Fe and ^{49}V peaks. To more conservatively estimate the upper limit of the axion signal, the continuum fit restrics the peak means μ to their literature values, so that its strength is not "absorbed" by artificially high cosmogenic values. The widths σ are fixed to the exposure-corrected resolution σ_{MJ}, which Table 5.3 shows to be slightly wider from the observed value in the high-amplitude peaks. Only the number of events in the Gaussian peaks is allowed to vary in this fit. The full fit was performed for both the $^{\text{enr}}$Ge and $^{\text{nat}}$Ge detectors, with and without the axion signal, in the region 1.5–20 keV. Without the

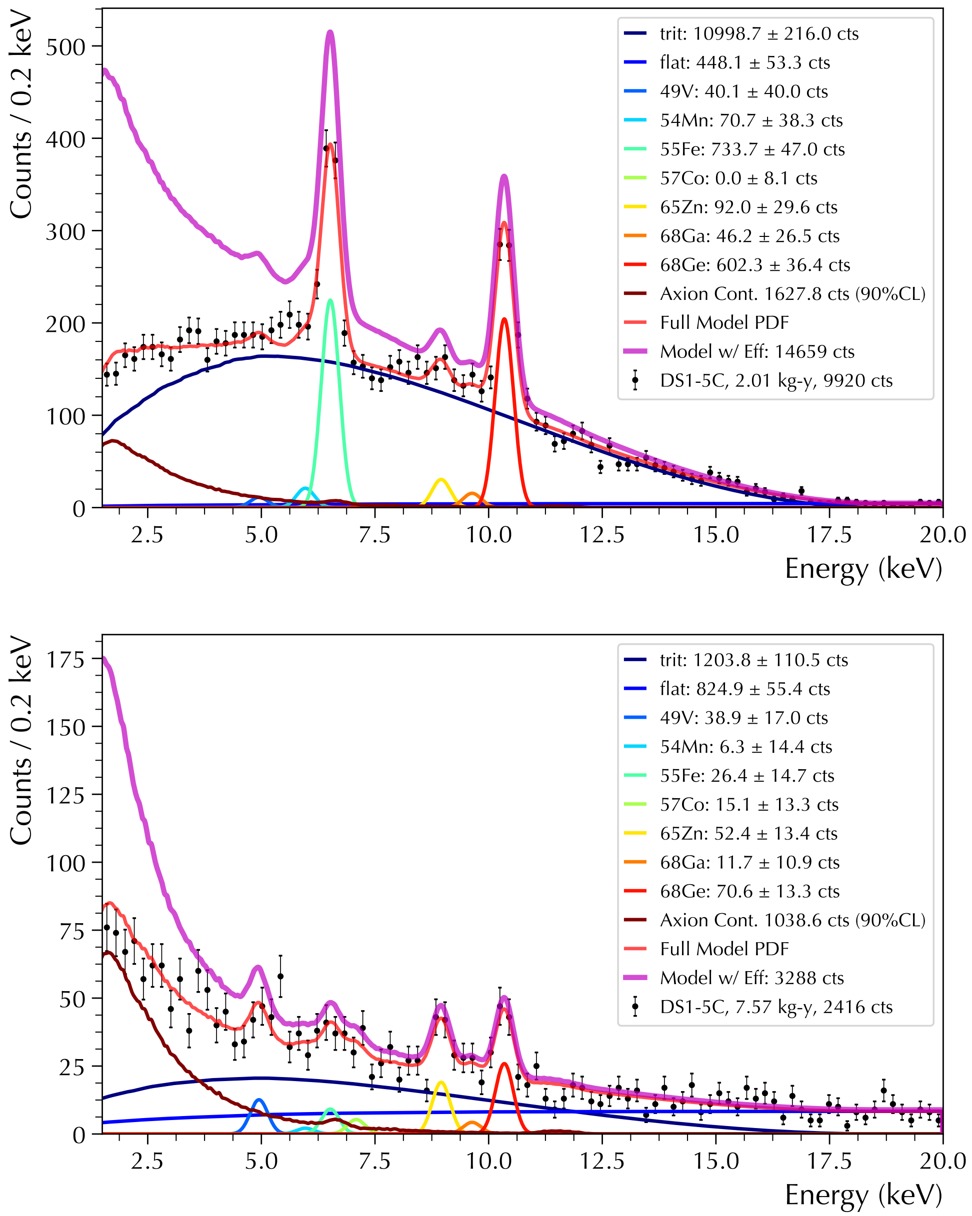

Figure 5.8: Top: Best fit $^{\mathrm{nat}}$Ge spectrum, for DS1–5C. Bottom: Best fit $^{\mathrm{enr}}$Ge spectrum for DS1–5C. The red curve contains the efficiency corrected PDFs, while the magenta curve shows the effect of removing the efficiency correction (once the fit is performed) to get a “true” number of counts. Both spectra show clear evidence of a new (previously unaccounted for) background under 5 keV.

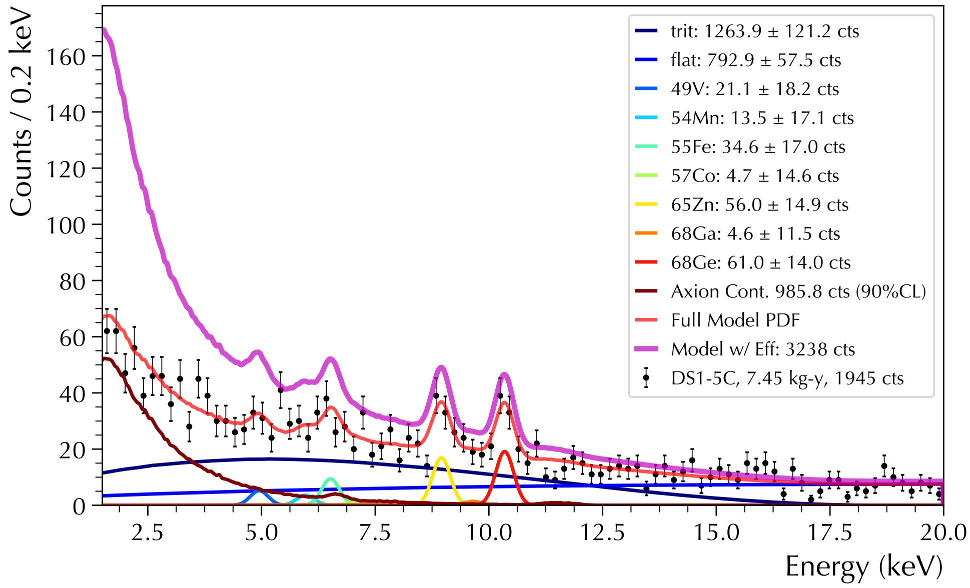

Figure 5.9: Example of using a tighter 90% cut on the `fitSlo` parameter. The shape of the rise at low energy does not appreciably change. (*Note: this Figure does not correspond to the results in Table 5.6.*)

axion signal, the low-energy excess in the ^{enr}Ge pulls the tritium level significantly outside the error bar of the data, and is not shown here.

Roughly exponential-shaped rises at low energy can be attributed to residual slow pulse contamination in the spectrum, and a study was performed to quantify this possibility. Chapter 4 described the tuning of the `fitSlo` cut to retain 95% of the `m2s238` population. To examine the dependence of the axion signal on the value of the `fitSlo` cut, a more aggressive 90% cut was applied to the LAT data, along with a more restrictive `tOffset` cut. The resulting spectrum is shown in Figure 5.9, and the 90% profile likelihood interval is given in Figure 5.11. Although a smaller number of signals is attributed to axions initially, the reduced efficiency under 5 keV causes the “true” counts to be inflated to (nearly) the same value as the 95% cut.

In addition to the tighter cut on `fitSlo`, another potential improvement was considered. The preliminary simulation discussed in Chapter 4 indicates that correcting for the slow pulse contamination in the `m2s238` population can lead to as much as a

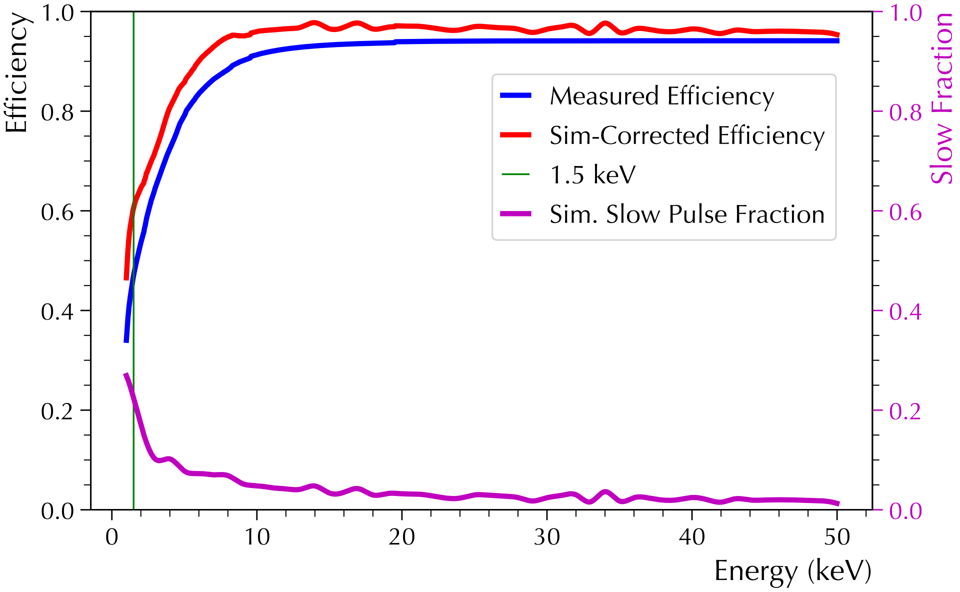

Figure 5.10: Effect of a (preliminary) slow pulse correction from simulations on the DS1–5C ${}^{\mathrm{enr}}$Ge efficiency.

15–20% improvement in fast pulse acceptance at lower energies. This correction is illustrated in Figure 5.10 for DS1–5C ${}^{\mathrm{enr}}$Ge, and the corresponding profile likelihood curve is shown in Figure 5.11.

In any case, the ${}^{\mathrm{enr}}$Ge shows a clear rise at low energy not accounted for by the current background model. This can perhaps be interpreted as the `fitSlo` cut losing its effectiveness in this energy region (possibly due to reduced S/N), or an indication that another radioactive background source is present. An important clue may be the observation of the 46.5 keV line from ^{210}Pb (shown in Figure 4.42), with roughly equal strength in all detectors. An upward rise below 5 keV could be caused by radioactive decay products originating very near the passivated surface of the detector. While a 5 keV beta or alpha would ordinarily be unable to penetrate the n^+ dead layer, the transition layer of the passivated surface is much thinner ($\sim 1\ \mu$m, Ref. [94]) and may allow these particles to deposit energy in the bulk. The requirement that the background source be near the passivated surface makes it a highly geometric effect, particular to the as-built construction of the Demonstrator. A future simulation

Table 5.6: Fit results for the $^{\text{enr}}$Ge DS1–5C, which gives the tightest bound on g_{ae}. The final counts are increased from their raw (efficiency corrected PDF) values by the factor f_ϵ.

Component	N_{fit}	$N_{\text{corr.}}$	f_ϵ
^{49}V	30.7 ± 13.45	38.85 ± 17.03	1.27
^{54}Mn	5.27 ± 11.99	6.31 ± 14.37	1.20
^{55}Fe	22.5 ± 12.47	26.43 ± 14.65	1.17
^{57}Co	13.1 ± 11.55	15.12 ± 13.33	1.15
^{65}Zn	47.23 ± 12.04	52.44 ± 13.36	1.11
^{68}Ga	10.67 ± 9.9	11.73 ± 10.88	1.10
^{68}Ge	64.68 ± 12.15	70.60 ± 13.27	1.09
Flat	710.63 ± 47.75	824.87 ± 55.43	1.16
Tritium	948.02 ± 87.04	1203.78 ± 110.52	1.27
Axion (min.)	563.17 ± 41.2	1038.55 ± 67.70	1.64

study must include proper detector response, and account for different sources of background at several different detector component locations, including contamination of the plastic insulators, tin on the point contact pin, etc. The behavior of charge carriers at or near the passivated dead layer is also not well-understood at this time, making a more detailed model and simulation study beyond the scope of this thesis. Prospects for future analysis are discussed in Section 5.7.

Since the simulated slow pulse correction remains preliminary, and the tighter 90% `fitSlo` cut does not have a significant effect on the shape of the low-energy excess, here we quote the 90% C.L. value for the DS1–5C $^{\text{enr}}$Ge spectrum, using the 95% `fitSlo` cut as the final best limit on g_{ae} given our current understanding of the background model. The resulting number of counts for this "best-fit" case in each background is given in Table 5.6. Figure 5.11 shows the three profile likelihood curves from these scenarios, and gives the corresponding upper limits. An estimate of the error in the best-fit result for g_{ae} is mainly dependent on the uncertainty in the efficiency curve, and is discussed below.

Setting a new limit on g_{ae} for a certain energy region requires taking the integral of the "expected" axion flux, with g_{ae}=1. As described in Chapter 1, the expression

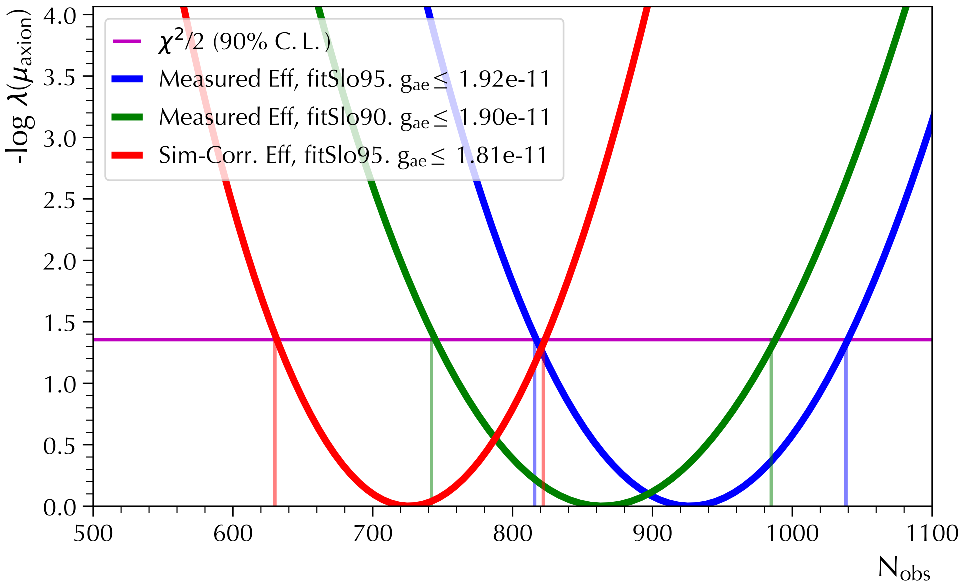

Figure 5.11: Three profile likelihood curves showing the best-fit DS1–5C ^{enr}Ge result. The most conservative curve is in blue, while the green and red curves show the effect of a tighter `fitSlo` cut and the potential effect of an improved efficiency correction from simulation.

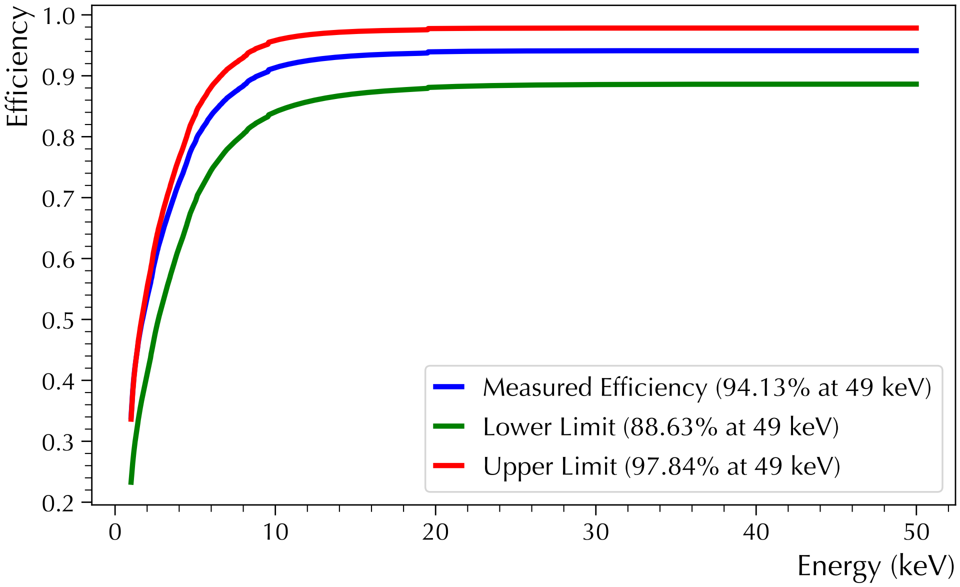

Figure 5.12: Upper, lower, and best-fit efficiency curves for the DS1–5C ^{enr}Ge data.

Table 5.7: Final results from the continuum fit, for various combinations of Data Sets.

Type	Data Sets	Exposure (kg-y)	N_{obs}	N_{exp}	$g_{ae} \leq$
$^{\mathrm{nat}}$Ge	1–5C	2.01	1635.73	2.01e+45	3.00e-11
$^{\mathrm{enr}}$Ge	0–5C	8.67	1357.05	8.68e+45	1.99e-11
$^{\mathrm{enr}}$Ge	1–5C	7.57	1038.41	7.58e+45	1.92e-11
$^{\mathrm{enr}}$Ge	1–4,5B,5C	5.31	726.43	5.33e+45	1.92e-11

for the "expected" number of detected axion interactions N_{exp} is calculated for a given energy region, and then scaled according to the exposure:

$$N_{\mathrm{exp}} = Mt \int_{E_1}^{E_2} \Phi_a \sigma_{ae} \, dE = Mt \, C \tag{5.14}$$

The upper limit is then calculated by taking the ratio with the number of counts observed in the data N_{obs} at 90% C.L.:

$$g_{ae} \leq \left(\frac{N_{\mathrm{obs}}}{N_{\mathrm{exp}}} \right)^{1/4} \tag{5.15}$$

Table 5.7 gives the bound on g_{ae} for various combinations of Data Sets. We note that excluding Data Set 5A gives the same result as including it, suggesting the residual noise contribution after cuts may be higher in this Data Set.

As described in Chapter 1, the relationship between g_{ae} and the axion energy scale factor is

$$g_{ae} \equiv \frac{C_e m_e}{f_a} = \frac{\cos^2(\beta) m_e}{3 f_a} \tag{5.16}$$

As discussed in Chapter 4, the uncertainty in the fast pulse acceptance is the most significant uncertainty in the analysis. It was quantified by creating two additional efficiency curves, corresponding to upper and lower limits. Figure 5.12 shows these curves for the DS1–5C $^{\mathrm{enr}}$Ge data. To calculate the error in g_{ae} introduced by this uncertainty, the axion analysis was performed for the upper, lower, and best-fit efficiencies. The corresponding profile likelihood curves are given in Figure 5.13. Using the resulting values of g_{ae}, we can give a systematic uncertainty to the best-fit number

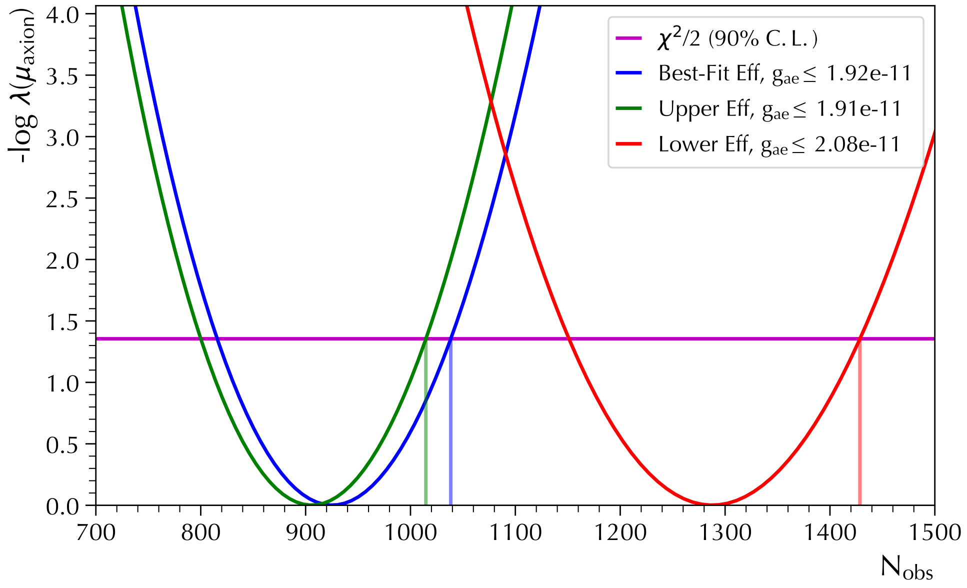

Figure 5.13: Profile likelihood curves for the best-fit DS1–5C $^{\rm enr}$Ge data showing the effect of the uncertainty in the fast pulse acceptance.

as a final result.

$$g_{ae} \leq 1.92^{+0.16}_{-0.01} \times 10^{-11} \tag{5.17}$$

For axions with keV-scale energies large compared to their mass, we can take $\cos^2 \beta \to 1$ and invert the formula to set a lower limit on the axion energy scale f_a, and a corresponding upper limit on the axion mass:

$$m_a = \frac{z^{1/2}}{1+z}\frac{f_\pi m_\pi}{f_a} = \frac{0.60 \text{ meV}}{f_a/10^{10}\text{GeV}} \tag{5.18}$$

Using the result on g_{ae} from the DS1–5C spectrum, at the 90% CL we find

$$f_a \geq 8.85 \times 10^6 \text{ GeV}, \quad m_a \leq 6.78 \text{ eV} \tag{5.19}$$

If the low-energy excess can be understood, the DEMONSTRATOR would see a significant improvement in the possible axion limit. Section 5.7 will discuss this possibility and offer a projected sensitivity to g_{ae}.

5.5 Shifted Peak Fit

An alternative to the continuum fit was explored, which takes advantage of the ∼0.1 keV energy resolution of the Demonstrator at low energy. The axion flux spectrum from Redondo [78] contains many peak features which are above the smooth continuum. It is possible to "bump hunt" for these peaks in the Demonstrator data at specific energies. This requires knowing the exact energies of the peaks, and the corresponding flux from only the component above the smooth continuum.

To begin, we remind the reader that the existence of peaks in the axion flux spectrum is due to the inclusion of axio-deexcitation and recombination processes occuring deep wthin the Sun (described in Chapter 1). In this plasma environment, elements are often highly ionized, and in many cases retain only enough electrons to make them hydrogenlike or heliumlike. The ionization changes the energy levels of a particular transition from what would be observed in vacuum, since the binding energies of ionized atoms are higher. As an example, the $K_{\alpha 1,\alpha 2}$ transitions of iron each produce a 6.4 keV photon (the separation in energy between the two is negligible with HPGe resolution), but close inspection of the axion flux spectrum shows that the peak is indeed closer to 6.6 keV. The calculation by Redondo used detailed libraries of monochromatic photon radiative opacities which accounted for this effect. The actual locations of these peaks can be estimated from the X-Ray Data Booklet [150], which provides data on the transition energies from the various n=2 states to the n=1 ground state for hydrogenlike and helium-like ions. As a further consistency check, one can analyze the raw data of the Redondo flux spectrum [151], to directly confirm the true peak locations. Figure 5.14 provides a generic level diagram depicting typical atomic transitions leading to the observed peaks. Figure 5.15 shows the fitted peak positions on the axion signal (with g_{ae}=1), and Table 5.8 provides the final energy values used in this analysis.

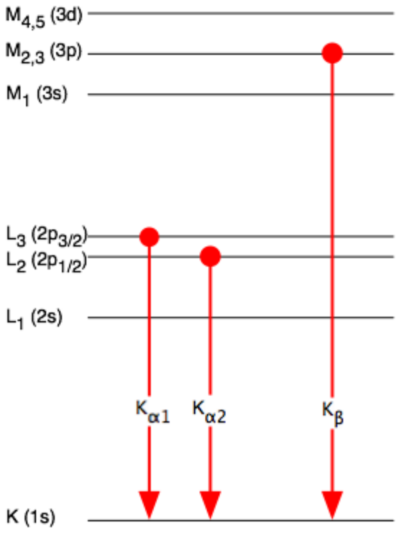

Figure 5.14: Depiction of transitions for a generic atom.

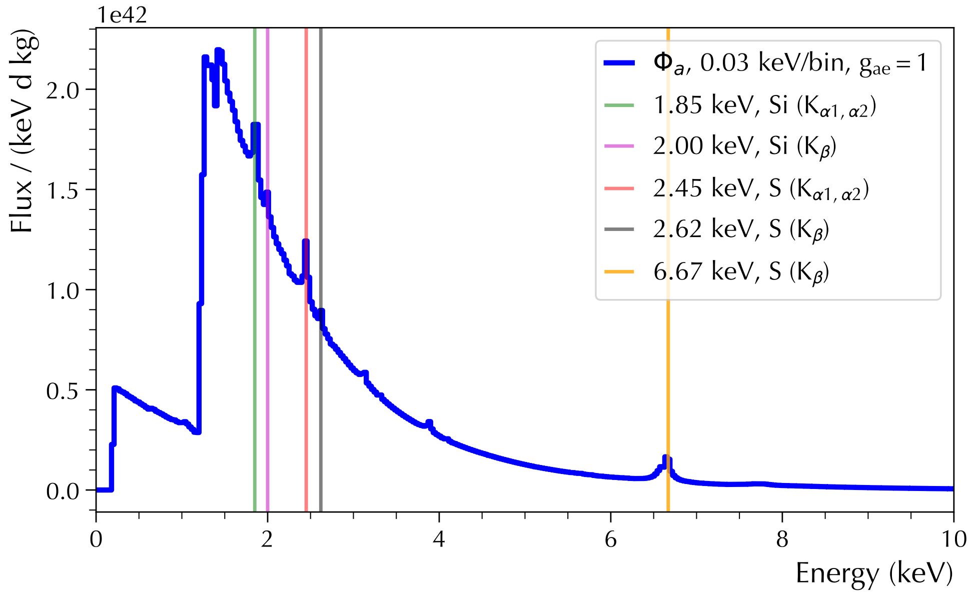

Figure 5.15: The continuum axion PDF, showing the fitted locations of five peaks.

Table 5.8: Source and expected energies of each axion line, with vacuum energies E_{vac} and sun energies E_{sun}.

Source	Transition	E_{vac} (keV)	E_{sun} (keV)	ΔE (keV)
Si($K_{\alpha1,\alpha2}$)	$2p \to 1s$	1.74	1.85	0.11
Si($K_{\beta1}$)	$3p \to 1s$	1.84	2.00	0.16
S($K_{\alpha1,\alpha2}$)	$2p \to 1s$	2.31	2.45	0.24
S($K_{\beta1}$)	$3p \to 1s$	2.46	2.62	0.16
Fe($K_{\alpha1,\alpha2}$)	$2p \to 1s$	6.40	6.65	0.15

Table 5.9: Predicted axion fluxes for each peak, assuming g_{ae}=1.

Source	E_{fit} (keV)	Flux (cts / cm^2 d)
Si($K_{\alpha1,\alpha2}$)	1.85	$5.534 \pm 0.224 \times 10^{38}$
Si($K_{\beta1}$)	2.00	$1.340 \pm 0.180 \times 10^{38}$
S($K_{\alpha1,\alpha2}$)	2.45	$4.671 \pm 0.199 \times 10^{38}$
S($K_{\beta1}$)	2.62	$8.858 \pm 1.83 \times 10^{37}$

The flux from the peaks above the continuum can be calculated employing a procedure very similar to the spectral peak fitting described in the previous section. Two independent measurements were performed. Using the `RooFit` toolkit, four narrow Gaussians (with a floating mean and width) and a single exponential background were fit to the energy region 1.5–3.0 keV. The sharpness of the β peaks caused convergence issues with this method, requiring finely tuned initial parameters. As a consistency check on the results, a sideband analysis of the background was performed using standard curve fitting routines from the `scipy.optimize` library [131]. Conservative energy windows around each peak were removed, and the resulting spectrum was fit to a single exponential. The peaks were then reintroduced and background-subtracted, and fit simultaneously to four Gaussians. This procedure is illustrated in Figure 5.16, and the measured flux is given in Table 5.9. The total flux in the continuum between 1.5–3.0 keV is 7.52×10^{39} cts/cm^2/d, and the peaks contribute 1.24×10^{39} or 16.5% of the total.

To search for the contribution of the axion peaks to the continuum, a novel method was suggested by Avignone [152], which was previously used to detect $2\nu\beta\beta$ decay of

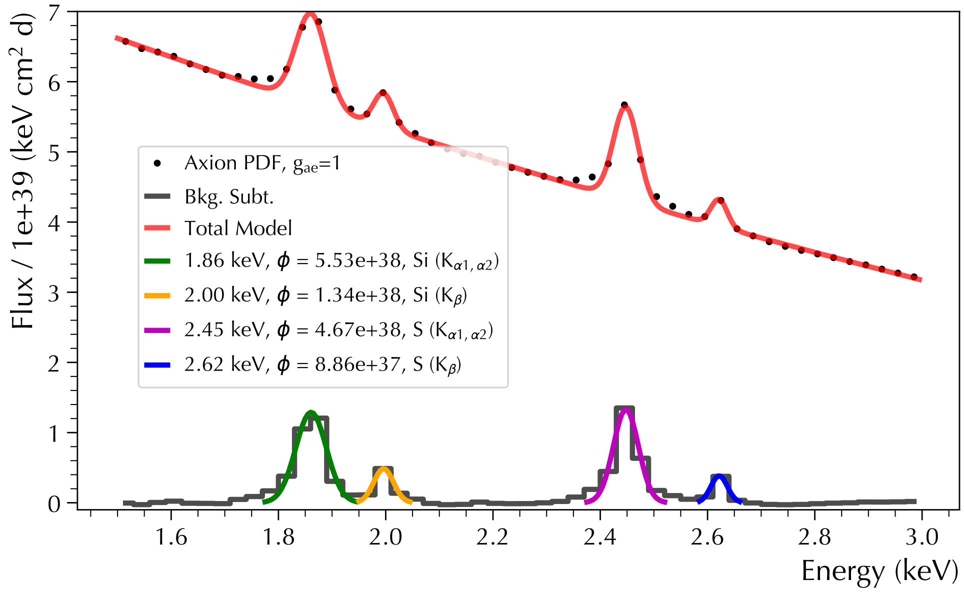

Figure 5.16: Flux due to the four axion peaks of interest.

^{100}Mo to the first excited 0^+ state in ^{100}Ru [153].[1] In this *peak shift* method, copies of the energy spectrum are aligned together such that the expected peaks overlap at the same energy. The appeal of this method can be seen by considering the case of a flat (but noisy) background, and multiple weak peaks at various locations. If the data are histogrammed, the error in each bin goes as $\sqrt{N}$. If multiple copies of the histogram are made, and shifted such that the peaks align at the same energy, the error in the bin of interest remains $\sqrt{N}$, but the signal (if present) increases as the number of counts N.

In an unbinned analysis the principle is the same. Multiple copies of the individual detector hits are made, with a constant offset applied to each hit energy. The expected axion flux at the shifted energy can be increased by aligning as many peaks as possible, and adding the corresponding axion peak fluxes. In this analysis, four copies of the DS1–5C low-energy LAT data were created and shifted in energy such that each axion

---

[1] The method is not explicitly discussed in the paper, but can be duplicated using Table 1.

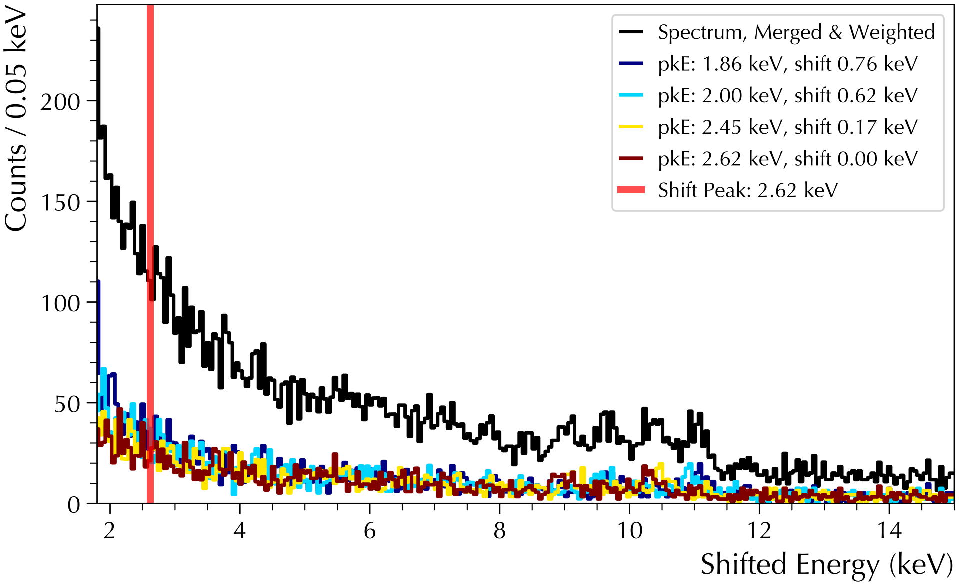

Figure 5.17: Four copies of the DS1–5C $^{\mathrm{enr}}$Ge spectrum, shifted and superimposed such that the expected axion peak appears at 2.62 keV (red line).

peak would appear at 2.62 keV, the highest-energy peak in Table 5.9. The resulting *shifted energy spectrum* is shown in Figure 5.17.

Unlike the continuum fit, it is not straightforward to apply the efficiency correction to the PDFs used to fit the shifted energy spectrum. To account for the energy-dependent efficiency of each spectrum, each hit energy was weighted according to its unshifted value. In this way, every event forming the combined spectrum has the appropriate weight applied, and no adjustment or scaling of the fit results is necessary to obtain the efficiency-corrected "true" number of counts in each background component.

The axion signal is modeled by a single Gaussian peak, with a fixed mean value, and a width matching the expectation σ_{MJ} for the $^{\mathrm{enr}}$Ge detectors at the highest peak energy 2.62 keV, since it has the broadest resolution. The choice to fix the mean is necessary, since the spectra are shifted to line up exactly at 2.62 keV. The results quoted below in Table 5.10 use a fixed signal peak width, and an optimized energy region 2.0–3.5 keV. These choices represent two potential sources of systematic error, and are discussed at the end of this section.

The choice of background model in this method has a significant impact on the result, since the choice is ultimately heuristic in this "bump hunt." This can be advantageous, since the only goal is to fit the observed continuum well, without necessarily requiring knowledge of its physical origin. In practice, the fit must include enough degrees of freedom that the amplitude of the peak signal is not excessively adjusted to compensate for flucutations in the background. This is especially apparent if only a single exponential is used. Ultimately a heuristic choice was made, of an exponential and flat background component. This had the least sensitivity to the initial fit parameters, and number of peaks (shifted spectra) n_{pk} included in the fit.

To facilitate a comparison with the best continuum fit, the $^{\mathrm{enr}}$Ge DS1–5C spectrum was used in this analysis. The shift peak fit was performed for four cases, adding shifted spectra successively to the unshifted spectrum, such that the axion signals would align at 2.62 keV. As a best-case scenario, a fixed-width signal peak was used, along with the optimal energy region 2.0–3.5 keV. Examples of the shifted fit for $n_{pk} = 3$ and $n_{pk} = 4$ are given in Figures 5.18 and 5.19, and the results from all four fits are given in Table 5.10. The parameters reported are the number of counts in each background, the shape of the exponential decay τ_{exp}, and the number of signal counts, using the same 90% profile likelihood confidence interval method discussed in the previous sections.

The effect of the low energy rise in the $^{\mathrm{enr}}$Ge data described in the previous sections also affects the shift peak fit, by bringing in additional background into the fit region. The lowest-energy axion peak considered in this fit is at 1.86 keV, and when its spectrum is shifted upwards to 2.62, it moves the accompanying low energy rise into the fit region. This effect can be seen in the Table 5.10, which shows a sharp rise in the contribution of the flat background for $n_{pk} = 4$. As a result, adding all four

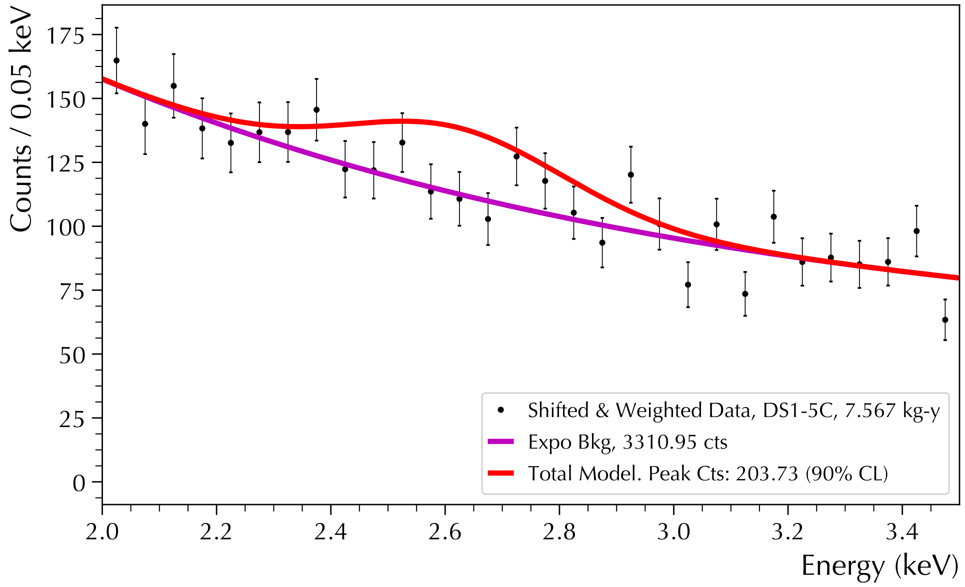

Figure 5.18: Peak fit for four copies of the DS1–5C energy spectrum with expected axion signals aligned at 2.62 keV.

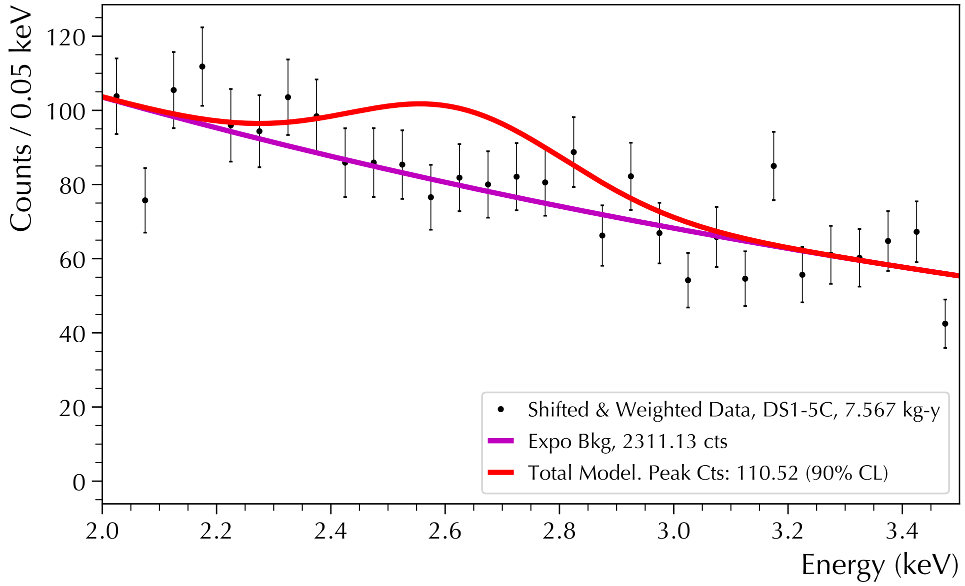

Figure 5.19: Peak fit for three copies of the spectrum (omitting the 1.85 keV axion peak), which gives the tightest bound on g_{ae}.

Table 5.10: Fit parameter results from the DS1–5C shited peak fit. The flat background component sharply increases for $n_{pk} = 4$. Large uncertainties are present in the flat background since it is correlated with the amplitude of the exponential component.

n_{pk}	n_{expo}	n_{flat}	τ_{expo} (keV^{-1})	N_{obs} (90% CL)
1	663 ± 80	1.001 ± 6767	-0.480 ± 0.104	65.93
2	1402 ± 64	1.008 ± 1052	-0.440 ± 0.064	93.69
3	2330 ± 143	1.001 ± 6697	-0.420 ± 0.053	110.52
4	2339 ± 3462	1012 ± 7495	-0.670 ± 0.845	203.73

Table 5.11: Peaks included, number of signal and expected counts, and the resulting bound on g_{ae} as more copies of the shifted spectrum are added to the fit. A fixed peak width and an energy region of 2.0–3.5 keV are used.

n_{pk}	E_{pk} (keV) included	N_{obs} (90%CL)	N_{exp}	$g_{ae} \leq$
1	2.62	65.93	2.45e+41	1.28e-10
2	2.62, 2.45	93.69	1.54e+42	8.84e-11
3	2.62, 2.45, 2.00	110.52	1.91e+42	**8.73e-11**
4	2.62, 2.45, 2.00, 1.85	203.73	3.44e+42	8.78e-11

peaks does not produce the best limit on g_{ae} in this analysis. The best result, given in Table 5.11 is obtained from the $n_{pk} = 3$ fit. Figure 5.20 shows the corresponding profile likelihood curves. None of the profile minima are less than zero, so including a positive shift to the profile likelihood curve as discussed in Section 5.2 is not necessary. Since the peak shifting method does not appear to be competitive with the continuum shift, we neglect this adjustment.

Two sources of systematic error were investigated for the shift peak fit; the effect of the energy region, and the effect of fixing the signal width. The relatively narrow energy region used (2.0–3.5 keV) tends to allow a floating peak width to compensate for fluctuations not accounted for by the continuum background model. Table 5.12 gives a comparison of fit parameters for a fixed-width and floating-width signal. Allowing the peak to float has the effect of broadening the width from the expectation σ_{MJ}, attributing more counts to axions, and weakening the bound on g_{ae}.

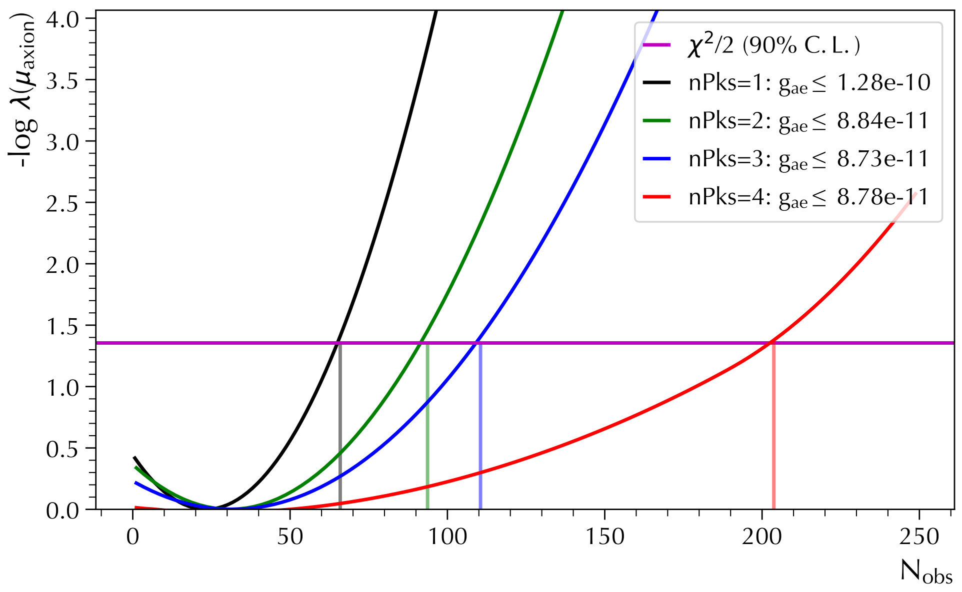

Figure 5.20: Profile likelihood curves for $n_{pk} = 1$ through 4.

Table 5.12: Systematic comparison of a fixed versus floating signal peak width. As before, large uncertainties are present in the flat background component.

	n_{expo}	τ_{expo} (keV^{-1})	n_{flat}	N_{obs} (90% CL)
Fixed $\sigma = \sigma_{MJ}$	2330 ± 143	-0.420 ± 0.053	1 ± 6697	109.3
Float (±0.3 σ_{MJ})	2310 ± 238	-0.418 ± 0.063	1 ± 9190	152.5

Qualitatively, the shifted energy spectrum in Figure 5.17 in the energy range 2.0–3.5 keV is steadily decreasing, and just under 2 keV moves upward significantly. As the lower-energy peaks are moved up to 2.62 keV, they bring the heaviest-weighted data points into the fit region. This makes the fit extremely sensitive to the energy region selected, and the number of peaks (shfted spectra) included. By extending the lower energy threshold 0.1 keV, the result for g_{ae} is affected by ∼10%.

Extending the energy region and allowing the peak to float both result in a weaker limit on g_{ae}, which can be seen in Figure 5.21. The choice of fixed peak width and optimal energy region was made to investigate the best-case effectiveness of the peak shift method, in comparison with the continuum fit. We find that the continuum fit

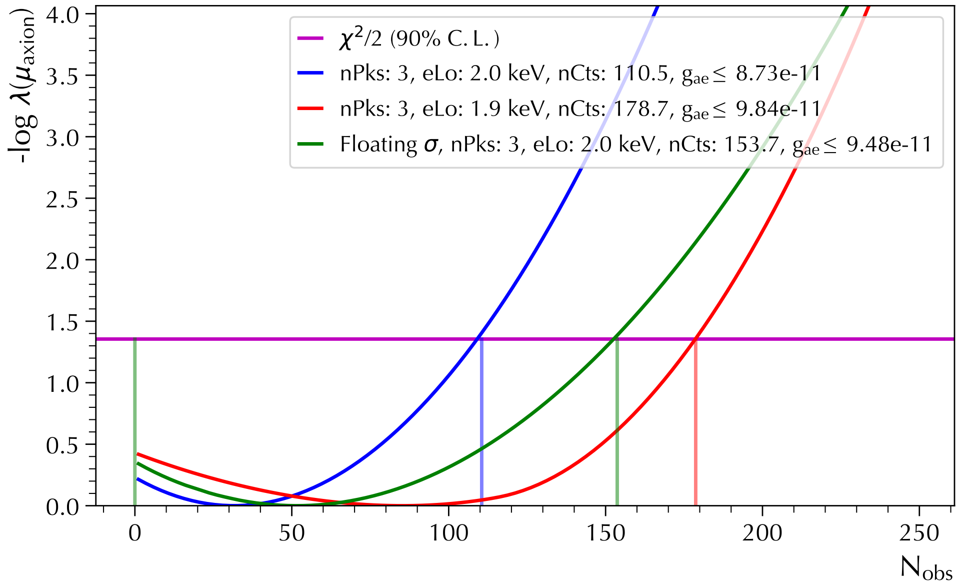

Figure 5.21: Systematic error in the best case $n = 3$ fit. Blue: Fixed-width, 2.0 keV threshold (best case). Green: Floating-width, 2.0 keV threshold. Red: Fixed-width, 1.9 keV threshold. In all cases, the inclusion of systematic effects results in a weaker bound on g_{ae}.

provides a better bound on g_{ae} by more than a factor 4 even in the best case, making further systematic checks of this method unnecessary.

5.6 14.4 keV Solar Axion Search

The flux of axions from the M1 atomic transition of ^{57}Fe in the Sun has been calculated by Ref. [80]:

$$\Phi_a(14.4 \text{ keV}) = \beta^3 \, (g_{aN}^{\text{eff}})^2 \; 4.56 \times 10^{23} \; [\text{cm}^{-2} \text{ s}^{-1}] \tag{5.20}$$

Here, the factor β represents the ratio of the momenta of the outgoing axion and photon. For a 14.4 keV photon, this can be written in terms of the axion mass m_a:

$$\beta = \frac{k_a}{k_\gamma} = \sqrt{\frac{14.4^2 - m_a^2}{14.4^2}} \tag{5.21}$$

This effect is not dependent on the solar axion flux due to the axion-electron coupling calculation described in the previous sections.

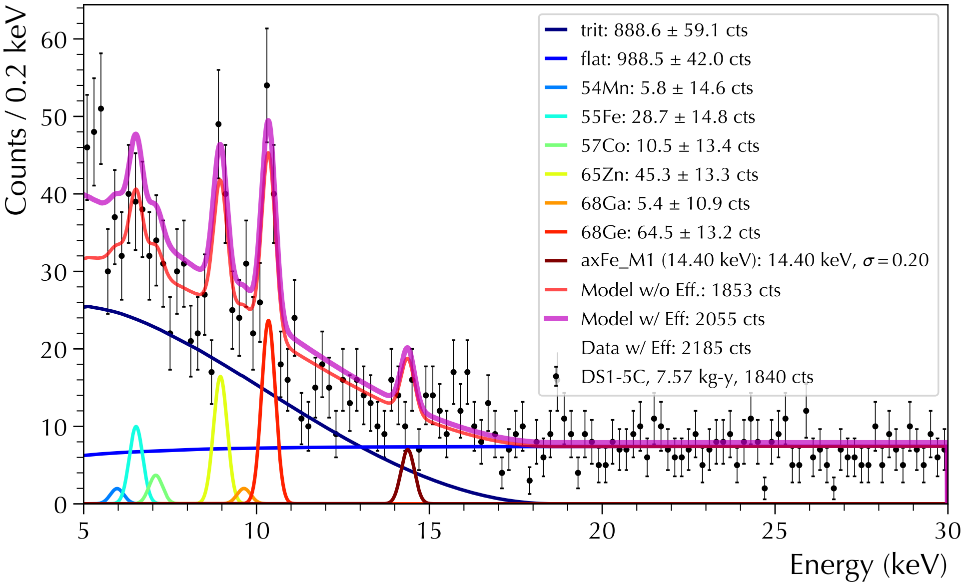

Figure 5.22: DS1–5C fitted spectrum from 5–30 keV, with a 90% CL axion signal at 14.4 keV and a floating peak width.

The background model for the Data Set 0 analysis consisted of tritium and flat backgrounds, and a single cosmogenic peak for ^{68}Ge. With the combined DS1–5C spectrum, additional features are present. The low-energy excess observed in the $^{\mathrm{enr}}$Ge spectrum tends to inflate the counts in cosmogenic peaks and cause them to broaden, and in this search we fix each to their expectation values σ_{MJ}.

The width of the 14.4 keV signal peak is a source of systematic error in the analysis. To examine this contribution, the width of the signal peak was allowed to float, with a Gaussian constraint of $\sigma = 0.1$ keV from the expected value σ_{MJ}. We find that allowing the width of the peak to float allows the most counts to be attributed to the axion signal. We conservatively take this to be the upper limit on the observed counts N_{obs} to a 90% confidence level. Table 5.13 gives the fit results comparing the fixed and floating width 14.4 keV peak. The fit result from 5–30 keV is given in Figure 5.22, and the resulting profile likelihood curves are shown in Figure 5.23.

As in Section 5.4, the effect of the uncertainty in the fast pulse acceptance was considered. At 14.4 keV, this is a relatively smaller effect than below 5 keV. Fig-

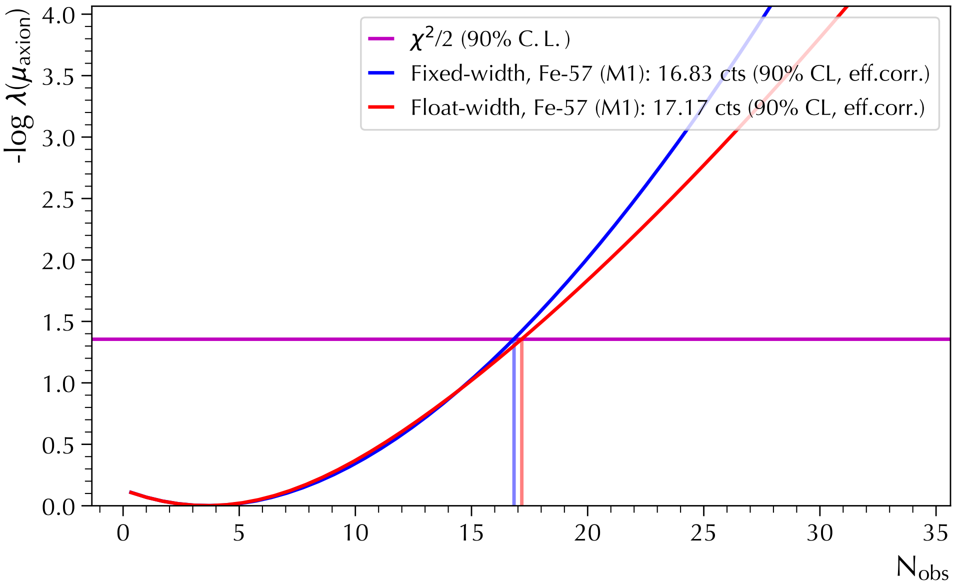

Figure 5.23: Profile likelihood curves for fixed (blue) and floating (red) peak widths.

Table 5.13: Fit results for the 14.4 keV axion study. (Counts are efficiency-corrected.)

Component	Fixed-width 14.4 peak	Floating-width 14.4 peak
n_{trit}	888.78 ± 59.22	888.95 ± 59.19
n_{flat}	988.25 ± 41.99	988.36 ± 41.98
n_{54Mn}	5.58 ± 14.71	5.56 ± 14.71
n_{55Fe}	28.71 ± 14.81	28.71 ± 14.81
n_{57Co}	10.53 ± 13.41	10.51 ± 13.41
n_{65Zn}	45.26 ± 13.34	45.23 ± 13.34
n_{68Ga}	5.40 ± 10.87	5.39 ± 10.86
n_{68Ge}	64.48 ± 13.23	64.47 ± 13.23
n_{axion} (90%)	16.831	17.165
σ_{axion}	0.2028 keV	0.19 ± 0.11 keV

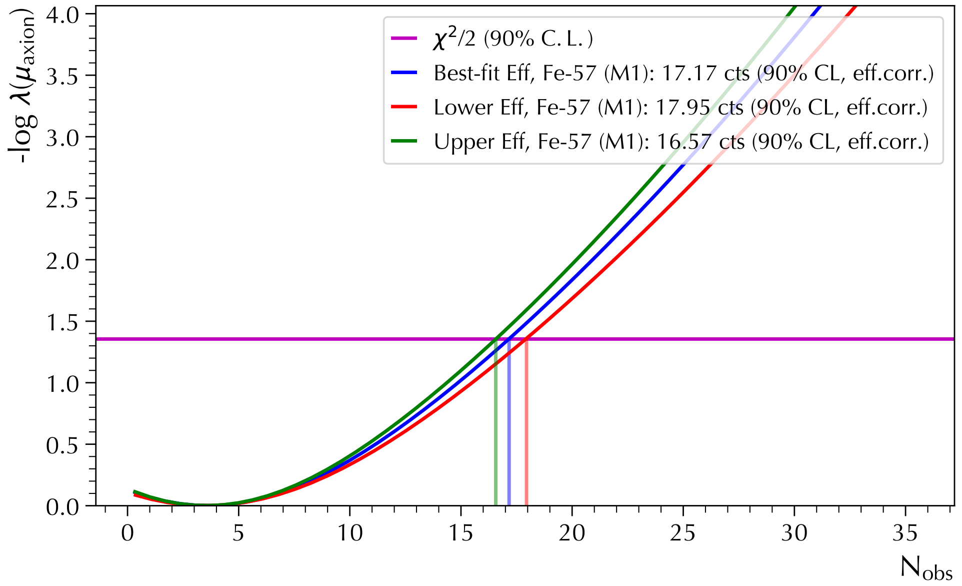

Figure 5.24: Profile likelihood curves obtained by considering the lower and upper bounds on the efficiency.

ure 5.24 shows the effect of repeating the fit using the upper and lower efficiency curves given in Figure 5.12. The number of axion counts observed varies by less than 1 count.

To set a limit on the coupling $g_{ae}\ g_{aN}^{\mathrm{eff}}$, a procedure similar to the previous sections is followed. The expected number of axion counts can be expressed in terms of the axion flux, axioelectric effect, and the detector exposure η:

$$N_{\mathrm{exp}} = \Phi_a'\ \sigma_{ae}'\ \eta \tag{5.22}$$

$$= (g_{ae}\ g_{aN}^{\mathrm{eff}})^2\ \Phi_a\ \sigma_{ae}\ \eta \tag{5.23}$$

As before, the number of "observed" counts is determined from the 90% CL upper limit of the profile likelihood (assuming no signal is seen). It is also corrected for the detection efficiency, as in previous sections.

A bound on the product $g_{ae}\ g_{aN}^{\mathrm{eff}}$ can then be set:

$$\left|g_{ae}\ g_{aN}^{\mathrm{eff}}\right| \leq \left(\frac{N_{\mathrm{obs}}}{\Phi_a\ \sigma_{ae}\ \eta}\right)^{1/2} \tag{5.24}$$

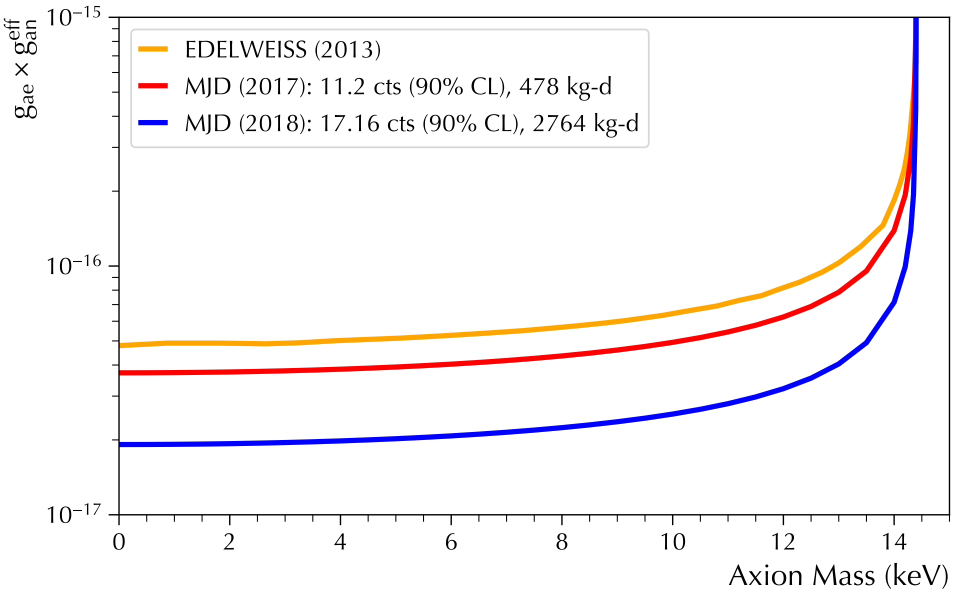

Figure 5.25: Limit on $g_{ae}\ g_{aN}^{\text{eff}}$ as a function of axion mass m_a.

Along with the β parameter, the axioelectric cross section σ_{ae} can be written as a function of axion mass (Equation 1.35). This allows the bound on $g_{ae}\ g_{aN}^{\text{eff}}$ to be calculated as a function of axion mass as well. This strategy was first used by EDELWEISS [80], and improved upon by MAJORANA in the analysis from Data Set 0 [79]. The increased exposure of the DS1–5C analysis, in conjunction with the lower backgrounds due to installation of the UGEFCu inner shield, allows an improved result on the $g_{ae}\ g_{aN}^{\text{eff}}$ coupling, by roughly a factor two. Figure 5.25 shows the bound on $g_{ae}\ g_{aN}^{\text{eff}}$ as a function of axion mass.

Taking into account the systematic error from the efficiency uncertainty, we obtain a limit for $m_a = 0$:

$$g_{ae}g_{aN}^{\text{eff}} \leq 1.92^{+0.04}_{-0.03} \times 10^{-17} \tag{5.25}$$

5.7 CONCLUSION AND OUTLOOK

The LAT analysis described in Chapters 4 and 5 is the lowest-energy threshold rare event search to date with the DEMONSTRATOR.[2] The LAT waveform fit, threshold analysis, high-frequency noise removal, and burst cut algorithms reduced the noise in the raw data under 5 keV by more than 5 orders of magnitude (Figure 4.37), without an excessive reduction in detector exposure. The small-angle Compton scatter method for determining the fast pulse acceptance will increase in accuracy as more calibration data are taken. Work is ongoing by MAJORANA to incorporate a model of the transition (dead) layer into simulations, which may also be used to improve the acceptance measurement. The search for solar axions from the axion-electron coupling resulted in a best lower bound on the axion-electron coupling constant, $g_{ae} \leq 1.92^{+0.16}_{-0.01} \times 10^{-11}$ at the 90% confidence level. This is an improvement over the MALBEK result [132], but the discovery of a background below 5 keV not accounted for in the model significantly affects the sensitivity of the search. Ongoing efforts to understand this background are discussed below. The search for solar axions from the nuclear transition of ^{57}Fe to its first excited state resulted in a factor of two improvement over the previous MAJORANA result, with a value $g_{ae}\ g^{\mathrm{eff}}_{aN} \leq 1.92^{+0.04}_{-0.03} \times 10^{-17}$ for axion mass $m_a = 0$.

Many rare-event searches beyond the ones described here in Chapter 5 are possible with the 1 keV LAT spectrum. Improvements on the 2017 Data Set 0 result [79] for bosonic pseudoscalar (axionlike) and vector dark matter, Pauli exclusion principle-violating decays, and electron decay are all possible. A study is already ongoing to search for coherent Bragg scattering from solar axions, setting a limit on the axion-photon coupling $g_{a\gamma}$ by searching the low energy spectrum for a relatively complicated time-dependent signal [72]. A search for low-mass WIMPs is still feasible, though a

---

[2] The LIPs study [90] also quoted a 1 keV threshold, but used a high-multiplicity event requirement not compatible with an axion or WIMP search.

Table 5.14: Additional nuclear transition energies for solar axions.

Isotope	E (keV)	Ref.	Note
^{169}Tm	8.41	[154]	Strong overlapping ^{65}Zn line in $^{\text{enr}}$Ge at 8.98 keV
^{83}Kr	9.40	[155]	Weak overlapping line ^{68}Ga at 9.66 keV
^{57}Fe	14.4	[82]	Section 5.6 finds $g_{ae}\ g_{aN}^{\text{eff}} \leq 1.916 \times 10^{-17}$.
^{55}Mn	126	[82]	Energy outside current analysis range
^{23}Na	440	[82]	”
^{7}Li	478	[156]	”
^{3}He	5500	[156]	”

significant effort may be necessary to improve the fast signal acceptance efficiency below 1 keV. Though the Demonstrator in many cases does not improve on limits set by dedicated dark matter search experiments such as LUX, it provides an important cross-check on these experiments by using a different isotope for detection.

There also exist additional predicted axion peaks from nuclear transitions beyond the 14.4 ^{57}Fe peak. These are listed in Table 5.14. The lower-energy lines overlap with known cosmogenic backgrounds in the $^{\text{enr}}$Ge and would likely produce a weak limit. At higher energies (outside the current analysis region), the low background rate of the Demonstrator may be competitive.

The origin of the upward rise of events in the $^{\text{enr}}$Ge spectrum, most significantly below 5 keV, remains unknown at present. Likely explanations for the excess are residual slow pulse contamination, and radioactive backgrounds not in the current model, including alpha-related interactions from ^{210}Po and other Rn daughters. Section 5.4 discussed the effect of a tighter slow pulse cut, which reduced the overall number of events in the spectrum but did not fundamentally change the shape of the distribution. The reduced thickness of the passivated transition layer may allow very low energy events into the detector bulk which would ordinarily be stopped by the thicker n^{+} dead layer. A radioactive background originating from detector components very near the passivated surface of the detectors may cause a low energy continuum of events. The existence of the spectral line from ^{210}Pb at 46.5 keV (and

Table 5.15: Detector rates 1–5 keV in Modules 1 and 2, $^{\mathrm{enr}}$Ge and $^{\mathrm{nat}}$Ge, for different Data Set combinations. (Rates are in cts/keV/kg-d.)

DS	$r_{\mathrm{enr,M1}}$	$r_{\mathrm{enr,M2}}$	$r_{\mathrm{nat,M1}}$	$r_{\mathrm{nat,M2}}$
0	0.318(30)	–	3.34(24)	–
1	0.216(19)	–	4.75(96)	–
2	0.198(44)	–	7.66 ± 2.90	–
3	0.139(21)	–	3.00(37)	–
4	–	0.230(60)	–	2.81(60)
5A	0.158(20)	0.179(39)	2.30(23)	2.03(15)
5B	0.142(17)	0.231(42)	2.48(19)	1.99(18)
5C	0.168(35)	0.203(78)	1.81(31)	1.48(27)
0–5C	0.191(09)	0.207(24)	2.75(11)	2.00(11)
1–5C	0.169(09)	0.207(24)	2.53(13)	2.00(11)
1–4,5B,5C	0.175(10)	0.227(31)	2.74(15)	1.98(15)

its apparent weakness in the $^{\mathrm{nat}}$Ge detectors) may be an indicator that other ^{210}Pb decay products, such as x-rays and Auger electrons from internal conversion [135], are responsible for the excess.

Two preliminary studies were performed in an attempt to determine if the excess is localized to a particular Module or set of detectors. Table 5.15 gives the rate from 1–5 keV in the $^{\mathrm{enr}}$Ge and $^{\mathrm{nat}}$Ge detectors in both Modules, for different Data Set combinations. We find that Module 2 $^{\mathrm{enr}}$Ge detectors have slightly higher rates than the Module 1 $^{\mathrm{enr}}$Ge detectors, by ∼0.1–0.2 cts/kg-d, but find no obvious outliers to account for the excess events. The height of the 46.5 keV peak in an individual detector may be correlated with its 1–5 keV rate. To check this possibility, the individual detector spectra from DS1–5C were first weighted by exposure and efficiency corrected. The height of the 46 keV peak above the background was measured for each detector by computing the background rate in the side-band region r_{bkg}, and the rate in the peak r_{peak}. Figure 5.26 shows the comparison of the peak-to-background ratio $r_{\mathrm{peak}}/r_{\mathrm{bkg}}$ to the 1–5 keV rate r_{1-5} in cts/kg-d. There is no obvious correlation at this time between the two features, but the uncertainties are relatively large, and the study would benefit from the inclusion of Data Set 6 and beyond.

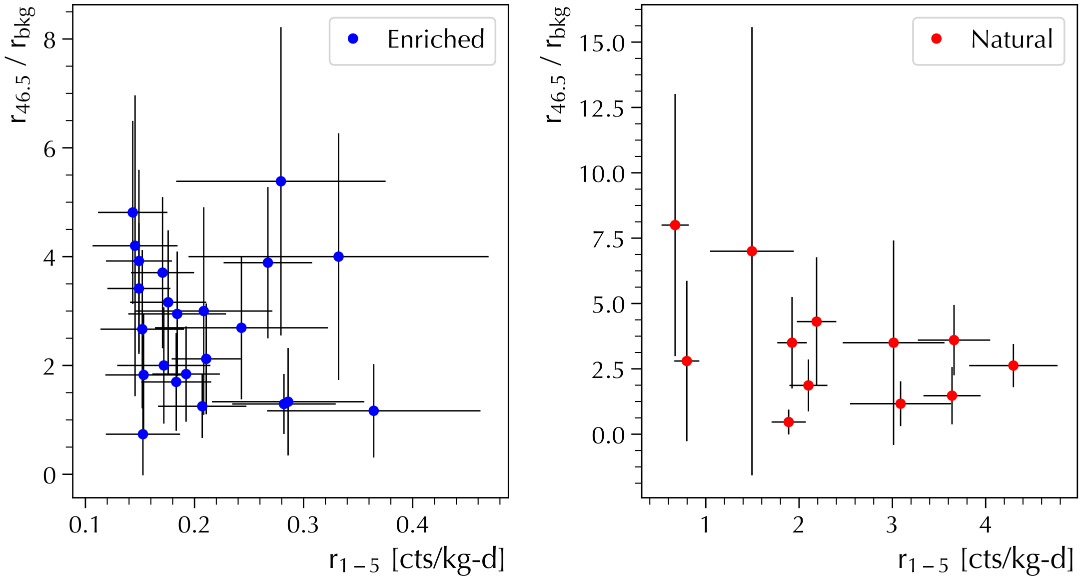

Figure 5.26: Relative height of the 46.5 keV peak in each detector in DS1–5C, compared with its rate from 1–5 keV. No obvious correlation is present.

The development of a comprehensive background model at low energy from simulations is an attractive goal. Work has already been done by MAJORANA to incorporate an improved simulated transition layer by matching to calibration data. If the excess is caused by ^{210}Pb or one of its associated decay products, it will also be necessary to simulate radioactivity from different positions and combinations of detector components to find the one that most closely matches the observed spectrum. One preliminary simulation of this background is shown in Figure 5.27, which shows a rising component at low energy, whose amplitude is constrained by the height of the 46.5-keV line. Further work is also needed to understand the behavior of charge carriers at or near the passivated transition layer. It is also possible that the excess is related to the observed α event background removed at high energy by the DCR cut. Work by Gruszko [94] indicates these α events are originating from Rn daughters plated out on the surface of the PTFE bushing holding the point contact pin.

As discussed in Chapter 1, an approximate estimate of the obtainable limit on g_{ae} can be found by assuming that the axion signal is on average, no larger than the

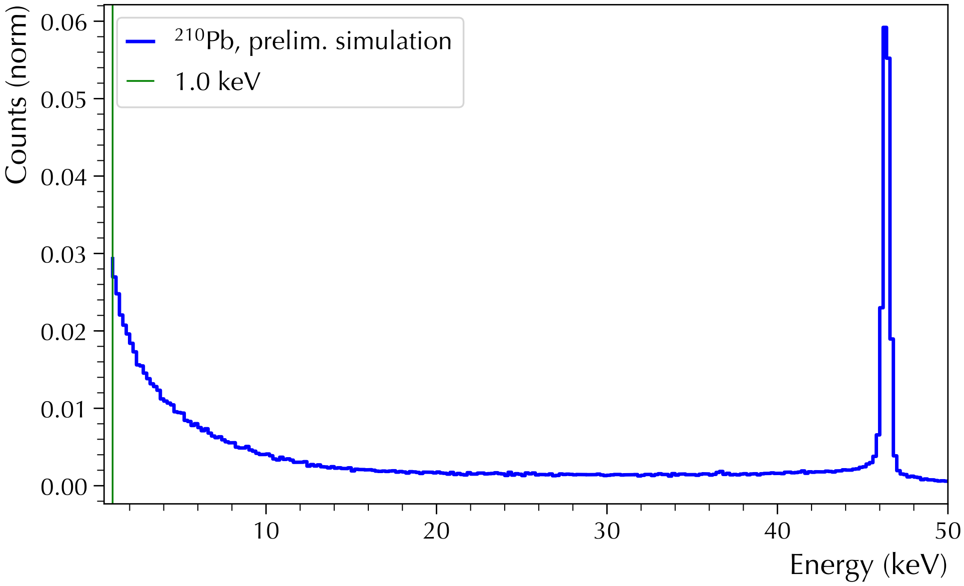

Figure 5.27: Preliminary ^{210}Pb PDF from simulation, including a low-energy rise component limited by the height of the 46.5-keV peak.

statistical $\sqrt{N}$ error in the energy region of interest:

$$N_{\text{obs}} = \begin{cases} N_{\text{fit}} & \text{if spectrum is known} \\ \sqrt{B \Delta E M t} & \text{if projection} \end{cases} \tag{5.26}$$

The bound on g_{ae} from the DS1–5C analysis is significantly weaker than projected by this formula, since the "observed" axion signal is much larger than the error bar in the data. If a future background model can explain the observed low energy rise (perhaps in terms of new radioactive backgrounds), the resulting strength of the axion component may be consistent with zero counts, as originally expected. The exclusion limit is then dependent on the size of the error bar in the data, which in turn depends on the dominant background component. If the background excess is not from slow pulses and cannot be removed by improved PSA, then it will drive the rate at low energy higher. If the excess can be removed by PSA, we expect to be dominated by tritium. Figure 5.28 shows the projected sensitivity to g_{ae} for these two background levels.

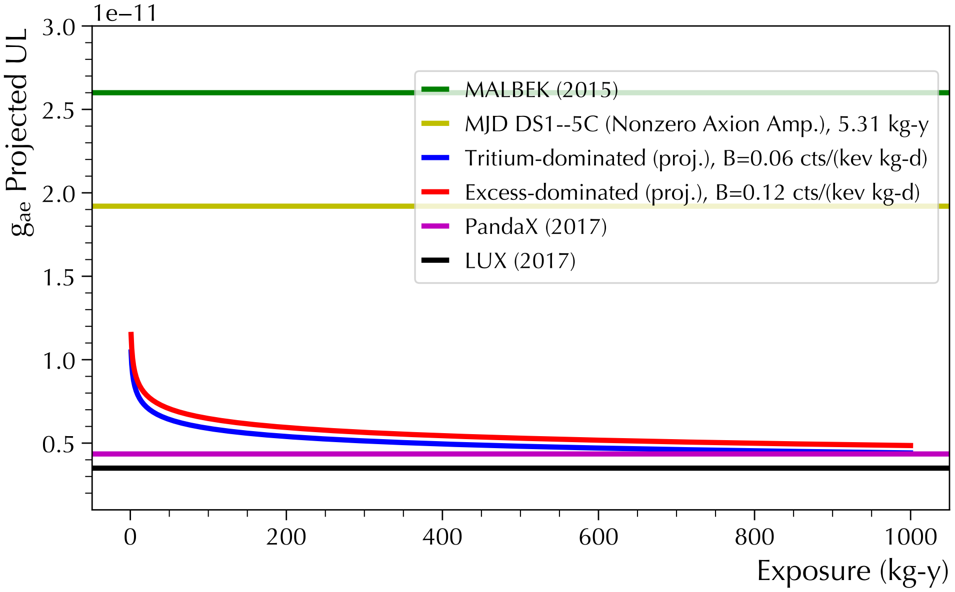

Figure 5.28: Projections of the possible limit on g_{ae} with Majorana for two cases. Red: The excess of events remains after PSA cuts ("excess-dominated") but is accounted for by an improved background model. Blue: The excess is cut and the dominant background is tritium ("tritium-dominated").

The performance of the planned next-generation LEGEND experiment [36] at low energy remains an open question at this time. The liquid argon active veto used by the GERDA experiment created an overwhelming low-energy background due to the beta decay of ^{39}Ar, but feasibility studies for obtaining depleted argon (with potentially reduced backgrounds) are underway. The ultimate exposure goal would be 10 ton-years of enriched exposure, with significantly lower backgrounds at high energy. As a final projection, Figure 5.29 gives a possible exclusion limit on g_{ae} for the LEGEND experiment with a 1 keV threshold.

In the case of the axion-electron coupling, Figure 5.29 suggests that a large-scale Ge experiment would not provide a large advantage over current results from liquid xenon TPC experiments. Since the flux peaks near 1 keV, improvements to the energy threshold would not significantly affect the result, which will mainly be determined by the exposure. However, this is only one example of the rare event searches possible with germanium technology. Incorporating precise dead layer and crystal axes

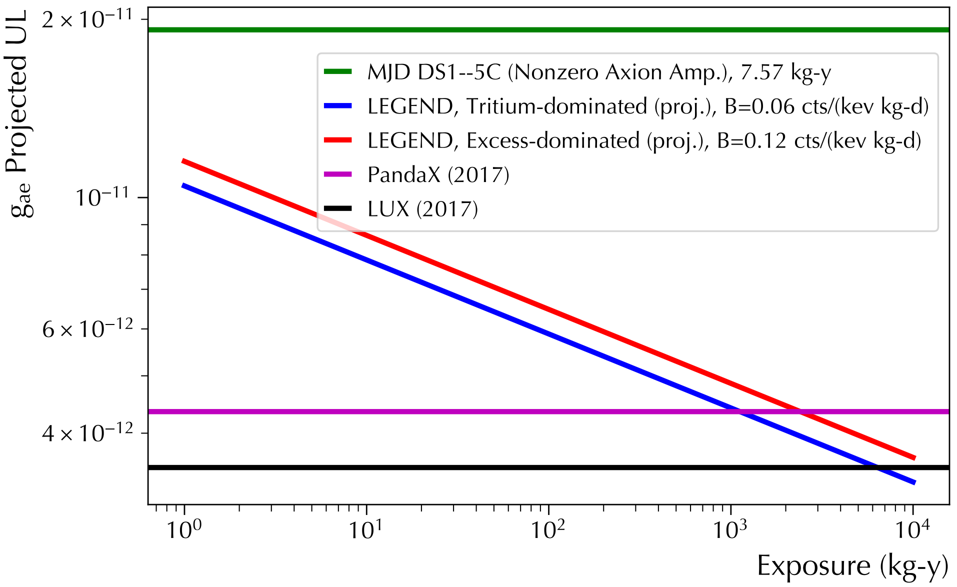

Figure 5.29: Sensitivity to g_{ae} for a 10 ton-year exposure with the LEGEND experiment.

measurements in the LEGEND detectors would reduce systematic uncertainties from the slow pulse backgrounds and allow competitive measurements of the $g_{a\gamma}$ coupling via Bragg scattering. Energy thresholds well below 1 keV have been achieved by the small-scale CoGeNT, MALBEK, and CDEX detectors, and a large detector mass with a low threshold would enable significant improvements over these previous Ge results, surpassing what is possible with the DEMONSTRATOR.

Maintaining a low-energy capability in the LEGEND experiment should be carefully considered. The MAJORANA low energy program has significantly extended the physics reach of the DEMONSTRATOR, making searches for axions, bosonic dark matter, LIPs, WIMPs, and many other rare event searches possible. The expected limits often do not surpass experiments specifically dedicated to these searches, but results from Ge provide an important cross-check on other results and increase the scientific impact of LEGEND.

Bibliography

[1] CS Wu et al. “Experimental Test of Parity Conservation in Beta Decay”. *Physical Review* 105.4 (1957), p. 1413.

[2] M Goldhaber, L Grodzins, and AW Sunyar. “Evidence for circular polarization of bremsstrahlung produced by beta rays”. *Physical Review* 106.4 (1957), p. 826.

[3] M Shaevitz. *CP Violation*. `https://www.nevis.columbia.edu/daedalus/motiv/cp.html`. Accessed: 2018-04-01.

[4] JM Pendlebury et al. “Revised experimental upper limit on the electric dipole moment of the neutron”. *Physical Review D* 92.9 (2015), p. 092003.

[5] B Graner et al. “Reduced Limit on the Permanent Electric Dipole Moment of Hg 199”. *Physical Review Letters* 116.16 (2016), p. 161601.

[6] Nicola Cabibbo. “Unitary symmetry and leptonic decays”. *Physical Review Letters* 10.12 (1963), p. 531.

[7] Makoto Kobayashi and Toshihide Maskawa. “CP-violation in the renormalizable theory of weak interaction”. *Progress of Theoretical Physics* 49.2 (1973), pp. 652–657.

[8] Ziro Maki, Masami Nakagawa, and Shoichi Sakata. “Remarks on the unified model of elementary particles”. *Progress of Theoretical Physics* 28.5 (1962), pp. 870–880.

[9] Fred L Wilson. “Fermi’s theory of beta decay”. *American Journal of Physics* 36.12 (1968), pp. 1150–1160.

[10] Frederick Reines et al. “Detection of the free antineutrino”. *Physical Review* 117.1 (1960), p. 159.

[11] Gaillard Danby et al. “Observation of high-energy neutrino reactions and the existence of two kinds of neutrinos”. *Physical Review Letters* 9.1 (1962), p. 36.

[12] K Kodama et al. “Observation of tau neutrino interactions”. *Physics Letters B* 504.3 (2001), pp. 218–224.

[13] Raymond Davis Jr, Don S Harmer, and Kenneth C Hoffman. “Search for neutrinos from the sun”. *Physical Review Letters* 20.21 (1968), p. 1205.

[14] Bruce T Cleveland et al. “Measurement of the solar electron neutrino flux with the Homestake chlorine detector”. *The Astrophysical Journal* 496.1 (1998), p. 505.

[15] John N Bahcall, Neta A Bahcall, and Giora Shaviv. “Present Status of the Theoretical Predictions for the Cl 37 Solar-Neutrino Experiment”. *Physical Review Letters* 20.21 (1968), p. 1209.

[16] Kohji S Hirata et al. “Observation of ^{8}B solar neutrinos in the Kamiokande-II detector”. *Physical Review Letters* 63.1 (1989), p. 16.

[17] V Gribov and B Pontecorvo. “Neutrino astronomy and lepton charge”. *Physics Letters B* 28.7 (1969), pp. 493–496.

[18] Y Fukuda et al. “Evidence for oscillation of atmospheric neutrinos”. *Physical Review Letters* 81.8 (1998), p. 1562.

[19] A Gando et al. “Reactor on-off antineutrino measurement with KamLAND”. *Physical Review D* 88.3 (2013), p. 033001.

[20] Ivan Esteban et al. “Updated fit to three neutrino mixing: exploring the accelerator - reactor complementarity”. *Journal of High Energy Physics* 2017.1 (2017), p. 87.

[21] J Engel, M Ramsey-Musolf, and P Vogel. “School on the Physics of Neutrinoless Double Beta Decay”. UMass Amherst Center For Fundamental Interactions Seminar Series. 2017.

[22] VN Aseev et al. “Upper limit on the electron antineutrino mass from the Troitsk experiment”. *Physical Review D* 84.11 (2011), p. 112003.

[23] Ch Kraus et al. “Final results from Phase II of the Mainz Neutrino Mass Search in Tritium β-decay”. *The European Physical Journal C-Particles and Fields* 40.4 (2005), pp. 447–468.

[24] Ettore Majorana and Luciano Maiani. “A symmetric theory of electrons and positrons”. *Ettore Majorana Scientific Papers.* Springer, 2006, pp. 201–233.

[25] Andrei D Sakharov. “Violation of CP invariance, C asymmetry, and baryon asymmetry of the universe”. *Soviet Physics Uspekhi* 34.5 (1991), p. 392.

[26] Steven Weinberg. “Baryon-and lepton-nonconserving processes”. *Physical Review Letters* 43.21 (1979), p. 1566.

[27] M Fukugita and Tsutomu Yanagida. “Barygenesis without grand unification”. *Physics Letters B* 174.1 (1986), pp. 45–47.

[28] Frans R Klinkhamer and Nicholas S Manton. “A saddle-point solution in the Weinberg-Salam theory”. *Physical Review D* 30.10 (1984), p. 2212.

[29] Maria Goeppert-Mayer. “Double beta-disintegration”. *Physical Review* 48.6 (1935), p. 512.

[30] SR Elliott, AA Hahn, and MK Moe. “Direct evidence for two-neutrino double-beta decay in Se 82”. *Physical Review Letters* 59.18 (1987), p. 2020.

[31] Stefano Dell’Oro et al. “Neutrinoless double beta decay: 2015 review”. *Advances in High Energy Physics* 2016 (2016).

[32] WH Furry. “On transition probabilities in double beta-disintegration”. *Physical Review* 56.12 (1939), p. 1184.

[33] J Schechter and José WF Valle. “Neutrino decay and spontaneous violation of lepton number”. *Physical Review D* 25.3 (1982), p. 774.

[34] Frank T Avignone III, Steven R Elliott, and Jonathan Engel. “Double beta decay, Majorana neutrinos, and neutrino mass”. *Reviews of Modern Physics* 80.2 (2008), p. 481.

[35] Jonathan Engel and Javier Menéndez. “Status and future of nuclear matrix elements for neutrinoless double-beta decay: a review”. *Reports on Progress in Physics* 80.4 (2017), p. 046301.

[36] N Abgrall et al. “The Large Enriched Germanium Experiment for Neutrinoless $\beta\beta$ Decay: LEGEND-200 at LNGS”. Proposal submitted to LNGS. Preprint at `https://github.com/legend-exp/legend200-proposal-lngs/releases/tag/v03.02`.

[37] A Gando et al. “Search for Majorana neutrinos near the inverted mass hierarchy region with KamLAND-Zen”. *Physical Review Letters* 117.8 (2016), p. 082503.

[38] Anna Julia Zsigmond. *New results from GERDA Phase II.* 2018. DOI: `10.5281/zenodo.1287604`. URL: `https://doi.org/10.5281/zenodo.1287604`.

[39] Vincente Guiseppe. *New Results from the* MAJORANA DEMONSTRATOR *Experiment.* 2018. DOI: `10.5281/zenodo.1286900`. URL: `https://doi.org/10.5281/zenodo.1286900`.

[40] C Alduino et al. "First Results from CUORE: A Search for Lepton Number Violation via $0\nu\beta\beta$ Decay of Te 130". *Physical Review Letters* 120.13 (2018), p. 132501.

[41] M Agostini et al. "Improved Limit on Neutrinoless Double-β Decay of ^{76}Ge from GERDA Phase II". *Physical Review Letters* 120.13 (2018), p. 132503.

[42] CE Aalseth et al. "Search for Neutrinoless Double-β Decay in ^{76}Ge with the MAJORANA DEMONSTRATOR". *Physical Review Letters* 120.13 (2018), p. 132502.

[43] N Abgrall et al. "The large enriched germanium experiment for neutrinoless double beta decay (LEGEND)". *AIP Conference Proceedings.* Vol. 1894. 1. AIP Publishing. 2017, p. 020027.

[44] C. Patrignani et al. "Review of Particle Physics". *Chin. Phys.* C40.10 (2016), p. 100001. DOI: `10.1088/1674-1137/40/10/100001`.

[45] Pierre Sikivie. "The pooltable analogy to axion physics". *arXiv preprint hep-ph/9506229* (1995).

[46] Roberto D Peccei and Helen R Quinn. "CP conservation in the presence of pseudoparticles". *Physical Review Letters* 38.25 (1977), p. 1440.

[47] Frank Wilczek. "Problem of Strong P and T Invariance in the Presence of Instantons". *Physical Review Letters* 40.5 (1978), p. 279.

[48] Steven Weinberg. "A new light boson?" *Physical Review Letters* 40.4 (1978), p. 223.

[49] Joerg Jaeckel and Andreas Ringwald. "The low-energy frontier of particle physics". *Annual Review of Nuclear and Particle Science* 60 (2010), pp. 405–437.

[50] Georg G Raffelt. "Axions: motivation, limits and searches". *Journal of Physics A: Mathematical and Theoretical* 40.25 (2007), p. 6607.

[51] Duane A Dicus et al. “Astrophysical bounds on very-low-mass axions”. *Physical Review D* 22.4 (1980), p. 839.

[52] Jihn E Kim. “Weak-interaction singlet and strong CP invariance”. *Physical Review Letters* 43.2 (1979), p. 103.

[53] Michael Dine, Willy Fischler, and Mark Srednicki. “A simple solution to the strong CP problem with a harmless axion”. *Physics letters B* 104.3 (1981), pp. 199–202.

[54] AR Zhitnitsky. “Possible suppression of axion-hadron interactions”. *Sov. J. Nucl. Phys.* 31 (1980), p. 260.

[55] CL Bennett et al. “Nine-year Wilkinson Microwave Anisotropy Probe observations: final maps and results”. *The Astrophysical Journal Supplement Series* 208.2 (2013), p. 20.

[56] Maurizio Giannotti et al. “Stellar recipes for axion hunters”. *Journal of Cosmology and Astroparticle Physics* 2017.10 (2017), p. 010.

[57] Jordi Isern et al. “White dwarfs as physics laboratories: the case of axions”. *arXiv preprint arXiv:1204.3565* (2012).

[58] Alejandro H Córsico et al. “An asteroseismic constraint on the mass of the axion from the period drift of the pulsating DA white dwarf star L19-2”. *Journal of Cosmology and Astroparticle Physics* 2016.07 (2016), p. 036.

[59] Georg G Raffelt. *Astrophysical axion bounds*. Springer, 2008, pp. 51–71.

[60] GW Fraser et al. “Potential solar axion signatures in X-ray observations with the XMM–Newton observatory”. *Monthly Notices of the Royal Astronomical Society* 445.2 (2014), pp. 2146–2168.

[61] Paolo Gondolo and Georg G Raffelt. “Solar neutrino limit on axions and keV-mass bosons”. *Physical Review D* 79.10 (2009), p. 107301.

[62] Nicolás Viaux et al. “Neutrino and axion bounds from the globular cluster M5 (NGC 5904)”. *Physical Review Letters* 111.23 (2013), p. 231301.

[63] Alexander Friedland, Maurizio Giannotti, and Michael Wise. “Constraining the axion-photon coupling with massive stars”. *Physical Review Letters* 110.6 (2013), p. 061101.

[64] Jochen Keller and Armen Sedrakian. “Axions from cooling compact stars: Pair-breaking processes”. *Nuclear Physics A* 897 (2013), pp. 62–69.

[65] P Sikivie. “Experimental tests of the “invisible” axion”. *Physical Review Letters* 51.16 (1983), p. 1415.

[66] Pierre Sikivie. “Detection rates for “invisible”-axion searches”. *Physical Review D* 32.11 (1985), p. 2988.

[67] M Arik et al. “Search for solar axions by the CERN axion solar telescope with He 3 buffer gas: Closing the hot dark matter gap”. *Physical Review Letters* 112.9 (2014), p. 091302.

[68] E Armengaud et al. “Conceptual design of the International Axion Observatory (IAXO)”. *Journal of Instrumentation* 9.05 (2014), T05002.

[69] N Du et al. “Search for Invisible Axion Dark Matter with the Axion Dark Matter Experiment”. *Physical Review Letters* 120.15 (2018), p. 151301.

[70] RJ Creswick et al. “Theory for the direct detection of solar axions by coherent Primakoff conversion in germanium detectors”. *Physics Letters B* 427.3-4 (1998), pp. 235–240.

[71] FT Avignone III et al. “Solar axion experiments using coherent Primakoff conversion in single crystals”. *Nuclear Physics B-Proceedings Supplements* 72 (1999), pp. 176–182.

[72] Wenqin Xu and Steven R Elliott. “Solar axion search technique with correlated signals from multiple detectors”. *Astroparticle Physics* 89 (2017), pp. 39–50.

[73] D Li et al. “Theoretical Estimate of the Sensitivity of the CUORE Detector to Solar Axions”. *Journal of Cosmology and Astroparticle Physics* 2015.10 (2015), p. 065.

[74] Savas Dimopoulos, Glenn D Starkman, and Bryan W Lynn. “Atomic enhancements in the detection of weakly interacting particles”. *Phys. Lett.* 168.ITP-802-STANFORD (1985), pp. 145–150.

[75] FT Avignone III et al. “Laboratory limits on solar axions from an ultralow-background germanium spectrometer”. *Physical Review D* 35.9 (1987), p. 2752.

[76] DS Akerib et al. “First searches for axions and axionlike particles with the LUX experiment”. *Physical Review Letters* 118.26 (2017), p. 261301.

[77] Changbo Fu et al. “Limits on Axion Couplings from the First 80 Days of Data of the PandaX-II Experiment”. *Physical Review Letters* 119.18 (2017), p. 181806.

[78] Javier Redondo. “Solar Axion Flux From the Axion-Electron Coupling”. *Journal of Cosmology and Astroparticle Physics* 2013.12 (2013), p. 008.

[79] N Abgrall et al. “New Limits on Bosonic Dark Matter, Solar Axions, Pauli Exclusion Principle Violation, and Electron Decay from the MAJORANA DEMONSTRATOR”. *Physical Review Letters* 118.16 (2017), p. 161801.

[80] E Armengaud et al. “Axion searches with the EDELWEISS-II experiment”. *Journal of Cosmology and Astroparticle Physics* 2013.11 (2013), p. 067.

[81] FT Avignone III et al. “Search for axions from the 1115-keV transition of Cu 65”. *Physical Review D* 37.3 (1988), p. 618.

[82] WC Haxton and KY Lee. “Red-giant evolution, metallicity, and new bounds on hadronic axions”. *Physical Review Letters* 66.20 (1991), p. 2557.

[83] Jaret Heise. “The Sanford Underground Research Facility at Homestake”. *Journal of Physics: Conference Series*. Vol. 606. 1. IOP Publishing. 2015, p. 012015.

[84] PN Luke et al. “Low capacitance large volume shaped-field germanium detector”. *IEEE Transactions on Nuclear Science* 36.1 (1989), pp. 926–930. ISSN: 0018-9499. DOI: `10.1109/23.34577`.

[85] Craig E Aalseth et al. “CoGeNT: A search for low-mass dark matter using p-type point contact germanium detectors”. *Physical Review D* 88.1 (2013), p. 012002.

[86] N Abgrall et al. “The MAJORANA DEMONSTRATOR Neutrinoless Double-Beta Decay Experiment”. *Advances in High Energy Physics* 2014 (2014).

[87] N Abgrall et al. “The Processing of Enriched Germanium for the MAJORANA DEMONSTRATOR and R&D for a Next Generation Double-Beta Decay Experiment”. *NIM A* 877 (2018), pp. 314–322.

[88] N Abgrall et al. “Muon Flux Measurements at the Davis Campus of the Sanford Underground Research Facility with the MAJORANA DEMONSTRATOR Veto System”. *Astroparticle Physics* 93 (2017), pp. 70–75.

[89] N Abgrall et al. “The MAJORANA DEMONSTRATOR Calibration System”. *NIM A* 872 (2017), pp. 16–22.

[90] SI Alvis et al. “First Limit on the Direct Detection of Lightly Ionizing Particles for Electric Charge as Low as $e/1000$ with the MAJORANA DEMONSTRATOR”.

Phys. Rev. Lett. 120 (21 2018), p. 211804. DOI: `10.1103/PhysRevLett.120.211804`.

[91] N Abgrall et al. “The Majorana Demonstrator Radioassay Program”. *NIM A* 828 (2016), pp. 22–36.

[92] N Abgrall et al. “The Majorana Parts Tracking Database”. *NIM A* 779 (2015), pp. 52–62.

[93] I Guinn. “Low background signal readout electronics for the Majorana Demonstrator”. *AIP Conference Proceedings*. Vol. 1672. 1. AIP Publishing. 2015, p. 030001.

[94] Julieta Gruszko. “Surface Alpha Interactions in P-Type Point-Contact HPGe Detectors: Maximizing Sensitivity of ^{76}Ge Neutrinoless Double-Beta Decay Searches”. PhD thesis. University of Washington, 2017.

[95] Mark A Howe et al. “Sudbury Neutrino Observatory Neutral Current Detector Acquisition Software Overview”. *IEEE Transactions on Nuclear Science* 51.3 (2004), pp. 878–883.

[96] Sergio Zimmermann et al. “Implementation and Performance of the Electronics and Computing System of the Gamma Ray Energy Tracking In-Beam Nuclear Array (GRETINA)”. *IEEE Transactions on Nuclear Science* 59.5 (2012), pp. 2494–2500.

[97] Rene Brun and Fons Rademakers. “ROOT – an object oriented data analysis framework”. *NIM A* 389.1-2 (1997), pp. 81–86.

[98] M Agostini et al. “The MGDO software library for data analysis in Ge neutrinoless double-beta decay experiments”. *Journal of Physics: Conference Series*. Vol. 375. 4. IOP Publishing. 2012, p. 042027.

[99] D-M Mei and A Hime. “Muon-induced background study for underground laboratories”. *Physical Review D* 73.5 (2006), p. 053004.

[100] W Bugg, Y Efremenko, and S Vasilyev. “Large Plastic Scintillator Panels with WLS Fiber Readout: Optimization of Components”. *NIM A* 758 (2014), pp. 91–96.

[101] C Wiseman. *Muon Veto Analysis for the* Majorana Demonstrator *(Internal)*. Tech. rep. 2016. URL: `http://mjwiki.npl.washington.edu/pub/Majorana/AnalysisReports/Wiseman_mu_analysis.pdf`.

[102] R Massarczyk. *Update on Muon Simulations (Internal)*. Tech. rep. 2016.

[103] A Reine et al. *Run selection and data cleaning of DS5 (M1 and M2) (Internal).* Tech. rep. 2017-020. URL: `https://mjdoc.npl.washington.edu/record/1868`.

[104] C Wiseman et al. *Livetime and Exposure for* Majorana Demonstrator *Data Sets 0-5 (Internal).* Tech. rep. 2017-016. URL: `https://mjdoc.npl.washington.edu/record/1863`.

[105] J Myslik and T Caldwell. *Data Cleaning in DS0-DS5 for* $0\nu\beta\beta$*-decay Analysis (Internal).* Tech. rep. 2017-018. URL: `https://mjdoc.npl.washington.edu/record/1866?ln=en`.

[106] M Buuck. *Calculating the Active Mass of the* Majorana *Module 1 Detectors (Internal).* Tech. rep. 2016. URL: `http://mjwiki.npl.washington.edu/pub/Majorana/AnalysisReports/ActiveMassCalc.pdf`.

[107] C Wiseman. *LN Fill Tagging for the* Majorana Demonstrator*(Internal).* Tech. rep. 2016. URL: `http://mjwiki.npl.washington.edu/pub/Majorana/AnalysisReports/Wiseman_lnFills.pdf`.

[108] C Cuesta. *Multi-site Event Discrimination for the* Majorana Demonstrator. Tech. rep. 2017-014. URL: `https://mjdoc.npl.washington.edu/record/1858`.

[109] J Gruszko and S Alvis. *Delayed Charge Recovery Tagging (Internal).* Tech. rep. 2017-015. URL: `https://mjdoc.npl.washington.edu/record/1860`.

[110] W Xu et al. *Statistical Analysis for setting limit on the Neutrinoless Double Beta Decay for the* Majorana Demonstrator *(Internal).* Tech. rep. 2017-024. URL: `https://mjdoc.npl.washington.edu/record/1872`.

[111] R Nave. *HyperPhysics.* 2018. URL: `http://hyperphysics.phy-astr.gsu.edu/hbase/Solids/dsem.html` (visited on 05/04/2018).

[112] Glenn F Knoll. *Radiation Detection and Measurement.* John Wiley & Sons, 2010.

[113] AJ Tavendale and GT Ewan. “A High-resolution lithium-drift germanium gamma-ray spectrometer”. *Nucl. Instr. Methods* 25 (1963).

[114] Jens Lindhard et al. “Integral equations governing radiation effects”. *Mat. Fys. Medd. Dan. Vid. Selsk* 33.10 (1963), pp. 1–42.

[115] D Barker and D-M Mei. “Germanium detector response to nuclear recoils in searching for dark matter”. *Astroparticle Physics* 38 (2012), pp. 1–6.

[116] BJ Scholz et al. “Measurement of the low-energy quenching factor in germanium using an ^{88}Y/Be photoneutron source”. *Physical Review D* 94.12 (2016), p. 122003.

[117] William Shockley. “Currents to conductors induced by a moving point charge”. *Journal of Applied Physics* 9.10 (1938), pp. 635–636.

[118] PS Barbeau, JI Collar, and O Tench. “Large-mass ultralow noise germanium detectors: performance and applications in neutrino and astroparticle physics”. *Journal of Cosmology and Astroparticle Physics* 2007.09 (2007), p. 009.

[119] Benjamin E Shanks. “High Precision Modeling of Germanium Detector Waveforms Using Bayesian Machine Learning”. PhD thesis. University of North Carolina, 2017.

[120] Valentin T Jordanov et al. “Digital techniques for real-time pulse shaping in radiation measurements”. *NIM A* 353.1-3 (1994), pp. 261–264.

[121] Dušan Budjáš et al. “Pulse shape discrimination studies with a Broad-Energy Germanium detector for signal identification and background suppression in the GERDA double beta decay experiment”. *Journal of Instrumentation* 4.10 (2009), P10007.

[122] Reynold J Cooper et al. “Effect of a surface channel on the performance of a P-type Point Contact HPGe detector”. *NIM A* 680 (2012), pp. 48–55.

[123] J Gruszko. “Delayed charge recovery discrimination of passivated surface alpha events in P-type point-contact detectors”. *Journal of Physics: Conference Series*. Vol. 888. 1. IOP Publishing. 2017, p. 012079.

[124] Paul Mullowney et al. “Computational models of germanium point contact detectors”. *NIM A* 662.1 (2012), pp. 33–44.

[125] DS Akerib et al. “First Results From the Cryogenic Dark Matter Search in the Soudan Underground Laboratory”. *Physical Review Letters* 93.21 (2004), p. 211301.

[126] GK Giovanetti et al. “A Dark Matter Search with MALBEK”. *Physics Procedia* 61 (2015), pp. 77–84.

[127] HB Li et al. “Differentiation of bulk and surface events in p-type point-contact germanium detectors for light WIMP searches”. *Astroparticle Physics* 56 (2014), pp. 1–8.

[128] LT Yang et al. "Bulk and surface event identification in p-type germanium detectors". *NIM A* (2018).

[129] Wei Zhao et al. "Search of low-mass WIMPs with a p-type point contact germanium detector in the CDEX-1 experiment". *Physical Review D* 93.9 (2016), p. 092003.

[130] *SciPy, `scipy.stats.exponnorm`*. `https://docs.scipy.org/doc/scipy-0.16.0/reference/generated/scipy.stats.exponnorm.html`. Accessed: 2018-05-25.

[131] *SciPy, Optimization*. `https://docs.scipy.org/doc/scipy/reference/tutorial/optimize.html`. Accessed: 2018-05-25.

[132] Graham K Giovanetti. "P-Type Point Contact Germanium Detectors and Their Application in Rare-Event Searches". PhD thesis. University of North Carolina, 2015.

[133] G Lee et al. *`PyWavelets` - Wavelet Transforms in Python"*. `https://github.com/PyWavelets/pywt`. Accessed: 2018-05-26. 2006.

[134] Arthur H Compton. "A quantum theory of the scattering of X-rays by light elements". *Physical review* 21.5 (1923), p. 483.

[135] *National Nuclear Data Center, information extracted from the Chart of Nuclides database*. `http://www.nndc.bnl.gov/chart/`. Accessed: 2018-06-08.

[136] *XCOM: Photon Cross Sections Database*. `https://physics.nist.gov/PhysRefData/Xcom/html/xcom1.html`. Accessed: 2018-06-09.

[137] *SciPy, `scipy.stats.weibull_min`*. `https://docs.scipy.org/doc/scipy/reference/generated/scipy.stats.weibull_min.html`. Accessed: 2018-06-11.

[138] *StatsModels: `proportion_confint`*. `http://www.statsmodels.org/dev/generated/statsmodels.stats.proportion.proportion_confint.html`. Accessed: 2018-06-19.

[139] John W Tukey. *Exploratory Data Analysis*. Vol. 2. Reading, Mass., 1977.

[140] C Wiseman et al. *Livetime and Exposure for* MAJORANA DEMONSTRATOR *Data Sets 0-6 (Internal)*. Tech. rep. 2018-032. URL: `https://mjdoc.npl.washington.edu/record/1909?ln=en`.

[141] Wouter Verkerke and David Kirkby. "The RooFit toolkit for data modeling". *Statistical Problems in Particle Physics, Astrophysics and Cosmology*. World Scientific, 2006, pp. 186–189.

[142] Roger Barlow. "Extended Maximum Likelihood". *NIM A* 297 (1990), pp. 496–506.

[143] R.J. Barlow. *Statistics: A Guide to the Use of Statistical Methods in the Physical Sciences*. Manchester Physics Series. Wiley, 1989. ISBN: 9780471922957. URL: `https://books.google.com/books?id=qqKgx47QMX8C`.

[144] Samuel S Wilks. "The Large-Sample Distribution of the Likelihood Ratio for Testing Composite Hypotheses". *The Annals of Mathematical Statistics* 9.1 (1938), pp. 60–62.

[145] S Mertens et al. "Sensitivity of next-generation tritium beta-decay experiments for keV-scale sterile neutrinos". *Journal of Cosmology and Astroparticle Physics* 2015.02 (2015), p. 020.

[146] Brandon R. White. Private communication.

[147] R Agnese et al. "Production Rate Measurement of Tritium and Other Cosmogenic Isotopes in Germanium with CDMSlite". *arXiv:1806.07043* (2018).

[148] P Chu et al. *Unidoc of Energy Performance of* Majorana Demonstrator *(Internal)*. Tech. rep. 2017-012. URL: `https://mjdoc.npl.washington.edu/record/1856/files/energy_unidocV3.pdf`.

[149] P Bandyopadhyay and CU Segre. *MuCal*. `http://www.csrri.iit.edu/mucal.html`. Accessed: 2017-05-25.

[150] *X-Ray Data Booklet, LBNL*. `http://xdb.lbl.gov/`. Accessed: 2018-06-20.

[151] J Redondo. *Supplemental Material for "Solar Axion Flux From the Axion-Electron Coupling"*. `http://www.mpp.mpg.de/members/redondo/material.html`. Accessed: 2017-02-17.

[152] FT Avignone III. Private communication.

[153] AS Barabash et al. "Two neutrino double-beta decay of 100Mo to the first excited 0+ state in 100Ru". *Physics Letters B* 345.4 (1995), pp. 408–413.

[154] AV Derbin et al. "Search for solar axions produced by Compton process and bremsstrahlung using the resonant absorption and axioelectric effect". *arXiv preprint arXiv:1312.0187* (2013).

[155] K Jakovcic et al. “A search for solar hadronic axions using Kr-83”. *arXiv preprint nucl-ex/0402016* (2004).

[156] S Andriamonje et al. “Search for solar axion emission from ^{7}Li and D(p, γ) ^{3}He nuclear decays with the CAST γ-ray calorimeter”. *Journal of Cosmology and Astroparticle Physics* 2010.03 (2010), p. 032.